ADVANCING OUR UNDERSTANDING OF STRUCTURE AND FUNCTION IN THE BRAIN: DEVELOPING NOVEL APPROACHES FOR NETWORK INFERENCE AND EMERGENT PHENOMENA

EDITED BY: Chris G. Antonopoulos, Nicolás Rubido, Antonio Batista and Murilo S. Baptista

PUBLISHED IN: Frontiers in Physics, Frontiers in Neuroscience and Frontiers in Computational Neuroscience

frontiers Research Topics

frontiers

ISSN 1664-8714
ISBN 978-2-88966-472-6
DOI 10.3389/978-2-88966-472-6

About Frontiers

Frontiers is more than just an open-access publisher of scholarly articles: it is a pioneering approach to the world of academia, radically improving the way scholarly research is managed. The grand vision of Frontiers is a world where all people have an equal opportunity to seek, share and generate knowledge. Frontiers provides immediate and permanent online open access to all its publications, but this alone is not enough to realize our grand goals.

Frontiers Journal Series

The Frontiers Journal Series is a multi-tier and interdisciplinary set of open-access, online journals, promising a paradigm shift from the current review, selection and dissemination processes in academic publishing. All Frontiers journals are driven by researchers for researchers; therefore, they constitute a service to the scholarly community. At the same time, the Frontiers Journal Series operates on a revolutionary invention, the tiered publishing system, initially addressing specific communities of scholars, and gradually climbing up to broader public understanding, thus serving the interests of the lay society, too.

Dedication to Quality

Each Frontiers article is a landmark of the highest quality, thanks to genuinely collaborative interactions between authors and review editors, who include some of the world's best academicians. Research must be certified by peers before entering a stream of knowledge that may eventually reach the public - and shape society; therefore, Frontiers only applies the most rigorous and unbiased reviews.
Frontiers revolutionizes research publishing by freely delivering the most outstanding research, evaluated with no bias from both the academic and social point of view. By applying the most advanced information technologies, Frontiers is catapulting scholarly publishing into a new generation.

What are Frontiers Research Topics?

Frontiers Research Topics are very popular trademarks of the Frontiers Journals Series: they are collections of at least ten articles, all centered on a particular subject. With their unique mix of varied contributions from Original Research to Review Articles, Frontiers Research Topics unify the most influential researchers, the latest key findings and historical advances in a hot research area! Find out more on how to host your own Frontiers Research Topic or contribute to one as an author by contacting the Frontiers Editorial Office: frontiersin.org/about/contact

ADVANCING OUR UNDERSTANDING OF STRUCTURE AND FUNCTION IN THE BRAIN: DEVELOPING NOVEL APPROACHES FOR NETWORK INFERENCE AND EMERGENT PHENOMENA

Topic Editors:
Chris G. Antonopoulos, University of Essex, United Kingdom
Nicolás Rubido, Universidad de la República, Uruguay
Antonio Batista, Universidade Estadual de Ponta Grossa, Brazil
Murilo S. Baptista, University of Aberdeen, United Kingdom

Citation: Antonopoulos, C. G., Rubido, N., Batista, A., Baptista, M. S., eds. (2021). Advancing Our Understanding of Structure and Function in the Brain: Developing Novel Approaches for Network Inference and Emergent Phenomena. Lausanne: Frontiers Media SA. doi: 10.3389/978-2-88966-472-6

Table of Contents

frontiers in Physics

EDITORIAL
published: 15 January 2021
doi: 10.3389/fphy.2020.626093

Editorial: Advancing Our Understanding of Structure and Function in the Brain: Developing Novel Approaches for Network Inference and Emergent Phenomena

Chris G. Antonopoulos[1]*, *Nicolás Rubido*[2,3], *Antonio M. Batista*[4] and *Murilo S. Baptista*[5]

[1]Department of Mathematical Sciences, University of Essex, Colchester, United Kingdom, [2]Aberdeen Biomedical Imaging Centre, University of Aberdeen, Aberdeen, United Kingdom, [3]Instituto de Física de Facultad de Ciencias, Facultad de Ciencias, Universidad de la República, Montevideo, Uruguay, [4]Department of Mathematics and Statistics, State University of Ponta Grossa, Ponta Grossa, Brazil, [5]Department of Physics, Institute for Complex Systems and Mathematical Biology (ICSMB), University of Aberdeen, Aberdeen, United Kingdom

Keywords: biophysics, network inference, synchronisation, structure and function in the brain, complex systems, emergent phenomena

OPEN ACCESS

Edited by:
Silvina Ponce Dawson,
University of Buenos Aires, Argentina

Reviewed by:
Luis Diambra,
National University of La Plata, Argentina

****Correspondence:***
Chris G. Antonopoulos
canton@essex.ac.uk

Specialty section:
This article was submitted to Biophysics, a section of the journal Frontiers in Physics

Received: *04 November 2020*
Accepted: *10 November 2020*
Published: *15 January 2021*

Citation:
Antonopoulos CG, Rubido N, Batista AM and Baptista MS (2021) Editorial: Advancing Our Understanding of Structure and Function in the Brain: Developing Novel Approaches for Network Inference and Emergent Phenomena. Front. Phys. 8:626093. doi: 10.3389/fphy.2020.626093

Editorial on the Research Topic

Advancing Our Understanding of Structure and Function in the Brain: Developing Novel Approaches for Network Inference and Emergent Phenomena

Complex systems are ubiquitous in nature and are the subject of intense research in the last decades [1]. A complex system is composed of a large number of non-trivially interacting components whose collective behavior cannot be determined from the behavior of the components [2]. Many real-world systems can be modeled as complex, such as stock markets, the Internet and the brain [3].

In the brain, a massive number of microscopic components (neurons or cortical areas) interact in nonlinear ways, where important information resides in the relationships among them and not necessarily within their individual dynamics. Hence, studying the dynamics of these components without knowing how they are interconnected does not allow for the understanding of the behavior of the brain as a whole. Furthermore, connectivity is often unknown and difficult to infer due to large system-sizes and multiple time and spatial scales. This poses significant challenges and open questions.

The work in this Research Topic advances our understanding on complex systems at large and on the inner workings of the brain. The reader will find novel analytical and computational results on these fields as well as the mathematical-models pertaining to complex systems and network neuroscience.

In the first paper by Lassa Ortiz et al., the open problem of the nervous system representation of a motor program is addressed. In birdsong production, it has been proposed that some special temporal instances are preferentially represented in the cortex. The authors computed these temporal instances for two species and reported which of them is better suited to test the proposed coding and alternative models, against data.

The mechanisms underlying effective propagation of high intensity information over a background of irregular firing and response latency in cognitive processes remain unclear. To address this open problem, the author in He proposes a synchronous spiking cortical column propagation integration circuit (SSCCPI). Using numerical simulations, it was demonstrated that SSCCPI circuits provide a possible mechanism of effective signal propagation in cortical networks.

Interactions between different temporal scales of the information flow in complex networks were studied in Sotero et al. and were found to be stronger in scale-free than in Erdős-Rényi networks. It was also found that phase-amplitude coupling decreased in subjects with Alzheimer's disease compared to healthy controls. These results suggest a link between cognitive impairment and multi-scale information flow in the brain.

Imagined activities can be a cognitive basis for creative thinking. However, it is still unknown how they are related to the architecture of the brain. The authors in Baravalle et al. used an information theoretical approach accounting for the time causality of the signal and the closeness centrality of different nodes. They discovered the pertinence of the alpha band while performing and distinguishing specific imaginary or visuomotor assignments.

Excitatory neurons in the visual cortex are significant in understanding brain functions. However, some neuron types and their morphological properties have not been fully deciphered. The authors in Zhang et al. applied the brain-wide positioning system to image the entire brain of two Thy1-eYFP H-line male mice. Their results demonstrate a paradigm for resolving the visual cortex through single-neuron-level quantification and show potential to be extended to reveal the connectome of other sensory and motor systems.

Excessively high neural synchronization has been associated with epileptic seizures, one of the most common brain diseases worldwide. In Protachevicz et al., the authors studied neural synchronization in a random network where the dynamics on the nodes are given by adaptive exponential integrate-and-fire neurons with excitatory and inhibitory synapses. Their results demonstrate that external electrical stimulation not only can trigger synchronous behavior, but more importantly, can be used to reduce abnormal synchronization and thus, control epileptic seizures.

Time-keeping in the medial premotor cortex is governed by four kinds of ramp cell populations. In Wei et al., a spiking neuron model is presented and used to construct a complete circuit for temporal processing. The authors showed that it can reflect many of the physiological neural circuits in the brain and explain some of the phenomena in the temporal-perception process.

Connectivity and biophysical processes determine the functionality of neural networks. The authors in Kim et al. developed a real-time framework, called Neural Interactome, to visualize simultaneously and interact with the structure and dynamics of neural networks. They examined scenarios studied experimentally, such as touch response circuits and explored new scenarios that did not undergo elaborate experimental studies.

Recurrent neural networks can produce sustained state-to-state transitions without any driving inputs, where their dynamical properties are determined by neural connection strengths. In Krauss et al., the authors used multi-dimensional scaling to study similarity relations among topologically distinct motifs. Strikingly, they reported that the key parameter that controls motif dynamics is the ratio of excitatory to inhibitory connections.

Finally, a new computational framework that implements asynchronous neural dynamics was used in Bronzon to address the duality between synchronous vs asynchronous processes and their relation to conscious vs unconscious behaviors. The new framework proposes a tool to study the emergence of brain structures that might be associated with higher level cognitive capabilities.

AUTHOR CONTRIBUTIONS

All authors listed have made substantial, direct, and intellectual contribution to the work and approved it for publication.

REFERENCES

1. Thurner S, Hanel R, Klimek P. *Introduction to the theory of complex systems*. Oxford, UK: (Oxford University Press (2018).
2. Barrat A, Barthelemy M, Vespignani A. *Introduction to the modelling and analysis of complex systems*. Cambridge, England: Cambridge University Press (2008).
3. Sayama H. *Introduction to the Modelling and Analysis of Complex Systems*. OPEN SUNY: Textbooks (2015).

Conflict of Interest: The authors declare that the research was conducted in the absence of any commercial or financial relationships that could be construed as a potential conflict of interest.

frontiers in Computational Neuroscience

ORIGINAL RESEARCH
published: 07 February 2019
doi: 10.3389/fncom.2019.00005

Analysis of Structure and Dynamics in Three-Neuron Motifs

Patrick Krauss[1]*, *Alexandra Zankl*[1], *Achim Schilling*[1], *Holger Schulze*[1] and *Claus Metzner*[1,2]

[1] Experimental Otolaryngology, Neuroscience Lab, University Hospital Erlangen, Friedrich-Alexander University Erlangen-Nürnberg (FAU), Erlangen, Germany, [2] Department of Physics, Chair for Biophysics, Friedrich-Alexander University Erlangen-Nürnberg (FAU), Erlangen, Germany

Recurrent neural networks can produce ongoing state-to-state transitions without any driving inputs, and the dynamical properties of these transitions are determined by the neuronal connection strengths. Due to non-linearity, it is not clear how strongly the system dynamics is affected by discrete local changes in the connection structure, such as the removal, addition, or sign-switching of individual connections. Moreover, there are no suitable metrics to quantify structural and dynamical differences between two given networks with arbitrarily indexed neurons. In this work, we present such permutation-invariant metrics and apply them to motifs of three binary neurons with discrete ternary connection strengths, an important class of building blocks in biological networks. Using multidimensional scaling, we then study the similarity relations between all 3,411 topologically distinct motifs with regard to structure and dynamics, revealing a strong clustering and various symmetries. As expected, the structural and dynamical distance between pairs of motifs show a significant positive correlation. Strikingly, however, the key parameter controlling motif dynamics turns out to be the ratio of excitatory to inhibitory connections.

Keywords: three-node network motifs, neural networks, Boltzmann neurons, structure, dynamics

OPEN ACCESS

Edited by:
Chris G. Antonopoulos, University of Essex, United Kingdom

Reviewed by:
Masami Tatsuno, University of Lethbridge, Canada
Ernest Barreto, George Mason University, United States

***Correspondence:**
Patrick Krauss
patrick.krauss@uk-erlangen.de

Received: *02 November 2018*
Accepted: *18 January 2019*
Published: *07 February 2019*

Citation:
Krauss P, Zankl A, Schilling A, Schulze H and Metzner C (2019) Analysis of Structure and Dynamics in Three-Neuron Motifs. Front. Comput. Neurosci. 13:5. doi: 10.3389/fncom.2019.00005

INTRODUCTION

Recently, a number of projects seek to map the human connectome, aiming to connect its structure to function and behavior (Markram, 2012; Van Essen et al., 2013; Glasser et al., 2016). However, even if the connectome would be known completely, it remains an unresolved problem how to translate this detailed structural data into meaningful information processing functions and algorithms (Jonas and Kording, 2017). For instance, the connectome of *C. elegans* has been known for decades, and involves only 302 neurons. Nevertheless, even this relatively small system is not yet understood in terms of its dynamics, let alone at a functional level (Hobert, 2003; Gray et al., 2005).

Moreover, the problem is complicated by the fact that very similar dynamics of a neural network at a macroscopic level might be realized by very different structures at the microscopic level (Newman, 2003). Therefore, an important step toward extracting function from structure is a tool to quantitatively compare different structures and dynamics.

In a neural network, all relevant structural information is encoded in a weight matrix, containing the mutual connection strength of all neurons (Hertz et al., 1991; LeCun et al., 2015; Schmidhuber, 2015; Goodfellow et al., 2016). Quantifying the similarity of two weight matrices by standard measures, such as the sum of squared differences between corresponding matrix elements, is

however not sufficient because of possible permutations of the neuron indices. Similarly, the dynamical properties of a neural network are encoded in a matrix of transition probabilities between all possible network states. As mentioned before, comparing the sum of squared differences between corresponding matrix elements fails in case of neuron permutations.

To solve this problem, we develop permutation-invariant metrics for the structural distance $d_{str}(A, B)$ and for the dynamical distance $d_{dyn}(A, B)$ of two given networks A and B. By construction, these distance-measures yield $d_{str}(A, B) = 0$ and $d_{dyn}(A, B) = 0$ whenever B is topologically identical to A, even though the corresponding weight and transition matrices of A and B may differ due to inconsistent neuron indices.

We apply these distance metrics to so-called motifs, a class of small recurrent networks which have been shown to be fundamental building blocks of various complex networks (Milo et al., 2002), such as gene regulatory networks (Shen-Orr et al., 2002; Alon, 2007), the world wide web (Milo et al., 2002), and the human brain (Song et al., 2005).

We exhaustively compute the structural and dynamical distances between all possible pairs of the 3,411 different classes of three-neuron motifs with ternary connection strengths, resulting in two distance matrices with 3,411 × 3,411 entries each. Based on these matrices, we use classical multidimensional scaling (Kruskal, 1964a,b; Cox and Cox, 2000; Borg et al., 2017; Krauss et al., 2018) to visualize the structural and dynamical similarity relations between different motifs on a two-dimensional plane.

Remarkably, it turns out that the distribution of motifs, both in structural and dynamical "space," is not uniform, but strongly clustered and highly symmetrical. Moreover, the position of a motif within structural and dynamical space correlates with the ratio of excitatory and inhibitory connections (balance) in the motif's connection matrix.

METHODS

Three-Neuron Motifs

Our study is based on Boltzmann neurons (Hinton and Sejnowski, 1983) without bias. The total input $z_i(t)$ of neuron i at time t is calculated as:

$$z_i(t) = \sum_{j=1}^{N} w_{ij}\, y_j(t-1) \tag{1}$$

where $y_j(t-1)$ is the binary state of neuron j at time $t-1$ and w_{ij} is the corresponding weight from neuron j to neuron i. The probability $p_i(t)$ of neuron i to be in state $y_i(t) = 1$ is given by:

$$p_i(t) = \sigma(z_i(t)), \tag{2}$$

where $\sigma(x)$ is the logistic function

$$\sigma(x) = \frac{1}{1 + e^{-x}}. \tag{3}$$

We investigate the set of all possible network motifs that can be built from 3 Boltzmann neurons with ternary connections $w_{ij} \in \{-1, 0, +1\}$, where self connections w_{ii} are permitted (**Figure 1A**). In principle there are $3^9 = 19,683$ possible ternary 3×3 weight matrices. However, due to permutation of the neuron indices, not every matrix corresponds to a unique motif class.

We have exhaustively listed all possible ternary weight matrices in a set. We then partitioned this set into equivalence classes, defining two matrices as equivalent if they can be made element-wise identical by a suitable permutation of neuron indices. By this way, we found that there are exactly 3,411 distinct motif classes. For later convenience we label all motif classes with unique indices, which are derived from the corresponding weight matrices.

State Transition Matrices of Motifs

Since every neuron can be in one of two binary states, a 3-node motif can be in $2^3 = 8$ possible motif states. Given the momentary motif state and the weight matrix, the probabilities for all eight successive motif states can be computed, thus defining the 8×8 state transition matrix of a Markov process (**Figure 1B**). All information theoretical properties of 3-neuron motifs, such as entropy or mutual information of successive states, are determined by the state transition matrix. We therefore calculate the transition matrices for each of the 3,411 motif classes.

Motif Classes

A motif class A is defined as the set $\{A^{(m)} : m = 1 \ldots 6\}$ of weight matrices, which are all related to each other by index permutations, such as $a_{i,j} \rightarrow a_{i,j}^{(m)} = a_{\pi_m(i),\pi_m(j)}$, where π_m is the m-th permutation (**Figure 2**).

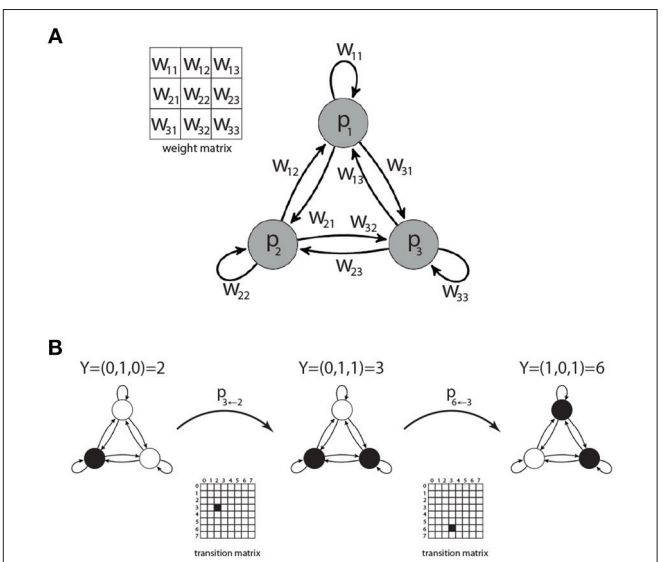

FIGURE 1 | Motifs of three coupled Boltzmann neurons. Each motif is characterized by a 3×3 weight matrix W **(A)**, defining the connection strength between the neurons. There are $2^3 = 8$ possible states $Y = 0 \ldots 7$ for each motif. The transition probabilities between these states are summarized in a 8×8 state transition matrix **(B)**.

Unique Labels of Motif Classes

The nine entries of the weight matrix $W = \begin{pmatrix} a & b & c \\ d & e & f \\ g & h & i \end{pmatrix}$ of one motif class are treated as a vector $\mathbf{w} = (abcdefghi)$. The components of this vector are then treated as the digits of a number in the ternary system:

$$a \cdot 3^8 + b \cdot 3^7 + c \cdot 3^6 + d \cdot 3^5 + e \cdot 3^4 + f \cdot 3^3 + g \cdot 3^2 + h \cdot 3^1 + i \cdot 3^0. \quad (4)$$

It can be simplified to

$$name = \sum_{i=0}^{8} \mathbf{w}[i] \cdot 3^{8-i}. \quad (5)$$

Here, $\mathbf{w}[0]$ equals the first entry of the vector $\mathbf{w}$ and the value of the sum is the name of the motif. Due to the possible entries $\mathbf{w}[i] \in \{-1, 0, 1\}$ the motif names range between "−9,841" and "9,841," starting with the motif with just "−1" as entries and finishing in the motif with just "1" as entries. Of course not every number in this range is assigned a motif class as there are in total only 3411 motif classes. This version of the formula is used because the motif class with just zeros as entries gets the name "0" and the names are approximately symmetrical around that motif class. Furthermore, in order to make the system more balanced, each motif class is represented by the weight matrix with the smallest absolute value of *name* among all of its permutations (**Figure 2**).

Structural Distance Between Motif Classes

The dynamical distance is calculated as follows (**Figure 3**): Given are two motif classes A, B. For each class we derive all six permuted weight matrices $A^{(m)}$ and $B^{(n)}$. For each of the 36 pairs of weight matrices $A^{(m)}$ and $B^{(n)}$, we compute a generalized Hamming distance $\hat{h}$, defined as the number of different ternary matrix elements:

$$\hat{h}(A^{(m)}, B^{(n)}) = \sum_{i,j} (1 - \delta_{a_{i,j}^{(m)}, b_{i,j}^{(n)}}), \quad (6)$$

where $\delta_{x,y}$ is the Kronecker symbol. The structural distance d_{str} between motif classes matrices A, B is defined as the smallest of the above 36 Hamming distances

$$d_{str}(A, B) = \min_{m,n} \left(\hat{h}(A^{(m)}, B^{(n)}) \right) \quad (7)$$

Dynamical Distance Between Motif Classes

The dynamical distance is calculated as follows (**Figure 4**): For each motif classes A, we compute general features $F(A)$, which can be scalars, vectors or matrices. In the case of matrix-like features F and G (e.g., state transition probability matrices), the Euclidean distance is defined as

$$d(F, G) = \sqrt{\sum_{i,j} (f_{i,j} - g_{i,j})^2} \quad (8)$$

To compute the dynamical distance $d_{dyn}(A, B)$ between two motif classes A and B, we derive all 36 pairs of features

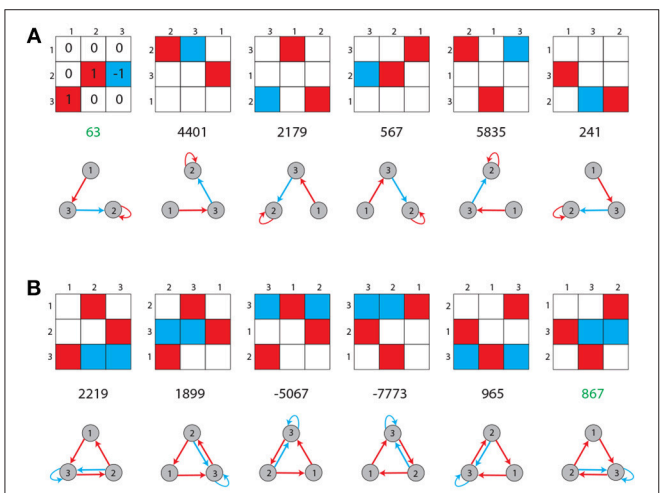

FIGURE 2 | Unique labeling of motif classes. Possible entries in the 3 × 3 weight matrix of a motif are −1 (blue), 0 (white), and +1 (red). Shown are all possible permutations of topologically equivalent motifs for two arbitrary chosen cases **(A,B)**. Each motif class is assigned a unique label (green numbers), as described in the Methods section.

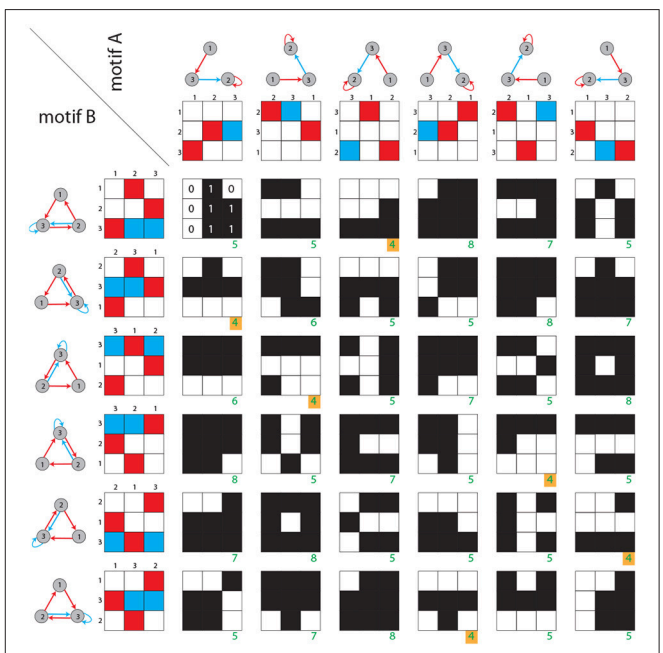

FIGURE 3 | Structural distance between motif classes. Rows and columns show the six possible permutations of two given motif classes. For each of the 36 combinations, the generalized Hamming distance $\hat{h}$ (green numbers) is computed. Black and white matrices indicate the Hamming distances between corresponding matrix elements. As described in the Methods section, the structural distance is defined as the minimum of all 36 generalized Hamming distances (green numbers with yellow background).

(e.g., the state transition matrix) from permuted weight matrices $\left(F(A^{(m)}), F(B^{(n)})\right)$ and calculate the Euclidean distance $d\left(F(A^{(m)}), F(B^{(n)})\right)$ of each pair. The dynamical distance d_{dyn} between motif classes A, B is defined as the smallest of the 36 Euclidean distances

$$d_{dyn}(A,B) = \min_{m,n}\left(d(\, F(A^{(m)}), F(B^{(n)})\,)\right) \tag{9}$$

Multidimensional Scaling

We compute the pair-wise structural and dynamical distances between all 3,411 motif classes. In order to visualize their similarity relations, we use classical multidimensional scaling (Kruskal, 1964a,b; Cox and Cox, 2000; Borg et al., 2017; Krauss et al., 2018). This method assigns to each motif class a point on the two-dimensional plane, so that the mutual geometric distances between the points reflect the structural or dynamical distances between the motif classes. In contrast to alternative visualization methods such as t-SNE (Maaten and Hinton, 2008) where the results depend crucially on the choice of parameters (Wattenberg et al., 2016), classical multidimensional scaling has no adjustable parameters and therefore produces more robust and reproducible results.

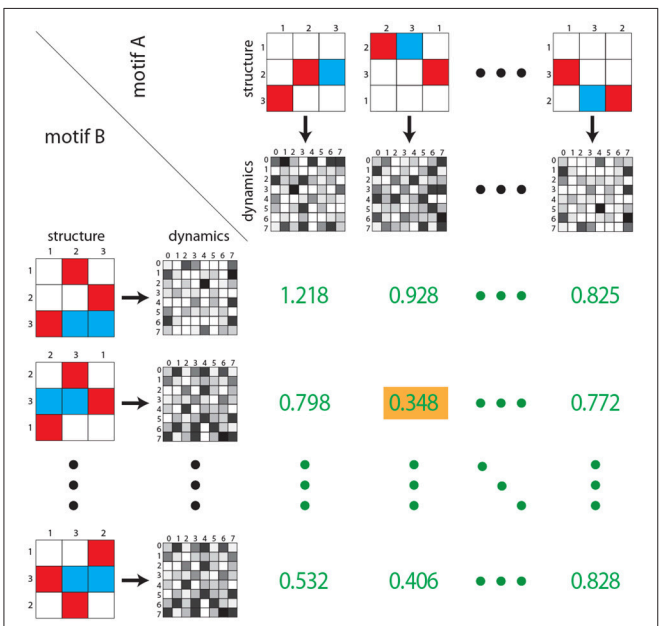

FIGURE 4 | Dynamical distance between motif classes. As in **Figure 3**, rows and columns contain the six possible permutations of two given motif classes (structure). For each permutation the corresponding state transition matrix is calculated (gray shaded matrices). Subsequently, for each of the 36 combinations, the Euclidean distance between each pair of state transition matrices is calculated (green numbers). As described in the Methods section, the dynamical distance is defined as the minimum of all 36 Euclidean distances (green number with yellow background). Note that green numbers do not correspond to actual distances, but are for illustration purposes only.

RESULTS

By an exhaustive listing of all possible weight matrices and a subsequent numerical sorting into equivalence classes, we could show that there exist 3,411 structurally distinct three-neuron motif classes with ternary connection strengths. We computed the structural and dynamical distances between all possible pairs of these motif classes, resulting in two 3,411 × 3,411 distance matrices.

In a first step, we tested the intuitive expectation that the dynamical distance d_{dyn} between motifs should grow, at least as a general trend, with their structural distance d_{str}. For this purpose, we produced a scatter plot of d_{dyn} versus d_{str}, including all $3,411^2$ pairs of motif classes (**Figure 5**). We found that for each given structural distance (except for $d_{str} = 0$), the distribution of possible dynamical distances is very large. Nevertheless, there is a clear positive correlation of $r = 0.59$ ($p < 0.001$) between structure and dynamics, thus confirming the expectation.

In a next step, we investigated the similarity relations between motif classes, as they are contained in the two 3,411 × 3,411 matrices of structural and dynamical distances. For this purpose, we have used classical multidimensional scaling (MDS) (Kruskal, 1964a,b; Cox and Cox, 2000; Borg et al., 2017; Krauss et al., 2018) to arrange all motif classes as points on a two-dimensional plane, so that the mutual geometric distances between the points reflect the corresponding structural or dynamical distances.

This two-dimensional representation reveals that the distribution of motif classes in both structural and dynamical "space" is not uniform, but instead is strongly clustered (**Figure 6**). The structural distribution (**Figures 6a,c**) also reveals

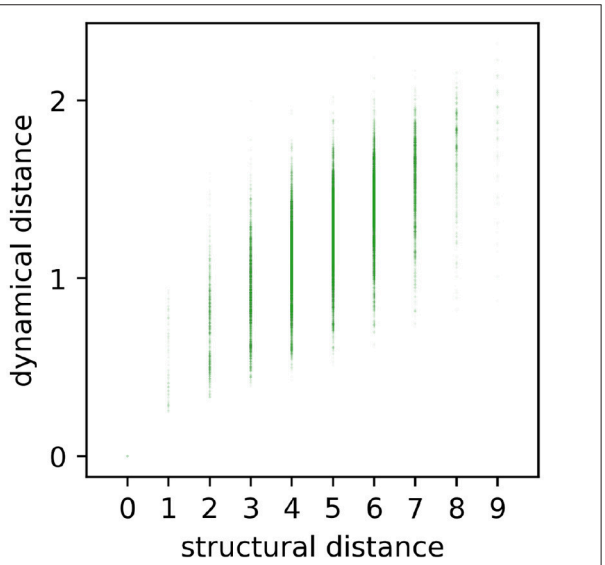

FIGURE 5 | Scatterplot of all pairwise dynamical and structural distances. Each point (d_{str}, d_{dyn}) represents the relation between structural distance d_{str} and dynamical distance d_{dyn} of a certain motif. Dynamical and structural distances are significantly correlated ($r = 0.59$, $p < 0.001$), but also show a large variance.

a six-fold rotation symmetry, which might be due to the six possible permutations of 3-neuron motifs.

As a final step, we investigated how motifs are affected by the *statistical* properties of the weight matrix. In particular, we considered the statistical parameters "density," defined as the fraction of non-zero connections among all possible connections, as well as "balance," the ratio between excitatory and inhibitory connections. We computed the values of these two statistical parameters for all motif classes and color-coded them correspondingly in the two-dimensional MDS representations (**Figure 6**).

We find that the density parameter is not at all related to the position of a motif class in the structural or dynamical plane (**Figures 6c,d**). By contrast, there is a clear linear ordering of motif classes with respect to the balance parameter (**Figures 6a,b**), both in the structural and in the dynamical plane. Indeed, altering the ratio between excitatory and inhibitory connections has a much more pronounced effect on the motif dynamics than changing the structural distance itself.

DISCUSSION

The relation of structure and function is a long-standing topic in biology (Bullock and Horridge, 1965; Estes and Cohen, 1989; Blackburn, 1991; Harris, 1996; Missale et al., 1998; Mitchell et al., 2011). On the one hand, the micro-structure of a biological system determines the set of possible functions that this system can serve. On the other hand, human observers may not be able to deduce the function of a system from its structure alone: even if we know all neural connection strengths in some sub-network of the animal brain, as well as all its input and output signals, the specific purpose of this sub-network within the whole of the organism may remain elusive (Hobert, 2003; Gray et al., 2005; Jonas and Kording, 2017). Indeed, "function" is not a property of the isolated subsystem alone, but can only be defined in the context of its embedding global system. For this reason, we focus in this work not on the function of neural systems, but on their dynamics—a property that is completely determined by the network structure and, if present, the system's input signals.

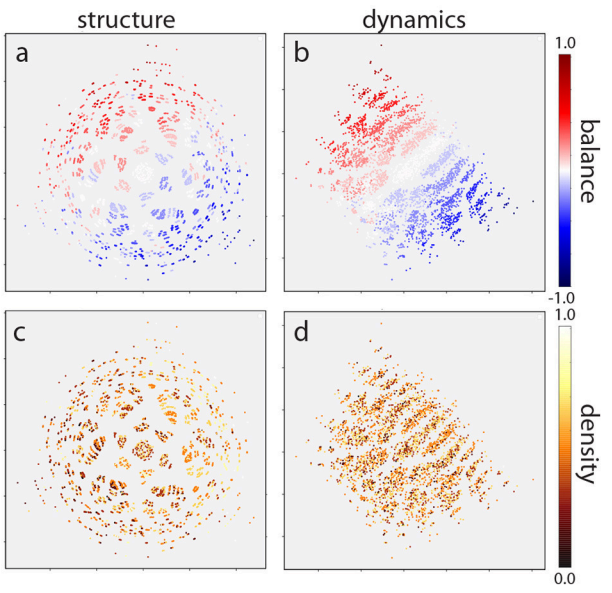

FIGURE 6 | Multidimensional scaling of motif distribution in structural **(a,c)** and dynamical **(b,d)** space. Plots are color coded according to balance **(a,b)** and density **(c,d)** parameters. The structural distribution reveals a six-fold rotation symmetry due to the six possible permutations of 3-neuron motifs. In addition, motifs are ordered linearly according to the balance parameter, in both structural **(a)** and dynamical **(b)** space. By contrast, motifs are not ordered with respect to the density parameter **(c,d)**. Note that absolute coordinates of points have no particular meaning other than scaling relative distances between any pair of points.

An additional advantage of this approach is that dynamics, just as structure, can be conveniently expressed in the form of matrices. Based on these matrices, we have developed suitable metrics that measure the distance of two neural networks in structural or dynamical space respectively. Using this tool, we can investigate how sensitive network dynamics reacts to small changes in network structure. Robustness with respect to structural changes is crucial in biological brains, as the synaptic weights cannot be adjusted with extremely high accuracy (Pinneo, 1966; Faisal et al., 2008; Rolls and Deco, 2010).

For the case of isolated three-neuron networks, we have found that the question of robustness has no definitive answer on the microscopic level of individual neuron connection strength: a small topological change in the connection matrix (i.e., adding or removing a connection, or inverting its sign), can have, both, small and large dynamical consequences. By contrast, a much clearer correlation is found between certain statistical (macroscopic) properties of a network's weight matrix and its dynamics. In particular, the ratio of excitatory to inhibitory connections (balance) affects network dynamics very strongly, while the ratio of non-zero connections (density) is much less important. This is in line with recent micro-anatomical studies of the hippocampus and the neocortex, where it was found that the balance is conserved (Megías et al., 2001; Gal et al., 2017).

This result suggests that a recurrent neural network can gain or lose a large random fraction of neural connections without drastically changing its dynamical state, provided the balance remains unchanged. We speculate that, in the brain, this surprising robustness may help to keep the cortex functional in periods of increasing density during development and contribute to the phenomenon of graceful degradation (Rolls and Treves, 1990).

In this work we abstracted from biological detail in that we included all possible three-neuron motifs with ternary connection strengths. By contrast, in the human brain the vast majority of neurons is either purely excitatory or purely inhibitory. However, there are prominent exceptions to this rule, such as the dopaminergic transmission within the basal ganglia (Kandel et al., 2000).

Future work will need to investigate whether our results extend to larger neural networks, to networks with continuous rather than ternary connection strengths between the neurons, and to networks based on alternative neuron models, such as non-probabilistic threshold units. It might also be interesting to consider networks built from mixed neuron types. Finally, we

note that our choice of probabilistic Boltzmann neurons together with zero bias leads to a firing probability of 0.5 without any input, which is not biologically realistic. Neurons with a low spontaneous firing rate might lead to other interesting dynamics and might therefore also be investigated in future work.

AUTHOR CONTRIBUTIONS

PK and CM designed the study and developed the theoretical approach. AZ performed computer simulations. PK, AS, and AZ prepared the figures. PK and CM wrote the paper. HS and AZ provided helpful discussion. All authors read and approved the final manuscript.

FUNDING

This work was supported by the Deutsche Forschungsgemeinschaft (DFG, grant SCHU1272/12-1). The authors are grateful for the donation of two Titan Xp GPUs by the NVIDIA Corporation.

REFERENCES

Alon, U. (2007). Network motifs: theory and experimental approaches. *Nat. Rev. Genet.* 8, 450–461. doi: 10.1038/nrg2102

Blackburn, E. H. (1991). Structure and function of telomeres. *Nature* 350, 569–573. doi: 10.1038/350569a0

Borg, I., Groenen, P. J., and Mair, P. (2017). *Applied Multidimensional Scaling and Unfolding*. New York, NY: Springer.

Bullock, T., and Horridge, G. A. (1965). *Structure and Function in the Nervous Systems of Invertebrates*. San Francisco, CA: W.H. Freeman.

Cox, T. F., and Cox, M. A. (2000). *Multidimensional Scaling*. Chapman and Hall/CRC.

Estes, M. K., and Cohen, J. (1989). Rotavirus gene structure and function. *Microbiol. Rev.* 53, 410–449.

Faisal, A. A., Selen, L. P., and Wolpert, D. M. (2008). Noise in the nervous system. *Nat. Rev. Neurosci.* 9, 292–303. doi: 10.1038/nrn2258

Gal, E., London, M., Globerson, A., Ramaswamy, S., Reimann, M. W., Muller, E., et al. (2017). Rich cell-type-specific network topology in neocortical microcircuitry. *Nat. Neurosci.* 20, 1004–1013. doi: 10.1038/nn.4576

Glasser, M. F., Smith, S. M., Marcus, D. S., Andersson, J. L., Auerbach, E. J., Behrens, T. E., et al. (2016). The human connectome project's neuroimaging approach. *Nat. Neurosci.* 19, 1175–1181. 87. doi: 10.1038/nn.4361

Goodfellow, I., Bengio, Y., Courville, A., and Bengio, Y. (2016). *Deep Learning, Vol. 1*. Cambridge:MIT Press.

Gray, J. M., Hill, J. J., and Bargmann, C. I. (2005). A circuit for navigation in caenorhabditis elegans. *Proc. Natl. Acad. Sci. U.S.A.* 102, 3184–3191. doi: 10.1073/pnas.0409009101

Harris, C. C. (1996). Structure and function of the p53 tumor suppressor gene: clues for rational cancer therapeutic strategies. *J. Natl. Cancer Inst.* 88, 1442–1455.

Hertz, J., Krogh, A., and Palmer, R. G. (1991). *Introduction to the Theory of Neural Computation*. Addison-Wesley/Addison Wesley Longman.

Hinton, G. E., and Sejnowski, T. J. (1983). "Optimal perceptual inference," in *Proceedings of the IEEE Conference on Computer Vision and Pattern Recognition* (Piscataway, NJ: Citeseer), 448–453.

Hobert, O. (2003). Behavioral plasticity in *C. elegans*: paradigms, circuits, genes. *J. Neurobiol.* 54, 203–223. doi: 10.1002/neu.10168

Jonas, E., and Kording, K. P. (2017). Could a neuroscientist understand a microprocessor? *PLoS Comput. Biol.* 13:e1005268. doi: 10.1371/journal.pcbi.1005268

Kandel, E. R., Schwartz, J. H., Jessell, T. M., Jessell, M. B. T., Siegelbaum, S., and Hudspeth, A. J. (2000). *Principles of Neural Science, Vol. 4*. New York, NY: McGraw-hill.

Krauss, P., Metzner, C., Schilling, A., Tziridis, K., Traxdorf, M., Wollbrink, A., et al. (2018). A statistical method for analyzing and comparing spatiotemporal cortical activation patterns. *Sci. Rep.* 8:5433. doi: 10.1038/s41598-018-23765-w

Kruskal, J. B. (1964a). Multidimensional scaling by optimizing goodness of fit to a nonmetric hypothesis. *Psychometrika* 29, 1–27.

Kruskal, J. B. (1964b). Nonmetric multidimensional scaling: a numerical method. *Psychometrika* 29, 115–129.

LeCun, Y., Bengio, Y., and Hinton, G. (2015). Deep learning. *Nature* 521, 436–444. doi: 10.1038/nature14539

Maaten, L. v. d., and Hinton, G. (2008). Visualizing data using t-SNE. *J. Mach. Learn. Res.* 9, 2579–2605.

Markram, H. (2012). The human brain project. *Sci. Am.* 306, 50–55.

Megías, M., Emri, Z., Freund, T., and Gulyás, A. I. (2001). Total number and distribution of inhibitory and excitatory synapses on hippocampal ca1 pyramidal cells. *Neuroscience* 102, 527–540. doi: 10.1016/S0306-4522(00)00496-6

Milo, R., Shen-Orr, S., Itzkovitz, S., Kashtan, N., Chklovskii, D., and Alon, U. (2002). Network motifs: simple building blocks of complex networks. *Science* 298, 824–827. doi: 10.1126/science.298.5594.824

Missale, C., Nash, S. R., Robinson, S. W., Jaber, M., and Caron, M. G. (1998). Dopamine receptors: from structure to function. *Physiol. Rev.* 78, 189–225.

Mitchell, G. F., van Buchem, M. A., Sigurdsson, S., Gotal, J. D., Jonsdottir, M. K., Kjartansson, Ó., et al. (2011). Arterial stiffness, pressure and flow pulsatility and brain structure and function: the age, gene/environment susceptibility–reykjavik study. *Brain* 134, 3398–3407. doi: 10.1093/brain/awr253

Newman, M. E. (2003). The structure and function of complex networks. *SIAM Rev.* 45, 167–256. doi: 10.1137/S003614450342480

Pinneo, L. R. (1966). On noise in the nervous system. *Psychol. Rev.* 73:242.

Rolls, E., and Deco, G. (2010). *The Noisy Brain: Stochastic Dynamics as a Principle of Brain Function* (Oxford University Press).

Rolls, E. T., and Treves, A. (1990). The relative advantages of sparse versus distributed encoding for associative neuronal networks in the brain. *Netw. Comput. Neural Syst.* 1, 407–421.

Schmidhuber, J. (2015). Deep learning in neural networks: an overview. *Neural Netw.* 61, 85–117. doi: 10.1016/j.neunet.2014.09.003

Shen-Orr, S. S., Milo, R., Mangan, S., and Alon, U. (2002). Network motifs in the transcriptional regulation network of *Escherichia coli*. *Nat. Genet.* 31:64. doi: 10.1038/ng881

Song, S., Sjöström, P. J., Reigl, M., Nelson, S., and Chklovskii, D. B. (2005). Highly nonrandom features of synaptic connectivity in local cortical circuits. *PLoS Biol.* 3:e68. doi: 10.1371/journal.pbio.0030068

Van Essen, D. C., Smith, S. M., Barch, D. M., Behrens, T. E., Yacoub, E., Ugurbil, K., et al. (2013). The WU-minn human connectome project: an overview. *Neuroimage* 80, 62–79. doi: 10.1016/j.neuroimage.2013.05.041

Wattenberg, M., Viégas, F., and Johnson, I. (2016). How to use t-SNE effectively. *Distill* 1:e2. doi: 10.23915/distill.00002

Conflict of Interest Statement: The authors declare that the research was conducted in the absence of any commercial or financial relationships that could be construed as a potential conflict of interest.

frontiers in Computational Neuroscience

ORIGINAL RESEARCH
published: 12 February 2019
doi: 10.3389/fncom.2019.00001

Symbolic Modeling of Asynchronous Neural Dynamics Reveals Potential Synchronous Roots for the Emergence of Awareness

*Pierre Bonzon**

Department of Information Systems, Faculty of HEC, University of Lausanne, Lausanne, Switzerland

A new computational framework implementing asynchronous neural dynamics is used to address the duality between synchronous vs. asynchronous processes, and their possible relation to conscious vs. unconscious behaviors. Extending previous results on modeling the first three levels of animal awareness, this formalism is used here to produce the execution traces of parallel threads that implement these models. Running simulations demonstrate how sensory stimuli associated with a population of excitatory neurons inhibit in turn other neural assemblies i.e., a kind of neuronal asynchronous wiring/unwiring process that is reflected in the progressive trimming of execution traces. Whereas, reactive behaviors relying on configural learning produce vanishing traces, the learning of a rule and its later application produce persistent traces revealing potential synchronous roots of animal awareness. In contrast, to previous formalisms that use analytical and/or statistical methods to search for patterns existing in a brain, this new framework proposes a tool for studying the emergence of brain structures that might be associated with higher level cognitive capabilities.

Keywords: symbolic modeling, neural dynamics, asynchronous process, synchronous process, emergence of awareness

OPEN ACCESS

Edited by:
Chris G. Antonopoulos,
University of Essex, United Kingdom

Reviewed by:
Cartik Sharma,
Neuromorph, Canada
Li Su,
University of Cambridge,
United Kingdom

***Correspondence:**
Pierre Bonzon
pierre.bonzon@unil.ch

Received: *29 September 2018*
Accepted: *08 January 2019*
Published: *12 February 2019*

Citation:
Bonzon P (2019) Symbolic Modeling of Asynchronous Neural Dynamics Reveals Potential Synchronous Roots for the Emergence of Awareness. Front. Comput. Neurosci. 13:1. doi: 10.3389/fncom.2019.00001

INTRODUCTION

A recurring debate about the functioning of the brain concerns the characteristics and the roles played both at the neurological and cognitive levels by *synchronous* vs. *asynchronous* processes, their relation to *conscious* vs. *unconscious* behaviors, and a possible fundamental *duality* in neural dynamics. While the synchronous activation of brain processes is widely used for describing the functioning of the cortex (Singer, 1993), diverging views apply to the specialized tasks supported by these synchronized processes. Experimental results have revealed in particular the existence of transient long-range phase synchronization leading to the hypothesis that synchronization vs. desynchronization is a candidate mechanism for controlling visual attention (Gross et al., 2004). Other studies related to the integration of attributes in a visual scene suggest that there is no central neural clock involved in this mechanism, thus making the brain a massively asynchronous organ (Zeki, 2015). In support of this diversity, results from a large scale simulation (Markram et al., 2015) report "a spectrum of network states with a sharp transition from synchronous to asynchronous activity." While no definite link between neural activity and conscious behavior (which would constitute *neural correlates of consciousness*) have been identified yet, it is common to postulate the existence of a dynamical *stream of consciousness* mediated by a global workspace (Baars, 1988)

defined as a distributed brain state connected to various brain areas, thus making perceptual information available to different tasks. In one of these theories (Dehaene and Naccache, 2001) pertaining to the particular case of conscious perception (referred to also as *access consciousness*), sensory stimuli are associated with a population of excitatory neurons that in turn inhibits other neural assemblies, thus preventing the conscious processing of other stimuli.

More generally, an emergent picture of the brain shows opposing spiking patterns in populations of neurons engaged in a competition (Zagha et al., 2015). The demonstration of temporal competition in eligibility traces for long term potentiation and depreciation (*LTP/LTD*) designates these traces as plausible synaptic substrate for reward-based learning (He et al., 2015). Together, these findings enforce a fundamental principle in circuit neuroscience according to which inhibition in neuronal networks allows in turn for disinhibition and stands as a key mechanism for circuit plasticity, learning, and memory retrieval (Letzkus et al., 2015). Ideally, brain simulations should trace cognition down to these neurological. The usual way to simulate a brain today however still basically follows one of two bottom up approaches using either finite-state automata or differential equations. The first approach, which relies on weighted connections between neural cells to implement threshold logic without regard to the actual internal functioning of these cells, has led to the development of artificial neural networks (Hopfield, 1982; Hinton et al., 2006). These networks represent the most powerful tools available today in the field of *machine learning* and have been used to model circuits that reproduce human capabilities in pattern recognition. Their biological plausibility however is a subject of controversy, and their relevance to the study of the brain is thus questionable. The second approach simulates the electrical processes surrounding neurons, and thus details the functioning of the ground level constituents of real brains. So far these *neural networks simulators* (Hines and Carnevale, 1997; Markram et al., 2015) have not been applied to drive significant cognitive processes, but seem rather to expect and rely for that on the spontaneous emergence of higher level functions.

The "*what*" and "*how*" of *computational cognitive neuroscience* (Ashby and Helie, 2011) i.e., where computer and cognitive sciences meet in order to propose biologically plausible models supporting cognitive tasks, are traditionally described using the historical "tri-level" hypothesis (Marr, 1982) that distinguishes *computational*, *algorithmic,* and *implementation* levels. A fourth *behavioral learning* dimension in brain and cognition studies has been advocated (van der Velde and de Kamps, 2015) for by arguing that cognitive processes are executed in connection structures that link sensory circuits (i.e., perception) with motor (i.e., action). Bottom-up analytical tools such as differential equations, artificial neural networks as well as methods related to dynamical systems theory (Wright and Bourke, 2013), and more recently top-down approaches using abstract mathematical tools such Bayesian inference rules (Ma and Pouget, 2008), are well-suited for describing computations in Marr's sense, but "*fail to identify algorithms and underlying circuits*" (Frégnac and Bathellier, 2015), a task that calls for a "*middle-out*" approach that can identify plausible structures linking biology and cognition.

An assessment of the present situation in this field can be found in the special issue (Stern, 2017) of the *Science* journal entitled "*Neuroscience: In search for new concepts,*" which contains insightful reviews questioning present approaches, proposing conceptual challenges and asking neuroscientists to think about new ways to investigate them. Firstly, in order to identify the mechanisms which support the human brain, both Yarstev (2017) and Frégnac (2017) call for a *comparative approach* refining similar functions in specific behavior of relevant species where dynamic entities of simulated brains grow and interact with their environment. Next, as argued by Frégnac, "big data is not knowledge" i.e., the roadmap from data to knowledge should be mapped out across successive levels of integration distinguishing *micro-scale* and *meso-scale* functions. The causal link between sub-cellular/cellular mechanisms and behavior should be achieved through successive levels of analysis, as exemplified by Marr's *tri-level hypothesis*, which means that mappings need to be expressed in *algorithmic* terms and not just in a correlative way. In order to take into account intermediate levels of circuit integration, canonical operations should be defined as *invariant* computations. Furthermore, simulations elaborated from static atlases, or connectomes, are not sufficient to model brain functions where neurons participate in multiple functional sub-networks. Toward this end, Frégnac eventually suggests that a formalism based on virtual free "*quasi-particles*" may simplify the analytical treatment. Finally, Buzsaki and Llinas (2017) note that the neuronal mechanisms associated with navigation and memory are similar, meaning they process *messages* regardless of their origin. Toward this goal, a new approach (Bonzon, 2017) to modeling neural dynamics that enforces the tri-level framework based on synaptic plasticity illustrated in Frégnac (2017) has been proposed. In order to handle messages, synaptic plasticity is abstracted through *asynchronous communication* protocols and used to link perception and action. This formalism is used here to address the duality between synchronous vs. asynchronous processes, and their possible relation to conscious vs. unconscious behaviors.

MATERIALS AND METHODS

A New Approach to Modeling Abstract Brain Functionalities

A new approach to modeling neural dynamics (Bonzon, 2017) that enforces the tri-level framework based on synaptic plasticity illustrated in Frégnac (2017) has been proposed. In order to handle messages, synaptic plasticity is abstracted through *asynchronous communication* protocols and used to link perception and action. This has been illustrated (Bonzon, 2017) though the simulation of simple animal behaviors. In this formalism, brain processes are first abstracted through virtual *microcircuits* representing canonical *invariant* computations as called for above. Sets of microcircuits are then assembled into *mesoscale* virtual circuits linking perceptions and actions. *Virtual*

circuits giving rise to streams can be compiled into *virtual code implications* to be eventually used just in time to deduce *virtual code instructions* that are finally interpreted by a virtual machine (see the **Supplementary Information** section).

While the usual approach to simulating neural dynamics starts with current flows represented by differential equations, we opted for a conceptual abstraction of synaptic plasticity represented by communicating processes between concurrent *threads*, which correspond either to a single or to a group of neurons possibly interleaved at a higher level. Contrary to traditional neuron models in which incoming signals are summed in some integrated value, thread inputs can be processed individually, thus allowing for threads to maintain parallel asynchronous communications. Threads can be grouped into disjoint sets, or *fibers*, to model neural assemblies (Huyck and Passmore, 2013), and discrete *weights* (e.g., integer numbers) can be attached to pairs of threads that communicate within the same fiber. A fiber containing at least one active thread constitutes a *stream*. On this basis, a short term cache memory (*STM*) as well as a long term associative memory (*LTM)* relying on *LTP/LTD* were defined. This eventually led to the modeling (Bonzon, 2017) of animal behaviors exhibiting, among others, rule learning capabilities (Zentall et al., 1981; Katz et al., 2008) demonstrating primitive forms of animal consciousness according a typology (Pepperberg and Lynn, 2000) proposed in the context of comparative zoology.

Basic Concepts

To introduce the basic concepts of this formalism, let us consider a simple case of synaptic transmission between any two threads **P** and **Q** (*NB throughout this text, identifiers starting with a capital letter stand for variable parameters*). This can be represented by the circuit fragment (or wiring diagram) contained in the simple stream given in **Figure 1**, where the symbol **->=>-** represents a synapse.

This circuit fragment can be represented by two symbolic expressions involving a pair of **send/receive** processes as shown in **Figure 2**.

In **Figure 2**, the thread **P** e.g., a sensor thread **sense(s)**, will fire in reaction to the capture of an external stimulus **s**, with the **send** process corresponding to the signal, or spike train, carried by a pre-synaptic neuron's axon. In the thread **Q** [e.g., an effector thread **motor(X)**, where the variable **X** becomes instantiated as the result of the stimulus], the **receive** process represents the possible reception of this signal by a post-synaptic neuron. The compilation of these expressions will give rise to virtual code implications implementing the communication protocol given in **Figure 3**.

This protocol corresponds to an *asynchronous* blocking communication subject to a threshold. It involves a predefined weight between the sender **P** and the receiver **Q** that can be either incremented or decremented**.** On one side, thread **P** fires thread **Q** if necessary and sends it a signal. On the other side, thread **Q** waits for the reception of a signal from thread **P** and proceeds only if the weight between **P** and **Q** stands above a given threshold. The overall process amounts to opening a temporary *pathway* between **P** and **Q** and allows for passing data by instantiating variable parameters (see example below).

A Simple Model of Classical Conditioning

As an example, let us consider a simple model of classical conditioning in which a conditioned stimulus **cs** elicits a weak reflex, and a unconditioned stimulus **us** produces a massive reflex. After a few pairings of **cs** and **us**, where **cs** slightly precedes **us**, a stimulus **cs** alone triggers an enhanced reflex. This is represented by the virtual circuit given in **Figure 4**.

In **Figure 4**, the threads **sense(us)** and **sense(cs)** correspond to sensory neurons, and **motor(X)** to a motor neuron, where **X** is a variable that will be instantiated into **us** or **cs**. Finally, the thread **ltp** (for *long term potentiation*) acts as a facilitatory interneuron reinforcing the pathway (i.e., augmenting its *weight*) between **sense(cs)** and **motor(cs)**. The protocols depicted by the symbols **->=>-** and **/|** represent, respectively, a *synapse* and the modulation of a synapse, the sign * indicates the conjunction of converging signals, and the sign + either the splitting of a diverging signal, as used in the lower branch, or, a choice between converging signals, as used in the right branch instantiating the thread **motor(X)**. Classical conditioning then follows from hebbian learning i.e., "neurons that fire together wire together." Though it is admitted today that classical conditioning in aplysia is mediated by multiple neuronal mechanisms including a post-synaptic retroaction on a presynaptic site, the important issue is that the learning of a new behavior requires a conjoint activity of multiple neurons that leads to implement the thread **ltp** as a *detector of coincidence*, as done in **Figure 5**.

The generic microcircuit abstracting the mechanism of long term potentiation *(***ltp**) is given in **Figure 5**. In order to detect the coincidence of **P** and **Q**, thread **P** fires an **ltp** thread that in turn calls on process **join** to wait for a signal from thread **Q**. In parallel, thread **Q** calls on process **merge** to post a signal for **ltp** and then executes a **send(R)** command to establish a link with thread **R**. After its synchronization with thread **Q**, thread **ltp** increments the weight between **Q** and **R**.

A Model of a Simple Case of Operant Conditioning

As another example, let us consider a simple form of *operant conditioning* in which an organism, as a result of a perception, generates either an *excite* or an *inhibit* internal stimulus and associates this feedback with either an *accept* or *reject* action. This gives rise to two competing neural populations, as represented in the circuit given in **Figure 6** in which inputs are represented by a vector *I* of external perceptions.

At the beginning of the simulation, the pathways from **sense(I)** to learn[accept(I)] is open, while the pathways to both accept(I) and reject(I) are closed. After a few trials, the pigeon will have learned to close learn[accept(I)] through an **ltd** process and to open either accept(I) or reject(I)through an ltp process. This procedure matches a fundamental principle in circuit neuroscience according to which *inhibition* in neuronal networks during baseline conditions allows in turn for *disinhibition*, which then stands as a key

```
…-P->=>-Q-…
```

FIGURE 1 | Circuit fragment implementing a synaptic transmission.

```
thread(P,[…,send(Q)])
thread(Q,[receive(P),…])
```

FIGURE 2 | Thread patterns for a synaptic transmission.

```
P:  …
    send(Q)          activate Q if Q is not active and post a signal for Q
Q:  receive(P)       wait for a signal from P and proceed if weight(P,Q)>0
    …
```

FIGURE 3 | Communication protocol for an asynchronous communication.

```
      sense(cs)-*->=>-
               /|\     |
               ltp    +-motor(X)
                |      |
      sense(us)-+->=>-z
```

FIGURE 4 | A mesoscale virtual circuit implementing classical conditioning.

mechanism for circuit plasticity, learning, and memory retrieval (Letzkus et al., 2015).

Communication Protocols

As illustrated and briefly discussed above, virtual circuits rely on communication protocols that are pictured in thread diagrams by iconic symbols representing themselves microcircuits. These protocols are defined by pairs of procedures:

- **send/receive**, denoted by the symbols ->=>- or -<=<-, represents a synaptic transmission
- **join/merge**, denoted by /|\ or \|/, implements long term potentiation/depression (**ltp/ltd**)
- **push/pull**, denoted by -<A>-, models a short term cache memory (**stm**)
- **store/retrieve**, denoted by -{P}-, models an associative memory (**ltm**) based on long term storage and retrieval (**lts/ltr**)

The microcircuits implementing these protocols are detailed in Bonzon (2017).

Virtual Machine Definition

The virtual machine (Bonzon, 2017), which was originally designed to execute a *"sense-act"* cycle of embodied cognition, is extended here to implement a *"sense-act-reflect"* cycle that allows for tracing down the sequences of *synchronized* events associating a thread and a stimulus (see **Figure 7** for the functional definition of this machine, and the online **Supplementary Information** for its complete operational specifications).

Let us just mention some characteristics of this machine that clearly distinguish it from traditional computers of the von Neumann type. First, it does not involve stored program acting on stored data. Consequently, this machine doesn't have an instruction register holding the current instruction being executed after its retrieval from an addressable memory. The *ist* predicate (standing for "is true") implements *contextual deduction* (Bonzon, 1997). A register *clock (T)*, which corresponds to a program counter in traditional machines, is associated with each thread and hold its local time *T*. These registers are used in turn to deduce an instruction. Whenever an instruction succeeds, its thread clock is advanced and the next instruction is deduced, and whenever it fails, it is executed again until it eventually succeeds. Altogether, this amounts to descending into a thread instruction tree, with its local clock time corresponding to the currently reached depth. In other words, as postulated for instance by Zeki (2015), there is no central clock,

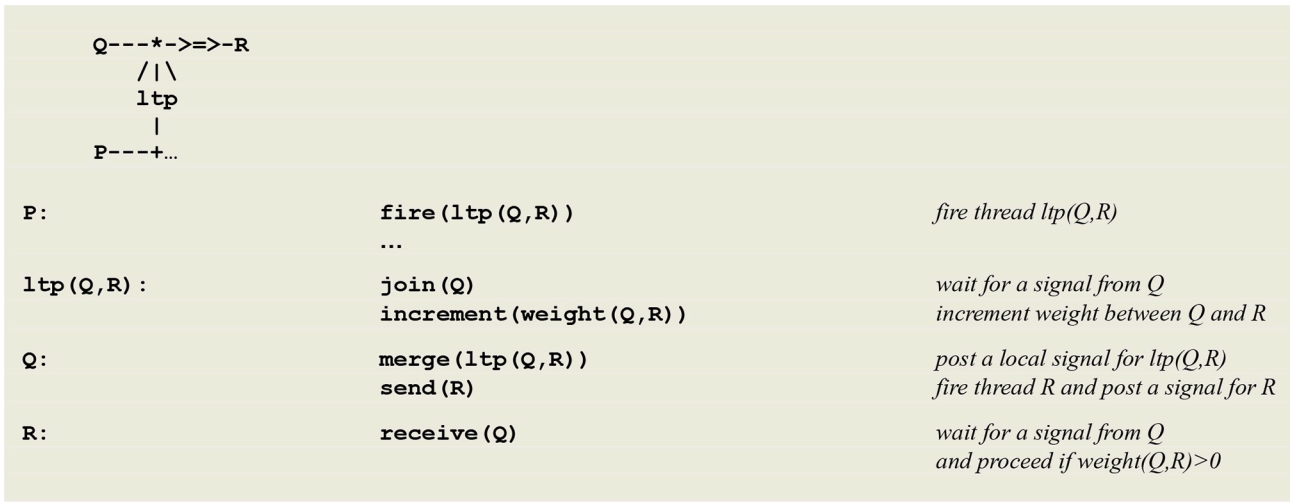

FIGURE 5 | Micro-circuit and communication protocol for *ltp*.

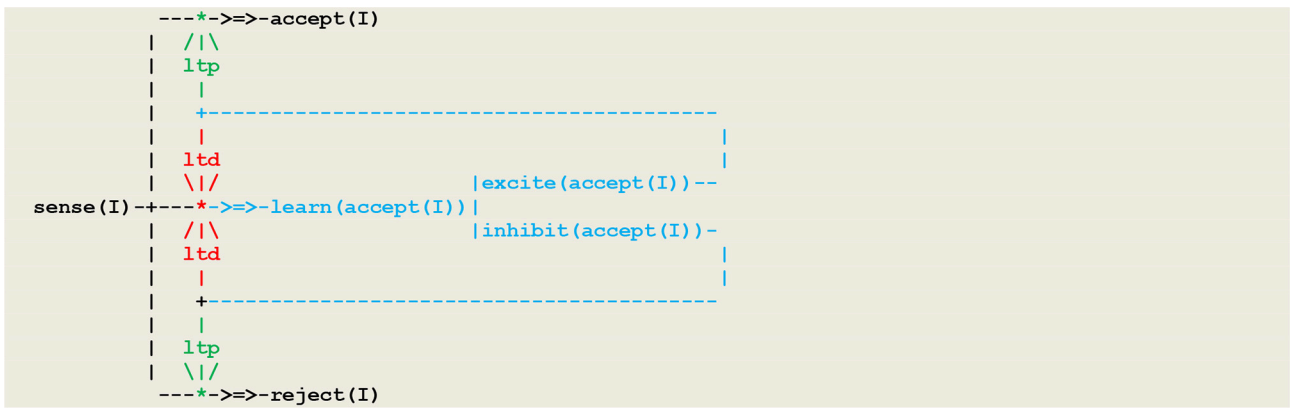

FIGURE 6 | A virtual circuit implementing simple operant conditioning.

thus "making of the brain a massively asynchronous organ." The execution of virtual instructions leads to a wiring/unwiring process that produces model configurations that are akin to plastic brain states. By interpreting code deduced configurations that are akin to brain states, the overall architecture of this system could thus turn out to be close to that of a brain.

The core of a simulation platform implementing the formalism described above is defined by a logic program of about 300 lines. This platform can be run on any PC equipped with a Prolog compiler, which thus allows for an easy reproduction of results.

RESULTS

Simulating Simple Animal Behaviors

In order to explore a possible duality between synchronous vs. asynchronous processes and conscious vs. unconscious behaviors, we used our extended formalism to perform a series of simulation of simple animal behaviors exhibiting in turn the first three level of animal consciousness according to Pepperberg and Lynn's typology (Pepperberg and Lynn, 2000). While this taxonomy is not the definite source on the subject, their proposal does comply with the requirements listed in our Introduction i.e.,

- they follow a *comparative approach* refining similar functions in the behavior of relevant species
- they include an *evolutive learning* dimension
- they can be implemented by canonical operations defined as *invariant* computations that constitute particular cases of *operant conditioning* linked to plausible neural processes.

Briefly, the first level of animal awareness corresponds to the ability to follow a simple rule involving the perception of a specific item or event and then either its acceptation or its rejection (e.g., a case of *matching/oddity* to sample). Whereas, this first level does not allow for an immediate transfer to a similar task, an organism with the second level is aware enough of a rule to transfer it across situations and thus to adopt for

Let *Model* represent the state of the virtual machine holding virtual code implications compiled from fibers.
A virtual machine *run* is constituted by a loop comprising a *sense-react-reflect* cycle

```
run(Model)
 loop sense(Model)
      react(Model)
      reflect(Model)
```

The *sense* loop implements the capture of an input *interrupt* directed to a *stream*

```
sense(Model)
 if   interrupt(Stream(Input))
 then input(Model(Stream),Input)
```

The *react* loop calls on each asynchronous *thread* within each *stream* to deduce a virtual *instruction* at its local clock time *T* and execute it

```
react(Model)
 for each  Stream(Thread),T:Instruction,
 such that  ist(Model(Stream)(Thread),(clock(T), T:Instruction))
 do  execute(Model(Stream)(Thread), T:Instruction)
```

The reflecting loop calls on each *stream* at its global sequence number *I* to report its synchronization with a *stimulus* processed by a *thread*

```
reflect(Model)
 for each  Stream, I:Thread:Stimulus ,
 such that  ist(Model(Stream),(seq(I), I:Thread:Stimulus))
 do  report(Model(Stream), I:Thread:Stimulus)
```

FIGURE 7 | High level definition of a virtual machine run.

example a *win/stay lose/shift* rule (or strategy) relying on a short-term memory. In order to make a categorical judgment (e.g., to *sort* items by recalling their properties), the third level of animal awareness provides an organism with the additional capacity to integrate two different sets of stored information. This implies in turn some kind of associative long term memory.

A Simulation of the First Level of Animal Awareness

Our first simulation refers to an experiment (Wright, 1997) that was designed in order to discriminate between two possible strategies for solving a *non-matching-to sample* (*NMTS*) task (Katz et al., 2008). In this experiment, a subject (e.g., a pigeon) is presented with a sample that can be of one of two colors (e.g., red or green), and then confronted with a pair of buttons (e.g., one left and one right button) of two different colors, one of them matching the color of the sample. In order to get a reward, the subject must choose the button that doesn't have the same color as the sample. A first strategy, called *configural learning*, is to learn the correct choice associated with each combination of colors (or external stimuli). The resulting unconscious reactive behavior then relies on memorized *links* between perception and action. This strategy is implemented in the circuit given in **Figure 8** that constitutes an extension of **Figure 6** including an internal *fetch* stimulus that triggers a random choice between the two buttons.

The execution trace of a running simulation is given in **Figure 9**. In this example, the same vector i.e., **[sensor(left([green]),right([red]),sample([red]))]** was repeatedly presented as input. The prefixes **1:, 2:, 3**:, etc., represent the stream's sequence numbers ***I*** akin to a global time series and the arguments (3), (4), (3), (3), etc., are threads local times. These traces contain first a transient part (**Figures 9A–C)** corresponding to the learning process. This process is implemented via successive internal fetch and excite/inhibit stimuli that give rise in turn to the increment/decrement of synaptic weights. This demonstrates how internal stimuli associated with a population of excitatory neurons inhibit in turn other neural assemblies i.e., a kind of neuronal wiring/unwiring process that is reflected in the progressive trimming of the execution trace. The second part (**Figures 9D,E**), void of any internal stimulus, then reflects an unconscious reactive behavior associating a *sensor* and an *effector*.

Another strategy, called *relational learning*, is to compare in turn each button with the sample, learn to match colors, and then choose the button that doesn't match the sample. In other words, subjects do not learn to choose a color, but to match colors and then avoid the matching color i.e., to choose the non-match. This behavior corresponds to the first *level* of animal consciousness defined as the ability to learn and apply a simple *rule* associating the perception of a specific concept or event and then either

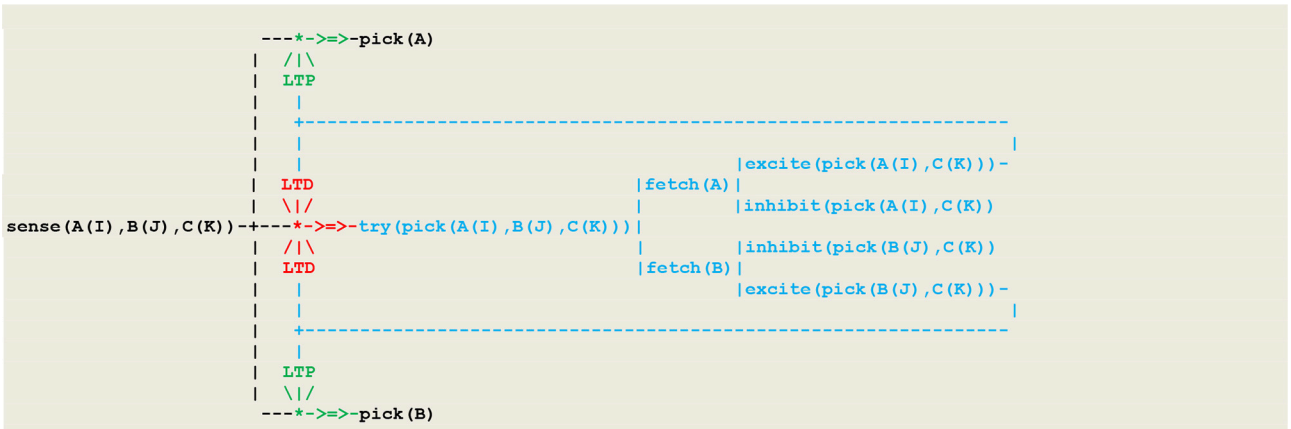

Visual stimuli captured by sensors are represented by expressions `A(I)`, `B(J)`, `C(K)`, where `A`, `B`, `C` correspond to the left and right buttons and to the sample, respectively, and the vector parameters `I`, `J`, `K` can take the value `[green]` or `[red]`.

FIGURE 8 | Circuit for configural learning.

its acceptation or its rejection (Pepperberg and Lynn, 2000). This strategy is implemented in the circuit given in **Figure 10**, where two additional layers implement learning to match and eventually choosing to avoid the match.

The same configuration i.e.,

[sensor(left([green]),right([red]),sample([red])),
sensor(left([green]),sample([red])),
sensor(right([red]),sample([red]))]

was repeatedly presented as input. The execution trace, which reflects the learning of a rule followed by its repeated application, contains a *transient* part (**Figures 11A–D**) made of successive internal stimuli followed by a *persistent* part (**Figures 11E,F**) presenting the recurrent pattern of a single internal stimulus i.e., *inhibit*, which signals the application of the rue commanding to "avoid matching the color."

Simulating the Second and Third Level of Animal Awareness

Similar results have been obtained with simulations that were performed for experiments (Savage-Rumbaugh et al., 1980; Cole et al., 1982) characterizing, respectively, the second and third levels of animal consciousness. A subject with the second *level* is aware enough of a rule to transfer it across situations and thus to adopt for example a *win/stay lose/shift* rule. This implies a capacity to remember one's last choice, and has been implemented using a short term cache memory (*STM*) that allow for the modeling of a synchronized *recall* thread. The *third level* of animal awareness refers to the additional capacity to make a categorical judgment (e.g., to *sort* items) and has been implemented using an associative long term memory (*LTM*) that similarly allows for the *recall* of facts or events (see Bonzon, 2017 for details).

Summary of Results

The results of the simulations presented above can be summarized as follows:

- as illustrated in **Figure 9**, unconscious reactive behaviors relying on configural learning produce *transient* traces that reflect the *asynchronous* processing of internal stimuli
- as illustrated in **Figure 11**, behaviors relying on a rule produce traces containing a *transient* part that reflect the *asynchronous* processing of internal stimuli, followed by a *persistent* part that present a recurrent *synchronous* pattern corresponding to the rule conscious application.

From these results, we postulate as a principle:

- ***persistent recurrent patterns in execution traces reveal potential synchronous roots of consciousness.***

Let us recall from **Figure 7** that our formalism relies on a fiber structure, where asynchronous *threads* having each their own *local time* are grouped into *streams*, which represent disjoints sets of simultaneously active threads, each stream being associated with a sequence number akin to a *global time*. The *synchronization* defined on this basis then simply associates the instruction being executed at thread time *T* with its supporting stream at sequence number *I*. Each recurrent pattern thus actually reflects the synchronization of an internal stimulus with its supporting stream e.g., in **Figures 11E,F**, the synchronization of stimulus

inhibit(match(left([green]),sample([red])))
in thread
try(match(left([green]),sample([red])))

FIGURE 9 | Execution trace. **(A–C)** Transient part. **(D,E)** Void part.

at its local time (3) with its supporting stream at global time 1:
These recurring patterns constitute an example of emergent brain structures that might be associated with higher level cognitive capabilities**.** Following advances in the study of glial cells (Tadi et al., 2015; Dallérac and Rouach, 2016; Papouin et al., 2017), the possible relation of these synchronizations with consciousness could be found in the interaction between neurons and astrocytes. According to the "astrocentric hypothesis" (Robertson, 2013), conscious perception arises through a process of global synchrony in which information patterns carried by neuronal spike trains are transferred to astrocytic waves (Pereira and Furlan, 2009; Pereira et al., 2017). It is suggested that the persistent traces revealed in our simulation are at the roots of this transfer process.

DISCUSSION

This discussion will extend in three directions i.e., the hypothetical formal properties of the proposed formalism, its relevance to the study of consciousness, and its comparison with previous similar work.

Hypothetical Formal Properties

The assessment of a system's formal properties should include both its *validation* and a theoretical account of its *computational power*. A throughout development of these two points is out of the scope of this paper. We shall therefore restrict ourselves to situate the proposed formalism within these contexts. Its

FIGURE 10 | Circuit for rule learning.

various components are further presented below in the online **Supplementary Information**.

Validation

The validation of a system aims at providing a mathematical proof that its implementation satisfies its requirements i.e., that "*what it actually does*" is "*what it was designed to do*." To try and answer the first question, let us consider the functional signature that can associated with the function representing the run of a model. The concept of a virtual machine that we use allows for emulating the execution of a program given in a *symbolic* language S on a system having its own *logical* language L. On the cognitive side, *virtual circuits,* which somehow correspond to cognitive software written in language S, are compiled into virtual code implications of language L. On its neural side, these implications are used in turn to deduce just in time instructions that get interpreted by the virtual machine i.e., this virtual machine actually performs *contextual deductions* (Bonzon, 1997). In addition, languages I and O define, respectively, *input/output* sentences captured by *sensors* and delivered to *effectors*. Running a model on a virtual machine then defines the function:

$$run: I \times S \times (S \rightarrow L) \times L \rightarrow L \times O$$

According to classical results in computer science, symbolic expressions that have been compiled and then interpreted by a virtual machine get their operational semantics from the transitions they induced on the state of this machine. In other words, what the system actually does is to update the virtual machine state. As there is no specified final state, whichever state the machine is in at any given time is acceptable and represents the simulated subject's current state of mind.

As for the second question (i.e., "what was this machine designed for"), the goal of the present work was to study the emergence of brain structures that might be associated with higher level cognitive capabilities i.e., with processes that are still unknown. In this perspective, the whole idea of validation and/or model checking, which eventually should to lead to ask "*how to specify a given task,*" may look premature.

Computational Power

Following the pioneering work of Siegelmann and Sontag (Siegelmann and Sontag, 1995), the computational equivalence between *rational recurrent neural networks* and *Turing machines* has become the starting point for the study of devices with *super Turing* computational power. Various extensions incorporating

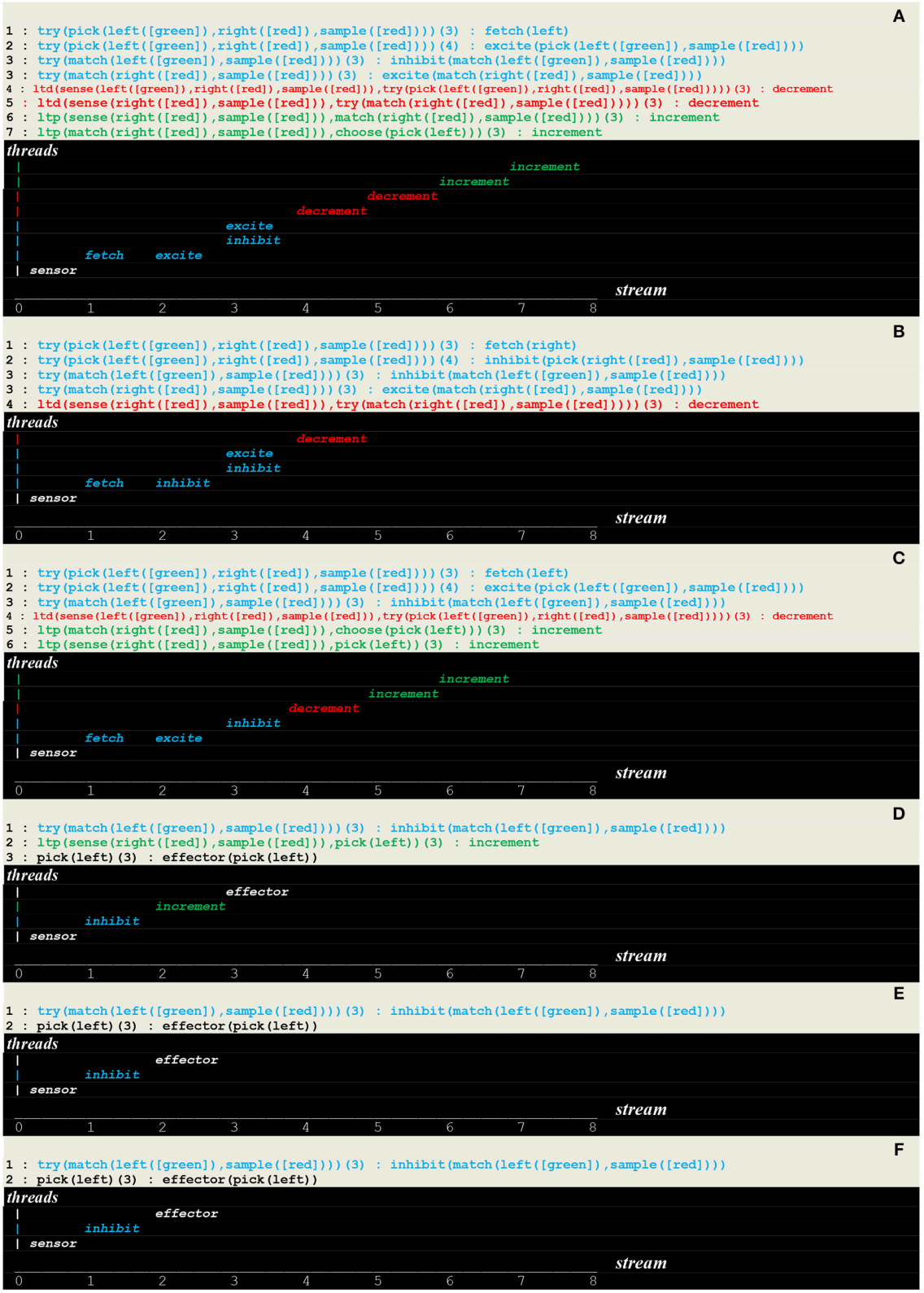

FIGURE 11 | Execution trace. **(A–D)** Transient part. **(E,F)** Persistent part.

concepts such as *rational* vs. *analog* machine and *interactive* vs. *evolutive* machines have recently culminated in a new equivalence stating that "*basic neural models combining the two crucial features of evolvability and interactivity are actually capable of super-Turing computational capabilities, irrespective of whether their synaptic weights are modeled by rational or real numbers*" (Cabessa, 2012; Cabessa and Villa, 2013). In other words, taking into account both evolving and interactive capabilities in a neural net model provides an "alternative and equivalent way to the incorporation of the power of the continuum toward the achievement of super-Turing computational capabilities." Intuitively, our own model, which incorporates both a mechanism of communication based on concurrent threads and an implementation of synaptic plasticity based on Hebbian learning, satisfies the conditions required to belong to the class of super Turing computational devices. The proof of this statement will eventually require a substantial effort toward mapping our formalism into the primitive operations that are allowed in such proofs.

Relevance With the Study of Consciousness

Very generally, unconscious and conscious behavior have been described, respectively, as lacking conscious attention and as enjoying an introspective reporting capability (Shanahan, 2010). Various studies have focused on the search for the signature of the neural activity that differentiates between the two, but their overall results appear inconsistent (Dehaene and Changeux, 2011). Some of these results however are compatible with our postulate as stated in section Summary of Results. As an example, experiments related to a delayed matching to sample task (Dehaene et al., 2003) have suggested that the neural signature of unconscious vs. conscious perception could be a *local coordination* vs. a *global synchronization* of neural activity. Further results (Dehaene et al., 2006; Melloni et al., 2007) about the same task have concluded that *transient synchronization* is the critical event that triggers an access to consciousness. Our postulate is also consistent with the proposal (Lamme, 2003) of recurrent interactions, first *locally* within the visual system, and then *globally* into parieto-frontal regions, as well as with the hypothesis (Zeki, 2003) of an *asynchronous* construction of visual perception in distributed sites before binding into a "macro-consciousness." By referring to synchronized events associating a stimulus with a sensory stream, it is also compatible with another approach (Morsella et al., 2015) concluding that the origin of consciousness could be found at the level of processing that is shared with "representations of the immediate external environment." Hypothetically, as noted in section Summary of Results, persistent traces revealed in our simulations could be at the root of the transfer process from neural spike trains to astrocytic waves (Pereira and Furlan, 2009). Our concept of a virtual machine offering an interface between two domains (see section Bottom Up Design of Virtual Circuits of the **Supplementary Information**) could constitute the adequate tool for modeling such a transfer.

Related Work

Previous work related to the modeling of brain and cognition using symbolic methods, and more generally to global brain simulations and the emergence of consciousness, are now reviewed.

In an extension of his early work on classical conditioning (Klopf, 1988), Klopf Johnson et al. (2001) did propose a computational model of learned avoidance that relies on an internal clock controlling both classically and instrumentally conditioned components, thus allowing for an explicit "proprioceptive feedback" i.e., a kind of primitive consciousness. This proposal opposed the then dominant paradigm requiring an evaluative feedback from the environment. This opposition did rest on the argument that "*animals do not receive error signals during learning,*" thus pointing out to the biological implausibility of error-correction back propagation i.e., an argument that, notwithstanding the proven effectiveness of this technique as a tool for functional approximation, is still valid today for brain research.

Using classical results on Hopfield networks and attractors (Hopfield, 1982), Balkenius and his co-workers (Balkenius et al., 2018) did implement a *memory model for robots*. In this model, a prototypal form of consciousness arises from sensory information filled in a memory that in turns produces memory transitions over time, thus creating an inner world that is used both to interpret external input and to support "thoughts disconnected from the present situation." A far reaching but questionable conclusion of this study is that "an inner world is a *sine qua non* for consciousness."

The work by Deco et al. (2008) falls in the category of "whole (or global) brain" simulations. Their theoretical account follows an overall *statistical* strategy. Degrees of freedom are successively reduced to resolve an otherwise intractable computational problem. Populations of spiking neurons get first reduced to distribution functions describing their probabilistic evolution, giving then rise to neural fields defined by differential operators involving both temporal and spatial terms. It finally proposes a measure for partitioning the brain into functionally relevant regions, this so-called "dynamical workspace of binding nodes" being supposedly responsible for binding information into conscious perceptions and memories. As in our own proposal, this formalism uses a multilevel architecture, which in this case distinguishes between the single neuron level, the mesoscopic describing how neural elements interact to yield emergent behavior, and the macroscopic level of dynamical large-scale neural systems such as cortical regions, the thalamus, etc. Each level of this description relates to neuroscience data, from single-unit recordings, through local field potentials to functional magnetic resonance imaging (fMRI). In conclusion, this formalism uses analytical and statistical tools to search for existing patterns in a functioning brain. In contrast, our own framework, which is constrained solely by a symbolic model of synaptic plasticity, proposes a tool for shaping the brain by linking perception to behavior trough a mechanism of hebbian learning.

Besold and Kühnberger (2015) envision a system that operates on different levels corresponding to the layers in a system's architecture in order to update network structures via the artificial equivalent of synaptic dynamics. Our formalism relying on a virtual machine can be considered as an attempt to implement this architecture via a conceptual abstraction of synaptic plasticity. Our formalism also bears some similarities with a new model of neural networks, namely *fibring neural networks* (Garcez and Gabbay, 2004) that, similarly to threads, allow for the activation of groups of neurons and thus represent different levels of abstraction.

With a few notable exceptions (e.g., Smith, 1992; Ruksénasz et al., 2009; Su et al., 2014), system validation is an issue that is seldom addressed in computational cognitive neuroscience. In order to obtain symbolic descriptions of neuronal behavior that allow for model checking, Su et al. have applied concurrency theory in a framework extending classical automata theory with communicating capabilities. A network of communicating automata is then mapped into a labeled transition system whose inference rules (for both internal transitions and automata synchronizations) define the semantics of the overall model. Su et al. further show that, in accordance with our own approach, asynchronous processing is not only a more biologically plausible way to model neural systems than do conventional artificial neural networks with synchronous updates, but also offers new perspectives for the cognitive modeling of higher level cognitive capabilities through emergent synchronous processes.

AUTHOR CONTRIBUTIONS

The author confirms being the sole contributor of this work and has approved it for publication.

SUPPLEMENTARY MATERIAL

The Supplementary Material for this article can be found online at: https://www.frontiersin.org/articles/10.3389/fncom.2019.00001/full#supplementary-material

REFERENCES

Ashby, F. G., and Helie, S. (2011). A tutorial on computational cognitive neuroscience, modeling the neurodynamics of cognition. *J. Math. Psychol.* 55, 273–289. doi: 10.1016/j.jmp.2011.04.003

Baars, B. A. (1988). *Cognitive Theory of Consciousness*. Cambridge, UK: Cambridge University Press.

Balkenius, C., Tjøstheim, T. A., Johansson, B., and Gärdenfors, P. (2018). From focused thought to reveries: a memory system for a conscious robot. *Front. Robot. AI* 5:29. doi: 10.3389/frobt.2018.00029

Besold, T., and Kühnberger, K. (2015). Towards integrated neural–symbolic systems for human level AI: two research programs helping to bridge the gaps. *Biol. Ins. Cogn. Arch.* 14, 97–110. doi: 10.1016/j.bica.2015.09.003

Bonzon, P. (1997). "A reflective proof system for reasoning in contexts," in *Proc AAAI97*. Available online at: www.aaai.org/Papers/AAAI/1997/AAAI97-061.pdf

Bonzon, P. (2017). Towards neuro-inspired symbolic models of cognition: linking neural dynamics to behaviors through asynchronous communications. *Cogn. Neurodyn.* 11, 327–353. doi: 10.1007/s11571-017-9435-3

Buzsaki, G., and Llinas, R. (2017). Space and time in the brain. *Science* 358, 482–485. doi: 10.1126/science.aan8869

Cabessa, J. (2012). "Interactive evolving recurrent neural networks are super-turing," in *ICAART*, eds J. Filipe and A. L. N. Fred (Setubal: SciTePress), 328–333.

Cabessa, J., and Villa, A. (2013). The super-turing computational power of interactive evolving recurrent neural networks. *LNCS* 8131, 58–56 doi: 10.1007/978-3-642-40728-4_8

Cole, S., Hainsworth, F. R., Kamil, A. C., Mercier, T., and Wolf, L. L. (1982). Spatial learning as an adaptation in hummingbirds. *Science* 217, 655–657. doi: 10.1126/science.217.4560.655

Dallérac, G., and Rouach, N. (2016). Astrocytes as new targets to improve cognitive functions. *Prog. Neurobiol.* 144, 48–67. doi: 10.1016/j.pneurobio.2016.01.003

Deco, G., Jirsa, V. K., Robinson, P. A., Breakspear, M., and Friston, K. (2008). The dynamic brain: from spiking neurons to neural masses and cortical fields. *PLoS Comput. Biol.* 4:e1000092. doi: 10.1371/journal.pcbi.1000092

Dehaene, S., and Changeux, J. P. (2011). Experimental and theoretical approaches to conscious processing. *Neuron* 70, 220–227. doi: 10.1016/j.neuron.2011.03.018

Dehaene, S., Changeux, J. P., Naccache, L., Sackur, J., and Sergent, C. (2006). Conscious, preconscious, and subliminal processing: a testable taxonomy. *Neuron* 10, 204–211. doi: 10.1016/j.tics.2006.03.007

Dehaene, S., and Naccache, L. (2001). Towards a cognitive neuroscience of consciousness: basic evidence and a workspace framework. *Cognition* 79, 1–37. doi: 10.1016/S0010-0277(00)00123-2

Dehaene, S., Sergent, C., and Changeux, J. P. (2003). A neuronal network model linking subjective reports and objective physiological data during conscious perception. *Proc. Nat. Acad. Sci. U.S.A.* 100, 8520–8525. doi: 10.1073/pnas.1332574100

Frégnac, Y. (2017). Big data and the industrialization of neuroscience: a safe roadmap for understanding the brain? *Science* 358, 470–477. doi: 10.1126/science.aan8866

Frégnac, Y., and Bathellier, B. (2015). Cortical correlates of low-level perception: from neural circuits to percepts. *Neuron* 88. doi: 10.1016/j.neuron.2015.09.041

Garcez, A., and Gabbay, D. (2004). "Fibring neural networks," in *Proceedings of the 19th Natl Confon Artificial Intelligence* (AAAI Press).

Gross, J., Schmitz, F., Schnitzler, I., Kessler, K., Shapiro, K., Hommel, B., et al. (2004). Modulation of long-range neural synchrony reflects temporal limitations of visual attention in humans. *Proc. Nat. Acad. Sci. U.S.A.* 101, 13050–13055. doi: 10.1073/pnas.0404944101

He, K., Huertas, M., Hong, S. Z., Tie, X., Hell, J. W., Shouval, H., et al. (2015). Distinct eligibility traces for LTP and LTD in cortical synapses. *Neuron* 88, 528–538. doi: 10.1016/j.neuron.2015.09.037

Hines, M. L., and Carnevale, N. T. (1997). The NEURON simulation environnement. *Neural Comput.* 9, 1179–1209. doi: 10.1162/neco.1997.9.6.1179

Hinton, G. E., Osindero, S., and The, Y. W. (2006). A fast learning algorithm for deep beliefs net. *Neural Comput.* 18, 1527–1554. doi: 10.1162/neco.2006.18.7.1527

Hopfield, J. J. (1982). Neural networks and physical systems with emergent collective computational abilities. *Proc. Natl. Acad. Sci. U.S.A.* 79, 2554–2558. doi: 10.1073/pnas.79.8.2554

Huyck, C., and Passmore, P. (2013). A review of cell assemblies. *Biol. Cybern.* 107, 263–288. doi: 10.1007/s00422-013-0555-5

Johnson, J., Li, W., Li, J., and Klopf, H. (2001). A computational model of learned avoidance behavior in a one-way avoidance experiment. *Adapt. Behav.* 9, 91–104. doi: 10.1177/105971230200900205

Katz, J. S., Bodily, K., and Wright, A. A. (2008). Learning strategies in matching to sample: if-then and configural learning by pigeons. *Behav. Proces.* 77, 223–230. doi: 10.1016/j.beproc.2007.10.011

Klopf, H. A. (1988). Neuronal model of classical conditioning. *Psychobiology* 16, 85–125.

Lamme, V. (2003). Why visual attention and awareness are different. *Trends Cogn. Sci.* 7, 12–18. doi: 10.1016/S1364-6613(02)00013-X

Letzkus, J., Wolff, S., and Lüthi, A. (2015). Disinhibition, a circuit mechanism for associative learning & memory. *Neuron* 88, 264–276. doi: 10.1016/j.neuron.2015.09.024

Ma, W., and Pouget, A. (2008). Linking neurons to behavior in multisensory perception: a computational review. *Brain Res.* 1242, 4–12. doi: 10.1016/j.brainres.2008.04.082

Markram, H., Muller, E., Ramaswamy, S., Reimann, M. W., Abdellah, M., Sanchez, C. A., et al. (2015). Reconstruction & simulation of neocortical microcircuitry. *Cell* 163, 456–492. doi: 10.1016/j.cell.2015.09.029

Marr, D. (1982). *Vision: A Computational Investigation into the Human Representation and Processing of Visual Information*. New York, NY: Freeman.

Melloni, L., Molina, C., Pena, M., Torres, D., Singer, W., and Rodriguez, E. (2007). Synchronization of neural activity across cortical areas correlates with conscious perception. *J. Neurosci.* 14, 2858–2865. doi: 10.1523/JNEUROSCI.4623-06.2007

Morsella, E., Godwin, C., Jantz, T., Krieger, S., and Adam Gazzaley, A. (2015). Homing in on consciousness in the nervous system: an action-based synthesis. *Behav. Brain Sci.* 39, 1–17. doi: 10.1017/S0140525X15000643

Papouin, T., Dunphy, J., Tolman, M., Foley, J. C., and Haydon, P. G. (2017). Astrocytic control of synaptic function. *Philos. Trans. R. Soc. B* 372:20160154. doi: 10.1098/rstb.2016.0154

Pepperberg, I., and Lynn, S. (2000). Possible levels of animal consciousness with reference to grey parrots (*Psittaccus erithacus*). *Am. Zool.* 40, 893–901. doi: 10.1093/icb/40.6.893

Pereira, A., Foz, B., and Rocha, A. (2017). The dynamical signature of conscious processing: From modality specific percepts to complex episodes. *Psychol. Consci. Theor. Res. Prac.* 4, 230–247. doi: 10.1037/cns0000115

Pereira, A., and Furlan, A. (2009). On the role of synchrony for neuron–astrocyte interactions and perceptual conscious processing. *J. Biol. Phys.* 35, 465–480. doi: 10.1007/s10867-009-9147-y

Robertson, J. (2013). Astrocyte domains and the three-dimensional and seamless expression of consciousness and explicit memories. *Med. Hypotheses* 81, 1017–1024. doi: 10.1016/j.mehy.2013.09.021

Ruksénasz, R, Back, J., Curzon, P., and Blandford, A. (2009). Verification-guided modeling of salience and cognitive load. *Formal Aspects Comput.* 21, 541–569. doi: 10.1007/s00165-008-0102-7

Savage-Rumbaugh, E. S., Rumbaugh, D. M., Smith, S., and Lawson, J. (1980). Reference, the linguistic essential. *Nature* 210, 922–925.

Shanahan, M. (2010). *Embodiment and the Inner Life: Cognition and Consciousness in the Space of Possible Minds*. Oxford: Oxford University Press.

Siegelmann, H., and Sontag, E. (1995). On the computational power of neural nets. *J. Comput. Syst. Sci.* 50, 132–150. doi: 10.1006/jcss.1995.1013

Singer, W. (1993). Synchronization of cortical activity and its putative role in information processing and learning. *Annu. Rev. Physiol.* 55, 349–374. doi: 10.1146/annurev.ph.55.030193.002025

Smith, L. (1992). A framework for neural net specification. *IEEE Trans. Softw. Eng.* 18, 601–612. doi: 10.1109/32.148478

Stern, P. H. (2017). Neuroscience: in search for new concepts. *Science* 358, 464–465 doi: 10.1126/science.358.6362.464

Su, L., Gomez, R., and Bowman, S. (2014). Analysing neurobiological models using communicating automata. *Formal Aspects Comput.* 26, 1169–1204. doi: 10.1007/s00165-014-0294-y

Tadi, M., Allaman, I., Lengacher, S., Grenningloh, G., and Magistretti, P. J. (2015). Learning-induced gene expression in the hippocampus reveals a role of neuron-astrocyte metabolic coupling in long term memory. *PLoS ONE* 10:e0141568. doi: 10.1371/journal.pone.0141568

van der Velde, F., and de Kamps, M. (2015). The necessity of connection structures in neural models of variable binding. *Cogn. Neurodyn.* 9, 359–337. doi: 10.1007/s11571-015-9331-7

Wright, A. A. (1997). Concept learning and learning strategies. *Psychol. Sci.* 8, 119–123 doi: 10.1111/j.1467-9280.1997.tb00693.x

Wright, J. J., and Bourke, P. D. (2013). On the dynamics of cortical development: synchrony and synaptic self-organization. *Front. Comput. Neurosci.* 7:4. doi: 10.3389/fncom.2013.00004

Yarstev, M. (2017). The emperor's new wardrobe: rebalancing diversity of animal models in neuroscience research. *Science* 358, 466–469. doi: 10.1126/science.aan8865

Zagha, E., Ge, X., and McCormick, D. A. (2015). Competing neural ensembles in motor cortex gate goal-directed motor output. *Neuron* 88, 565–577. doi: 10.1016/j.neuron.2015.09.044

Zeki, S. (2003). The disunity of consciousness. *Trends Cogn. Sci.* 7, 214–7218. doi: 10.1016/S1364-6613(03)00081-0

Zeki, S. (2015). A massively asynchronous, parallel brain. *Philos. Tran. R. Soc. B* 370:20140174. doi: 10.1098/rstb.2014.0174

Zentall, T., Edwards, C., Moore, B., and Hogan, D. (1981). Identity: the basis for both matching and oddity learning in pigeons. *J. Exp. Psychol.* 7, 70–86. doi: 10.1037/0097-7403.7.1.70

Conflict of Interest Statement: The author declares that the research was conducted in the absence of any commercial or financial relationships that could be construed as a potential conflict of interest.

frontiers in Computational Neuroscience

METHODS
published: 13 March 2019
doi: 10.3389/fncom.2019.00008

Neural Interactome: Interactive Simulation of a Neuronal System

Jimin Kim[1], *William Leahy*[2] *and Eli Shlizerman*[1,2]*

[1] Department of Electrical and Computer Engineering, University of Washington, Seattle, WA, United States, [2] Department of Applied Mathematics, University of Washington, Seattle, WA, United States

Connectivity and biophysical processes determine the functionality of neuronal networks. We, therefore, developed a real-time framework, called Neural Interactome[1,2], to simultaneously visualize and interact with the structure and dynamics of such networks. Neural Interactome is a cross-platform framework, which combines graph visualization with the simulation of neural dynamics, or experimentally recorded multi neural time series, to allow application of stimuli to neurons to examine network responses. In addition, Neural Interactome supports structural changes, such as disconnection of neurons from the network (ablation feature). Neural dynamics can be explored on a single neuron level (using a zoom feature), back in time (using a review feature), and recorded (using presets feature). The development of the Neural Interactome was guided by generic concepts to be applicable to neuronal networks with different neural connectivity and dynamics. We implement the framework using a model of the nervous system of *Caenorhabditis elegans* (*C. elegans*) nematode, a model organism with resolved connectome and neural dynamics. We show that Neural Interactome assists in studying neural response patterns associated with locomotion and other stimuli. In particular, we demonstrate how stimulation and ablation help in identifying neurons that shape particular dynamics. We examine scenarios that were experimentally studied, such as touch response circuit, and explore new scenarios that did not undergo elaborate experimental studies.

Keywords: *C. elegans*, brain simulation, connectome, neural dynamics, network visualization

OPEN ACCESS

Edited by:
Chris G. Antonopoulos, University of Essex, United Kingdom

Reviewed by:
Daqing Guo, University of Electronic Science and Technology of China, China
Masanori Shimono, Kyoto University, Japan

***Correspondence:**
Eli Shlizerman
shlizee@uw.edu

Received: *22 November 2018*
Accepted: *30 January 2019*
Published: *13 March 2019*

Citation:
Kim J, Leahy W and Shlizerman E (2019) Neural Interactome: Interactive Simulation of a Neuronal System. Front. Comput. Neurosci. 13:8. doi: 10.3389/fncom.2019.00008

INTRODUCTION

Modeling neuronal systems involves incorporating two modeling layers. The first fundamental layer is of neuronal connectivity (connectome). The layer on top of it is of biophysical processes of neural responses and interactions. In the recent years there has been significant progress in resolving and modeling both layers. Connectomes of several organisms and systems, such as the nematode *Caenorhabditis elegans (C. elegans),* the *Drosophila* medulla, the mouse retina, mouse primary visual cortex, and others have been fully or partially mapped on various scales: from macro to single neuron level (White et al., 1986; Open Connectome Project, 2010; Van Den Heuvel and Pol, 2010; Bock et al., 2011; Briggman et al., 2011; Haspel and O'Donovan, 2011; Varshney et al., 2011). Also, decades of research in describing and modeling biophysical processes have provided both experimental and computational foundations for modeling single neuron dynamics as well

[1] Web interface available at http://neuralcode.amath.washington.edu/neuralinteractome
[2] Source code available at https://github.com/shlizee/C-elegans-Neural-Interactome

as synaptic and electric processes between neurons (Koch and Segev, 1988; Wicks et al., 1996; Letinic et al., 2002; Koch, 2004; Söhl et al., 2005; Briggman et al., 2006; Skinner, 2012; Druckmann et al., 2014; Kunert et al., 2014). Due to these advances, models incorporating both layers have become more detailed and realizable for several neuronal systems. These models are called *Dynomes* as they correspond to dynamical system acting on top of the static connectome (Kopell et al., 2014).

Being closer to the realistic neuronal system, *dynome* studies have more potential to reveal neural pathways and functionalities of the network (Bargmann and Marder, 2013; Sporns and Bullmore, 2014; Liu et al., 2018). However, they also introduce challenges in finding appropriate methods for efficient studies of network capabilities (Mucha et al., 2010). Brute force approaches will typically produce formidable amounts of data, where extraction or characterization of relevant neural patterns can be cumbersome and time consuming. For that reason, collaborative initiatives such as Brian introduced generic simulation engines for neural dynamics and the OpenWorm project (incorporating Geppetto engine) suggested to apply generic neural models to *C. elegans* (Goodman and Brette, 2008, 2009; Raikov and De Schutter, 2012; Szigeti et al., 2014; Chen and De Schutter, 2017; Cantarelli et al., 2018; Sarma et al., 2018). Such frameworks are advantageous and allow flexibility to simulate various dynamics on top of generic connectomics.

Here, we have taken a complementary approach. We focus on *efficient* simulation of the *established* connectome of *C. elegans* somatic nervous system in conjunction with *established biophysical dynamics*. We have accompanied the simulation with interpretable visualization of dynamics-connectomics. The visualization is designed in such a way that it incorporates real-time interactive capabilities to investigate architecture and observe neural activity at the same time. Such a framework allows for a new way of investigating and simulating neuronal systems and as far as we know has not been introduced for any dynamic network, in particular nervous systems models. In such a framework, the necessary components are (i) ability to apply or modify stimuli to the network in real-time as in experiments; (ii) being able to observe the neural dynamics on various time and population scales, and (iii) allow for network structural changes. Furthermore, the framework is expected to perform seamless integration for such functions and include review capabilities for exploration of the system and dynamics in depth. In this work, we thereby develop the Neural Interactome, which is a generalized visualization framework incorporating such capabilities. The framework employs a graph visualization layout to represent the static connectome. On top of the layout, it incorporates dynamic visual components to represent real-time neural responses according to user interactions. These components are implemented via synchronization between the backend neural integrator of the *dynome* and the graph layout of the interactive interface. The backend neural integrator is connected to neurons stimuli panel, and permits setting external stimuli and changing the structure of the graph on demand. The framework also includes real-time plotting of neural activity as well as review, preset and save modes that allow for further exploration of simulated dynamics.

In this paper, we focus on applying the framework to the nervous system of *C. elegans* nematode, which consists of 302 neurons with three types (sensory, inter, motor). Such a system is thus relatively small to be fully reconstructed and analyzed. Indeed, the near-complete connectome of the nervous system has been resolved using serial section electron microscopy (White et al., 1986; Chen et al., 2006; Varshney et al., 2011). The connectome data includes enumeration of neural connections for the complete somatic nervous system (279 neurons) of *synaptic* type, where *GABAergic* neurons make inhibitory synapses, and *glutamergic* and *cholinergic* neurons form excitatory synapses. The connectome also enumerates *gap* junctions (electrical connections) for each pair of neurons. The connectome data is robust, since *C. elegans* neurons are recognizable and consistent throughout individual worms (White et al., 1986). Furthermore, *C. elegans* synaptic and gap connections are common across animals with more than 75% reproducibility (White et al., 1986; Durbin, 1987; Hall and Russell, 1991; Bargmann, 1993). In addition to the anatomical structure of the nervous system, biophysical *in-situ* recordings of membrane voltage response to input current injected into each individual neuron in the network have been performed (Wicks et al., 1996; Goodman et al., 2012). These revealed that *C. elegans* neurons are of non-spiking type with graded potential membrane voltage profile (Goodman et al., 1998). Following these studies, a set of mathematical models describing neural membrane voltage and interaction between the neurons were developed (Goodman et al., 1998; Kunert et al., 2014).

The availability of near-complete connectome data along with experimental quantification of responses and interactions provided a computational basis for reconstructing both static and dynamic layers of *C. elegans* neuronal network. Combination of these two layers was recently developed (Kunert et al., 2014). When applied with prescribed input stimuli, *C. elegans dynome* was capable of producing various forms of characteristic dynamics such as static, oscillatory, non-oscillatory and transient voltage patterns (Kunert-Graf et al., 2017). These dynamics indicated that *C. elegans dynome* is a valuable model for the worm's nervous system, and patterns observed are suggested to be consistent with the experimentally observed ones. In particular, stimulation of sensory PLM neurons with constant current resulted in a two-mode dominant oscillatory behavior in forward locomotion motor neurons (Kunert et al., 2014). The model is expected to include a variety of other additional patterns, however, their full validation is formidable to perform, as it requires many simulations with various stimuli amplitudes and combinations. For instance, in the context of touch response, it would be valuable to examine stimulation of ALM and AVM sensory neurons, which in experiments was identified as associated with anterior touch response and expressed as backward crawling (Chalfie et al., 1985; Driscoll and Kaplan, 1997). Furthermore, transitions from one type of dynamics to another (e.g., from oscillatory to non-oscillatory) are also

expected to exist when input stimuli shift from one value to another. It is thereby introduction of a framework that facilitates these studies can assist in such goal.

DESIGN AND IMPLEMENTATION

We first describe the main components of the Neural Interactome framework, and then continue to demonstrate its application to the nervous system of *C. elegans* worm for stimulation scenarios.

INTERACTIVE INTERFACE FOR NEURONAL NETWORK

The frontend of Neural Interactome is an interactive interface consisting of (i) neural stimulation/ablation interface, (ii) visualization of dynamics, (iii) control of simulation timescale, and (iv) review system.

Neural Stimulation and Ablation

Neural stimuli are controlled by stimulation panel located on the left side of the screen. The panel enslists and categorizes all neurons in the network into three group types (sensory, inter, motor). Each group type is given a characteristic color (sensory: blue, inter: green, motor: red). Each individual neuron on the panel is a clickable button with a scrollable bar, which allows setting amplitudes of constant stimulus, i.e., inject current to the neuron (of nA nano-ampere unit). The amplitude of the stimulus can be adjusted prior to running a simulation (as initial condition), or at any time during the simulation. When stimulus is being adjusted during the simulation, it effectively imitates "clamping" of neurons in the network. In addition, to allow for testing various structural configurations for the network, the panel is designed to support neural ablation of neurons. By clicking on a neuron while holding the shift key, the neuron is grayed-out in the interface. Such operation disconnects the neuron from all of its respective connections (both receiving and outgoing) in both synaptic and gap type and thus effectively removes it from the network. The ablation can also be undone (reinsertion) by repeating the operation of shift key + clicking on the ablated neuron. Similar to neural stimulation, both ablation and reinsertion can be performed prior and during network simulation.

Dynome Visualization

Connectivity Representation

Visualization of the *dynome* is on the right side of the interactive interface, with the connectome of the network represented as a graph (**Figure 1**). The nodes of the graph represent neurons, whereas the edges represent connections (either gap or synaptic) between each pair of neurons. The top panel of **Figure 2** shows *C. elegans*' synaptic connectome (left) as well as its gap connectome (right), where each node represents an individual neuron and colored according to its group type. Initially, prior to displaying the *dynome* dynamics, the radii of the nodes are set according to in/out synaptic degree of the respective neuron (i.e., the amount of synaptic connections of a neuron). Such visualization emphasizes neurons with higher degree (hub neurons) by displaying them with larger radius and de-emphasizes neurons with lower degree with smaller radius. The width of the edge between a pair of neurons is set according to maximum synaptic weight, such that for a pair of neurons A and B, $\text{width}_{\text{edge(A,B)}} = max(\text{n}_{\text{Syn(A}\rightarrow\text{B)}}, \text{n}_{\text{Syn(B}\rightarrow\text{A)}})$, where $n_{Syn(A\rightarrow B)}$ is the number of synapses from neuron A to B.

In addition, we use force-directed graph algorithm to arrange the nodes and edges in optimal positions (Bostock et al., 2011). The algorithm visualizes graphs by assigning forces to nodes and edges based on their relative positions and routings. For edges, spring-like attractive forces based on Hooke's law are used to attract pairs of endpoints toward each other. For the nodes, repulsive forces, e.g., Coulomb's law forces, are used to separate all pairs of nodes. Once forces are assigned, the algorithm minimizes the total energy potential of the system (i.e., equilibrium states for the system of forces) and displays optimal nodes and edges configuration. In this representation, the edges tend to have uniform lengths (due to spring forces) and the nodes not connected by an edge tend to be drawn further apart (due to repulsive forces) (Kobourov, 2012). We found such graph visualization more advantageous for neuronal networks than the anatomy based visualization method as it: (i) keeps approximately equal lengths for all neuron's connections thus avoiding "clumps" of neurons in one region, and (ii) arranges the nodes such that neurons that make connections with a particular neuron are found within its proximity. We also found that due to these properties, the configuration depicts the network in an intuitive way, by grouping the same type of neurons together (e.g., many of the motor neurons are clustered together on the left of the graph) and places the neurons with high synaptic degrees in the middle. To keep the same frame of reference, force-directed representation is pre-computed before the simulation such that the positions of the nodes remain constant at all times.

Neural Activity Visualization

Neural activity is represented as an additional layer on top of the static connectivity graph. We find that optimal approach to visualize the two layers is to alter graph components (nodes and edges) according to neural activity. This creates a "breathing graph" which represents network activity and structure in real-time. In particular, we propose dynamic change to radii and colors of the nodes to depict neural activity. Changes are typically noticeable when the visualized variable representing the activity is continuous and scaled. In addition, it is beneficial that the visualized variable will have a continuous and interpretable meaning. Notable candidates for such variables are SR calcium activation dynamics or instantaneous firing rates (*peri stimulus time histograms* PSTH) (Palm et al., 1988; Schatzmann, 1989; Egelman and Montague, 1999). SR calcium activation is a scalable continuous process representing transformation of membrane voltage dynamics (spiking, bursts separated by near-silent interburst periods, and graded voltage potentials) to an activation variable. It serves as a vital biophysical signal associated with activation of muscle activity (McMillen and Holmes, 2006). In addition, several recording techniques quantifying neural dynamics are capable to measure and monitor SR calcium activity and

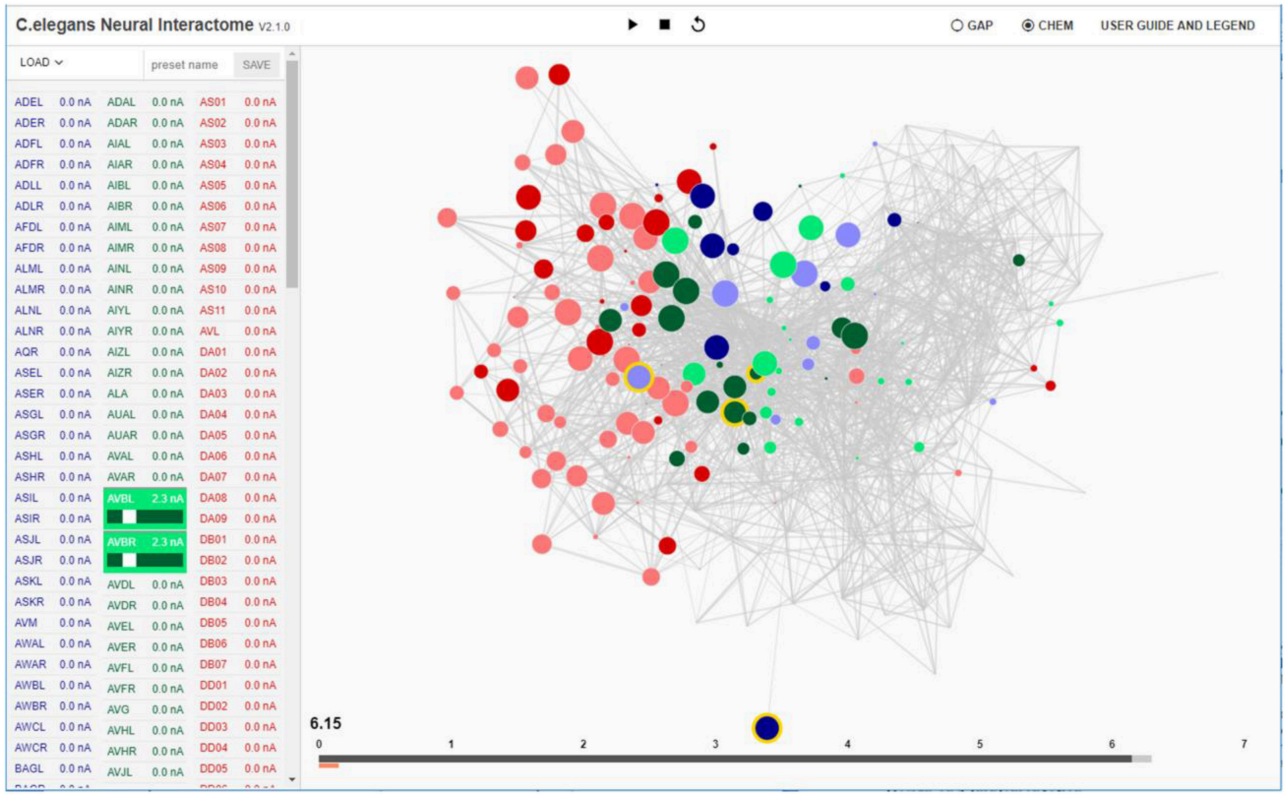

FIGURE 1 | Interactive interface for Neural Interactome. Left panel enlists all the neurons classified by type (sensory, inter and motor). Each neuron is a clickable button with a scroll option. Scrolling adjusts the magnitude of constant stimulus; shift + click ablates the neuron from the network. Right: Force-directed graph displays each neuron's membrane voltage (node color denotes the sign; radius denotes the magnitude) and connections between neurons (edges between each pair of nodes). At the bottom of the graph, time bar keeps track of visualized time point (dark gray), and of computed time by the backend neural integration (light gray).

can be directly compared with the visualization. The PSTH variable is computed from spiking dynamics and represents a spike count over a sliding window in time (Dayan and Abbott, 2001). Such a measure is applied to both measurements of spiking membrane voltage or a computational model that produces spike trains. PSTH is a continuous and scaled measure widely used for identification, classification and recognition of response patterns associated with stimuli (Riffell et al., 2014; Shlizerman et al., 2014).

To visualize these activity variables we propose to alter the radius and the color of the nodes. When the variable is a signed number (as in SR calcium activation) we use the radius to represent variable's amplitude and assign a color map to represent its sign. When the variable is unsigned, as in the case of PSTH, only one node component (either color or radius) is needed to represent its amplitude, and the other component can be utilized for visualization of additional information such as spike times. For example, when the radius is used to depict the PSTH amplitude, color flickering can be used to display the occurrence of spikes.

For *C. elegans* network we transform membrane voltage to SR calcium like activation variable to represent neural dynamics. In particular, membrane voltages, computed by backend neural integrator, described further in "*Backend Neural Integration*", are translated to the following metric of radius size according to:

$$|R_i| = \frac{R_{\max}\,|V_i|^2}{\rho + |V_i|^2} \qquad (1)$$
$$\text{sign}\,(\mathrm{R_i}) = \text{sign}(\mathrm{V_i})$$

where $R_{\max}$ is the maximum radii of the nodes and ρ is the slope factor. The sign of R_i is determined by the sign of the voltage V_i. Such scaling of membrane voltages allows discerning active neurons at each given time without having to visualize the raw voltages. While in *C. elegans* membrane voltages are graded potentials, similar scaling accommodates other diverse types of neural activity, e.g., bursts, oscillations, etc (Rahmati et al., 2016).

Observing the colors and radii scaling over time allows to visually capture the unique patterns of dynamics on a population level, specifically oscillations, sudden bursts, settling down of dynamics. For example, when a population of neurons exhibit oscillations, colors will distinguish representatives of particular groups that are active and dynamically change their tones to display the fluctuation between positive and negative voltages. Indeed, for *C. elegans* network we show how we can identify oscillatory sub circuits of motor neurons, which fluctuate from negative to positive values over the period of 2 sec, upon stimulation of PLM touch sensitive sensory neurons. To further

aid the investigation, the interface displays a plot of neuron's membrane voltage over time when the user hovers over a node.

Simulation Timescale

We implement the simulation timescale to be typically slower than the actual time in order to: (i) balance computations performed by the backend, and (ii) allow users to capture the details of the dynamics, as visualization in actual timescale tends to happen quickly. We also design the timescales of the stimulations to be dynamic, such that during stimuli transition or neural ablation, running time temporarily slows down to capture the dynamics that occur during the transition.

On the bottom of the interface we locate the time bar, which serves as the interface to interact with the timescales of the visualization (**Figure 1**). It consists of two bars; the dark gray bar shows the current time in visualization, while the light gray bar shows the computed time by the backend. We have developed the time bar to be similar to a streaming bar, which is widely implemented in popular video-hosting websites such as YouTube, and provides the interface to our *review system*, as we describe next.

Review System

The *review system* allows for isolating various time and population scales for further analysis (**Figures 2D**). Using the time bar, we add the ability to navigate back to any previously computed time by clicking on a desired time point within the time bar (analogous to navigating back and forth while playing a video). In such a case the network along with the dark gray bar are set to the state at the selected time point. Time navigation can be done either during simulation or when simulation is paused. In the former, the simulation will continue onward from the selected time point while for the latter, it will display the paused dynamics at that time point. In addition, we assign left and right arrow keys on the keyboard to control visualization speed (Fast FWD and Fast BWD). When activated during simulation or paused, the left and right arrow keys increase visualization speed while browsing through the dynamics in both directions.

An additional component of the *review system* is the dynamic zoom-in/out feature, which focuses into sub circuits within the network at any time during the simulation. It is implemented by

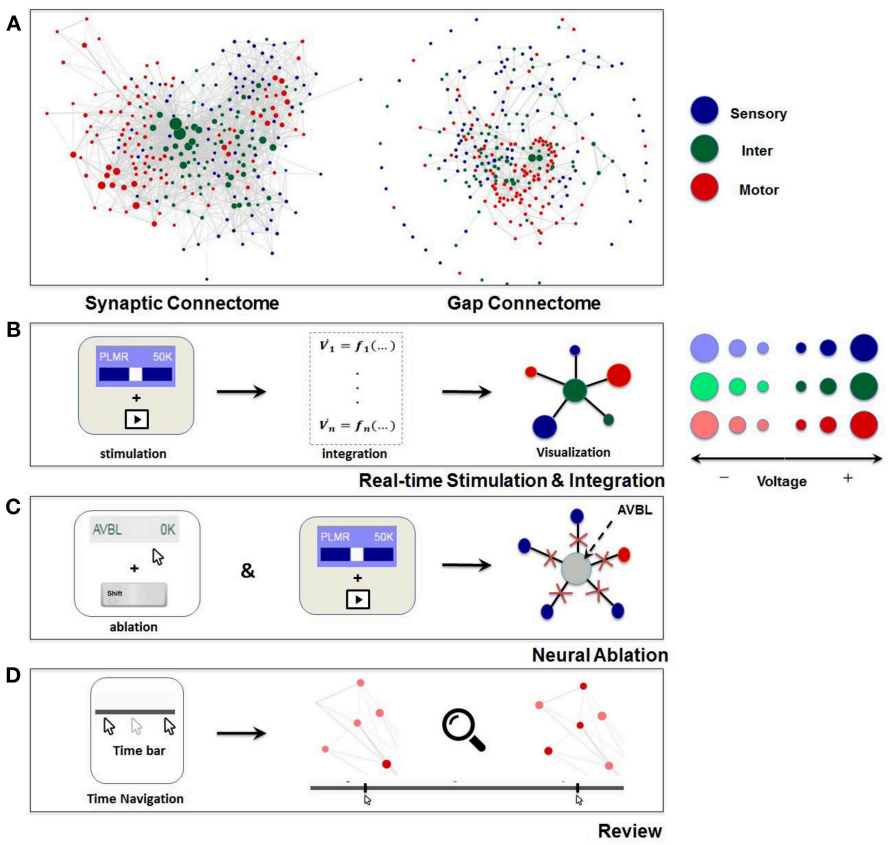

FIGURE 2 | Visualization and main functionalities of Neural Interactome. **(A)** Force-directed graph visualization of *C. elegans* worm's synaptic (chemical, left) and gap (electrical, right) connectomes. Each node represents individual neuron colored according to its group type and edges represent connections (either synaptic or gap). **(B)** Schematics of Neural Interactome real-time stimulation and integration component; when user stimulates a neuron with the interface, the backend integrator computes membrane voltages in response to the stimuli, which are then visualized on the graph in respect to their signs and magnitudes. **(C)** Neural ablation is performed by clicking on the neuron, while holding the shift key. Ablation disconnects all the connections of the neuron (both gap and synaptic). **(D)** The review system implements a clickable time bar to allow navigation to any previously computed time point in the simulated dynamics. This is further enhanced with dynamics zoom-in/zoom-out feature designed for in-depth analysis of connectivity structure and local dynamics of sub-circuits.

uniformly scaling the lengths of the edges and keeping the nodes radii the same. Effectively, such a method is optimal for observing a small group of neurons, as it increases the spacing between nodes and displays local sub circuit connectivity structure and dynamics (**Figure 2D**). Hovering with a mouse over a neuron will also highlight the connections it makes to neighbor neurons, and will display their labels categorized in different group type colors.

In addition, features such as "presets" and "save dynamics" are implemented as part of the review system. *Presets* allow users to save configurations of neurons stimuli panel whereas *save dynamics* stores the voltage time series data for all neurons during a single session as a file. *Presets* can be used to save stimuli configuration, ablation configuration, or both, whereas *save dynamics* can be used to perform detailed analysis/comparison with the experiments against the simulated dynamics. To create a preset, one can enter the name of the preset above the neurons stimuli panel while the panel is configured to desired setup (**Figure 1**) and click SAVE button. Upon exiting or resetting the interface, *save dynamics* will automatically save the time series data in npy file format (compatible with Python NumPy library) in "saved_dynamics" folder within the software directory.

BACKEND NEURAL INTEGRATION

Backend neural integration computes neural activity for the whole network for a time interval $[t,\ t + \Delta t]$ and transmits these values to the interactive interface for visualization. In *C. elegans*, the integrator is solving a system of non-linear ordinary differential equations with 558 dimensions (279 for neurons voltage and 279 for synaptic variables) that model the biophysical processes and interactions between neurons. Such high dimensional ODE system is not computationally trivial, thus we implement an efficient vectorized adaptive solution. Specifically, the following equations are being integrated (see Kunert et al., 2014 for more details):

$$C\frac{dV_i}{dt} = -G^c\,(V_i - E_{cell}) - I_i^{Gap}\left(\tilde{V}\right) - I_i^{Syn}\left(\tilde{V}\right) + I_i^{Ext} \quad (2)$$

$$I_i^{Gap}\left(\tilde{V}\right) = \sum_j G_{ij}^g (V_i - V_j) \quad (3)$$

$$I_i^{Syn}\left(\tilde{V}\right) = \sum_j G_{ij}^s s_j (V_i - E_j) \quad (4)$$

$$\frac{ds_i}{dt} = a_r \Phi\,(V_i; \beta, V_{th})\,(1 - s_i) - a_d s_i \quad (5)$$

$$\Phi\,(V_i; \beta, V_{th}) = \frac{1}{1 + \exp(-\beta\,(V_i - V_{th}))} \quad (6)$$

Where **C** is the cell membrane capacitance, G^c is the cell membrane conductance, E_{cell} is the leakage potential, and $I_i^{Gap}(\tilde{V})$, $I_i^{Syn}\left(\tilde{V}\right)$, and I_i^{Ext} each correspond to input current contributed by gap junctions, synapses, and external input stimuli. G_{ij}^g and G_{ij}^s each correspond to total conductivity of gap junctions between i and j and maximum total conductivity of synapses to i from j, where G_{ij}^s is modulated by synaptic activity variable s_i. The synaptic activity variable is governed by Equation (5), where a_r and a_d correspond to the synaptic activity rise and decay time, and Φ is the sigmoid function with width β. The equations are based on *in-situ* recordings of membrane voltage indicating that neuron responses are graded potentials and hence better fit to describe the voltage dynamics than standard multi-compartmental spiking neural activity models.

While *C. elegans* neural activity is expressed through graded membrane potential, for other systems, especially systems in which neural activity is expressed through fast spiking, factors such as synaptic transmission delays due to finite propagation speeds and time lapses could appear and impact the network dynamics (Guo et al., 2012, 2016). Mathematically, such delays can be incorporated by introducing autaptic inhibition term $I_{aut}(t)$ of form:

$$I_i^{syn}(t) = \sum_j g_{ij}^{aut} s_{ij}(t)\left(E_{syn} - V_i\right) \quad (7)$$

Where g_{ij}^{aut} is the autaptic coupling strength from neuron j to neuron i and the corresponding synaptic variable $s_{ij}(t)$ is described by identical first-order model as Equation. 5 with sigmoid function term Φ_d now including the transmission delay τ_d as follows:

$$\Phi_d = \frac{T_{max}}{1 + \exp[-\beta_d(V_j\,(t - \tau_d) - V_{th})]} \quad (8)$$

Where T_{max} is the maximal concentration of transmitter in the synaptic cleft, V_j is the pre-synaptic voltage. Since the computation of network activity is independent from the frontend visualization, the platform allows direct incorporation of such higher order effects.

Synchronization of Integration and Visualization

To support real-time interaction, we implement a synchronization procedure through a communication system between the interface and the backend. Specifically, we use an object ODE integrator which supports event handling and adaptive time-stepping. This functionality allows us to establish a robust protocol between the interface and the backend to support interactive changes to the simulation parameters in real-time between solution points. The protocol monitors the following quantities: $t_{computed}$: Computed time in the backend neural integration, $t_{visualization}$: Visualized time in the interactive interface, Δt: Data stack, i.e., time interval to be computed, t_{buffer} : Buffer size between $t_{computed}$ and $t_{visualization}$, τ: Internal refractory period for checking $t_{computed} - t_{visualization}$.

The system is implemented to keep $t_{computed} - t_{visualization} \cong t_{buffer}$ at all times such that backend neural integration is always responsive to real-time user interactions, but also accommodates

computation of new solutions before the visualization fully catches up with the computation.

Based on these principles the communication protocol is as follows:

(i) The interface sends a command to the backend to compute solutions for the time interval of $[t_{computed}, t_{computed} + \Delta t]$ given the condition:

$$t_{computed} - t_{visualization} \leq t_{buffer}. \quad (9)$$

(ii) Once the command has been sent, the interface waits for a new block of solution of size Δt from the backend.

(iii) Once the block is received, the interface resumes to poll whether condition (9) is satisfied. Polling is performed as follows: If the condition is met, the system applies (i). If not, the system goes through a refractory period of τ and then checks again for condition (9).

In **Figure 3** we include a diagram depicting how the synchronization method allows for stimulation of neurons at any given time and simultaneous inspection of network response to such actions. When the user stimulates a specific neuron (e.g., PLMR in **Figure 3**) or performs a neural ablation the interface sends a command to backend neural integration to modify necessary parameters. This is followed by an additional command from the interface to compute the solution for interval $[t_{stimulus}, t_{stimulus} + \Delta t]$. The backend, upon receiving the first command, modifies the input stimuli parameters for stimulation or connectivity matrices for ablation. It then executes the second command by computing the voltage values for all neurons for a given time interval. The computed voltage values are then transmitted to the interface for visualization. This cycle of command and data transmission is repeated indefinitely until the simulation is stopped.

Stimuli Transition

In addition to integration of the dynamical equations, the backend ensures that any modification of stimuli amplitude during stimulation is executed in a realistic manner (i.e., no sudden jumps or drops in the stimulus). Ensuring such continuity produces more realistic shift of stimuli from one value to the other. Explicitly, we determine the magnitude of stimulus during the transition through a combination of two hyperbolic tangent functions:

$$S_{transit}(\tau) = S_{old}\left(\frac{1}{2} - \frac{1}{2}\tanh\left(\frac{t - (t_{switch} + t_{offset})}{r}\right)\right) + S_{new}\left(\frac{1}{2} + \frac{1}{2}\tanh\left(\frac{t - (t_{switch} + t_{offset})}{r}\right)\right) \quad (10)$$

Where t_{switch} is the time when the input current was modified, and r, t_{offset} are the constant coefficients that determine the width and initial point of the transition, respectively. Such construction makes sure that every transition takes place in a continuous manner and supports variable transition speeds of r.

Neural Ablation

In addition, the backend implements neural ablation by instantaneous modification of connectivity matrices (both gap and synaptic). This step is followed by recalculation of the quantities in the network associated with the modified structure (e.g., the equilibrium states of the network Vth; see Materials and Methods section for more detail). Effectively, when the user ablates a neuron in the interface, an array that keeps track of active neurons (1-present, 0-ablated) is being updated. The modified array is then sent to the backend, where for each ablated neuron, say neuron i, all elements of the connectivity matrices in

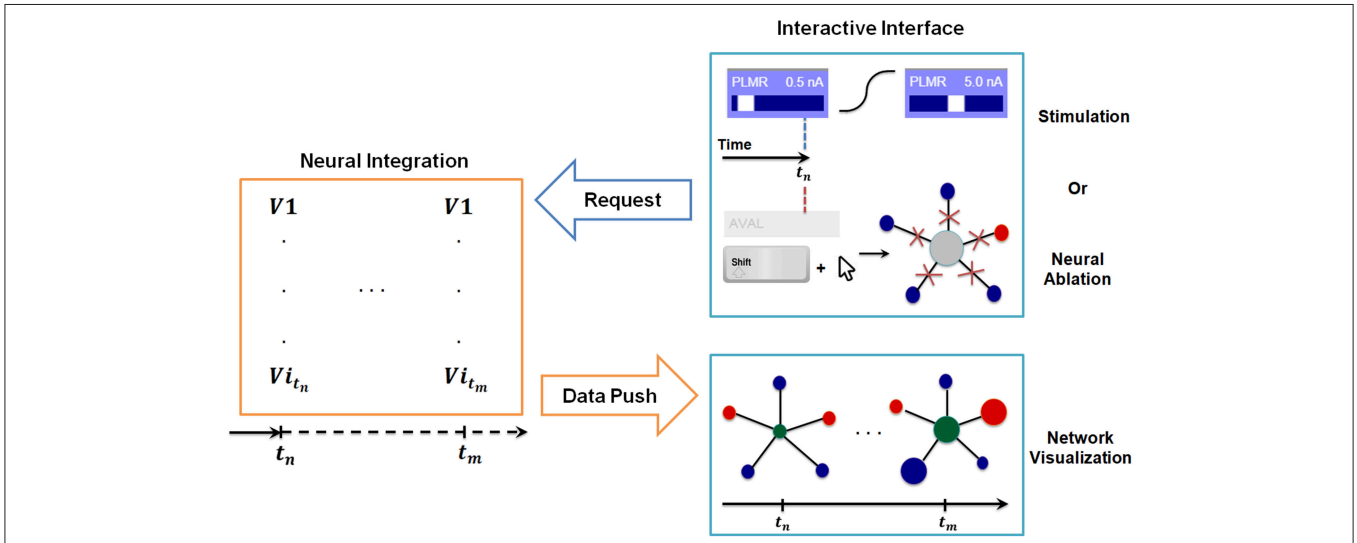

FIGURE 3 | Synchronization between interactive interface and backend neural integration. The backend computes membrane voltage values for future time interval requested by the interface, and transmits them to the graph for visualization. User driven change in the interactive interface, i.e., stimulation or neural ablation, invokes a process that passes the information to the backend where relevant parameters of integration are modified.

row and column i (corresponding to in/out connections) are set to zero.

Reinsertion of neurons after they were ablated implements the ablation operations in reverse order. Particularly, when the user reinserts the neuron, the interactive interface modifies the active neurons array, such that the corresponding neuron's entry is changed from 0 to 1. The modified array is then transmitted to the backend, where it will restore the corresponding row and column of the connectivity matrices to default values.

RESULTS

We proceed to demonstrate how application of Neural Interactome to *C. elegans* nervous system can assist in the study of neural dynamics. In particular, we target two sub circuits (i) a circuit associated with a touch response, which stimulation is known to be associated with forward and backward locomotion (ii) explore neural dynamic patterns induced by the excitation of sub group of sensory neurons, which recently were discovered to be associated with nictation behavior.

Posterior Touch Response Stimulation Scenario

PLM sensory neurons (PLML/PLMR) in *C. elegans* nervous system are known as posterior mechanoreceptors. When stimulated by tail touch, PLM neurons excite motor neurons associated with forward crawling motion (Chalfie et al., 1985). AVB interneurons (AVBL/AVBR) are also known as driver cells for forward movement of the worm. We stimulate PLM sensory neurons and AVB interneurons with constant stimuli to examine neural patterns associated with forward crawling motion as a result of posterior touch response. We adjust the magnitudes of the input currents by scrolling stimuli bars in the interface. Specifically, we set 1.4 nA for PLM neurons, and 2.3 nA for AVB interneurons, which result in profound oscillations.

As expected from experimental results and prior work, we observe oscillations in some populations of neurons. We therefore study their periodic cycle. In the top panel of **Figure 4A**, we show two snapshots of network dynamics taken at discrete percentages into the periodic cycle. We observe that the network graph responds with strong oscillation in about ∼40% of the neurons with mostly motor neurons (marked in red) being specifically active.

We identify more detailed properties of the dynamics by inspecting the dynamic graph in review mode (**Figure 4B**). The interface allows us to identify most responsive neurons and classify them into different types. In motor neurons, most active neurons (by maximum voltage amplitude above the threshold) appear to be Ventricular and Dorsal type B (VB, DB) neurons alongside with Ventricular and Dorsal type D (VD, DD) and AS motorneurons (AS01 – AS10). These neurons have identical oscillatory period of ∼2 s, however, their dynamics are out of phase to each other.

Most responsive interneurons turn out to be AVB, LUA, DVA, PVR, and PVC (**Figure 4A**). Indeed AVB, DVA, and PVC were experimentally shown to act as modulators for forward locomotion (Chalfie et al., 1985; Wicks et al., 1996; Driscoll and Kaplan, 1997). Notably, Neural Interactome also identifies relatively strong responses in LUA and PVR neurons. While these neurons have structural connections to PLM (LUA neurons are suggested to connect between PLM touch receptors, and PVR have gap junctions to PLM), their direct relation to forward locomotion was not affirmed (e.g., laser ablation of LUA did not lead to abnormalities of movement). Our analysis, however, suggests that these neurons are actively participating in the oscillations. These findings suggest that Neural Interactome can help find candidates of neurons correlated to particular dynamics, even for known sub circuits.

Anterior Touch Response Stimulation Scenario

ALM neurons sense touch to the anterior body region (i.e., frontal body) and induce motor neurons dynamics associated with backward locomotion (Chalfie et al., 1985). Aiding this process are the AVA, AVD, and AVE interneurons which act as modulators for the motion. We therefore stimulate these neurons with input currents that lead to profound dynamics, in particular: ALM = 5.8 nA, AVA = 2.0 nA, and AVD/AVE = 1.0 nA.

The snapshots of network dynamics while stimulating these neurons are shown in the middle panel of **Figure 4A** and labeled as Backward Scenario. Notably, comparing forward vs. backward neural responses, the dynamics for backward responses involve much larger number of neurons (∼90%) than that of forward responses. We find the most responsive motor neurons to be Ventricular Dorsal type A (VA, DA), Ventricular Dorsal type D (VD, DD) and AS (AS01-AS10). The oscillation behavior for each of these groups is of different phase, but their periods appear to be uniform around ∼3.5 s. The results are consistent with the experimental observations which reported the A-type and D-type motor neurons coordinating the backward motion (Chalfie et al., 1985; Chalfie and White, 1988).

Zooming into particular populations of motor neurons we observe that individual motor neurons exhibit more complex and irregular patterns than those of the forward stimulation. Unlike the oscillations observed in forward stimulation which are characterized by predominantly smooth sinusoidal form, here motor neurons appear to have oscillatory patterns with various waveforms: some motor neurons repeat steep fluctuations between negative and positive voltage while some exhibit triangular type oscillations above their thresholds.

We also observe more activity within the interneurons. Most prominent ones appear to be AVA, AVDR, AVE, PVR, DVA, ADA, and SABV. Some of these neurons are indeed identified in the literature, AVA, AVD, AVE are characterized to act as modulators for backward motion and DVA is characterized to maintain activity (Chalfie et al., 1985; Wicks et al., 1996; Driscoll and Kaplan, 1997; Gray et al., 2005). However, we also find high activity in neurons such as PVR, ADA, and SABV. While PVR makes gap junction with ALM, its role in backward locomotion has not been yet clarified. For both ADA and SABV, their functionality has not been fully specified yet.

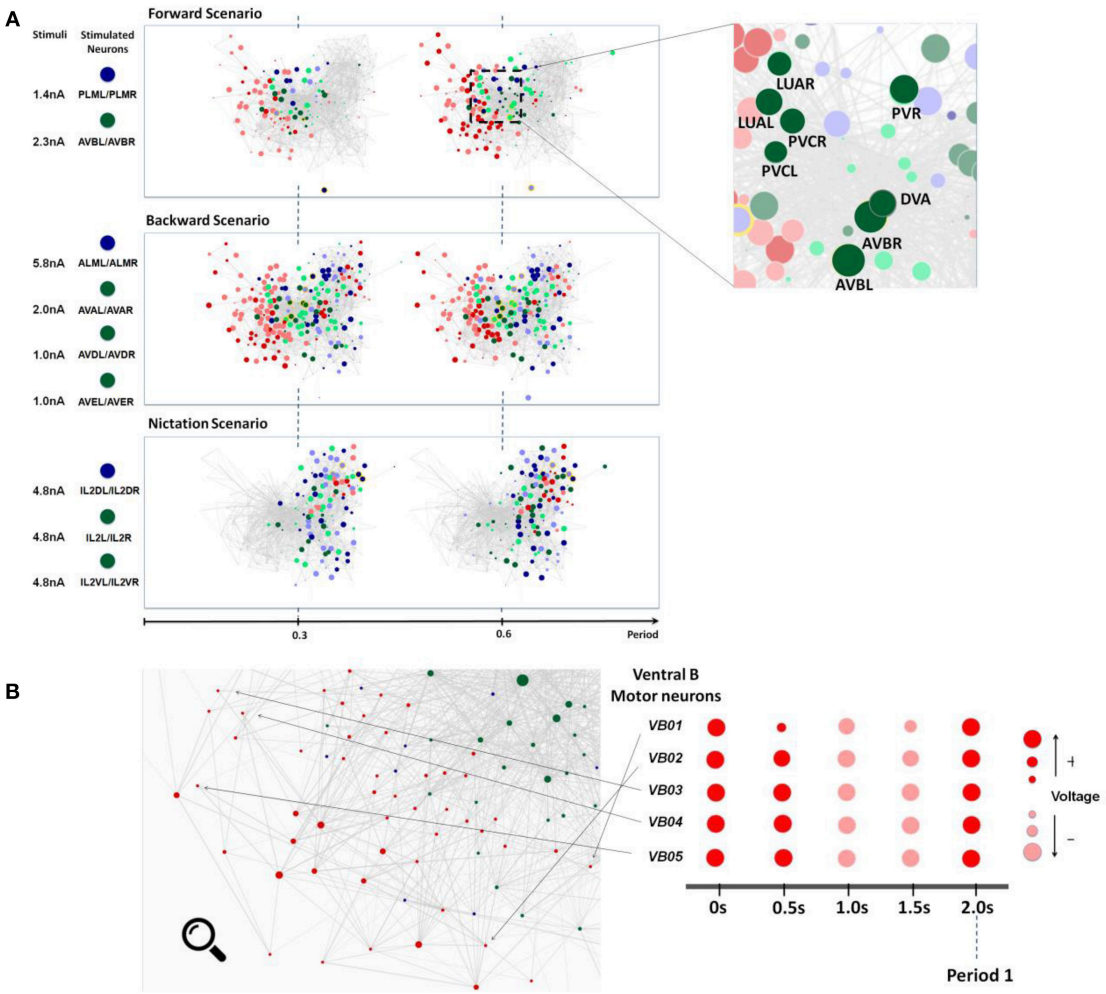

FIGURE 4 | (A) Snapshots of neuronal responses corresponding to locomotion forward, backward, and nictation scenarios visualized by Neural Interactome. Forward scenario shows the snapshots of neural dynamics in response to PLM and AVB neurons stimulation. Each snapshot is taken at 30% and 60% into the average period of motor neurons oscillatory dynamics. On the right panel, the most responsive interneurons are highlighted. Backward scenario displays the snapshots of neural dynamics as a result of stimulation of ALM/AVA/AVD/AVE neurons. Nictation scenario displays the snapshots of dynamics upon stimulation of IL2 neurons. **(B)** Identification of unique oscillatory dynamics during forward scenario using the review mode. Visualization of motor-neurons sub circuit using the review system zoom-in function (left). Snapshots of Ventricular B motor neurons (VB01 ∼ VB05) during forward scenario sampled five times with equal interval during 2 s periodic cycle (right).

As in the posterior touch response scenario, the discovery of these additional neurons participating in dynamics provides new insights regarding the neurosensory integration of anterior touch response behavior.

IL2 Neurons Stimulation Scenario

It has been recently shown that IL2 neurons regulate the *nictation* behavior in which a worm stands on its tail and waves its head. Such behavior is known to be observed within the *dauer* larva (i.e., developmental stage nematode worms) to transport itself via hosts such as flies or birds (Lee et al., 2012). For non-*dauers,* targeted activation of IL2 neurons does not induce nictation possibly because IL2 neurons undergo a significant structural change at the *dauer* stage. In this scenario, we stimulate IL2 neurons through Neural Interactome to investigate motor neuron dynamics possibly linked to such behavior or its remnant.

We present snapshots of network dynamics induced by IL2 (IL2DL/IL2DR, IL2L/IL2R, IL2VL/IL2VR) neurons stimulation in the bottom panel of **Figure 4A**. Notably, the network activates neurons located mostly on right side of the graph. This is a different pattern than forward and backward patterns. Most responsive motor neurons for such stimulation are RMG, RMH, and RMED along with moderate responses within SMD and RMEL/RMER motor neurons. The oscillatory periods for these neurons are uniform around ∼5.7 s with different phases. Particularly, RMHL and RMHR neurons each produce oscillations nearly anti-phase to each other. For RMG neurons, the oscillation wave of RMGL always preceded that of RMGR, suggesting phase displacement between oscillations of these two

neurons. Oscillations among four SMD motor neurons (SMDDL, SMDDR, SMDVL, and SMDVR) as well as of three RME motor neurons (RMEL, RMER, RMED) were observed to be approximately in phase.

In the literature, these motor neurons are known to be involved with control of head muscles. RMG and RMH motor neurons innervate lateral four rows of head muscles while RME neurons innervate all eight rows of head muscles (White et al., 1986). SMD motor neurons are also known to innervate head muscles involved with search behaviors such as omega-shaped turns under absence of food in the environment (Gray et al., 2005). Remarkably, Neural Interactome shows no response among the motor neurons associated with forward/backward locomotion (such as Ventricular Dorsal A, B and D) and only shows response of neurons modulating head muscles. Such results suggest that the activation of IL2 neurons leads to periodic head movements with absence of locomotory behavior in the rest of the body. While this does not necessarily imply that such motor neurons pattern is linked to nictation, these observations provide particular hypotheses and insights about the relatively unknown sub circuit for further empirical studies.

SCENARIOS: ABLATION

To validate Neural Interactome's application to investigation of network structural changes, we perform two ablations in conjunction with previously performed scenarios. In particular, we remove AVB and AVA interneurons from the network and repeat the posterior touch response scenario to observe their effects on the dynamics.

AVB Ablation

According to the literature, the removal of AVB neurons impedes forward locomotion (Chalfie et al., 1985). Indeed, we are able to confirm these experimental findings using Neural Interactome. Scenario C in **Figure 5** shows the three snapshots of full periodic cycle upon repeating the posterior touch response scenario with AVB neurons ablated. We observe that neural patterns involve far less neurons than that of a healthy network (**Figure 5**, Scenario A). In particular, examination of full network snapshots as well as of local groups of motor neurons shows considerably weaker responses in comparison to the healthy structure.

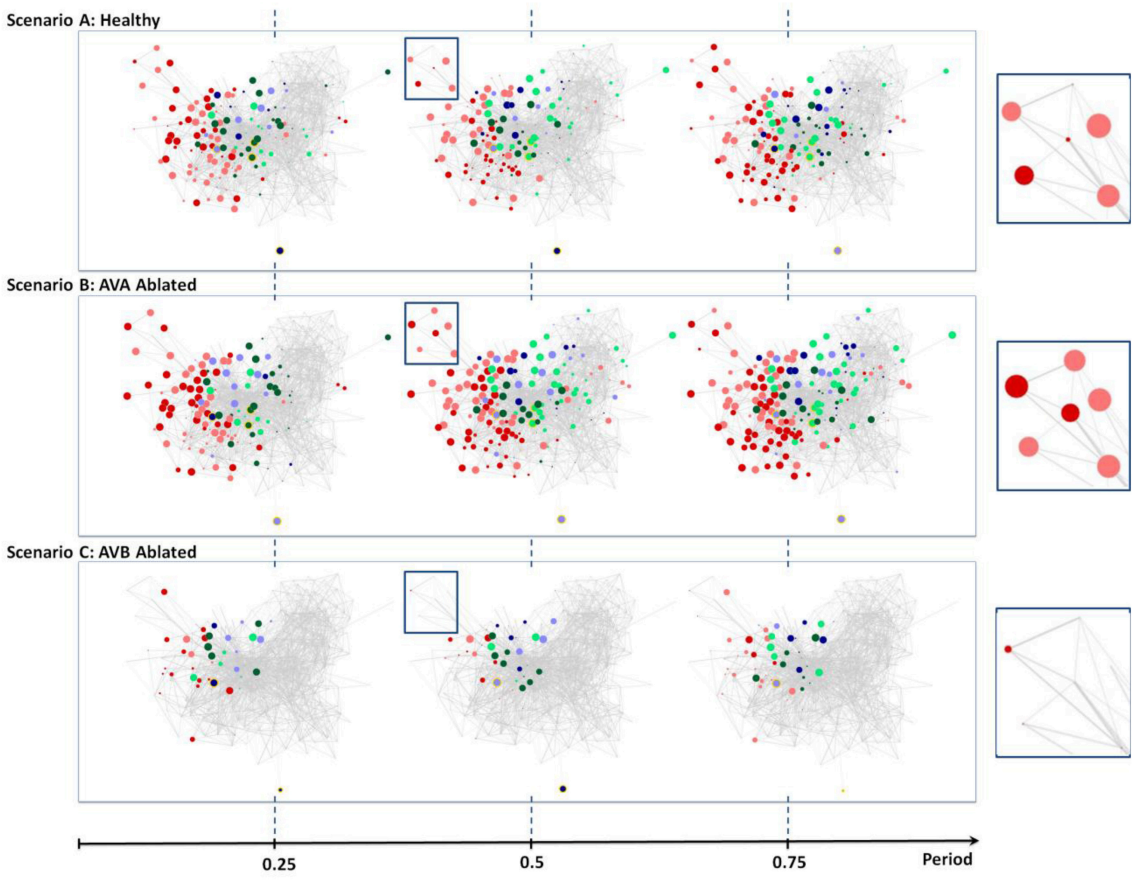

FIGURE 5 | Neural dynamics during forward scenario for different structures of the network (non-ablated and ablated neurons). **(A)** Three snapshots of dynamics with healthy network (i.e., no ablation). **(B)** Snapshots of dynamics when AVA inter neurons are ablated. **(C)** Snapshots of dynamics when AVB inter neurons are ablated. All snapshots are taken at 25%, 50%, and 75% into each dynamics' oscillation period.

The visualization does capture weak oscillations within a small group of motor neurons; particularly in Ventricular Dorsal B (VB, DB). Oscillation amplitudes are far less than the healthy dynamics, however, they remain to be relatively in phase and maintain an oscillatory period of ∼1.9 s. We are unable to find any oscillatory activity within Ventricular Dorsal type D (VD, DD) neurons, which were out of phase with the activity of B type (VB, DB) neurons in the healthy case. Acknowledging that the two oscillatory phases property is necessary for the worm to perform forward crawling motion (Stephens et al., 2008), such observation confirms the experimental findings that the ablation of AVB neurons hinders the worm's ability to perform forward motion.

AVA Ablation

Unlike the removal of AVB interneurons, experiments showed that the removal of AVA interneurons does not impact forward motion (Chalfie et al., 1985). Scenario B in **Figure 5** shows snapshots of posterior touch response scenario with AVA neurons ablated. It is interesting to observe that the dynamics have slightly longer oscillatory period of about ∼2.6 s. However, aside from that, the visualization shows that almost identical sets of neurons are active as in the healthy scenario (compare with **Figure 4**, Scenario A). We are also able to confirm, using the review mode, that the dynamics continue to exhibit strong oscillations in (VB, DB) & (VD, DD) motor neurons, with (VD, DD) neurons being out of phase to (VB, DB) neurons. Thus, our results for AVA ablation are consistent with experimental data in the literature.

Taken together our results show that Neural Interactome assists in confirming empirical results reported in the literature, and provides further insights regarding structure and activity associated with examined responses.

DISCUSSION

In this paper, we present a new visual interactive method, which we call Neural Interactome for studying the dynamics and the structure of a neuronal system (*dynome*). While it is important to simulate the full *dynome* to study network functionalities, multiple simulations of the *dynome* are formidable due to complexity in number of neurons and variations of stimuli. Neural Interactome approaches the problem through interactive real-time interface to the *dynome* and therefore significantly simplifies these studies. In particular, we show the simplicity of stimulating and ablating various groups of neurons in the framework.

To elucidate the overall structure and functionalities of the framework, we first define key components: (i) The interactive interface and (ii) the backend neural integration. Next, we apply it to *C. elegans* nematode, which connectome is resolved and the computational model describing both biophysical processes and interactions between neurons has been developed. We show that the framework provides novel possibilities to explore the worm's network structure and its unique neural patterns subject to stimuli. In particular, we demonstrate the Neural Interactome's capabilities using stimulations associated with the touch response: stimulation of PLM/AVB neurons for posterior touch, ALM/AVA/AVD/AVE neurons for anterior touch, and stimulation associated with nictation behavior: stimulation of IL2 sensory neurons. In all three scenarios, we observe clear visual characteristics of the induced neural patterns. For example, using the review features, we are able to identify most responsive neurons and additional properties of dynamics such as oscillation period and phase on individual and population level. By comparing such observations with behavioral and neural descriptions in the literature, we demonstrate that our results are consistent with the empirical observations of *C. elegans* locomotion and that they suggest additional novel insights.

In addition, we demonstrate the effectiveness and usability of the neural ablation feature in Neural Interactome by ablating hub interneurons (AVA or AVB). AVB ablation leads to network visualization with diminished activity in motor neurons as well as absence of characteristic out of phase oscillatory property required for such motion. The ablation of AVA interneurons, however, shows almost identical set of participating neurons as of the healthy network. We therefore believe that the framework has a potential to reveal other functionalities through multiple ablation scenarios, and provide further insights describing the role of the ablated neurons (Carrillo et al., 2013). In experiments, preparation and execution of ablation consumes significant time and usually requires special equipment, e.g., optogenetics. On the contrary, Neural Interactome can produce initial analyses for numerous ablation scenarios within seconds and consequently can be utilized as a pre-experiment tool to map scenarios for empirical exploration.

We designed the Neural Interactome to permit updates to both connectivity and dynamic models within the framework as they are further being refined in the future. Connectivity updates will merely require a change in the connectivity matrices. Replacement of a current model with more detailed one or different models (e.g., H-H type model) would merely require the replacement of the model itself, while the synchronization method between the neural neural integration and the interface will ensure that the computed values will be visualized properly. With such flexibility we expect that the framework will be similarly applicable to other neuronal systems: ranging from actual biological networks (such as that of *Drosophilla* medulla, the mouse retina, the mouse primary visual cortex) to artificial dynamic neural networks (e.g., Recurrent Neural Networks) and genetic networks (Alter, 2007). We also plan to keep adding more features to the framework to provide additional interaction possibilities with more detailed properties of the network, such as modification of individual synaptic or gap connections between a pair of neurons and more visualization options, such as plotting the comparison between multiple neuronal voltage dynamics. In addition to the functional features, we plan to incorporate more advanced computation methods such as parallel (GPU) computation for larger and more complex networks. The current simulation scheme is based on sequential time-stepping and supports event handling from user interactions. For network with moderate dimensionality such as *C. elegans* network, the overhead from incorporation of parallel computing for a single time step (i.e., GPU) and synchronization of the solution exceeds

the time of solving it sequentially with CPU. However, for very large networks the single step computation efficiency could be of greater importance.

Beyond the simulation of *C. elegans* nervous system, we also plan to connect the model to musculature/body movement as they are critical components for model validation and for the study of interaction between neural dynamics and behavior. Development of such a model and connection of it with the *C. elegans* neural interactome could help in understanding how the neuronal network translates neural activity into behavior.

Neural Interactome can be either downloaded from Github repository or accessed online via a web interface with following addresses:

Github: https://github.com/shlizee/C-elegans-Neural-Interactome

Web Interface: http://neuralcode.amath.washington.edu/neuralinteractome

MATERIALS AND METHODS

In this section, we describe the materials and the methods used for the development of Neural Interactome and its application to *C. elegans* nervous system. The source code of the software is available at Github repository (https://github.com/shlizee/C-elegans-Neural-Interactome).

Development Environment and Tools

We used two different programming languages for the development of Neural Interactome. We used Python to develop the backend neural integration, and Javascript to develop the frontend interactive interface. For establishing communication protocols between the interface and backend, we used flask-socketIO on Python side and Socket.IO on javascript side. Both flask-socketIO and Socket.IO are libraries that allow real-time bi-directional communication between the client (frontend) and the server (backend) through WebSocket protocols. In the context of Neural Interactome, they were used to establish robust command and data transactions between the interactive interface and backend neural integration.

Several third party libraries were used for each language as well. For Python, NumPy was used for mathematical computations and manipulations of matrices. Several functions from SciPy were used to construct the ordinary differential equation solver and solve the system of linear equations for computation of neural quantities such as $V_{threshold}$ values.

In Javascript, D3.js (Data-driven documents) platform was used to construct force-directed graph representation of neuronal network. For the main webpage development framework, we used AngularJS as it provides optimal functionalities for building dynamic, single page web apps (SPAs).

Threshold Potential ($V_{threshold}$) Computation

Threshold potential for each neuron is computed by imposing $\frac{dV_i}{dt} = 0$ (Equation 2 for *C. elegans*) and solving for V_i. This is equivalent to Solving the following system of linear equations

$$Ax = b \tag{11}$$

$$A = M_1 + M_2 + M_3; b = -b_1 - b_3 - I_{ext}, \tag{12}$$

where the solution x is $N \times 1$ vector with each entry being the threshold potential $V_{threshold}$ for the i_{th} neuron.

M_1 is a matrix of size $N \times N$ where N is the number of neurons (279 for *C. elegans*) with its diagonal terms populated with $-G^c$ (cell membrane capacitance).

M_2 is a diagonal matrix where diagonal term in i_{th} row corresponds to $-\sum_j G^g_{ij}$ i.e., the sum of total conductivity of gap junctions for the i_{th} neuron.

M_3 is a diagonal matrix where its i_{th} diagonal term corresponds to $-\sum_j s_{eq} G^s_{ij}$, where $s_{eq} = \frac{a_r}{a_r + 2a_d}$ and G^s_{ij} is maximum total conductivity of synapses to i from j. Note that s_{eq} is obtained by imposing $\frac{ds_i}{dt} = 0$ and synaptic activation $\Phi = 1/2$ in Equation 5.

$b_1 = G^{c*} E_c$ where E_c is a 1D vector of size $N \times 1$ in which all of its elements are E_c (leakage potential).

$b_3 = G^s \cdot (s^*_{eq} E_j)$ where E_j is a 1D vector of size $N \times 1$ that enlists the directionality of each neuron (0 if excitatory or -48 mV if inhibitory).

I_{ext} is the input stimuli vector where its i_{th} element determines the input current amplitude for the i_{th} neuron.

Parameters

Dynome Visualization

We used $Rmax = 15$ as the maximum radius of the nodes in Equation 1.

ODEs Integration Parameters

The following values were used for relative/absolute tolerance and minimum integration step size. Note that the step size is determined adaptively by the solver to guarantee the prescribed tolerances.

Relative tolerance: 10e-9
Absolute tolerance: 10e-10
Minimum step size: 10e-9s (1 ns).

Visualization Timescale

The following values were used for the temporal resolution of simulation and dynamic timescales for visualization. Note that these parameters are for visualization only and are not associated with the integration step in backend integrator.

Temporal resolution: 10 ms
Visualization rate (normal): 100 ms/s
Visualization rate (during transition or ablation): 40 ms/s.

Parameters for Neural Integration

The values of parameters for each connection described in Equation 2–6 are not precisely determined. However, we assume reasonable values reported in the literature (Wicks et al., 1996; Varshney et al., 2011). We assume each individual gap and synaptic junction has approximate conductance of $g = 100$ pS (Varshney et al., 2011), cell membrane conductance $G^c = 10$ pS, and membrane capacitance $C = 1.5$ pF (Varshney et al.,

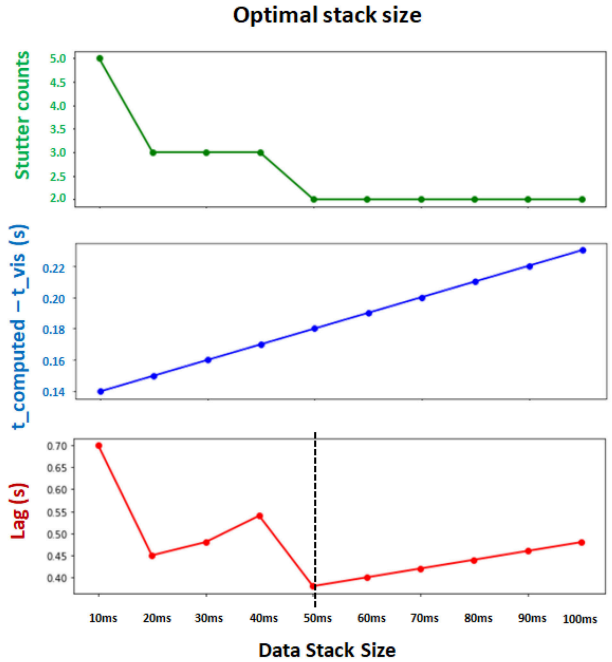

FIGURE 6 | Determining the optimal Δt (data stack size) for synchronization and computational efficiency. Two evaluation metrics are collected for different choices of stack size. t_computed − t_vis measures the synchronization between the leading integration time point in backend and leading visualization time point in frontend (lower is better). Stutter counts represents the computational efficiency by counting the number of stutters (i.e., when visualization pauses with t_computed = t_vis; lower is better). Both metrics are measured with identical sessions of 10 s simulation. Final evaluation metric (Lag) is obtained by multiplying these two metrics (lower is better). The results show that Δt = 50 ms achieves the minimum lag, and supports the best balance between synchronization and computational efficiency.

2011). We take leakage potential $E_{cell} = -35$ mV while reversal potential $E_j = 0$mV for excitatory synapses and $-48\ mV$ for inhibitory synapses (Wicks et al., 1996). For the synaptic activity variable, we take $a_r = \frac{1}{1.5}$, $a_d = \frac{5}{1.5}$ and width of the sigmoid $\beta = 0.125\text{mV}^{-1}$ (Wicks et al., 1996). Also for the initial condition of the membrane voltages V and synaptic activity variable s, we sample the normal distribution of $\mu = 0$ and $\sigma = 0.94$ with size 279 * 2 (for both V and s) and multiply by 10^{-4}. To validate the simulation and the choice of parameters we tested for robustness by perturbing (±20%) individual connection strengths and each neuron's parameters, showing that dynamic functionality persists.

Parameters for Synchronization

The optimal values for Δt, t_{buffer}, and internal refractory period τ in Equation 9 depend on computing power of the system. We found the parameters $\Delta t = 50$ ms, $t_{buffer} = 100$ ms and $\tau = 50$ ms (in actual time) to be of reasonable default values which achieve both computational efficiency and synchronization between the interface and backend (**Figure 6**). Note that Δt and t_{buffer} are in simulation timescale while τ is measured in computer's internal timer.

Parameters for Stimuli Transition

We use $t_{offset} = 150\ ms$, and $r = 0.025$ in Equation 10. We found these values to be the optimal choice since the transition curve does not induce abrupt shift in *dynome* dynamics, and the visualization rate remains to be fast enough. Given the value of r, the time it takes for complete transition from one stimulus amplitude to the other is approximately $2t_{offset}$. Thus, for our choice of parameters for *C. elegans* simulations, the transitional period is around 300 ms.

Computation of Input Current Unit

From Equation 2–4 and physiological parameters specified above, the unit of input current is $pS * mV = 10^{-15}A = fA$ (femto-ampere). However, in our implementation, we divided both sides of Equation 2 by conductance constant 100 pS. This gives 1arb (arbitrary unit of input) $= 10^{-13}A = 0.1\ pA$, implying 1000 arb = 100 pA = 0.1 nA. We verified these units with the I-V curves measured in Goodman et al. (1998).

AUTHOR CONTRIBUTIONS

ES and JK conceptualized the framework. ES acquired the funding for the study. ES, JK, and WL developed the methodology of the work. JK and WL developed the software. JK and ES validated the results. JK and ES wrote the original draft of manuscript. JK and ES edited and revised the manuscript.

FUNDING

This work was supported in part by National Science Foundation grant DMS-1361145 and Washington Research Fund to ES.

ACKNOWLEDGMENTS

We thank Dr. Mark Alkema and Dr. Vivek Venkatachalam for providing valuable feedback, Dr. Gal Haspel for providing updated connectome data, and Dr. Junho Lee for discussions on nictation and providing feedback. We are thankful to the reviewers for their constructive comments. We acknowledge the support of the departments of Applied Mathematics and Electrical & Computer Engineering, the Center of Computational Neuroscience (CNC), and the eScience Center at the University of Washington in conducting this research.

REFERENCES

Alter, O. (2007). Genomic signal processing: from matrix algebra to genetic networks. *Methods Mol. Biol.* 377, 17–60. doi: 10.1007/978-1-59745-390-5_2

Bargmann, C. I. (1993). Genetic and cellular analysis of behavior in *C. elegans*. *Ann. Rev. Neurosci.* 16, 47–71.

Bargmann, C. I., and Marder, E. (2013). From the connectome to brain function. *Nat. Methods* 10, 483–490. doi: 10.1038/nmeth.2451

Bock, D. D., Lee, W. C., Kerlin, A. M., Andermann, M. L., Hood, G., Wetzel, A. W., et al. (2011). Network anatomy and *in vivo* physiology of visual cortical neurons. *Nature* 471, 177–182. doi: 10.1038/nature09802

Bostock, M., Ogievetsky, V., and Heer, J. (2011). D^3 data-driven documents. *IEEE Transac. Visualiz. Comput. Graph.* 17, 2301–2309. doi: 10.1109/TVCG.2011.185

Briggman, K. L., Abarbanel, H. D., and Kristan Jr, W. B. (2006). From crawling to cognition: analyzing the dynamical interactions among populations of neurons. *Curr. Opin. Neurobiol.* 16, 135–144. doi: 10.1016/j.conb.2006.03.014

Briggman, K. L., Helmstaedter, M., and Denk, W. (2011). Wiring specificity in the direction-selectivity circuit of the retina. *Nature* 471, 183–188. doi: 10.1038/nature09818

Cantarelli, M., Marin, B., Quintana, A., Earnshaw, M., Gleeson, P., Dura-Bernal, S., et al. (2018). Geppetto: a reusable modular open platform for exploring neuroscience data and models. *Phil. Trans. R. Soc. B*. 373:20170380. doi: 10.1098/rstb.2017.0380

Carrillo, M. A., Guillermin, M. L., Rengarajan, S., Okubo, R. P., and Hallem, E. A. (2013). O2-sensing neurons control CO2 response in *C. elegans*. *J. Neurosci*. 33, 9675–9683. doi: 10.1523/JNEUROSCI.4541-12.2013

Chalfie, M., Sulston, J. E., White, J. G., Southgate, E., Thomson, J. N., and Brenner, S. (1985). The neural circuit for touch sensitivity in *Caenorhabditis elegans*. *J. Neurosci*. 5, 956–964. doi: 10.1523/JNEUROSCI.05-04-00956.1985

Chalfie, M., and White, J. G. (1988). "The nervous system," in *The nematode Caenorhabditis elegans,* ed W. B. Wood (Cold Spring Harbor, NY: Cold Spring Harbor), 337–392.

Chen, B. L., Hall, D. H., and Chklovskii, D. B. (2006). Wiring optimization can relate neuronal structure and function. *Proc. Natl. Acad. Sci. U. S. Am*. 103, 4723–4728. doi: 10.1073/pnas.0506806103

Chen, W., and De Schutter, E. (2017). Time to bring single neuron modeling into 3D. *Neuroinformatics* 15, 1–3. doi: 10.1007/s12021-016-9321-x

Dayan, P., and Abbott, L. F. (2001). *Theoretical Neuroscience*. Cambridge, MA: MIT Press.

Driscoll, M., and Kaplan, J. (1997). 23 Mechanotransduction. *Cold Spring Harbor Monograph Archive* 33, 645–677.

Druckmann, S., Feng, L., Lee, B., Yook, C., Zhao, T., Magee, J. C., et al. (2014). Structured synaptic connectivity between hippocampal regions. *Neuron* 81, 629–640. doi: 10.1016/j.neuron.2013.11.026

Durbin, R. M. (1987). *Studies on the Development and Organisation of the Nervous System of Caenorhabditis elegans.* PhD thesis, Cambridge, UK: University of Cambridge.

Egelman, D. M., and Montague, P. R. (1999). Calcium dynamics in the extracellular space of mammalian neural tissue. *Biophys. J.* 76, 1856–1867.

Goodman, D. F., and Brette, R. (2008). Brian: a simulator for spiking neural networks in Python. *Front. Neuroinform*. 2:5. doi: 10.3389/neuro.11.005.2008

Goodman, D. F., and Brette, R. (2009). The brian simulator. *Front. Neurosci.* 3:26.

Goodman, M. B., Hall, D. H., Avery, L., and Lockery, S. R. (1998). Active currents regulate sensitivity and dynamic range in *C. elegans* neurons. *Neuron* 20, 763–772. doi: 10.1016/S0896-6273(00)81014-4

Goodman, M. B., Lindsay, T. H., Lockery, S. R., and Richmond, J. E. (2012). Electrophysiological methods for *Caenorhabditis elegans* neurobiology. *Methods Cell Biol.* 107, 409–436. doi: 10.1016/B978-0-12-394620-1.00014-X

Gray, J. M., Hill, J. J., and Bargmann, C. I. (2005). A circuit for navigation in *Caenorhabditis elegans*. *Proc. Natl. Acad. Sci. U. S. A*. 102, 3184–3191. doi: 10.1073/pnas.0409009101

Guo, D., Chen, M., Perc, M., Wu, S., Xia, C., Zhang, Y., et al. (2016). Firing regulation of fast-spiking interneurons by autaptic inhibition. *EPL* 114:30001. doi: 10.1209/0295-5075/114/30001

Guo, D., Wang, Q., and Perc, M. (2012). Complex synchronous behavior in interneuronal networks with delayed inhibitory and fast electrical synapses. *Phys. Rev. E*. 85:061905. doi: 10.1103/PhysRevE.85.061905

Hall, D. H., and Russell, R. L. (1991). The posterior nervous system of the nematode *Caenorhabditis elegans*: serial reconstruction of identified neurons and complete pattern of synaptic interactions. *J. Neurosci*. 11, 1–22. doi: 10.1523/JNEUROSCI.11-01-00001.1991

Haspel, G., and O'Donovan, M. J. (2011). A perimotor framework reveals functional segmentation in the motoneuronal network controlling locomotion in *Caenorhabditis elegans*. *J. Neurosci*. 31, 14611–14623. doi: 10.1523/JNEUROSCI.2186-11.2011

Kobourov, S. G. (2012). Spring embedders and force directed graph drawing algorithms. arXiv preprint arXiv:1201.3011.

Koch, C. (2004). *Biophysics of Computation: Information Processing in Single Neurons.* Oxford, UK: Oxford university press.

Koch, C., and Segev, I. (1988). *Methods in Neuronal Modeling: From Synapses to Networks*. Cambridge, MA: MIT press.

Kopell, N. J., Gritton, H. J., Whittington, M. A., and Kramer, M. A. (2014). Beyond the connectome: the dynome. *Neuron* 83, 1319–1328. doi: 10.1016/j.neuron.2014.08.016

Kunert, J., Shlizerman, E., and Kutz, J. N. (2014). Low-dimensional functionality of complex network dynamics: neurosensory integration in the *Caenorhabditis elegans* connectome. *Phys. Rev. E* 89:052805. doi: 10.1103/PhysRevE.89.052805

Kunert-Graf, J. M., Shlizerman, E., Walker, A., and Kutz, J. N. (2017). Multistability and long-timescale transients encoded by network structure in a model of C. elegans connectome dynamics. *Front. Comput. Neurosci.* 11:53.

Lee, H., Choi, M. K., Lee, D., Kim, H. S., Hwang, H., Kim, H., et al. (2012). Nictation, a dispersal behavior of the nematode *Caenorhabditis elegans*, is regulated by IL2 neurons. *Nat Neurosci*. 15, 107–112. doi: 10.1038/nn.2975

Letinic, K., Zoncu, R., and Rakic, P. (2002). Origin of GABAergic neurons in the human neocortex. *Nature* 417, 645–650. doi: 10.1038/nature00779

Liu, H., Kim, J., and Shlizerman, E. (2018). Functional connectomics from neural dynamics: probabilistic graphical models for neuronal network of *Caenorhabditis elegans*. *Phil. Trans. R. Soc. B*. 373:20170377. doi: 10.1098/rstb.2017.0377

McMillen, T., and Holmes, P. (2006). An elastic rod model for anguilliform swimming. *J. Math. Biol*. 53, 843–886. doi: 10.1007/s00285-006-0036-8

Mucha, P. J., Richardson, T., Macon, K., Porter, M. A., and Onnela, J. P. (2010). Community structure in time-dependent, multiscale, and multiplex networks. *Science* 328, 876–878. doi: 10.1126/science.1184819

Open Connectome Project (2010). Available online at: http://www.openconnectomeproject.org.

Palm, G., Aertsen, A. M., and Gerstein, G. L. (1988). On the significance of correlations among neuronal spike trains. *Biol. Cybern*. 59, 1–1. doi: 10.1007/BF00336885

Rahmati, V., Kirmse, K., Marković D., Holthoff, K., and Kiebel, S. J. (2016). Inferring neuronal dynamics from calcium imaging data using biophysical models and Bayesian inference. *PLoS Comput Biol*. 12:e1004736. doi: 10.1371/journal.pcbi.1004736

Raikov, I., and De Schutter, E. (2012). The promise and shortcomings of XML as an interchange format for computational models of biology. *Neuroinformatics* 10, 1–3. doi: 10.1007/s12021-011-9136-8

Riffell, J. A., Shlizerman, E., Sanders, E., Abrell, L., Medina, B., Hinterwirth, A. J., et al. (2014). Flower discrimination by pollinators in a dynamic chemical environment. *Science* 344, 1515–1518. doi: 10.1126/science.1251041

Sarma, G. P., Lee, C. W., Portegys, T., Ghayoomie, V., Jacobs, T., Alicea, B., et al. (2018). OpenWorm: overview and recent advances in integrative biological simulation of *Caenorhabditis elegans*. *Phil. Trans. R. Soc. B*. 373:20170382. doi: 10.1098/rstb.2017.0382

Schatzmann, H. J. (1989). The calcium pump of the surface membrane and of the sarcoplasmic reticulum. *Ann. Rev. Physiol*. 51, 473–485.

Shlizerman, E., Riffell, J. A., and Kutz, J. N. (2014). Data-driven inference of network connectivity for modeling the dynamics of neural codes in the insect antennal lobe. *Front. Comput. Neurosci*. 8:70. doi: 10.3389/fncom.2014.00070

Skinner, F. K. (2012). Cellular-based modeling of oscillatory dynamics in brain networks. *Curr. Opin. Neurobiol*. 22, 660–669. doi: 10.1016/j.conb.2012.02.001

Söhl, G., Maxeiner, S., and Willecke, K. (2005). Expression and functions of neuronal gap junctions. *Nat. Rev. Neurosci*. 6, 191–200. doi: 10.1038/nrn1627

Sporns, O., and Bullmore, E. T. (2014). From connections to function: the mouse brain connectome atlas. *Cell* 157, 773–775. doi: 10.1016/j.cell.2014.04.023

Stephens, G. J., Johnson-Kerner, B., Bialek, W., and Ryu, W. S. (2008). Dimensionality and dynamics in the behavior of *C. elegans*. *PLoS Comput. Biol.* 4:e1000028.

Szigeti, B., Gleeson, P., Vella, M., Khayrulin, S., Palyanov, A., Hokanson, J., et al. (2014). OpenWorm: an open-science approach to modeling *Caenorhabditis elegans*. *Front. Comput. Neurosci.* 8:137. doi: 10.3389/fncom.2014.00137

Van Den Heuvel, M. P., and Pol, H. E. (2010). Exploring the brain network: a review on resting-state fMRI functional connectivity. *Eur. Neuropsychopharmacol.* 20, 519–534. doi: 10.1016/j.euroneuro.2010.03.008

Varshney, L. R., Chen, B. L., Paniagua, E., Hall, D. H., and Chklovskii, D. B. (2011). Structural properties of the *Caenorhabditis elegans* neuronal network. *PLoS Comput. Biol.* 7:e1001066. doi: 10.1371/journal.pcbi.1001066

White, J. G., Southgate, E., Thomson, J. N., and Brenner, S. (1986). The structure of the nervous system of the nematode *Caenorhabditis elegans*. *Philos. Trans. R Soc. Lond. B Biol. Sci.* 314, 1–340. doi: 10.1098/rstb.1986.0056

Wicks, S. R., Roehrig, C. J., and Rankin, C. H. (1996). A dynamic network simulation of the nematode tap withdrawal circuit: predictions concerning synaptic function using behavioral criteria. *J. Neurosci.* 16, 4017–4031. doi: 10.1523/JNEUROSCI.16-12-04017.1996

Conflict of Interest Statement: The authors declare that the research was conducted in the absence of any commercial or financial relationships that could be construed as a potential conflict of interest.

frontiers in Computational Neuroscience

ORIGINAL RESEARCH
published: 05 April 2019
doi: 10.3389/fncom.2019.00019

Bistable Firing Pattern in a Neural Network Model

*Paulo R. Protachevicz[1], Fernando S. Borges[2], Ewandson L. Lameu[3], Peng Ji[4,5], Kelly C. Iarosz[6], Alexandre H. Kihara[2], Ibere L. Caldas[6], Jose D. Szezech Jr.[1,7], Murilo S. Baptista[8], Elbert E. N. Macau[3], Chris G. Antonopoulos[9], Antonio M. Batista[1,7] and Jürgen Kurths[10,11]**

[1] Graduate in Science Program—Physics, State University of Ponta Grossa, Ponta Grossa, Brazil, [2] Center for Mathematics, Computation, and Cognition, Federal University of ABC, São Bernardo do Campo, Brazil, [3] National Institute for Space Research, São José dos Campos, Brazil, [4] Institute of Science and Technology for Brain-Inspired Intelligence, Fudan University, Shanghai, China, [5] Key Laboratory of Computational Neuroscience and Brain-Inspired Intelligence (Fudan University), Ministry of Education, Shanghai, China, [6] Institute of Physics, University of São Paulo, São Paulo, Brazil, [7] Department of Mathematics and Statistics, State University of Ponta Grossa, Ponta Grossa, Brazil, [8] Institute for Complex Systems and Mathematical Biology, SUPA, University of Aberdeen, Aberdeen, United Kingdom, [9] Department of Mathematical Sciences, University of Essex, Colchester, United Kingdom, [10] Potsdam Institute for Climate Impact Research, Potsdam, Germany, [11] Department of Physics, Humboldt University, Berlin, Germany

Excessively high, neural synchronization has been associated with epileptic seizures, one of the most common brain diseases worldwide. A better understanding of neural synchronization mechanisms can thus help control or even treat epilepsy. In this paper, we study neural synchronization in a random network where nodes are neurons with excitatory and inhibitory synapses, and neural activity for each node is provided by the adaptive exponential integrate-and-fire model. In this framework, we verify that the decrease in the influence of inhibition can generate synchronization originating from a pattern of desynchronized spikes. The transition from desynchronous spikes to synchronous bursts of activity, induced by varying the synaptic coupling, emerges in a hysteresis loop due to bistability where abnormal (excessively high synchronous) regimes exist. We verify that, for parameters in the bistability regime, a square current pulse can trigger excessively high (abnormal) synchronization, a process that can reproduce features of epileptic seizures. Then, we show that it is possible to suppress such abnormal synchronization by applying a small-amplitude external current on $> 10\%$ of the neurons in the network. Our results demonstrate that external electrical stimulation not only can trigger synchronous behavior, but more importantly, it can be used as a means to reduce abnormal synchronization and thus, control or treat effectively epileptic seizures.

Keywords: bistable regime, network, adaptive exponential integrate-and-fire neural model, neural dynamics, synchronization, epilepsy

OPEN ACCESS

Edited by:
Matjaž Perc,
University of Maribor, Slovenia

Reviewed by:
Daqing Guo,
University of Electronic Science and Technology of China, China
Subhas Khajanchi,
Presidency University, India

****Correspondence:***
Jürgen Kurths
kurths@pik-potsdam.de

Received: *08 February 2019*
Accepted: *18 March 2019*
Published: *05 April 2019*

Citation:
Protachevicz PR, Borges FS, Lameu EL, Ji P, Iarosz KC, Kihara AH, Caldas IL, Szezech JD Jr, Baptista MS, Macau EEN, Antonopoulos CG, Batista AM and Kurths J (2019) Bistable Firing Pattern in a Neural Network Model. Front. Comput. Neurosci. 13:19. doi: 10.3389/fncom.2019.00019

1. INTRODUCTION

Epilepsy is a brain disease that causes seizures and sometimes loss of consciousness (Chen et al., 2014, 2015). Epileptic seizures are associated with excessively high synchronous activities (Li et al., 2007; Jiruska et al., 2013; Wu et al., 2015) of neocortex regions or other neural populations (Fisher et al., 2005; Sierra-Paredes and Sierra-Marcuño, 2007; Engel et al., 2013; Geier and Lehnertz, 2017; Falco-Walter et al., 2018). Electroencephalography has been used to identify and classify seizures

(Noachtar and Rémi, 2009), as well as to understand epileptic seizures (Scharfman and Buckmaster, 2014). Abnormal activities have a short period of time, lasting from a few seconds to minutes (Trinka et al., 2015), and they can occur in small or larger regions in the brain (McCandless, 2012; Kramer and Cash, 2012). Two suggested mechanisms responsible for the generation of partial epilepsy are the decrease of inhibition and increase of excitation (McCandless, 2012). In experiments and simulations, the reduction of excitatory and the increase of inhibitory influence have been effective in suppressing and preventing synchronized behaviors (Traub et al., 1993; Schindler et al., 2008). Traub and Wong (1982) showed that synchronized bursts that appear in epileptic seizures depend on neural dynamics.

Single seizures can not kill neurons, however recurrent ones can do so and thus, can lead to chronic epilepsy (Dingledine et al., 2014). Evidence that supports this further is provided by abnormal anatomical alterations, such as mossy fiber sprouting (Danzer, 2017), dendritic reconfigurations (Wong, 2005, 2008), and neurogenesis (Jessberger and Parent, 2015; Cho et al., 2015). In fact, such alterations change the balance between inhibition and excitation (Holt and Netoff, 2013; Silva et al., 2003). Wang et al. (2017) demonstrated that a small alteration in the network topology can induce a bistable state with an abrupt transition to synchronization. Some *in vitro* seizures generated epileptiform activities when inhibitory synapses were blocked or excitatory synapses were enhanced (Traub et al., 1994; White, 2002). Several studies showed that epileptiform activities are related not only with unbalanced neural networks, but also with highly synchronous regimes (Uhlhaas and Singer, 2006; Andres-Mach and Adamu, 2017).

Different routes to epileptic seizures were reported by Silva et al. (2003). The authors considered epilepsy as a dynamical disease and presented a theoretical framework where epileptic seizures occur in neural networks that exhibit bistable dynamics. In the bistable state, transitions can happen between desynchronous and synchronous behaviors. Suffczynski et al. (2004) modeled the dynamics of epileptic phenomena by means of a bistable network.

Many works reported that periodic electrical pulse stimulation facilitates synchronization, while random stimulation promotes desynchronization in networks (Cota et al., 2009). Electrical stimulation can be applied in different brain areas, for instance in the hippocampus, thalamus, and cerebellum (McCandless, 2012). The mechanism for electrical stimulation to cease seizures is still not completely understood, however, signal parameters such as frequency, duration, and amplitude can be changed to improve the efficiency of the treatment of epilepsy (McCandless, 2012). The electrical stimulation has been used as an efficient treatment for epilepsy in the hippocampus (Velasco et al., 2007). In Antonopoulos (2016), the author studied external electrical perturbations and their responses in the brain dynamic network of the Caenorhabditis elegans soil worm. It was shown that when one perturbs specific communities, keeping the others unperturbed, the external stimulations propagate to some but not all of them. It was also found that there are perturbations that do not trigger any response at all and that this depends on the initially perturbed community.

Neural network models have been used to mimic phenomena related to neural activities in the brain. Guo et al. (2016a) built a network model where the postsynaptic neuron receives input from excitatory presynaptic neurons. They incorporated autaptic coupling (Guo et al., 2016b) in a biophysical model. Delayed models have been considered in biological systems (Khajanchi et al., 2018), for instance, Sun et al. (2018) analyzed the influence of time delay in neuronal networks. They showed that intra- and inter-time delays can induce fast regular firings in clustered networks. In this work, we build a random network with neural dynamics to study synchronization induced in a bistable state which is related to epileptic seizures. In particular, we consider a network composed of adaptive exponential integrate-and-fire (AEIF) neurons coupled by means of inhibitory and excitatory synapses. The AEIF model mimics phenomenological behaviors of neurons (Clopath et al., 2006) and is appropriate to study even large networks (Naud et al., 2008). Borges et al. (2017) verified that depending on the excitatory synaptic strength and connection probability, a random network of coupled AEIF neurons can exhibit transitions between desynchronized spikes and synchronized bursts (Protachevicz et al., 2018). In the network considered here, we observe the existence of bistability when it is unbalanced, namely that the decrease of synaptic inhibition induces a bistable state. We analyse the effects of the application of external square current pulses (SCP) by perturbing the neural dynamics on the network using parameters that lead to a bistable state, such as the excitatory and inhibitory synaptic conductances. We find that, depending on the duration and amplitude of the external current, SCP can either trigger or suppress synchronization in the bistability region, an idea that can be used further to treat epilepsy by suppressing excessive synchronization in affected brain regions.

2. METHODS

2.1. Neural Network Model

We build a random network of $N = 1,000$ adaptive exponential integrate-and-fire neurons (Brette and Gerstner, 2005) with probability p for the formation of connections among them equal to 0.1. The network consists of 80% excitatory and 20% inhibitory neurons (Noback et al., 2005). The dynamics of each neuron i, $i = 1, \ldots, N$ in the network is given by the set of equations

$$\begin{aligned} C_{\mathrm{m}}\frac{dV_i}{dt} &= -g_L(V_i - E_L) + g_L\Delta_T \exp\left(\frac{V_i - V_T}{\Delta_T}\right) \\ &\quad + I_i - w_i + \sum_{j=1}^{N}(V^j_{\mathrm{REV}} - V_i)M_{ij}g_j + \Gamma_i, \\ \tau_w\frac{dw_i}{dt} &= a_i(V_i - E_L) - w_i, \\ \tau_s\frac{dg_i}{dt} &= -g_i. \end{aligned} \tag{1}$$

The membrane potential V_i and adaptation current w_i represent the state of each neuron i. The capacitance membrane C_{m} is set to $C_{\mathrm{m}} = 200$ pF, the leak conductance to $g_L = 12$ nS, the resting potential to $E_L = -70$ mV, the slope factor to

$\Delta_T = 2.0$ mV and the spike threshold to $V_T = -50$ mV. The adaptation current depends on the adaptation time constant $\tau_w = 300$ ms and the level of subthreshold adaptation a_i that is randomly distributed in the interval $[0.19, 0.21]$ nS. We consider the injection of current I_i to each neuron i in terms of the relative rheobase current $r_i = I_i/I_{\text{rheobase}}$ (Naud et al., 2008). The rheobase is the minimum amplitude of the applied current to generate a single or successive firings. The application of this constant current allows neurons to change their potentials from resting potentials to spikes. The value of the rheobase depends on the neuron parameters. The external current arriving at neuron i is represented by Γ_i. We consider the external current according to a SCP with amplitude A_I and time duration T_I. The random connections in the network are described by the binary adjacency matrix M_{ij} with entries either equal to 1 when there is a connection from i to j or 0 in the absence of such a connection. g_i is the synaptic conductance, τ_s the synaptic time constant, and V_{REV} the synaptic reversal potential. We consider $\tau_s = 2.728$ ms, $V_{\text{REV}} = 0$mV for excitatory synapses, and $V_{\text{REV}} = -80$ mV for inhibitory synapses. The synaptic conductance decays exponential with a synaptic time constant τ_s. When the membrane potential of neuron i is above the threshold $V_i > V_{\text{thres}}$ (Naud et al., 2008), the state variable is updated by the rule

$$\begin{aligned} V_i &\rightarrow V_r = -58\text{mV}, \\ w_i &\rightarrow w_i + 70\text{pA}, \\ g_i &\rightarrow g_i + g_s, \end{aligned} \tag{2}$$

where g_s assumes the value of g_{exc} when neuron i is excitatory ($i \leq 0.8N$) and g_{inh} when neuron i is inhibitory ($i > 0.8N$). In this work, we study the parameter space (g_{exc},g_{inh}) and consider a relative inhibitory synaptic conductance $g = g_{\text{inh}}/g_{\text{exc}}$. We consider parameter values in which the individual uncoupled neurons perform spike activities. The initial values of V and w are randomly distributed in the interval $[-70, -50]$ mV and $[0, 70]$ pA, respectively. The initial g_i value is equal to 0.

2.2. Synchronization

The synchronous behavior in the network can be identified by means of the complex phase order parameter (Kuramoto, 1984)

$$R(t)\exp(\text{i}\Phi(t)) \equiv \frac{1}{N}\sum_{j=1}^{N}\exp(\text{i}\psi_j(t)), \tag{3}$$

where $R(t)$ and $\Phi(t)$ are the amplitude and angle of a centroid phase vector over time, respectively. The phase of neuron j is obtained by means of

$$\psi_j(t) = 2\pi m + 2\pi\frac{t - t_{j,m}}{t_{j,m+1} - t_{j,m}}, \tag{4}$$

where $t_{j,m}$ corresponds to the time of the $m-$th spike of neuron j ($t_{j,m} < t < t_{j,m+1}$) (Rosenblum et al., 1996, 1997). We consider that the spike occurs for $V_j > V_{\text{thres}}$. $R(t)$ is equal to 0 for fully desynchronized and 1 for fully synchronized patterns, respectively.

We calculate the time-average order parameter $\overline{R}$ (Batista et al., 2017) given by

$$\overline{R} = \frac{1}{t_{\text{fin}} - t_{\text{ini}}}\int_{t_{\text{ini}}}^{t_{\text{fin}}} R(t)dt, \tag{5}$$

where $t_{\text{fin}} - t_{\text{ini}}$ is the time window. We consider $t_{\text{fin}} = 200$s and $t_{\text{ini}} = 180$s.

2.3. Synaptic Input

We monitor the instantaneous synaptic conductances arriving at each neuron i through

$$I_i^{\text{ISC}}(t) = \sum_{j=1}^{N}(V_{\text{REV}}^j - V_i)M_{ij}g_j. \tag{6}$$

The instantaneous synaptic input changes over time due to the excitatory and inhibitory inputs received by neuron i. The average instantaneous synaptic conductances is given by

$$I_{\text{syn}}(t) = \frac{1}{N}\sum_{i=1}^{N} I_i^{\text{ISC}}(t). \tag{7}$$

2.4. Coefficient of Variation

The $m-$th inter-spike interval ISI_i^m is defined as the difference between two consecutive spikes of neuron i,

$$\text{ISI}_i^m = t_i^{m+1} - t_i^m > 0, \tag{8}$$

where t_i^m is the time of the $m-$th spike of neuron i.

Using the mean value of ISI_i, $\overline{\text{ISI}_i}$, and its standard deviation, σ_{ISI_i}, we calculate the coefficient of variation (CV)

$$\text{CV}_i = \frac{\sigma_{\text{ISI}_i}}{\overline{\text{ISI}_i}}. \tag{9}$$

The average of CV ($\overline{\text{CV}}$) is then obtained through

$$\overline{\text{CV}} = \frac{1}{N}\sum_{i=1}^{N}\text{CV}_i. \tag{10}$$

Finally, we use $\overline{\text{CV}}$ to identify spike (when $\overline{\text{CV}} < 0.5$) and burst fire patterns (when $\overline{\text{CV}} \geq 0.5$) (Borges et al., 2017; Protachevicz et al., 2018).

2.5. Instantaneous and Mean Firing-Rate

The instantaneous firing-rate in intervals of $t_{\text{step}} = 1$ms is given by

$$F(t) = \frac{1}{N}\sum_{i=1}^{N}\left(\int_{t}^{t+t_{\text{step}}}\delta(t' - t_i)dt'\right), \tag{11}$$

where t_i is the firing time of neuron i in the time interval ($t \leq t_i \leq t + 1$) ms. This measure allows to obtain the instantaneous

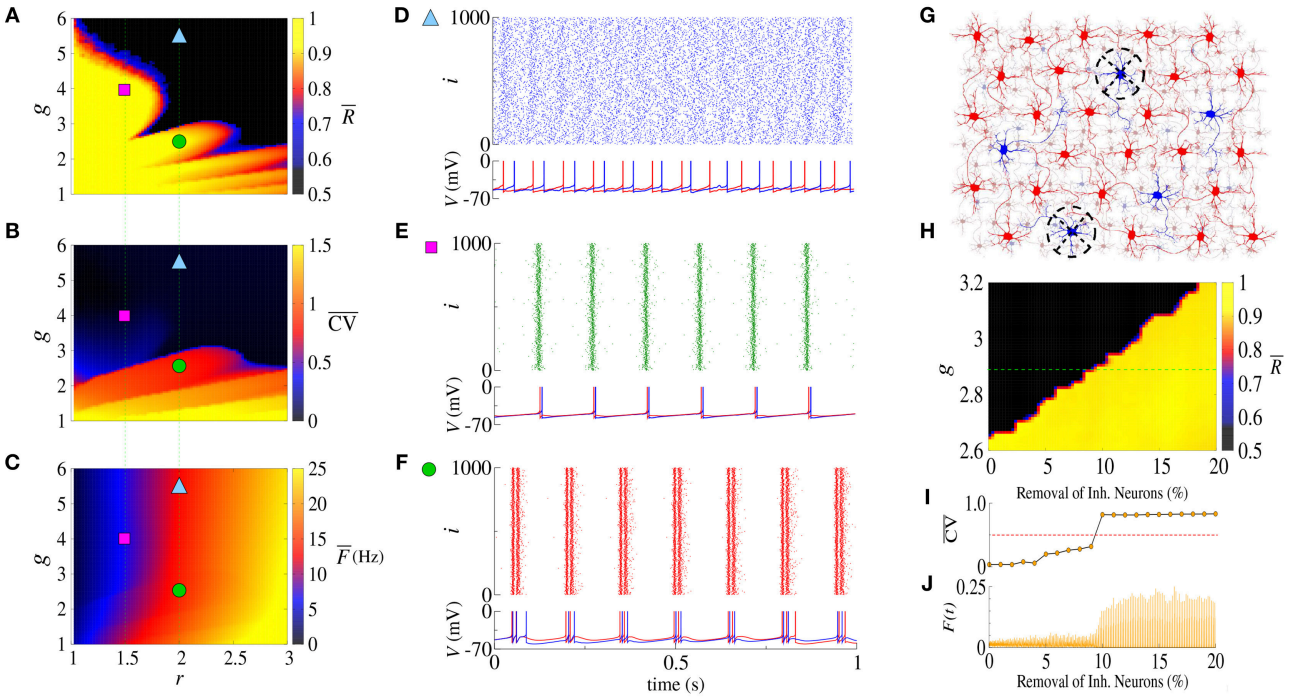

FIGURE 1 | Parameter space (g, r) for the **(A)** time-average order parameter ($\overline{R}$), **(B)** the mean coefficient of variation ($\overline{CV}$), and **(C)** the mean firing-rate ($\overline{F}$). Raster plot that displays the spiking activity over time and membrane potential are shown for **(D)** desynchronized spikes for $r = 2.0$ and $g = 5.5$ (cyan triangle), **(E)** synchronized spikes for $r = 1.5$ and $g = 4$ (magenta square), and **(F)** synchronized bursts for $r = 2.0$ and $g = 2.5$ (green circle). Here, we consider $g_{exc} = 0.4$nS. In **(G)**, we illustrate a network composed of excitatory (red) and inhibitory (blue) neurons, where some inhibitory neurons are removed (black dashed circle). **(H)** Shows the time-average order parameter for g vs. the percentage of inhibitory neurons removed from the network. The green dashed line corresponds to $g = 2.9$. The values of $\overline{CV}$ and instantaneous firing-rate are shown in **(I,J)**, respectively.

population activity in the network. The mean firing-rate can then be calculated by means of

$$\overline{F} = \frac{1}{\overline{ISI}}, \tag{12}$$

where $\overline{ISI}$ is the average ISI obtained over all N neurons in the network, that is $\overline{ISI} = \frac{1}{N}\sum_{i=1}^{N} \overline{ISI}_i$.

3. RESULTS

3.1. Inhibitory Effect on Synchronous Behavior

The balance between excitation and inhibition generates an asynchronous activity in the network (Lundqvist et al., 2010; Ostojic, 2014). However, for the unbalanced network we observe synchronized spikes and bursts. **Figures 1A–C** show the time-average order parameter ($\overline{R}$), the mean coefficient of variation ($\overline{CV}$) and the mean firing-rate ($\overline{F}$), respectively, for the parameter space (g, r), where g is the ratio between inhibitory (g_{inh}) and excitatory (g_{exc}) synaptic conductances, and r the relative rheobase current. For $g_{exc} = 0.4$nS and $g > 6$, we observe that $\overline{R} < 0.5$ and that $\overline{CV} < 0.5$, corresponding to desynchronized spikes. In **Figure 1D**, we see the raster plot and membrane potential for 2 neurons in the network with a desynchronized spike-pattern for $g = 5.5$ and $r = 2$ (blue triangle). For $g = 4$ and $r = 1.5$ (magenta square), the dynamics exhibits synchronized spikes (**Figure 1E**), as a result of setting $\overline{R} > 0.9$ and $\overline{CV} < 0.5$. **Figure 1F** shows synchronized bursts of activity for $g = 2.5$ and $r = 2$ (green circle), where $\overline{R} > 0.9$ and $\overline{CV} \geq 0.5$. Within this framework, we have verified the existence of transitions from desynchronized spikes to synchronized bursting activities without significant changes in the mean firing-rate.

The appearance of synchronous behavior cannot only be related to the decrease of the inhibitory synaptic strength, but also to a loss of inhibitory neurons. In particular, we show this in **Figure 1G** which illustrates a network composed of excitatory (red) and inhibitory (blue) neurons, where some inhibitory neurons were removed (dashed circles). In **Figure 1H**, we see that the synchronous behavior depends on g and the percentage of removed inhibitory neurons. **Figure 1I** shows the transition from spiking dynamics ($\overline{CV} < 0.5$) to bursting dynamics ($\overline{CV} \geq 0.5$), and **Figure 1J** shows the instantaneous firing-rate $F(t)$. For $g = 2.9$ and $g_{exc} = 0.4$nS (green dashed line), the transition to synchronized bursts occurs when 10% of inhibitory neurons are removed from the network, and as a consequence $F(t)$ reaches the maximum value of 0.2.

Concluding, alterations in the inhibitory synaptic strength or in the number of inhibitory neurons can induce transition to synchronous patterns. Wang et al. (2017) presented results where synchronization transition occurs as a result of small changes in the topology of the network, whereas here, we study transitions

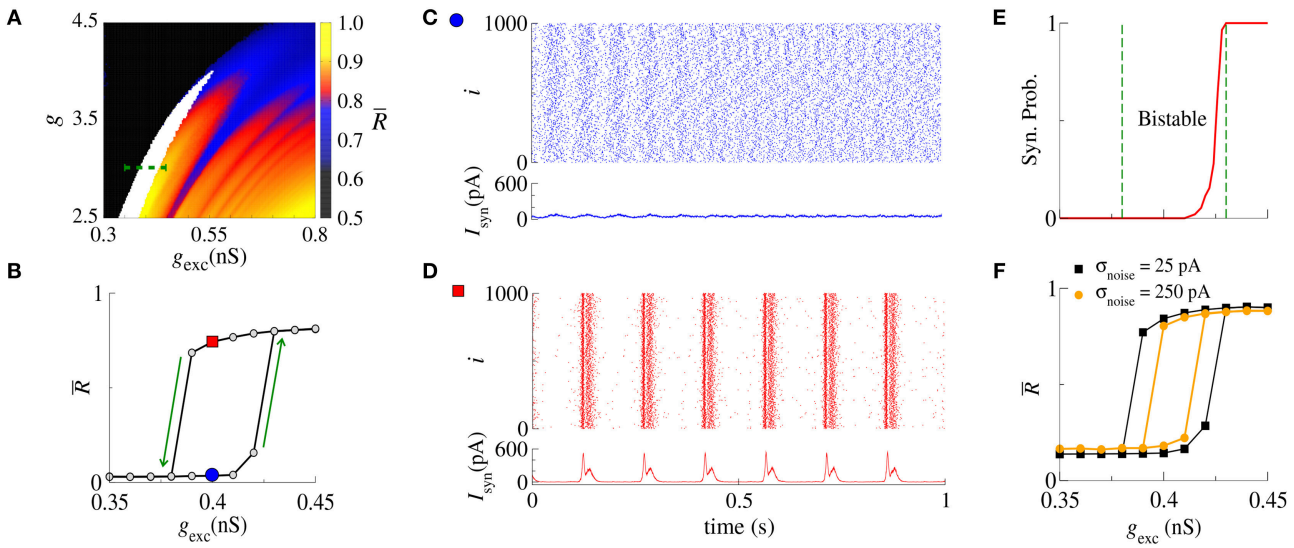

FIGURE 2 | (A) The parameter space (g, g_{exc}) for $r = 2$, where $\overline{R}$ is encoded in color. The black region corresponds to desynchronized activity, whereas colored regions indicate $\overline{R} > 0.6$ and the white region represents the bistable regime. **(B)** The bistable region indicated in the parameter space of **(A)** by means of a green dashed line. **(C,D)** Show the raster plots and I_{syn} for desynchronized spikes (blue circle) and synchronized bursts (red square), respectively. We identify bistability by checking when $\overline{R}_{backward} - \overline{R}_{forward} > 0.4$ and consider two trials for each set of parameter values. **(E)** The synchronization probability as a function of g_{exc}. **(F)** $\overline{R} \times g_{exc}$ for σ_{noise} equal to 25 pA and 250 pA.

caused due to changes in the inhibitory synaptic strength and the emergence of a bistable regime.

3.2. Bistable Regime

Next, we analyse synchronization in the parameter space (g, g_{exc}). In particular, **Figure 2A** shows $\overline{R}$ with values depicted in the color bar. The black region corresponds to desynchronized spike activity, while the remaining colored regions are associated with burst activities. The white region represents the bistable regime, where desynchronized spikes or synchronized bursts are possible depending on the initial conditions. In the bistable regime, decreasing g_{exc} (backward direction), $\overline{R}$ is higher than increasing g_{exc} (forward direction), as shown in **Figure 2B** for $g = 3$, $r = 2$, and $g_{exc} = [0.35, 0.45]$ nS (green dashed line in **Figure 2A**). We identify bistability (white region) in the parameter space when the condition $\overline{R}_{backward} - \overline{R}_{forward} > 0.4$ is fulfilled. The raster plot and instantaneous synaptic input for desynchronized spikes (blue circle) and synchronized bursts (red square) are shown in **Figures 2C,D**, respectively. When the dynamics on the random network is characterized by desynchronized spikes, the instantaneous synaptic inputs exhibit $I_{syn}(t) \approx 50$pA. For synchronized bursts, $I_{syn}(t) \approx 0$ when a large number of neurons in the network are silent (i.e., not firing), and $I_{syn}(t) > 200$ pA during synchronous firing activities. In **Figure 2E**, we compute the probability of occurrence of excessively high synchronicity within the bistable regime. We observe a small synchronization probability value in the bistable region. This result has a biological importance due to the fact that the seizure state is a relatively small probability event compared with the normal state. DaQing et al. (2017) showed that noise can regulate seizure dynamics in partial epilepsy. **Figure 2F** displays $\overline{R} \times g_{exc}$ for

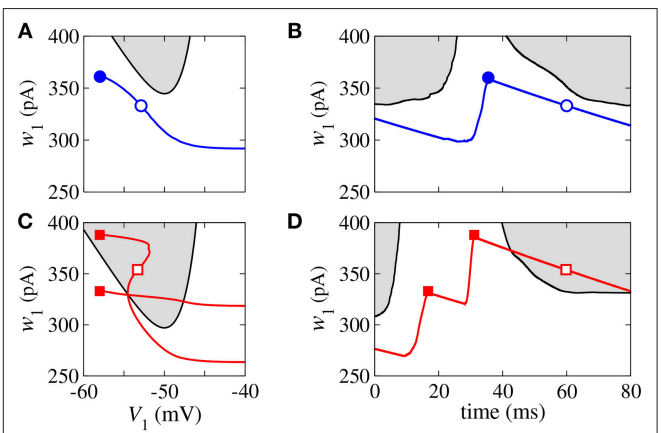

FIGURE 3 | Phase space (w_1, V_1) **(A,C)** and time evolution of w_1 **(B,D)** for spikes (blue) and burst activity (red). The gray regions correspond to $dV_1/dt < 0$ and the black line represents $dV_1/dt = 0$ (V-nullcline).

Gaussian noise with mean 0 and standard deviation σ_{noise} equal to 25 pA and 250 pA. We verify that the bistable region decreases when the noise level increases.

In the bistable regime, we investigate the evolution of a trajectory for a finite time interval in the phase space (w_i, V_i) and the time evolution of w_i shown in **Figure 3** for $i = 1$, where the gray regions correspond to $dV_i/dt < 0$. The boundary between the gray and white regions (black line) is given by $dV_i/dt = 0$, the V_i-nullcline (Naud et al., 2008). During spiking activity, the trajectory (see **Figure 3A**) and time evolution of w_i (see **Figure 3B**) do not cross the V_i-nullcline. For bursting

activities (see **Figures 3C,D**), we observe that w_i lies in the region enclosed by the V_i-nullcline. The emergence of the bistable behavior is related to changes in the V_i-nullcline caused by the variation of I_{syn}.

3.3. External Square Current Pulse

Here, following a similar idea as in Antonopoulos (2016), we investigate the effect of the application of SCP on the bistable regime. We apply SCP considering different values of A_I, T_I, and number of removed inhibitory neurons. The SCP is immediately switched off after T_I and the analysis of the effect on the dynamical behavior is started.

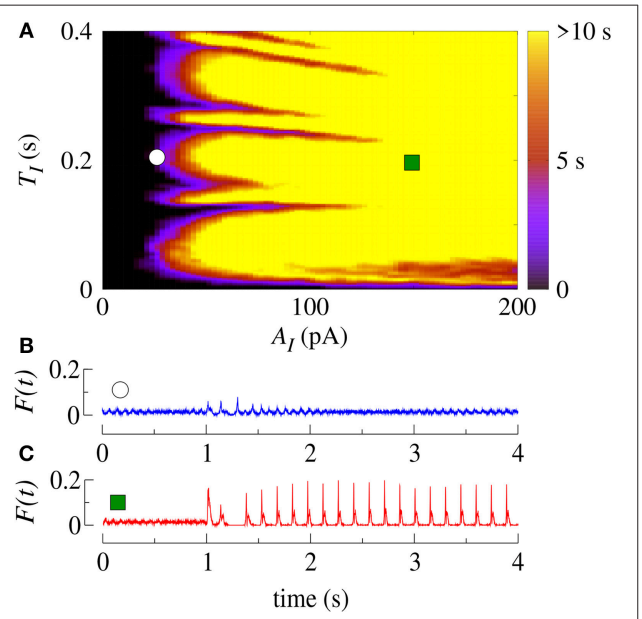

FIGURE 4 | (A) The parameter space (T_I, A_I) in the bistable regime, where the color bar indicates the time the system shows synchronized burst behavior after the application of SCP. Instantaneous firing-rate for values for **(B)** white circle ($A_I = 25$pA, $T_I = 0.2$s) and **(C)** green square ($A_I = 150$pA, $T_I = 0.2$s). Note that in this figure $g_{exc} = 0.4$nS, $g = 3$ and $r = 2$.

Initially, we apply SCP to all neurons in the network with parameter values in the bistable regime with desynchronous behavior (white region in **Figure 2A**). **Figure 4A** displays the time (in color scale) that the neurons show a synchronized pattern after the application of SCP. In the black region, we see that SCP does not change the dynamical behavior, namely the neurons remain in a regime of desynchronized behavior. The yellow region depicts the values of T_I and A_I of the SCP that induce a change in the behavior of the neurons from desynchronized spikes to synchronized bursts. Picking up one point close to the border of the black and blue regions (white circle), we see that the instantaneous firing-rate ($F(t)$) of Equation 11 (see **Figure 4B**, blue line) exhibits low-amplitude oscillations corresponding to desynchronized spikes. For T_I and A_I values in the yellow region, $F(t)$ (see **Figure 4C**, red line) exhibits a high-amplitude oscillation after the application of SCP, corresponding to synchronized bursts. For sufficiently large amplitudes, the change in the behavior induced by SCP does not depend on time. Importantly, perturbations with small amplitudes applied for short times is a sufficient condition for the induction of synchronous burst activity in the bistable regime. Therefore, our results suggest that even small excitatory stimuli in a random neural network arriving from other parts might be sufficient for the initiation of excessively high neural synchronization, related to the onset of epileptic seizures. Thus, further work on other neural networks that resemble brain activity might provide more insights on epileptogenesis.

Similarly, we apply SCP when the neurons in the network show synchronized bursts of firing activity in the bistable regime. Here, we aim to suppressing the synchronous behavior by means of applying SCP. We consider SCP with positive and negative amplitudes applied to 10% of the neurons in the random network. **Figure 5A** shows how long the bursts remain synchronized after SCP is switched off (color bar). We verified that both negative and positive amplitudes exhibit regions where the synchronous behaviors are suppressed, namely there is a transition from synchronized bursts to desynchronized spikes. In addition, for $T_I > 0.4$ s and considering the absolute value of the amplitudes, the transition occurs for positive values with smaller amplitudes than for negative values. In **Figure 5B**, we show the dependence

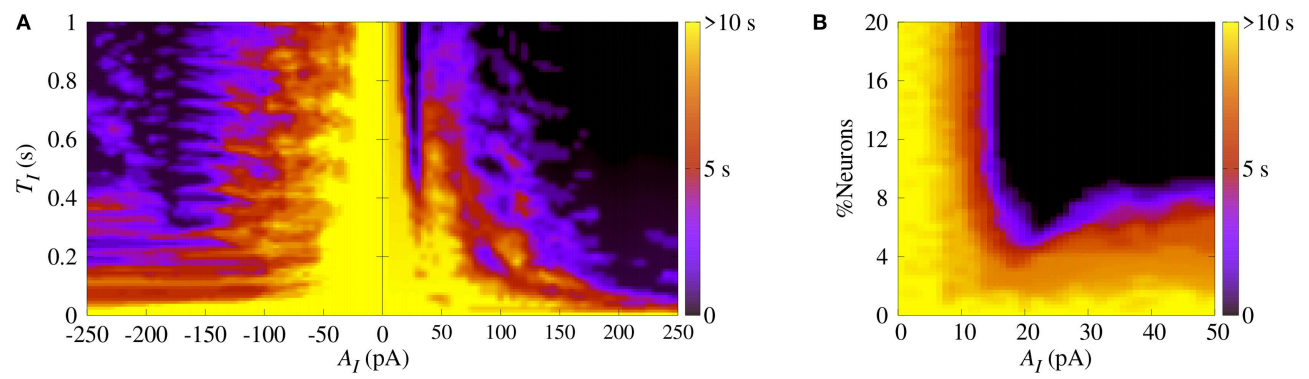

FIGURE 5 | (A) The parameter space (T_I, A_I), where the color bar indicates the time the system shows synchronized burst behavior after the application of SCP. **(B)** Number of perturbed neurons as a function of A_I. Note that in this figure we consider $g_{exc} = 0.4$nS, $g = 3$ and $r = 2$.

of the percentage of the perturbed neurons by the stimulus on the time the neurons remain in the bursting synchronous regime. The black region represents parameters for which the dynamics on the network does not remain synchronous, and therefore, synchronization is suppressed. In this figure, $T_I = 1$s. These results allow us to conclude that desynchronous behavior is achieved for $A_I > 15$pA and for at least 10% of the perturbed neurons.

4. DISCUSSION AND CONCLUSION

In this paper, we studied the influence of inhibitory synapses on the appearance of synchronized and desynchronized fire patterns in a random network with adaptive exponential integrate-and-fire neural dynamics. When the inhibitory influence is reduced by either decreasing the inhibitory synaptic strength or the number of inhibitory neurons, the dynamics on the network is more likely to exhibit synchronous behavior. The occurrence of synchronization results from the lack of balance between excitatory and inhibitory synaptic influences.

We found parameter values that shift to a bistable regime where the neurons can either exhibit desynchronous spiking or synchronized bursting behavior. In the bistability region, a desynchronous (synchronous) behavior becomes synchronous (desynchronous) by varying forward (backward) g_{exc}. The onset of synchronization is thus associated with a hysteresis-loop.

We showed that, in the bistable regime, synchronized bursts can be induced by means of applying square current pulses. Our study also showed that outside the bistable regime, square current pulses do not induce synchronization. Furthermore, in the bistable regime, when neurons are synchronized, square current pulses can be used to suppress it. Positive amplitudes of square current pulses are more effective in ceasing synchronized bursts than negative ones. In addition, we showed that when one applies square current pulses to >10% of the neurons in the network, it is enough to desynchronize the dynamics. Our work shows that a decrease of inhibition contributes to the appearance of excessively high synchronization, reminiscent of the onset of epileptic seizures in the brain, thus confirming previous experimental results and theoretical models. Both decreasing the number of inhibitory neurons and the inhibitory strength, induce excessively high synchronization, related to epilepsy.

Finally, within this framework, we hypothesize that low amplitude stimuli coming from some brain regions might be capable of inducing an epileptic seizure manifested by high neural (abnormal) synchronization in other brain regions. Therefore, the work in this paper supports the common approach of the induction of square current pulses to control or treat epileptic seizures, since we have shown that such external perturbations not only can induce, but more importantly can suppress synchronous behavior in random networks with neural dynamics.

AUTHOR CONTRIBUTIONS

PP, FB, EL, and KI designed the work, developed the theory and performed the numerical simulations. AB wrote the manuscript with support from IC, JS, MB, CA, and JK. PJ, AK, and EM revised the manuscript for several times and gave promising suggestions. All authors contributed to manuscript revision, read and approved the submitted version.

FUNDING

This study was possible by partial financial support from the following Brazilian government agencies: Fundação Araucária, CNPq (433782/2016-1, 310124/2017-4, and 428388/2018-3), CAPES, and FAPESP (2015/50122-0, 2015/07311-7, 2016/16148-5, 2016/23398-8, 2017/13502-5, 2017/18977-1, 2018/03211-6).

ACKNOWLEDGMENTS

We also wish to thank the Newton Fund, COFAP, and International Visiting Fellowships Scheme of the University of Essex. We also thank IRTG 1740 for support.

REFERENCES

Abdullahi, A. T., and Adamu, L. H. (2017). Neural network models of epileptogenesis. *Neurosciences* 22, 85–93. doi: 10.17712/nsj.2017.2.20160455

Antonopoulos C. G. (2016). Dynamic range in the *C. elegans* brain network. *Chaos* 26, 1054–1500. doi: 10.1063/1.4939837

Batista, C. A. S., Szezech Jr, J. D., Batista, A. M., Macau, E. E. N., and Viana, R. L. (2017). Synchronization of phase oscillators with coupling mediated by a diffusing substance. *Physica A* 470, 236–248. doi: 10.1016/j.physa.2016.11.140

Borges, F. S., Protachevicz, P. R., Lameu, E. L., Bonetti, R. C., Iarosz, K. C., Caldas, I. L., et al. (2017). Synchronised firing patterns in a random network of adaptive exponential integrate-and-fire neuron model. *Neural Networks* 90, 1–7. doi: 10.1016/j.neunet.2017.03.005

Brette, R., and Gerstner, W. (2005). Adaptive exponential integrate-and-fire model as an effective description of neural activity. *J. Neurophysiol.* 94, 3637–3642. doi: 10.1152/jn.00686.2005

Chen, M., Guo, D., Li, M., Ma, T., Wu, S., Ma, J., et al. (2015). Critical roles of the direct GABAergic pallido–cortical pathway in controlling absence seizures. *PLoS Comp. Biol.* 11:e1004539. doi: 10.1371/journal.pcbi.1004539

Chen, M., Guo, D., Wang, T., Jing, W., Xia, Y., Xu, P., et al. (2014). Bidirectional control of absencd sizures by the basal ganglia: a computational evidence. *PLoS Comp. Biol.* 10:e1003495. doi: 10.1371/journal.pcbi.1003495

Cho, K.-O., Lybrand, Z. R., Ito, N., Brulet, R., Tafacory, F., Zhang, L., et al. (2015). Aberrant hippocampal neurogenesis contributes to epilepsy and associated cognitive decline. *Nat. Commun.* 6:6606. doi: 10.1038/ncomms7606

Clopath, C., Jolivet, R., Rauch, A., Lüscher, H.-R., and Gerstner, W. (2007). Predicting neural activity with simple models of the threshold type: adaptive exponential integrate-and-fire model with two compartments. *Neurocomputing* 70, 1668–1673. doi: 10.1016/j.neucom.2006.10.047

Cota, V. R., Medeiros, D. C., Vilela, M. R. S. P., Doretto, M. C., and Moraes, M. F. D. (2009). Distinct patterns of electrical stimulation of the basolateral amygdala influence pentylenetetrazole seizure outcome. *Epilepsy Behav.* 14, 26–31. doi: 10.1016/j.yebeh.2008.09.006

Danzer, S. (2017). Mossy fiber sprouting in the epileptic brain: taking on the Lernaean Hydra. *Epilepsy Curr.* 17, 50–51. doi: 10.5698/1535-7511-17.1.50

DaQing, G., Chuan, X., ShengDun, W., TianJiao, Z., YangSong, Z., Yang, X., et al. (2017). Stochastic fluctuations of permittivity coupling regulate

seizure dynamics in partial epilepsy. *Sci. China Technol. Sci.* 60, 995–1002. doi: 10.1007/s11431-017-9030-4

Dingledine, R., Varvel, N. H., and Dudek, F. E. (2014). When and how do seizures kill neurons, and is cell death relevant to epileptogenesis? *Adv. Exp. Med. Biol.* 813, 109–122. doi: 10.1007/978-94-017-8914-1_9

Engel, J. Jr., Thompson, P. M., Stern, J. M., Staba, R. J., Bragin, A., and Mody, I. (2013). Connectomics and epilepsy. *Curr. Opin. Neurol.* 26, 186–194. doi: 10.1097/WCO.0b013e32835ee5b8

Falco-Walter, J. J., Scheffer, I. E., and Fisher, R. S. (2018). The new definition and classification of seizures and epilepsy. *Epilepsy Res.* 139, 73–79. doi: 10.1016/j.eplepsyres.2017.11.015

Fisher, R. S., van Emde Boas, W., Blume, W., Elger, C., Genton, P., Lee, P., et al. (2005). Epileptic seizures and epilepsy: Definitions proposed by the International League Against Epilepsy (ILAE) and the International Bureau for Epilepsy (IBE). *Epilepsia* 46, 470–472. doi: 10.1111/j.0013-9580.2005.66104.x

Geier, C., and Lehnertz, K. (2017). Which brain regions are important for seizure dynamics in epileptic networks? Influence of link identification and EEG recording montage on node centralities. *Int. J. Neural Syst.* 27:1650033. doi: 10.1142/S0129065716500337

Guo, D., Chen, M., Perc, M., Wu, S., Xia, C., Zhang, Y., et al. (2016). Firing regulation of fast-spiking interneurons by autaptic inhibition. *Europhys. Lett.* 114:30001. doi: 10.1209/0295-5075/114/30001

Guo, D., Wu, S., Chen, M., Perc, M., Zhang, Y., Ma, J., et al. (2016). Regulation of irregular neuronal firing by autaptic transmission. *Sci. Rep.* 6:26096. doi: 10.1038/srep26096

Holt, A. B., and Netoff, T. I. (2013). Computational modeling of epilepsy for an experimental neurologist. *Exp. Neurol.* 244, 75–86. doi: 10.1016/j.expneurol.2012.05.003

Jessberger, S., and Parent, J. M. (2015). Epilepsy and adult neurogenesis. *Cold Spring Harbor Persp. Biol.* 7, 1–10. doi: 10.1101/cshperspect.a020677

Jiruska, P., de Curtis, M., Jefferys, J. G. R., Schevon, C. A., Schiff, S. J., and Schindler, K. (2013). Synchronization and desynchronization in epilepsy: Controversies and hypotheses. *J. Physiol.* 591.4, 787–797. doi: 10.1113/jphysiol.2012.239590

Khajanchi, S., Perc, M., and Ghosh, D. (2018). The influence of time delay in a chaotic cancer model. *Chaos* 28:103101. doi: 10.1063/1.5052496

Kramer, M. A., and Cash, S. S. (2012). Epilepsy as a disorder of cortical network organization. *Neuroscientist* 18, 360–372. doi: 10.1177/1073858411422754

Kuramoto, Y (1984). *Chemical Oscillations, Waves, and Turbulence*. Berlin: Springer-Verlag. doi: 10.1007/978-3-642-69689-3

Li, X., Cui, D., Jiruska, P., Fox, J. E., Yao, X., and Jefferys, J. G. (2007). Synchronization measurement of multiple neural populations. *J. Neurophysiol.* 98, 3341–3348. doi: 10.1152/jn.00977.2007

Lundqvist, M., Compte, A., and Lansner, A. (2010). Bistable, irregular firing and population oscillations in a modular attractor memory network. *PLoS Comp. Biol.* 6:e1000803. doi: 10.1371/journal.pcbi.1000803

McCandless, D. W. (2012). *Epilepsy: Animal and Human Correlations*. New York, NY: Springer-Verlag. doi: 10.1007/978-1-4614-0361-6

Naud, R., Marcille, N., Clopath, C., and Gerstner, W. (2008). fire patterns in the adaptive exponential integrate-and-fire model. *Biol. Cyber.* 99, 335–347. doi: 10.1007/s00422-008-0264-7

Noachtar, S., and Rémi, J. (2009). The role of EEG in epilepsy: A critical review. *Epilepsy Behav.* 15, 22–33. doi: 10.1016/j.yebeh.2009.02.035

Noback, C. R., Strominger, N. L., Demarest, R. J., and Ruggiero, D. A. (2005). *The Human Nervous System: Structure and Function* (6th ed.). Totowa, NJ: Humana Press.

Ostojic, S. (2014). Two types of asynchronous activity in networks of excitatory and inhibitory spiking neurons. *Nat. Neurosci.* 17, 594–600. doi: 10.1038/nn.3658

Protachevicz, P. R., Borges, R. R., Reis, A. S., Borges, F. S., Iarosz, K. C., Caldas, I. L., et al. (2018). Synchronous behaviour in network model based on human cortico–cortical connections. *Physiol. Measur.* 39:074006. doi: 10.1088/1361-6579/aace91

Rosenblum, M. G., Pikowsky, A. S., and Kurths, J. (1996). Phase synchronization of chaotic oscillators. *Phys. Rev. Lett.* 76, 1804–1807. doi: 10.1103/PhysRevLett.76.1804

Rosenblum, M. G., Pikowsky, A. S., and Kurths, J. (1997). From phase to lag synchronization in coupled chaotic oscillators. *Phys. Rev. Lett.* 78, 4193–4196. doi: 10.1103/PhysRevLett.78.4193

Scharfman, H. E., and Buckmaster, P. S. (2014). *Issues in Clinical Epileptology: A View From the Bench*. New York, NY: Springer.

Schindler, K. A., Bialonski, S., Horstmann, M. T., Elger, C. E., and Lehnertz, K. (2008). Evolving functional network properties and synchronizability during human epileptic seizures. *Chaos* 18:033119. doi: 10.1063/1.2966112

Sierra-Paredes, G., and Sierra-Marcuño, G. (2007). Extrasynaptic GABA and glutamate receptors in epilepsy. *CNS Neurol. Disord. Drug Targets* 6, 288–300. doi: 10.2174/187152707781387251

Silva, F. H. L., Blanes, W., Kalitzin, S. N., Parra, J., Suffczynski, P., and Velis, D. N. (2003). Dynamical diseases of brain systems: Different routes to epileptic seizures. *IEEE Trans. Biomed. Eng.* 50, 540–548. doi: 10.1109/TBME.2003.810703

Suffczynski, P., Kalitzin, S., and Da Silva, F. H. L. (2004). Dynamic of non-convulsive epileptic phenomena modeled by a bistable network. *Neuroscience* 126, 467–484. doi: 10.1016/j.neuroscience.2004.03.014

Sun, X., Perc, M., Kurths, J., and Lu, Q. (2018). Fast regular firings induced by intra- and inter-time delays in two clustered neuronal networks. *Chaos* 28:106310. doi: 10.1063/1.5037142

Traub, R. D., Jefferyst, J. G. R., and Whittington, M. A. (1994). Enhanced NMDA conductance can account for epileptiform activity induced by low Mg2+ in the rat hippocampal slice. *J. Physiol.* 478, 379–393. doi: 10.1113/jphysiol.1994.sp020259

Traub, R. D., Miles, R., and Jefferys, J. G. R. (1993). Synaptic and intrinsic conductances shape picrotoxin-induced synchronized after-discharges in the guinea-pig hippocampal slice. *J. Physiol.* 461, 525–547. doi: 10.1113/jphysiol.1993.sp019527

Traub, R. D., and Wong, R. K. S. (1982). Cellular mechanism of neural synchronization in epilepsy. *Science* 216, 745–747. doi: 10.1126/science.7079735

Trinka, E., Cock, H., Hesdorffer, D., Rossetti, A., Scheffer, I. E., Shinnar, S., et al. (2015). A definition and classification of status epilepticus-report of the ILAE task force on classification of status epilepticus. *Epilepsia* 56, 1515–1523. doi: 10.1111/epi.13121

Uhlhaas, P. J., and Singer, W. (2006). Neural synchrony in brain disorders: relevance for cognitive dysfunctions and pathophysiology. *Neuron* 52, 155–168. doi: 10.1016/j.neuron.2006.09.020

Velasco, A. L., Velasco, F., Velasco, M., Trejo, D., Casto, G., and Carrillo-Ruiz., J. D. (2007). Electrical stimulation of the hippocampal epileptic foci for seizure control: a double-blind, long-term follow-up study. *Epilepsia* 48, 1895–1903. doi: 10.1111/j.1528-1167.2007.01181.x

Wang, Z., Tian, C., Dhamala, M., and Liu., Z. (2017). A small change in network topology can induce explosive synchronization and activity propagation in the entire network. *Sci. Rep.* 7:561. doi: 10.1038/s41598-017-00697-5

White, H. S. (2002). Animal models of epileptogenesis. *Neurology* 59, 7–14. doi: 10.1212/WNL.59.9_suppl_5.S7

Wong, M. (2005). Modulation of dendritic spines in epilepsy: cellular mechanisms and functional implications. *Epilepsy Behav.* 7, 569–577. doi: 10.1016/j.yebeh.2005.08.007

Wong, M. (2008). Stabilizing dendritic structure as a novel therapeutic approach for epilepsy. *Exp. Rev. Neurother.* 8, 907–915. doi: 10.1586/14737175.8.6.907

Wu, Y., Liu, D., and Song. Z. (2015). Neural networks and energy bursts in epilepsy. *Neuroscience* 287, 175–186. doi: 10.1016/j.neuroscience.2014.06.046

Conflict of Interest Statement: The authors declare that the research was conducted in the absence of any commercial or financial relationships that could be construed as a potential conflict of interest.

frontiers in Computational Neuroscience

ORIGINAL RESEARCH
published: 28 June 2019
doi: 10.3389/fncom.2019.00041

A Temporal Signal-Processing Circuit Based on Spiking Neuron and Synaptic Learning

Hui Wei and Yi-Fan Du*

Laboratory of Cognitive Model and Algorithm, Shanghai Key Laboratory of Data Science, Department of Computer Science, Fudan University, Shanghai, China

Time is a continuous, homogeneous, one-way, and independent signal that cannot be modified by human will. The mechanism of how the brain processes temporal information remains elusive. According to previous work, time-keeping in medial premotor cortex (MPC) is governed by four kinds of ramp cell populations (Merchant et al., 2011). We believe that these cell populations participate in temporal information processing in MPC. Hence, in this the present study, we present a model that uses spiking neuron, including these cell populations, to construct a complete circuit for temporal processing. By combining the time-adaptive drift-diffusion model (TDDM) with the transmission of impulse information between neurons, this new model is able to successfully reproduce the result of synchronization-continuation tapping task (SCT). We also discovered that the neurons that we used exhibited some of the firing properties of time-related neurons detected by electrophysiological experiments in other studies. Therefore, we believe that our model reflects many of the physiological of neural circuits in the biological brain and can explain some of the phenomena in the temporal-perception process.

Keywords: time-related neuron, time-processing circuit, spiking-neuron, synaptic learning, ramp activity, SCT

OPEN ACCESS

Edited by:
Chris G. Antonopoulos, University of Essex, United Kingdom

Reviewed by:
Hugo Merchant, National Autonomous University of Mexico, Mexico
Francois Rivest, Royal Military College of Canada, Canada

****Correspondence:***
Hui Wei
weihui@fudan.edu.cn

Received: *16 December 2018*
Accepted: *11 June 2019*
Published: *28 June 2019*

Citation:
Wei H and Du Y-F (2019) A Temporal Signal-Processing Circuit Based on Spiking Neuron and Synaptic Learning. Front. Comput. Neurosci. 13:41. doi: 10.3389/fncom.2019.00041

INTRODUCTION

When we use visual cues to observe the environment, we need to grasp both the time interval and the sequence of various events. When we wish to understand speech, we need to distinguish between the arrival times of the audio signals. We need to accurately control the order of execution of motor commands to skeletal muscle to perform activities such as speaking and playing the piano. When we solve problems, we also need to plan the chronological order of all sub-goals. These frequent daily tasks indicate that the capacity for temporal information processing, like other cognitive abilities such as working memory, must be one of the basic functions of the brain. Clearly, humans can perceive a broad spectrum of time scales. At present, the neurocognitive community usually divides the temporal-processing range of the brain into four categories: microsecond-scale processing, millisecond-scale processing, second-to-minutes-scale processing, and circadian-rhythm processing (Merchant and Lafuente, 2014). In our work, we focus on millisecond-scale processing. The processing of millisecond-scale timing information is the most common, and it is usually accompanied by various types of sensing and motor control. Most research on millisecond-scale processing concerns motion control and auditory time perception. Temporal processing in the hundreds of milliseconds is quite sophisticated. And its neural underpinnings are largely unknown yet. In a study on motion control, researchers discovered that neurons in the motor cortex convey information via spike timing far more often than via spike rate (Tang et al., 2014). In addition,

they found that the amount of information conveyed at the millisecond timescale greatly exceeds the information available from spike counts. The findings of this important study have guided our time-perception model.

There are many tasks used to study perceptual and motor timing. Perceptual timing is considered as a subjective judgement of perceived timing and is not defined by movement. However, motor timing is a kind of temporal process where the temporal decision is intrinsically tied with movement. Hence, perceptual and motor tasks represent two different kinds of tasks used to study temporary-processing mechanisms in our brain. Classic motor and perceptual timing tasks have been summarized previously (Merchant and Lafuente, 2014). The task applied in our work, called the synchronization-continuation tapping task (SCT), is a kind of motor timing task.

In the current paper, we present a complex network in order to simulate the synchronization-continuation experiment with as much biological feasibility as possible. Here, we designed our model from the perspective of structure just like the work we used to do (Wei et al., 2017; Hui and Dawei, 2018). We considered not only complex topologies, but also synaptic plasticity in order to determine the time interval. And via the considered structure, we were able to simulate the SCT experiment and obtain the spiking neuron with a firing rate similar to that observed in electrophysiological experiments.

Synchronization-Continuation Tapping Task

In this study, the model we employed was based on experiments on the millisecond scale. A recent study found that the activity of cells in the medial prefrontal cortex (MPC) of macaques could characterize the time course of SCT experiments (Merchant et al., 2014). In an SCT experiment, the subject first responds synchronously with a visual or auditory metronome and then continues to produce the same interval without the metronome (**Figure 1**). In addition, they tested the neurophysiological properties of two macaque MPCs in the SCT experiment and found that the timing function of the MPC is determined by different cell populations. These researchers proposed four different types of neurons, which they labeled as swing cells, relative-timing cells, absolute-timing cells, and time-accumulator cells. During the SCT experiment, these neuronal types were discovered to display different forms of ramp activity, which encodes the elapsed time since the last motion or the remaining time until the next tap. This experiment showed that the MPC has a mechanism for the time-correlated analysis of rhythmic, time-series, and repetitive signals. This was a sub-second task. It remains to be elucidated what kind of neural circuit can acquire the time interval during the synchronization phase and repeat the action at this time frequency in the continuous phase.

There are several neurophysiological underpinnings of beat-based timing during SCT investigations (Merchant and Bartolo, 2018). In addition to the ramp activity in SCT mentioned above (Merchant et al., 2011), another study found that MPC neuronal populations dynamically represent the duration and serial order during the SCT (Crowe et al., 2014). It has also been found

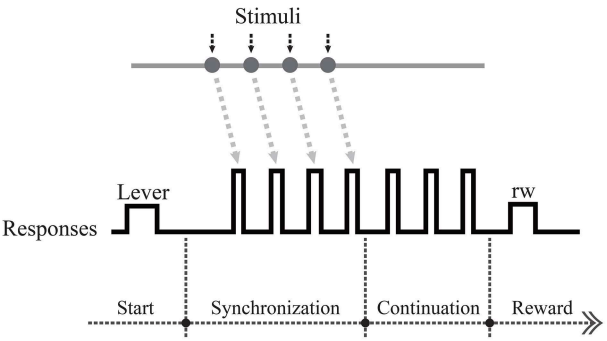

FIGURE 1 | Schematic overview of intervals in the synchronization-continuation tapping task (SCT), showing periodic stimuli (gray line), and push button responses (black line). Each trial began when the monkey held a lever.

that there is tuning for interval and/or serial order as an orderly change in the power of transient modulations in β- and γ- bands across putaminal LFPs during the execution of the SCT (Bartolo et al., 2014). Recent research shows that the neural population trajectories during SCT in SMA/preSMA can act as a neural clock (Gámez et al., 2019). However, the neural code linked to the temporal production of this neural clock during SCT remains unknown. Moreover, elucidating the neural underpinnings of motor timing is critical to understanding how sensorimotor systems can predict the regular pulse and then respond with temporal precision.

The two goals of the current paper are as follows: (1) to establish a network circuit model of spiking neuron to simulate pyramidal cells and interneurons in order to achieve the time interval learning of the synchronous phase and the spontaneous follow-up function of the continuous phase in the SCT experiment; and (2) to simulate the SCT experiment in macaques by implementing the ramp activity of the four different neuron types proposed previously by Merchant et al. (2011).

Ramp Activity

One of the most important tasks of the brain is to anticipate upcoming events in order to prepare for behavior, anticipate reactions, and plan. The phenomenon of ramping firing rates prior to behavioral responses is commonly observed in behavioral neuroscience, and—in many cases—is anticipatory in nature.

Ramp activity, which can be defined as delayed activity that steadily increases between two subsequent stimuli, has been associated with the anticipation of various events, such as motor responses (Constantinidis and Steinmetz, 1996), the end of the delay interval (Romo et al., 1999; Reutimann et al., 2001), or the identity of the sample or match stimulus in delayed matching-to-sample (DMS) tasks [retrospective vs. prospective coding (Rainer et al., 1999; Mongillo et al., 2003)]. The increasing delayed activity can also be associated with reward expectation, such as that found in the prefrontal cortex (Watanabe, 1996), striatum (Kawagoe et al., 1998; Hassani et al., 2001), thalamus (for review, see Schultz, 2000; Komura et al., 2001), and motor cortex (Merchant et al., 2004). Some experiments have addressed

the question of how a change in the duration of the delay period is reflected in the time-varying delay activity (Kojima and Goldman-Rakic, 1982; Komura et al., 2001; Brody et al., 2003). In these experiments the build-up of activity is stretched in time, rather than shifted. The stretching causes the slope of the activity profile to decrease with the length of the delay period. This is in agreement with the scaling property of interval timing found in psychophysical studies on humans (Rakitin et al., 1998) and has recently confirmed by *in vivo* experiments in monkeys (Leon and Shadlen, 2003). When the duration of a time interval is estimated, the error distribution scales linearly with the length of the interval.

Prediction requires animals to extract and exploit the temporal structure of their world, or the temporal relationship between environmental events or their own behavior and associated effects. Prediction is seen as a symbol of expectation in time-perception tasks. Ramp activity, sometimes referred to as climbing activity, is considered to be prospective. Recordings from different areas in the cortices of monkeys suggest the existence of neurons representing time by ramp (climbing) activity, which is triggered by an initial event and peaks at the expected time of a second event, such as a visual stimulus and a reward. The activity of this neuron is often a good indicator of the duration of the two events. In studies provided by Leon and Shadlen (2003), we see that different slopes of climbing activity can be used to calibrate different time intervals. This not only reveals that the slope of neuronal climbing activity can be used to characterize time, also that different time intervals can be learned by determining the slope of the climbing activity.

Structure of This Paper

The remainder of this paper details our research as follows: related works are presented in section Related Work. Section A Spiking-Neuron Circuit For Temporal Signal-Processing describes our spiking-neuron circuit for temporal signal-processing and the synaptic learning algorithm we used. In this section, we also introduce the structure of our neural circuit in detail. In section Computational Simulation Results, we compare the simulation results of our computational model with biological results found in SCT experiments from previous studies and explain some electrophysiological phenomena. Finally, we present conclusions and discuss our research in section Conclusion and Discussion.

RELATED WORK

There are many computational models for time-dependent signal processing, including pacemaker accumulator models (Treisman, 1963), state dependent network models (Buonomano and Maass, 2009), long short-term memory models(LSTM) (Rivest et al., 2010), time-adaptive drift–diffusion models (TDDM) (Rivest and Bengio, 2011), and recurrent synaptic networks (Mendoza et al., 2018).

The pacemaker accumulator model is a traditional time model proposed many years ago (Treisman, 1963), the concept of which was derived from mechanical clocks. This model assumes that there is a pacemaker or an oscillator in our brain that sends pulses consistently at a certain frequency, and these are received and recorded by an accumulator. Within this framework, the pulse count provides a linear metric of time, and temporal judgments rely on comparing the current pulse count with that of a reference time. This process becomes the foundation for characterizing time in this model. The pacemaker accumulator model has proven to be effective in providing a framework for many psychophysical data related to time processing (Church, 1984; Meck, 2005). The downside of this model, however, is that it lacks biological feasibility. Mounting evidence indicates that clock models are not entirely consistent with the experimental data (for reviews see Mauk and Buonomano, 2004; Buhusi et al., 2005).

The state-dependent network model recently proposed by Buonomano et al. differs from these above models. This model is able to tell and encode time as a result of dynamic change in the state of spiking neural networks. It is based on the assumption that there is an interaction between each sensory event and the current state of the network, forming a network state pattern that naturally encodes each event in the context of recent stimuli—similar to the interaction between different ripples generated by each raindrop falling in a pond instantly or previously. State-dependent models have the powerful ability to characterize time since they are inherently high dimensional. However, the deficiency of this model is that it encodes time via the firing rate of each neuron in the model, which is contrary to the result of Buonomano's motor-control experiment, in which the spiking time conveyed more information than the spiking rate [millisecond-scale motor encoding in a cortical vocal area].

In addition, LSTM and temporary difference learning (TD) algorithms have been used to propose a small neural network based on artificial neurons that can encode a specific time into a ramp-like activity (Rivest et al., 2010). Although they introduced many biological concepts into their model, the basis of the model is the artificial neuron which is far from the bioneuron compared to the spiking neuron.

TDDM was independently proposed by Rivest and Bengio (2011) and Simen et al. (2011) which utilizes a simple and more abstract neural model based on a drift-diffusion process of climbing neural activity. The drift-diffusion model is often used in decision-making under noisy stimuli. This work extends it by developing a learning rule so that their model can be used to learn time intervals rapidly. Additionally, Weber's law for time can be explained in this study.

There is another excellent model. Recently, a kind of model called a recurrent synaptic network has been proposed (Mendoza et al., 2018). It simulates a cortical ensemble and makes use of paired-pulse facilitation and slow inhibitory synaptic currents to not only produce interval selective responses but also to follow the biases and scalar properties (Pérez and Merchant, 2018).

In addition to the millisecond-range time-processing model mentioned above, there are several time-processing models in seconds to minutes range such as striatal beat frequency model (SBF), which is proposed by Matell and Meck (2004). SBF suggests that in the thalamo-cortico-striatal loops, the coincidence detection of neuronal oscillations in the cortex is the neural basis for the characterization of time information. Cortical neurons will act as oscillators and the striatum located

in the basal ganglia can detect the oscillation pattern of cortical neurons. At the beginning of time interval processing, the release of dopamine in the brain prompts timing and synchronizes cortical oscillations, and resets the state level of striatum spinous neurons. The cortical oscillators oscillate a fixed frequency throughout the criterion interval. At the end of time interval processing, dopamine is released again, which changes the synaptic connections of spinous neurons, and forms the neural representation of time interval.

A SPIKING-NEURON CIRCUIT FOR TEMPORAL SIGNAL-PROCESSING

Neuron Model

In this paper, a simple spiking neuron model known as the Izhikevich neuron model was used to simplify the Hodgkin–Huxley (HH) model into a 2-D system with sufficient biological plausibility and high computational efficiency (Izhikevich, 2003). The form of the ordinary differential equation is shown in Equation 1 where V represents the membrane potential of the neuron, u represents a membrane recovery variable, and a, b, c, and d are dimensionless parameters. We have the following:

$$\begin{aligned} \frac{dV}{dt} &= 0.04V^2 + 5V + 140 - u + I \\ \frac{du}{dt} &= \mathrm{a(bV - u)} \\ \mathrm{If\ V} &\geq 30, \text{ then } \begin{cases} V &\leftarrow c \\ u &\leftarrow u + d \end{cases} \end{aligned} \tag{1}$$

In this study, typical values of the parameters for an excitatory neuron were: $a = 0.02$, $b = 0.2$, $c = -65$, and $d = 8$. Typical values of the parameters for an inhibitory neuron were: $a = 0.1$, $b = 0.2$, $c = -65$, and $d = 2$. The firing mode of the excitatory and inhibitory neurons we utilized in our model are shown in **Figure 2**.

In order to adequately describe the relationship between the firing rate of neurons and the time interval, we also introduce another kind of neuron model, as shown in the following equation (the equation from Gavornik et al., 2009).

$$\gamma_m \frac{dV_i}{dt} = -V_i + I_{ext,i} + \sum_{j=1}^{N} L_{ij} V_j \tag{2}$$

In the equation, the firing rate of the single neuron j is approximated by an activity variable V, γ_m is an intrinsic neuronal time constant, $I_{ext,i}$is the external feed-forward input to neuron i and L_{ij} is the weight connecting the presynaptic cell j to the postsynaptic cell i.

Time-Adaptive Drift-Diffusion Models (TDDM)

In order to realize time adaptation, we referred to time-adaptive drift-diffusion models (TDDM). This model is also used to reflect the ability to learn the timing of events, but it is a simpler and more abstract neural model. TDDM takes advantage of the drift-diffusion model, commonly used in decision simulations, to encode specific time intervals by accumulating evidence of elapsed time with the drift rate (Rivest and Bengio, 2011). In TDDM, the memory of the time interval to be learned is stored in the drift rate, so that it can control the signal's slope as time elapses. This signal changes over time in a form very similar to the ramp activity observed in the MPC of macaques. Therefore, we believe that TDDM can be used to simulate the ramp activity of some neurons in the MPC, which can be used as our model's main learning interval mechanism for synaptic learning algorithms.

In the TDDM implementation process, the semaphore ϕ (t) is 0 at the beginning of the stimulus, and continuously accumulates as time passes. The overall process is similar to an accumulator, which integrates continuously over time with a drift rate w and noise ε(t). The main function of the model is expressed in the following form, which is similar to the drift-diffusion model:

$$\phi\,(\mathrm{t}) = \phi(\mathrm{t} - 1) + \mathrm{w} \triangle \mathrm{t} + \epsilon(\mathrm{t}) \tag{3}$$

Where Δt is the time step and ε(t) is the Gaussian noise with a mean value of 0 and variance σ^2 [N(0, σ^2]. It is also stipulated that when the amount of information reaches its peak, a certain reward will be given, leading to the renewal of the drift rate. By constantly updating w through the experiments, our information volume can reach one near the target interval. Obviously, the learning process of this model involves two situations (as shown below).

As mentioned previously, ramp activity is considered to be prospective and can be used to express expectations of upcoming events. Here we use reward to represent the upcoming event, while the moment the semaphore ϕ(t) reaches one is called expected.

In the first cases (shown in **Figure 3A**), reward occurs earlier than expected, and the drift rate w toward the observed interval can be corrected at once using Equations (4) and (6) to increase the slope of the accumulator when reward occurs. We have the following:

$$\triangle\,\mathrm{w\,(n)} = \mathrm{w(n)}\frac{(1 - \varphi\,(t))}{\varphi(t)} \tag{4}$$

In the second case (shown in **Figure 3B**) is that in which expectation occurs earlier than the reward, and the drift rate w toward the observed interval can be corrected using Equations (5) and (6) to reduce the slope of the accumulator since ϕ reaches one. The rate change for that trial Δw(n) is accumulated until the next reward occurs.

$$\begin{aligned} \triangle \mathrm{w\,(n,t)} &= \triangle \mathrm{w\,(n,t-1)} - (\mathrm{w\,(n)} + \triangle \mathrm{w\,(n,t-1)})^2 \triangle t \quad (5) \\ \mathrm{w\,(n+1)} &= \mathrm{w\,(n)} + \alpha \triangle \mathrm{w(n)} \quad (6) \end{aligned}$$

where n denotes the number of training experiments, and α is the learning rate.

In the original paper (Rivest and Bengio, 2011), the above model was considered relatively simple and abstract. In order to apply it to our spiking neural network, we assume that the semaphore ϕ in the TDDM was the activity variable (V_i) of the

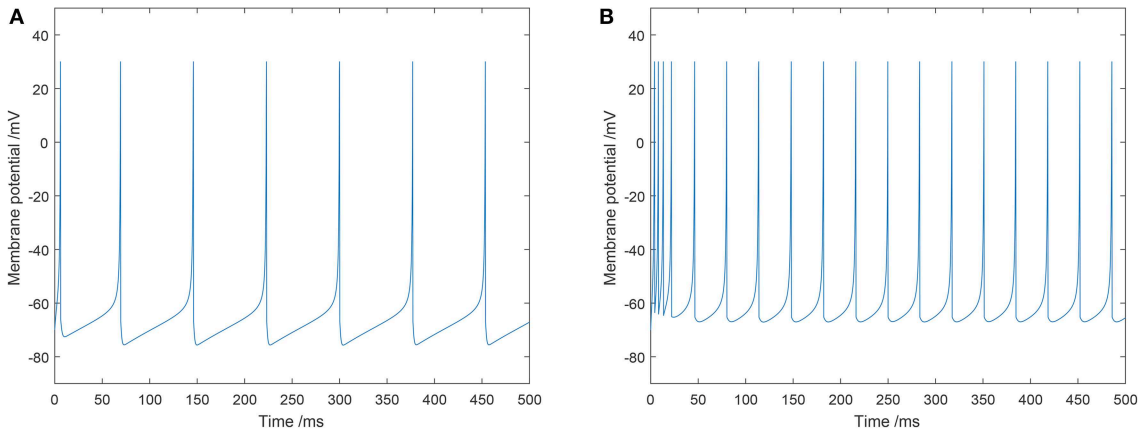

FIGURE 2 | Two types of spiking patterns: **(A)** regular spiking for excitatory neurons; **(B)** fast spiking for inhibitory neurons.

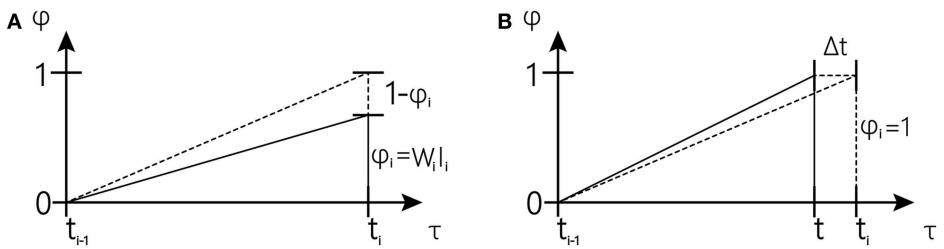

FIGURE 3 | Schematic overview of one tapping interval in the synchronization-continuation tapping task (SCT), showing periodic stimuli (vertical dashed lines), and preparation signal for push button responses (vertical solid lines).The inclined dash line represents the desired trajectory; The inclined solid line represents actual trajectory (The figure is modified from Rivest and Bengio, 2011).

spiking neuron in Equation (2), thus establishing Equation (2) and (3), which is as follows:

$$\gamma_m \left(w \triangle t + \varepsilon \left(t \right) \right) = -V_i + I_{ext,i} + \sum_{j=1}^{N} L_{ij} V_j \qquad (7)$$

According to the above equation, the relationship between the drift rate and the weight of neural connections can be established. Therefore, the weights of the spiking neuron can be updated via the drift-rate-updating method described above in Equation (4) and (6).

In summary, the TDDM is a fast-learning model, and due to its drift feature, we can apply it to simulate ramp activity. The modified TDDM algorithm, like any other synaptic plasticity algorithm, can be explained as being affected by various neurotransmitters in the process of neuronal firing, thus dynamically adjusting synaptic weights.

There exists some other models to simulate ramp activity. Simen's work (Simen et al., 2011) has proposed that a specific form of diffusion model arises from simple assumptions about neural integration to achieve ramp activity. In this study, the model incorporates a rapid duration-learning procedure and accounts for a variety of physiological and behavioral finding by the diffusion model. The ideas of this research are similar to ours. However, there are substantial differences in the details between our work and their work. The form of the individual neuron model for our work is the ordinary differential equation, but for theirs is non-homogeneous Poisson spike generator. In addition, their diffusion model of interval timing is established at a high level, while ours is located in the connection between neurons.

Neural-Circuit Model

Our neural circuit model was designed based on previous study (Merchant et al., 2011). In that study, electrophysiological SCT experiments were performed, in which five types of time-related cells were discovered in the MPCs of rhesus macaques, including motor cells, swing cells, relative-timing cells, absolute-timing cells, and time-accumulator cells. An obvious feature of these cells is ramp activity. It can be seen from the discharge rate diagram of the various neuronal types presented in the right column of **Figure 10** that all neurons—with exception of motor cells—will change their type of activity when changing the target interval. It can be observed that these cell types are all involved in the task of temporary processing. The conclusions from the Merchant et al. paper can be summarized as follows:

Relative-timing cells display monotonically rising ramp activity characteristics after time measurement begins. When

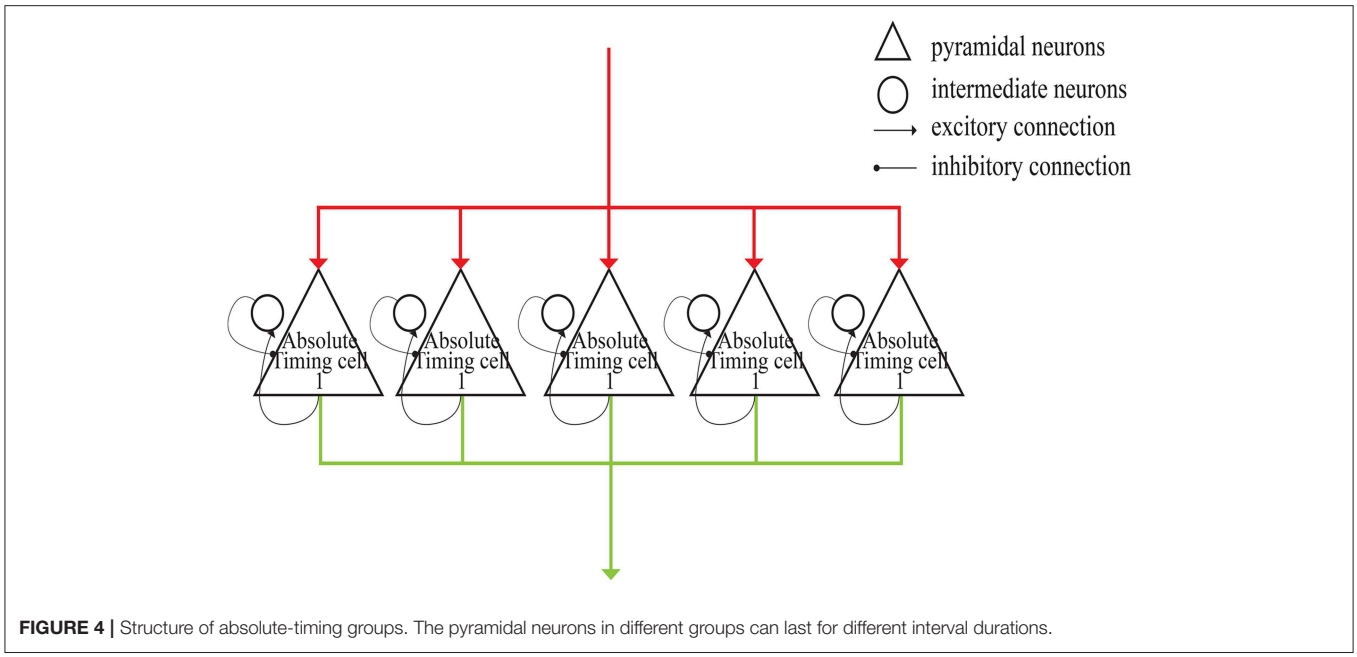

FIGURE 4 | Structure of absolute-timing groups. The pyramidal neurons in different groups can last for different interval durations.

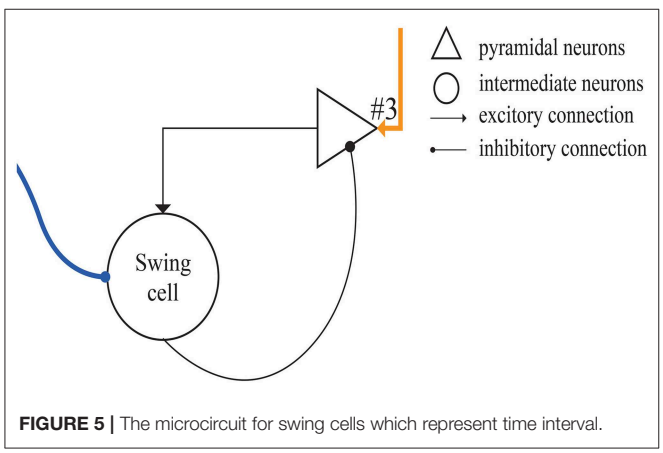

FIGURE 5 | The microcircuit for swing cells which represent time interval.

they reach the threshold value, they will cause motor control, and then rapidly decline.

- Relative-timing cells interact with absolute-timing cells and their activity becomes locked at some point, resulting in a balanced loop mechanism for executing motor sequences with tight time structures.
- Neuronal activity of an absolute-timing cell exhibits an increase in its up-down profile of activation across different intervals. And they found that the duration of the up-down cycle of activity in absolute timing cells is associated with subjective time.
- The discharge diagram of a time-accumulator cell is similar to that of absolute-timing cells which represents the passage of time since the previous movement. And in time-accumulator cells, there is an additional increase in peak magnitude as a function of elapsed time. Thus, their slopes are similar across different target time intervals.
- As the target interval increases, the discharge period of swing cells increases. In addition the firing rates of swing cells always decrease and then increase within a target interval. We consider that the effect of swing cells may be to represent the interval length.

According to the above points, we assume that the entire neural circuit in the brain has the following time-processing procedure. First, absolute-timing cells are activated by the synchronization signal, and then the pulse-signal is simultaneously issued by the absolute-timing groups of various time scales. Next, due to the impetus of the absolute-timing cells, ramp activity of the relative-timing, and time-accumulator cells begins. In the meantime, in order to learn and reproduce the time interval, some synaptic plasticity (like the TDDM) is required in the connections between the absolute-timing and relative-timing cells. Finally, swing cells can represent the interval length through the learned interval from the relative-timing cells.

As shown in **Figure 4**, each absolute-timing group receives external stimuli simultaneously, with the differences among groups consisting of the weights of the excitatory and inhibitory connections between pyramidal neurons and interneurons. By setting various weights for different absolute-timing groups the firing rate of pyramidal neurons in each group can exhibit discharge curves similar to those found in a previous study (Merchant et al., 2011). In our design, the absolute-timing groups spanned different interval durations, which were not affected by the target interval.

Figure 5 shows the microcircuit we designed for swing cells based on the summary above. In Merchant's paper, there is little information about swing cells, leaving us to infer that the effect of swing cells may be to explicitly represent the interval duration on the basis of the discharge curve measured from them in the electrophysiological experiments. From the right column of

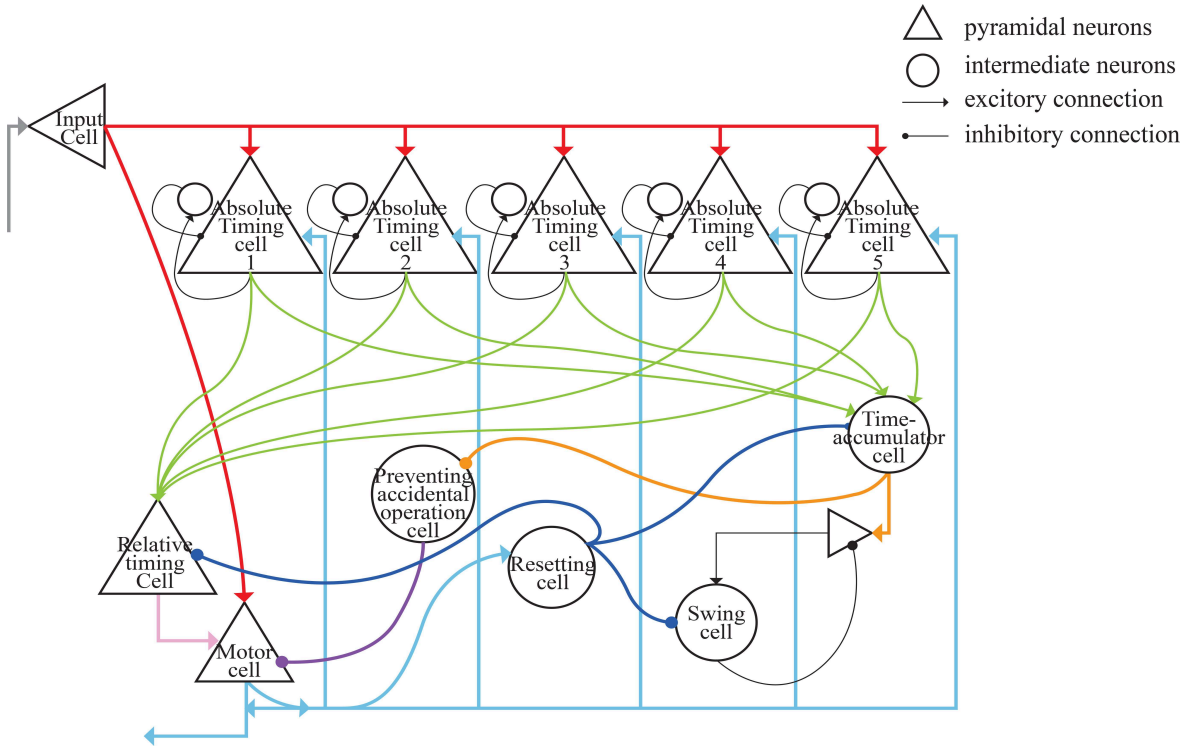

FIGURE 6 | Architecture of the neural circuit in this study. In the figure, triangles represent pyramidal cells and circles are interneurons. These neurons, with the exception of relative-timing cells, were all simulated using the Izhikevich neuron model.

Figure 10D, a period can be represented by the decrease and increase of the firing rate. That is, the high firing rate represents the start and the end of the duration. Similarly, the microcircuit is composed of a pyramidal neuron and an interneuron which is called swing cell. In the discharge diagram of swing cells, the firing rates decrease after the tap with lower and lower slopes and then increase when excitability becomes stronger than inhibition. Thus, the microcircuit receives two inputs, one (the blue line) from resetting cells and the other (the orange line) from time-accumulator cells. After tapping, resetting cells are activated to inhibit swing cells. At the same time, time-accumulator cells are also activated to excite the pyramidal neurons. As time passes, the inhibitory effect becomes weaker and the excitatory effect becomes stronger.

The architecture of our model is presented in **Figure 6**. The gray lines represent the input of external light or sound stimuli as synchronous signals to the input cells which lasted for only 100 ms. The red lines are the output connections from input cells. The input cells simultaneously activate absolute-timing cells that characterize different time intervals, and each absolute-timing group forms a microcircuit with interneurons (**Figure 4**), so that the slope of the ramp activity in each absolute-timing group is different. Since the motor cells perform a tap each time the input cells receive a synchronous stimulus during the synchronization phase of the SCT, there are connections between the input cells and the motor cells, as represented by the red lines. The green lines show that each group of absolute-timing cells simultaneously transmits spikes to the relative-timing cells, such that their firing rate continues to rise. As summarized above, there are also connections between absolute-timing cells and time-accumulator cells due to the ramp activity of time-accumulator cells which is similar to that of relative-timing cells. In order to make their slopes the same and their peaks rise as the target interval increases, the synaptic connections between the absolute-timing and time-accumulator cells must be different from those between the absolute-timing and relative-timing cells. The orange line shows the accident preventing operation cell we set up in order to prevent the motor cells from being activated prematurely by the connection represented by the purple line. Since the firing rate of swing cells has a down-up form, we constructed a microcircuit with the pyramidal neurons. When tapped, they receive the inhibitory stimulus of the resetting cells, and the discharge rate decreases. As time passes, the enhancement of the excitatory stimulation of the pyramidal cells in the microcell circuit leads to an increase in the firing rate of the swing cells, and the slope becomes less steep as it approaches the target interval. The pyramidal cells in the microcircuit receive the stimuli from the time-accumulator cells. The pink line shows that there is a threshold for the relative-timing cells. When the ramp activity reaches this threshold, we hypothesize that it is the achievement of the expectation time that causes the relative-timing cell to activate the motor cell, causing a tapping action. The light blue lines show that during the continuous phase of the SCT, since the

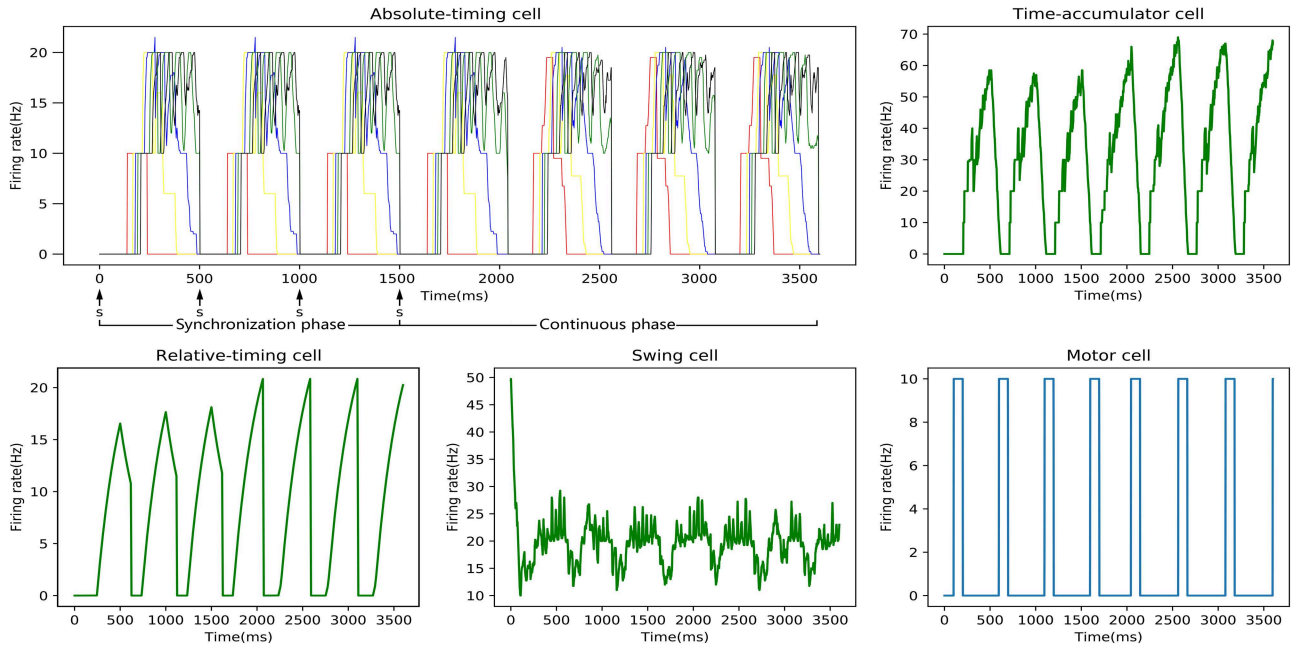

FIGURE 7 | Discharge-rate curves of all neuronal types for the 500 ms experiment in an SCT time interval with our model. In the absolute-timing cell diagram, there are five firing rate curves of the pyramidal neurons in five absolute-timing groups. Due to the stimulus signal, the peak firing rate of the relative-timing cell in the synchronous phase that is lower than that in the continuous phase. The discharge rate of the swing cell represents a cyclical change from down to up. The motor cell was activated either after the external synchronization signals appeared or the firing rate of the relative cells reached the threshold.

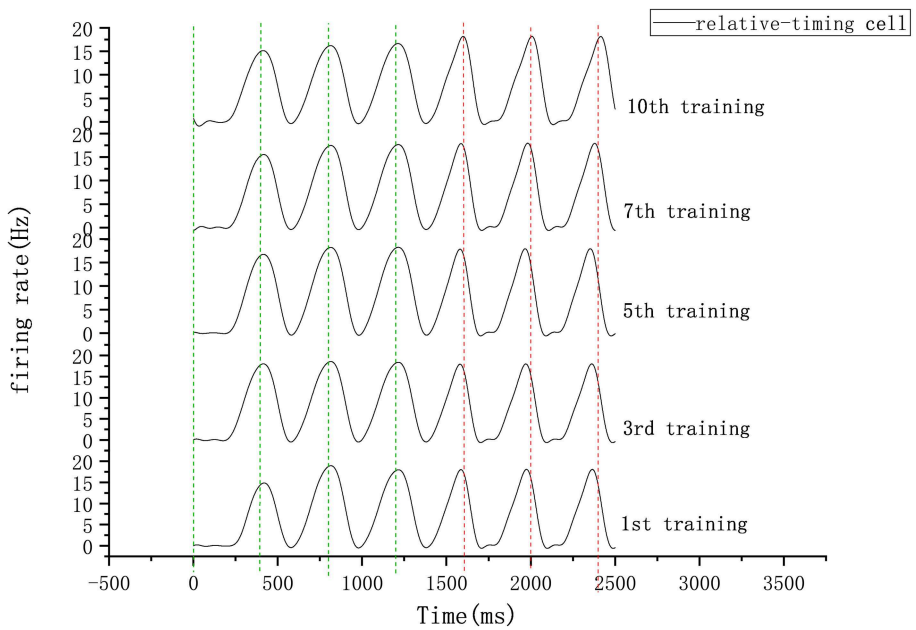

FIGURE 8 | Firing rate diagram (after smoothing) of relative-timing cells during several training sessions. Here the interval length is 400 ms. The green-dashed lines represent the occurrence of external synchronization signals and the red-dashed lines indicate the desired tapping time points in the continuous phase.

external synchronous stimulus no longer exists, the motor cells need to act as synchronous signals via their connections with the absolute-timing cells. Meanwhile, in order to restart the period, the resetting cell—which is connected with the relative-timing, time-accumulator, and swing cells (represented by the blue lines)—should be activated by the motor cell.

The relationship between our model and the TDDM can be easily observed from the connection between the relative-timing and absolute-timing cells. As concluded above, for different target time intervals, the discharge rates of relative-timing cells will peak at different slopes. The process of increasing the firing rate corresponds to the process of accumulating evidence of time passing in the TDDM. Using the TDDM, we can achieve a kind of synaptic plasticity learning to fit the duration between the start and end of the ramp activity to the target interval time. Here, we have made some improvements to the TDDM. Compared with the original TDDM, the firing rate of the relative-timing cells can be regarded as the semaphore $\phi(t)$. Therefore, the peak of $\phi(t)$ is no longer one but is now the threshold of the firing rate. The initial weights between absolute-timing cells and relative-timing cells are set to the appropriate values. When the firing rate of relative-timing cells reaches the threshold earlier than the next synchronous signals, the weights will be tuned using TDDM until the next synchronous signals appear. Similarly, when the firing rate comes to the threshold later than the next synchronous signals, the weights will be immediately corrected using TDDM. Thus, our model can transform the collection of evidence of time passing into the accumulation of the firing rate by the synaptic weight.

COMPUTATIONAL SIMULATION RESULTS

With the SCT experiments, we realized the learning of the time interval via the neural circuit we designed and we reproduced the discharge patterns of various neuronal groups described previously (Merchant et al., 2011).

In our experiments, we examined three time intervals— 400, 500, and 600 ms—and set the threshold of the relative-timing cells to 20 Hz. We considered an SCT experiment to be a training process in which there was a synchronous and a continuous phase. There were four taps during the synchronization phase and we made adjustments to the synaptic weights in the circuit three times (applying the TDDM algorithm). The continuous phase was based on all of the previous weight adjustments, and the tapping of the time interval to be learned was reproduced when there was no external synchronization-signal stimulus.

One SCT experiment was one training process, and the discharge rate curve of each neuronal type in one experiment is shown in **Figure 7**. It can be seen that the relative-timing cells did not reach the threshold at the target time when a tap was performed in the synchronization phase, and the synaptic-weight adjustment was carried out three times in order to make the discharge rate closer to the threshold of 20 Hz. Obviously, the implementation of our synaptic-learning algorithm was beneficial to our time-learning model. After several training processes, the synaptic weights will stabilize within a certain range. The duration from a firing rate of 0 to the firing-rate peak of the relative-timing cell was our target duration. It is reasonable that there was a delay between the activation time of the motor cell and the time at which either the external stimulus appeared or the firing rate of relative cells reached threshold.

In our circuit, the relative-timing cell is considered to be the key to indicating the desired interval. The periodicity exhibited by each of the other neuronal groups is driven by the relative-timing cells. The discharge diagram of the relative-timing cells during several training sessions is shown in **Figure 8**. As the number of training sessions increase, the peak of the relative timing cells gets closer

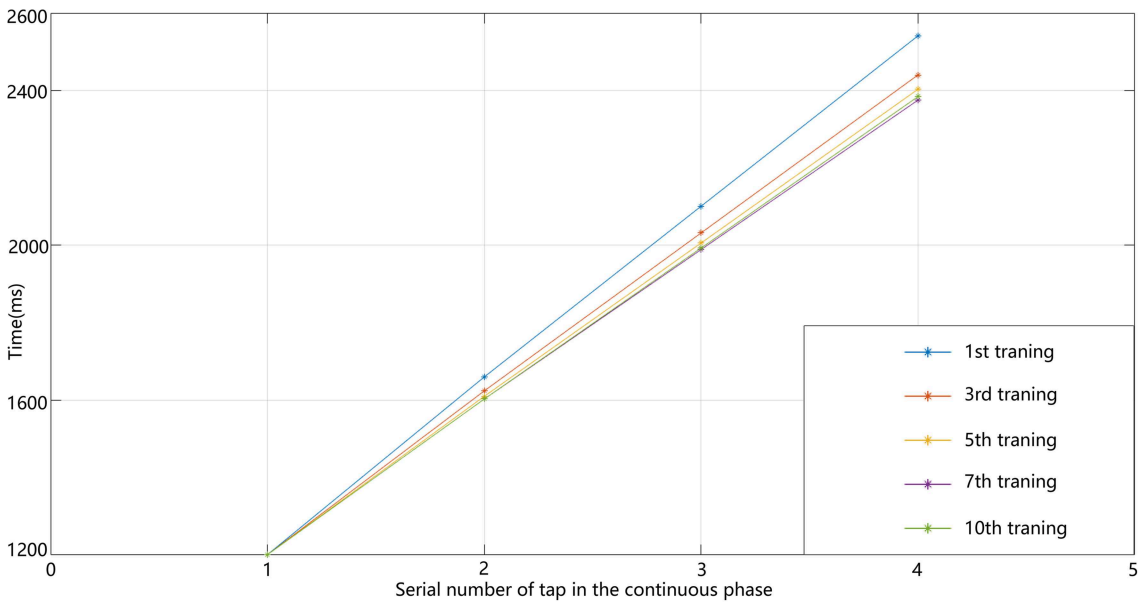

FIGURE 9 | Line graph of four taps times in the continuous phase of the 400 ms experiment.

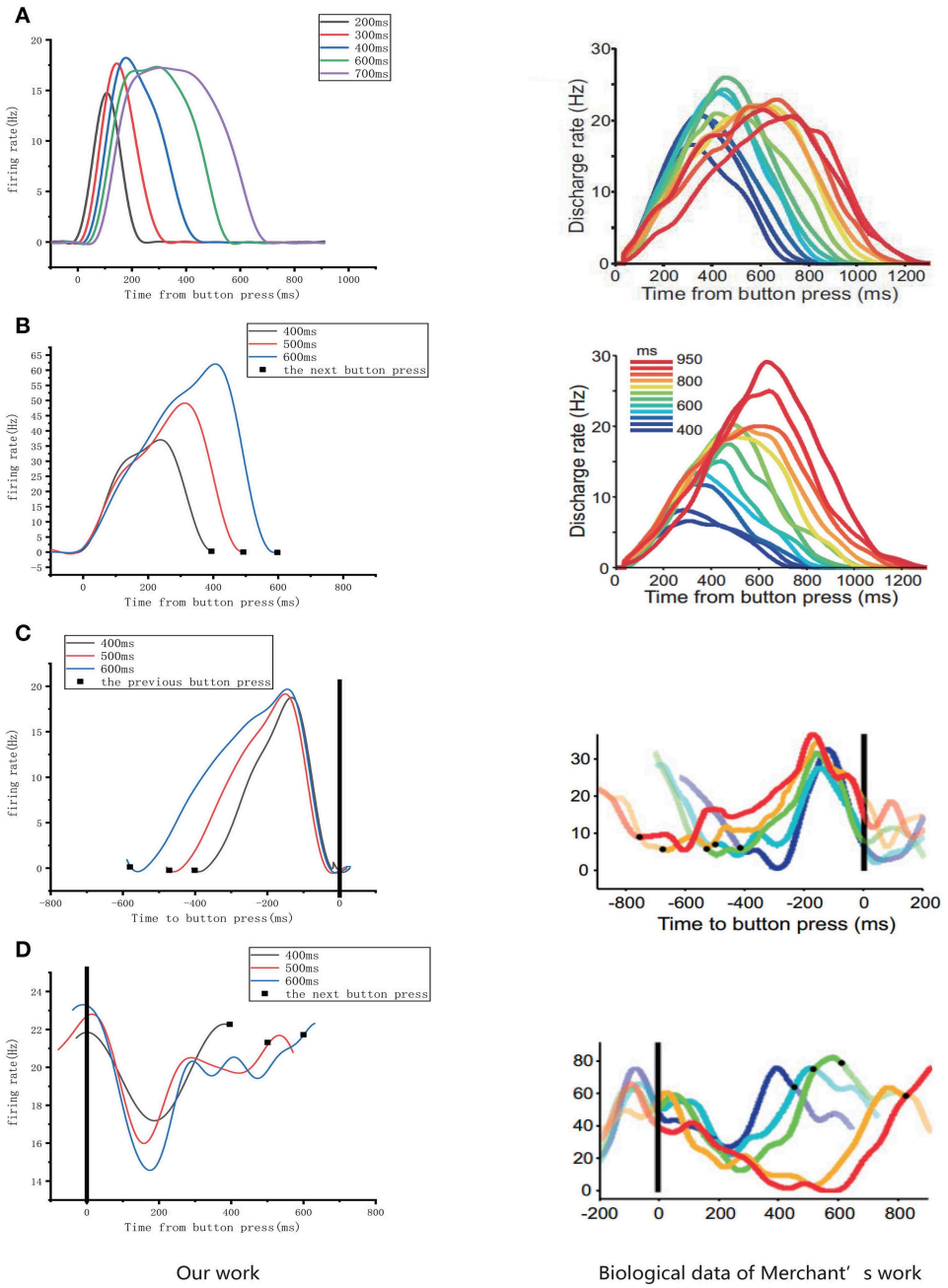

FIGURE 10 | Comparison of the firing rates of all of the neurons in our model with results from electrophysiological measurements (Merchant et al., 2011). The left column is the discharge curve (smoothed) of the neurons in our model. The right column shows the discharge curves for all types of neurons from electrophysiological experiments. **(A–D)** respectively, illustrate the results for absolute-timing cells, time-accumulator cells, relative-timing cells, and swing cells (The right column of the figure is modified from Merchant et al., 2011).

to the desired tap moment (red-dashed line). **Figure 9** is a plot of the times the model learned. In the figure, the points of the continuous phase of each training session have been fitted with a straight line. It can be observed that our model's ability to learn the interval duration improved.

As mentioned above, four types of cells related to time processing have been described previously (Merchant et al., 2011). These four types of neurons also exist in the neural circuits we designed. We compared them with the electrophysiological measurements of the firing patterns of neurons as shown in **Figure 10**. It is obvious that the neurons in our neural circuits

Algorithm 1: The flow of our models which interprets the architecture shown in **Figure 6**.

Initialize: S ← the parameters of all spiking neurons;
W ← the weights of each other neuron in our neural circuit;
T ← An array which contains the time when the external stimulus begins to appear;
r ← drift rate;
t ← time(ms)
$I_{external}$ ← the current of external stimulus;
$V_{threshold}$ ← the firing rate threshold of relative-timing cells for TDDM
$V_{relative}$ ← the firing rate of relative-timing cells
while t>0 **do**
  if t in synchronous phase **then**
    if t in T **then**
      $I_{external}$ stimulates the input cells for only 100 ms(gray line)
      if t!=0 AND t in T **then**
        if $V_{relative} < V_{threshold}$ **then**
          Implement the Equations 4 and 6 to modify r.
        else
          Implement the equation 6 to modify r.
        end if
        And then according to equation 7 update w in the connections between absolute-timing cells and relative-timing cells.
      end if
  else
        if $V_{relative} > V_{threshold}$ **then**
          Implement the equation 5 to obtain Δr:
        end if
      end if
    end if
    According to the architecture in **Figure 6**, compute all the neurons.
    Compute the state of the input cells using equation 1.
    Compute the state of absolute-timing cells using equation 1.
    Compute the state of the time-accumulator cells using equation 1.
    Compute the state of the relative-timing cells using equation 2.
    Compute the state of the motor cells using equation 1.
    Compute the state of the other cells using equation 1.
end while

exhibit periodicity and produce discharge curves similar to those observed in physiological experiments. In the left column of **Figure 10A**, the curves represent the firing rate of five absolute-timing groups which increase with different climbing rates for each color and span different time intervals. Similar to the right column of **Figure 10B**, the time-accumulator cells we designed increased with rising at the same climbing rates as their electrophysiological counterparts, although the peaks differed for different time intervals. In order to be consistent with the discharge rate diagram of relative-timing cells in the reference, the figure in the left column of **Figure 10C** was plotted in the same form. It can be seen that our relative-timing cells exhibited the same features as those in the discharge rate diagram. **Figure 10D** shows the firing rates of the swing cells in our model and those of the electrophysiological experiment.

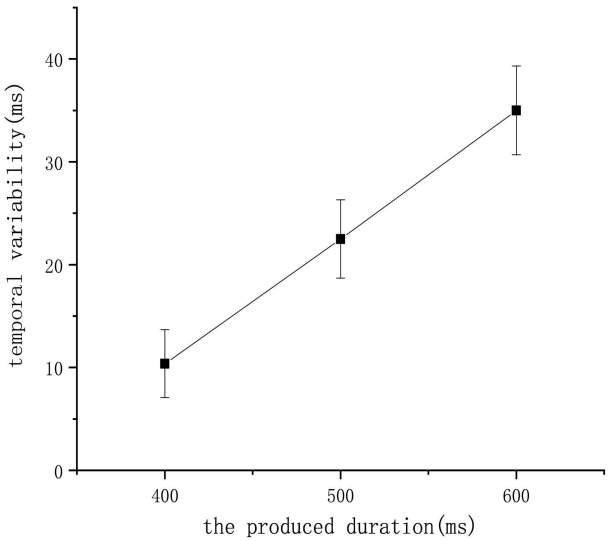

FIGURE 11 | The relationship between temporal variability and the produced duration in our model.

Although there are some differences in the curves of the two graphs of **Figure 10D**, our swing cells retained the characteristics of the bio-cell discharge rate. One period of the neurons we designed in the left column of **Figure 10D** can represent the target-time interval; the amplitude of the curve increases as the target interval duration increases. We believe that the reason for the difference between the curves of our experimental results and those of electrophysiological experiments has to do with the fact that our results were somewhat smoothed and also that the time-window selection used to calculate the discharge rate of neurons in our model differed from that used in the electrophysiological experiments. Therefore, we consider that the differences observed in the curves of **Figure 10D** are acceptable.

Finally, we tested our model to check whether it satisfies an additional biological property called the scalar property (Gibbon et al., 1997), which tells us that the uncertainty is proportional to the interval being estimated. This property has been interpreted to indicate that the variability of an underlying temporal distribution should exhibit a constant coefficient of variation (σ/μ). **Figure 11** shows that repeated the experiment eight times and recorded the mean of the learned duration in the 400 ms experiment, 500 ms experiment, and 600 ms experiment receptively. According to the figure, the scalar property was followed by our model, which further confirms the biological interpretability of our work.

CONCLUSION AND DISCUSSION

In this study, in order to explore a possible time-processing mechanism in the human brain, we examined the time processing behind the electrophysiological phenomena observed in the SCT experiment (Merchant et al., 2011),

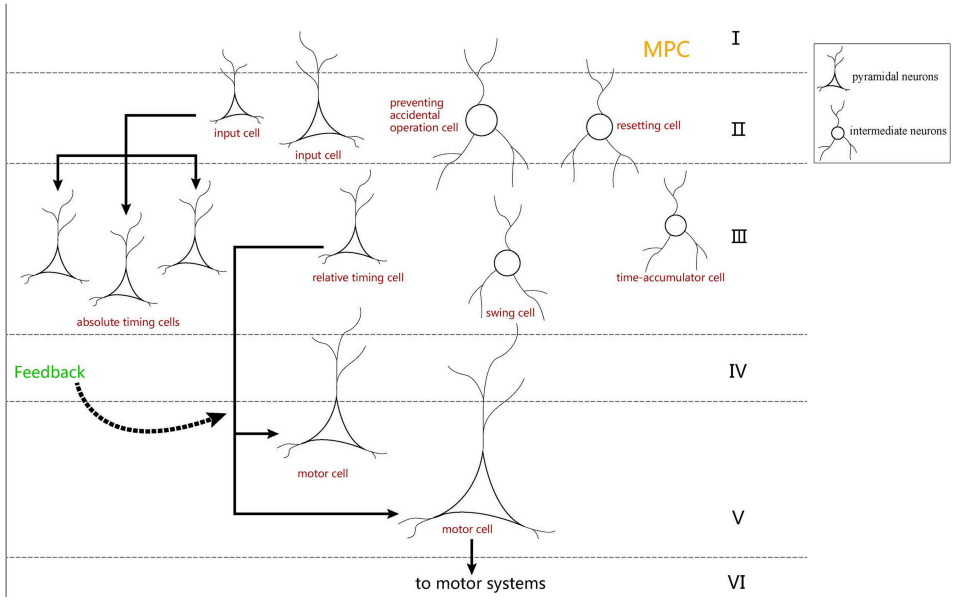

FIGURE 12 | The distribution hypothesis of our neuron-circuit model. We hypothesize that the input cells used as the cue cells should reside in the superficial layers which receive the stimuli from the outside environment. Additionally, the motor cells used as the output cell are suitable for layer V, where the cells transmit out signals for movement. Finally, layer III is always used to integrate the information, so the four kinds of ramp cells should reside in layer III.

and we presented a new neural circuit based on specific neural-connection structures utilizing a TDDM algorithm as the synaptic learning mechanism. This neural circuit was successful in determining time intervals in SCT experiments and in expressing the time intervals learned, indicating that our proposed method is reasonable and effective. Although computational simulation results— which are often more idealized— tend to differ from those of electrophysiological experiments, our simulation experiments and physiological test results were completely consistent with those of electrophysiological experiments. This suggests that the circuit we designed is similar to the endogenous circuit of the macaque brain in terms of achieving this particular timing and periodicity operation.

In neurobiology, the cerebral cortex can be divided into different regions according to different functions. The hierarchical structure of each brain region is essentially the same, and it is composed of six layers of neurons: molecular layer, external granular layer, external pyramidal layer, internal granular layer, internal pyramidal layer, and multiform layer (Le Be', 2007).These six layers of neurons are arranged vertically in each brain region. According to previous literature (Merchant et al., 2014), it is known that MPC is more active in SCT experiments. Additionally, there are many time-related cells in the MPC. We believe that the neurons in the neural circuit we designed may also be distributed in the six layers of the MPC (**Figure 12**).

The most significant difference between our model and previous simulations is that our model is more biologically interpretable. Compared with the LSTM model (Rivest et al., 2010), the drift diffusion model during the SCT (Merchant and Averbeck, 2017), and time-adaptive drift–diffusion model (Rivest and Bengio, 2011), spiking neuron which models the real biological neurons are used in our model. And Recreating the discharge rate curves observed and scalar property in electrophysiology is another advantage of our model compared with pacemaker accumulator models (Treisman, 1963) and state dependent network models (Buonomano and Maass, 2009). The downside of our model is that it can only learn very precise interval durations. In our model, we make use of TDDM algorithm, which is considered to be a fast and accurate time-learning mechanism for determining interval durations. Although humans can learn target time, there must exist some biases between the time learned and target time. Hence, the high accuracy which is the advantage of TDDM algorithm cannot be interpreted biologically. A certain degree of biases are necessarily presented in human experiments. We believe our model can become more biologically plausible by adjusting the parameters of TDDM algorithm such as $\varepsilon(t)$.

Knudsen et al. (2014) found the same four types of ramping cells in the primary motor cortex in a single interval reproduction task in rats. Their work provided us more information to improve our model in the future. In addition, we will improve our learning-mechanism algorithm to satisfy additional biological properties and be flexible in more temporal-processing experiments. And now this work is based on the property called ramp activity, but future studies will explore other properties as well. We believe

that as more and more time-related biological properties are adopted, our model will become closer to endogenous biological processing mechanisms.

AUTHOR CONTRIBUTIONS

HW carried out the computational neuroscience model and neural circuit design studies, experiment design, and writing the paper. Y-FD designed algorithms, coded simulation program and collected experimental data, and wrote the paper. All authors read and approved the final manuscript.

FUNDING

This work was supported by the NSFC Project (Project Nos. 61771146 and 61375122), (in part) by Shanghai Science and Technology Development Funds (Project Nos. 13dz2260200 and 13511504300).

REFERENCES

Bartolo, R., Prado, L., and Merchant, H. (2014). Information processing in the primate basal ganglia during sensory-guided and internally driven rhythmic tapping. *J. Neurosci.* 34, 3910–3923. doi: 10.1523/JNEUROSCI.2679-13.2014

Brody, C. D., Herna'ndez, A., Zainos, A., and Romo, R. (2003). Timing and neural encoding of somatosensory parametric working memory in macaque prefrontal cortex. *Cereb. Cortex* 13, 1196–1207. doi: 10.1093/cercor/bhg100

Buhusi, C. V., Perera, D., and Meck, W. H. (2005). Memory for timing visual and auditory signals in albino and pigmented rats. *J. Exp. Psychol.* 31, 18–30. doi: 10.1037/0097-7403.31.1.18

Buonomano, D. V., and Maass, W. (2009). State-dependent computations: spatiotemporal processing in cortical networks. *Nat. Rev. Neurosci.* 10, 113–125. doi: 10.1038/nrn2558

Church, R. M. (1984). Properties of the internal clock a. *Ann. N. Y. Acad. Sci.* 423, 566–582. doi: 10.1111/j.1749-6632.1984.tb23459.x

Constantinidis, C., and Steinmetz, M. A. (1996). Neuronal activity in posterior parietal area 7a during the delay periods of a spatial memory task. *J. Neurophysiol.* 76, 1352–1355. doi: 10.1152/jn.1996.76.2.1352

Crowe, D. A., Zarco, W., Bartolo, R., and Merchant, H. (2014). Dynamic representation of the temporal and sequential structure of rhythmic movements in the primate medial premotor cortex. *J. Neurosci.* 34, 11972–11983. doi: 10.1523/JNEUROSCI.2177-14.2014

Gámez, J., Mendoza, G., Prado, L., Betancourt, A., and Merchant, H. (2019). The amplitude in periodic neural state trajectories underlies the tempo of rhythmic tapping. *PLoS Biol.* 17:e3000054. doi: 10.1371/journal.pbio.3000054

Gavornik, J. P., Shuler, M. G. H., Loewenstein, Y., Bear, M. F., and Shouval, H. Z. (2009). Learning reward timing in cortex through reward dependent expression of synaptic plasticity. *Proc. Natl. Acad. Sci.* 106, 6826–6831. doi: 10.1073/pnas.0901835106

Gibbon, J., Malapani, C., Dale, C. L., and Gallistel, C. R. (1997). Toward a neurobiology of temporal cognition: advances and challenges. *Curr. Opin. Neurobiol.* 7, 170–184. doi: 10.1016/S0959-4388(97)80005-0

Hassani, O. K., Cromwell, H. C., and Schultz, W. (2001). Influence of expectation of different rewards on behavior-related neuronal activity in the striatum. *J. Neurophysiol.* 85, 2477–2489. doi: 10.1152/jn.2001.85.6.2477

Hui, W., and Dawei, D. (2018). A plausible method for assembling a neural circuit for decision-making. *Biol. Inspired Cogn. Archit.* 25, 72–87. doi: 10.1016/j.bica.2018.07.001

Izhikevich, E. M. (2003). Simple model of spiking neurons. *IEEE Trans. Neural Netw.* 14, 1569–1572. doi: 10.1109/TNN.2003.820440

Kawagoe, R., Takikawa, Y., and Hikosaka, O. (1998). Expectation of reward modulates cognitive signals in the basal ganglia. *Nat. Neurosci.* 1, 411–416. doi: 10.1038/1625

Knudsen, E. B., Powers, M. E., and Moxon, K. A. (2014). Dissociating movement from movement timing in the rat primary motor cortex. *J. Neurosci.* 34, 15576–15586. doi: 10.1523/JNEUROSCI.1816-14.2014

Kojima, S., and Goldman-Rakic, P. S. (1982). Delay-related activity of prefrontal neurons in rhesus monkeys performing delayed response. *Brain Res.* 248, 43–50. doi: 10.1016/0006-8993(82)91145-3

Komura, Y., Tamura, R., Uwano, T., Nishijo, H., Kaga, K., and Ono, T. (2001). Retrospective and prospective coding for predicted reward in the sensory thalamus. *Nature* 412, 546–549. doi: 10.1038/35087595

Le Be', J.-V. (2007). *Structure and Dynamics of the Neocortical Microcircuit Connectivity*. Technical reports, EPFL

Leon, M. I., and Shadlen, M. N. (2003). Representation of time by neurons in the posterior parietal cortex of the macaque. *Neuron* 38, 317–327. doi: 10.1016/S0896-6273(03)00185-5

Matell, M. S., and Meck, W. H. (2004). Cortico-striatal circuits and interval timing: coincidence detection of oscillatory processes. *Cogn. Brain Res.* 21, 139–170. doi: 10.1016/j.cogbrainres.2004.06.012

Mauk, M. D., and Buonomano, D. V. (2004). The neural basis of temporal processing. *Annu. Rev. Neurosci.* 27, 307–340. doi: 10.1146/annurev.neuro.27.070203.144247

Meck, W. H. (2005). Neuropsychology of timing and time perception. *Brain Cogn.* 58, 1–8. doi: 10.1016/j.bandc.2004.09.004

Mendoza, G., Me'ndez, J. C., Pérez, O., Prado, L., and Merchant, H. (2018). Neural basis for categorical boundaries in the primate pre-sma during relative categorization of time intervals. *Nat. Commun.* 9:1098. doi: 10.1038/s41467-018-03482-8

Merchant, H., and Averbeck, B. B. (2017). The computational and neural basis of rhythmic timing in medial premotor cortex. *J. Neurosci.* 37, 4552–4564. doi: 10.1523/JNEUROSCI.0367-17.2017

Merchant, H., and Bartolo, R. (2018). Primate beta oscillations and rhythmic behaviors. *J. Neural Transm.* 125, 461–470. doi: 10.1007/s00702-017-1716-9

Merchant, H., Bartolo, R., Pérez, O.,Me'ndez, J. C., Mendoza, G., Gámez, J., et al. (2014). "Neurophysiology of timing in the hundreds of milliseconds: multiple layers of neuronal clocks in the medial premotor areas," in *Neurobiology of Interval Timing* eds H. Merchant and V. de Lafuente (New York, NY: Springer), 143–154. doi: 10.1007/978-1-4939-1782-2_8

Merchant, H., Battaglia-Mayer, A., and Georgopoulos, A. P. (2004). Neural responses during interception of real and apparent circularly moving stimuli in motor cortex and area 7a. *Cereb. Cortex* 14, 314–331. doi: 10.1093/cercor/bhg130

Merchant, H., and Lafuente, V. D. (2014). *Neurobiology of Interval Timing (Advances in Experimental Medicine and Biology 829)*. New York, NY: Springer. doi: 10.1007/978-1-4939-1782-2

Merchant, H., Zarco, W., Pérez, O., Prado, L., and Bartolo, R. (2011). Measuring time with different neural chronometers during a synchronization-continuation task. *Proc. Natl. Acad. Sci. U.S.A.* 108, 19784–19789. doi: 10.1073/pnas.1112933108

Mongillo, G., Amit, D. J., and Brunel, N. (2003). Retrospective and prospective persistent activity induced by hebbian learning in a recurrent cortical network. *Eur. J. Neurosci.* 18, 2011–2024. doi: 10.1046/j.1460-9568.2003.02908.x

Pérez, O., and Merchant, H. (2018). The synaptic properties of cells define the hallmarks of interval timing in a recurrent neural network. *J. Neurosci.* 38, 4186–4199. doi: 10.1523/JNEUROSCI.2651-17.2018

Rainer, G., Rao, S. C., and Miller, E. K. (1999). Prospective coding for objects in primate prefrontal cortex. *J. Neurosci.* 19, 5493–5505. doi: 10.1523/JNEUROSCI.19-13-05493.1999

Rakitin, B. C., Gibbon, J., Penney, T. B., Malapani, C., Hinton, S. C., and Meck, W. H. (1998). Scalar expectancy theory and peak-interval timing in humans. *J. Exp. Psychol.* 24, 15–33. doi: 10.1037//0097-7403.24.1.15

Reutimann, J., Fusi, S., Senn, W., Yakovlev, V., and Zohary, E. (2001). A model of expectation effects in inferior temporal cortex. *Neurocomputing* 38, 1533–1540. doi: 10.1016/S0925-2312(01)00551-3

Rivest, F., and Bengio, Y. (2011). Adaptive drift-diffusion process to learn time intervals. *arXiv[Preprint].arXiv:1103.2382.*

Rivest, F., Kalaska, J. F., and Bengio, Y. (2010). Alternative time representation in dopamine models. *J. Comput. Neurosci.* 28, 107–130. doi: 10.1007/s10827-009-0191-1

Romo, R., Brody, C. D., Herna'ndez, A., and Lemus, L. (1999). Neuronal correlates of parametric working memory in the prefrontal cortex. *Nature* 399, 470–473. doi: 10.1038/20939

Schultz, W. (2000). Multiple reward signals in the brain. *Nat. Rev. Neurosci.* 1, 199–207. doi: 10.1038/35044563

Simen, P., Balci, F., Cohen, J. D., and Holmes, P. (2011). A model of interval timing by neural integration. *J. Neurosci.* 31, 9238–9253. doi: 10.1523/JNEUROSCI.3121-10.2011

Tang, C., Chehayeb, D., Srivastava, K., Nemenman, I., and Sober, S. J. (2014). Millisecond-scale motor encoding in a cortical vocal area. *PLoS Biol.* 12:e1002018. doi: 10.1371/journal.pbio.1002018

Treisman, M. (1963). Temporal discrimination and the indifference interval: Implications for a model of the "internal clock." *Psychol. Monogr.* 77, 1–31. doi: 10.1037/h0093864

Watanabe, M. (1996). Reward expectancy in primate prefrental neurons. *Nature* 382, 629–632. doi: 10.1038/382629a0

Wei, H., Bu, Y., and Dai, D. (2017). A decision-making model based on a spiking neural circuit and synaptic plasticity. *Cogn. Neurodyn.* 11, 415–431. doi: 10.1007/s11571-017-9436-2

Conflict of Interest Statement: The authors declare that the research was conducted in the absence of any commercial or financial relationships that could be construed as a potential conflict of interest.

frontiers in Physics

ORIGINAL RESEARCH
published: 30 July 2019
doi: 10.3389/fphy.2019.00107

OPEN ACCESS

Edited by:
Chris G. Antonopoulos, University of Essex, United Kingdom

Reviewed by:
Paola Valsasina, San Raffaele Scientific Institute (IRCCS), Italy
Paul J. Laurienti, Wake Forest School of Medicine, United States
Mohsen Bahrami, Wake Forest School of Biomedical Engineering and Sciences, United States, in collaboration with reviewer PL

***Correspondence:**
Roberto C. Sotero
roberto.soterodiaz@ucalgary.ca

†Data used in preparation of this article were obtained from the Alzheimer's Disease Neuroimaging Initiative (ADNI) database (adni.loni.usc.edu). As such, the investigators within the ADNI contributed to the design and implementation of ADNI and/or provided data but did not participate in analysis or writing of this report. A complete listing of ADNI investigators can be found at: http://adni.loni.usc.edu/wp-content/uploads/how_to_apply/ADNI_Acknowledgment_List.pdf

Specialty section:
This article was submitted to Biophysics, a section of the journal Frontiers in Physics

Received: *18 March 2019*
Accepted: *08 July 2019*
Published: *30 July 2019*

Citation:
Sotero RC, Sanchez-Rodriguez LM, Dousty M, Iturria-Medina Y and Sanchez-Bornot JM (2019) Cross-Frequency Interactions During Information Flow in Complex Brain Networks Are Facilitated by Scale-Free Properties. Front. Phys. 7:107. doi: 10.3389/fphy.2019.00107

Cross-Frequency Interactions During Information Flow in Complex Brain Networks Are Facilitated by Scale-Free Properties

***Roberto C. Sotero*[1]*, *Lazaro M. Sanchez-Rodriguez*[1], *Mehdy Dousty*[2], *Yasser Iturria-Medina*[3] *and Jose M. Sanchez-Bornot*[4], *on behalf of the Alzheimer's Disease Neuroimaging Initiative*[†]**

[1] Department of Radiology, Hotchkiss Brain Institute, University of Calgary, Calgary, AB, Canada, [2] Institute of Biomaterials and Biomedical Engineering, University of Toronto, Toronto, ON, Canada, [3] Montreal Neurological Institute, McGill University, Montreal, QC, Canada, [4] Intelligent Systems Research Centre, Ulster University, Derry Londonderry, United Kingdom

We studied the interactions between different temporal scales of the information flow in complex networks and found them to be stronger in scale-free (SF) than in Erdos-Renyi (ER) networks, especially for the case of phase-amplitude coupling (PAC)—the phenomenon where the phase of an oscillatory mode modulates the amplitude of another oscillation. We found that SF networks facilitate PAC between slow and fast frequency components of the information flow, whereas ER networks enable PAC between slow-frequency components. Nodes contributing the most to the generation of PAC in SF networks were non-hubs that connected with high probability to hubs. Additionally, brain networks from healthy controls (HC) and Alzheimer's disease (AD) patients presented a weaker PAC between slow and fast frequencies than SF, but higher than ER. We found that PAC decreased in AD compared to HC and was more strongly correlated to the scores of two different cognitive tests than what the strength of functional connectivity was, suggesting a link between cognitive impairment and multi-scale information flow in the brain.

Keywords: complex networks, scale-free networks, random networks, brain networks, random walks, cross-frequency interactions, Alzheimer's disease, information flow

INTRODUCTION

The study of information flow and transport in complex biological and social networks by means of random walks has attracted increasing interest in recent years [1–4]. Random walks [5] are the processes by which randomly-moving objects wander away from their starting location. In the past decades, there has been considerable progress in characterizing first passage times, or the amount of time it takes a random walker to reach a target [6–9]. However, previous works have neglected the study of the temporal dynamics of the information flow in the network, which depends on how the walkers move and not just on their arrival time. Thus, we lack knowledge about how the different temporal scales in the information flow arise from the topological structure of the network, whether they interact, and how they do it. This paper aims to address such knowledge gap.

We hypothesize that random walk processes in complex networks have associated multiple temporal scales, depending on the network structure. Furthermore, these temporal scales

may interact. To study these scales, and their interaction, we use the empirical mode decomposition (EMD) [10], an adaptive and data-driven method that decomposes non-linear and non-stationary signals, like the movement of the random walkers, into fundamental modes of oscillations called intrinsic mode functions (IMFs), without the need for a predefined model as is the case for Fourier and wavelet transforms. Since IMFs are associated with different oscillatory modes, their interactions correspond to the phenomenon known as cross-frequency coupling (CFC) [11]. Three types of CFC are most widely studied: phase-amplitude coupling (PAC), the phenomenon where the instantaneous phase of a low frequency oscillation modulates the instantaneous amplitude of a higher frequency oscillation [12]; amplitude-amplitude coupling (AAC), which measures the co-modulation of the instantaneous amplitudes of two oscillations [13]; and phase-phase coupling (PPC), which corresponds to the synchronization between two instantaneous phases [14].

In this paper, we study cross-frequency interactions between the IMFs extracted from random walk processes occurring in different networks. First, we perform an exploratory analysis over simulated Erdos-Renyi (ER) [15] and scale-free (SF) [16] networks, models that incorporate properties measured in real networks. Later, we focus on real brain networks. These are estimated from resting-state functional magnetic resonance imaging (rs-fMRI) and diffusion weighted magnetic resonance imaging (DWMRI) data recorded from patients with Alzheimer's disease (AD) and healthy controls (HC). Our analysis reveals differences between health and disease in terms of the information flow over the networks.

MATERIALS AND METHODS

Ethics Statement

Data used in this article were obtained from the Alzheimer's Disease Neuroimaging Initiative (ADNI) database (adni.loni.usc.edu). The ADNI study was conducted according to Good Clinical Practice guidelines, the Declaration of Helsinki Principles, US 21CFR Part 50-Protection of Human Subjects, and Part 56-Institutional Review Boards, and pursuant to state and federal HIPAA regulations (adni.loni.usc.edu). Study subjects and/or authorized representatives gave written informed consent at the time of enrollment for sample collection and completed questionnaires approved by each participating sites Institutional Review Board.

The authors obtained approval from the ADNI Data Sharing and Publications Committee for data use and publication, see documents: http://adni.loni.usc.edu/wpcontent/uploads/how_to_apply/ADNI_Data_Use_Agreement.pdf and http://adni.loni.usc.edu/wpcontent/uploads/how_to_apply/ADNI_Manuscript_Citations.pdf.

Data Description and Processing

Construction of Simulated Networks

Two types of simulated complex networks are considered here, ER and SF networks. An ER network is a random graph where each possible edge has the same probability p of existing [15]. The degree of a node i (k_i) is defined as the number of connections it has to other nodes. The degree distribution $P(k)$ of an ER network is a binomial distribution, which decays exponentially for large degrees k, allowing only very small degree fluctuations [17]. On the other hand, SF networks are constructed with the Barabasi and Albert's (BA) model [16], or "rich-gets-richer" scheme, which assumes that new nodes in a network are not connected at random but with high probability to those which already possess a large number of connections (also known as hubs). In the BA model, $P(k)$ decays as a power law, which yields scale-invariance, and allows for large degree fluctuations. We generate ER and SF networks by means of the MATLAB (The MathWorks Inc., Natick, MA, USA) toolbox CONTEST [18].

Construction of Brain Networks

Brain structural T1-weighted 3D images were acquired for all subjects in the ADNI dataset. For a detailed description of acquisition details, see http://adni.loni.usc.edu/methods/documents/mriprotocols/. All images underwent non-uniformity correction using the N3 algorithm [19]. Next, they were segmented into gray matter, white matter, and cerebrospinal fluid (CSF) probabilistic maps, using SPM12 (www.fil.ion.ucl.ac.uk/spm). Gray matter segmentations were standardized to MNI space [20] using the DARTEL tool [21]. Each map was modulated to preserve the total amount of signal/tissue. Mean gray matter density and determinant of the Jacobian (DJ) [21] values were calculated for 78 regions covering all the brain's gray matter [22].

DWMRI data was acquired for 51 HC subjects from ADNI using a 3T GE scanner. For each diffusion scan, 46 separate images were acquired, including 5 b_0 images (no diffusion sensitization) and 41 diffusion-weighted images ($b = 1{,}000\ s/mm^2$). Other acquisition parameters were: 256×256 matrix, voxel size: $2.7 \times 2.7 \times 2.7\ mm^3$, $TR = 9{,}000\ ms$, 52 contiguous axial slices, and scan time, 9 *min*. ADNI aligned all raw volumes to the average $b0$ image, corrected head motion and eddy current distortion. Probabilistic axonal connectivity values between each brain voxel and the surface of each considered gray matter region were estimated using a fully automated fiber tractography algorithm [23] and the intravoxel fiber distributions (ODFs) of the 51 HC subjects. ODF reconstructions were based on Spherical Deconvolution [24]. A maximum of 500 *mm* trace length and a curvature threshold of $\pm 90^\circ$ were imposed as tracking parameters. Based on the resulting voxel-region connectivity maps, the individual region-region anatomical connection density matrices [23, 25] were calculated. For any subject and pair of regions i and j, the $ACD_{i,j}$ measure ($0 \leq ACD_{i,j} \leq 1$, $ACD_{i,j} = ACD_{j,i}$) reflects the fraction of the region's surface involved in the axonal connection with respect to the total surface of both regions. A network backbone, containing the dominant connections in the average network, was computed [26]. For this, a maximum spanning tree, which connects all nodes of the network such that the sum of its weights is maximal, was extracted; then, additional edges were added in order of their weight until the average node degree was 4 [26]. The anatomical backbone was then transformed into a matrix of zeros (no connection existing between two nodes) and ones (a link exists). A limitation of using the backbone

matrix is its symmetrical configuration, which is a consequence of the inherent symmetrical properties of DWMRI techniques (distinction between afferent and efferent fiber projections it is not possible yet). Nevertheless, a previous work [27] reported that around 85% of the total possible connections between 73 primate brain areas are reciprocals.

Additionally, rs-fMRI images were obtained from 31 AD patients and 44 HCs from a different ADNI subset (this was forced by the fact that subjects with DWMRI data in ADNI lacked fMRI data) using an echo-planar imaging sequence on a 3T Philips scanner. Acquisition parameters were: 140 time points, repetition time (TR) = 3,000 ms, echo time (TE) = 30 ms, flip angle = 80°, number of slices = 48, slice thickness = 3.3 mm, spatial resolution = $3 \times 3 \times 3$ mm^3 and in plane matrix = 64×64. Preprocessing steps included: (1) motion correction, (2) slice timing correction, (3) spatial normalization to MNI space using the registration parameters obtained for the structural T1 image with the nearest acquisition date, and (4) signal filtering to keep only low frequency fluctuations (0.01–0.08 Hz) [28].

Average time series were extracted for each subject from the 78 anatomical regions of interest. Then, we estimated the functional connectivity (FC) by computing the absolute value of the Pearson's correlation between all possible pairs of time series, creating a 78×78 FC matrix. Each FC matrix was multiplied by the anatomical backbone, resulting in a new matrix we denote as $\boldsymbol{W}$. Thus, the random walkers flow in the structural network, but their movement is influenced by the brain's activity. This guarantees that the dynamics of the information flow will change if instead of the resting-state we study a different condition such as stimulation or anesthesia [29, 30].

Constructing the Time Series of the Random Walks

We start by considering an unweighted network consisting of N nodes. We place a large number K ($K \gg N$) of random walkers onto this network. At each time step, the walkers move randomly between the nodes that are directly linked to each other. We allow the walkers to perform T time steps. As a walker visits a node, we record the fraction of walkers present at it. Thus, after T time steps, we obtain K time series reflecting different realizations of the flow of information in the network.

In the case of weighted networks, the transition probability p_{ij} from brain area i to brain area j is given by $p_{ij} = \frac{w_{ij}}{\sum_{j=1}^{N} w_{ij}}$, where w_{ij} is the weight of the connection from area i to area j [31]. Since both the FC and the anatomical backbone are symmetric matrices, we have: $w_{ij} = w_{ji}$, and $p_{ij} = p_{ji}$. Note that it is possible to construct a transition probability where walkers move preferentially to positively correlated nodes. However, in our case we are interested in brain networks. To our knowledge, there is not physiological reason to assume positive connections should be preferred over negative connections, since there can be a strong information flow between anticorrelated brain areas. Thus, in this paper, the probability of a random walker moving from one node to another node depends on the strength of the connection (i.e., its absolute value) and not on its sign.

Empirical Mode Decomposition

EMD is a non-linear method that decomposes a signal into its fundamental modes of oscillations, called intrinsic mode functions or IMFs. An IMF satisfies two criteria: (1) the number of zero-crossings and extrema are either equal or differ by one, and (2) the mean of its upper and lower envelopes is zero. Thus, to be successfully decomposed into IMFs, a signal must have at least one maximum and one minimum. The sifting process of decomposing a signal $x(t)$ into its IMFs is described by the following algorithm [10]:

1 All extrema are identified, and upper, $x_u(t)$, and lower, $x_l(t)$, envelopes are constructed by means of cubic spline interpolation.
2 The average of the two envelopes is subtracted from the data: $d(t) = x(t) - (x_u(t) + x_l(t))/2$.
3 The process for $d(t)$ is repeated until the resulting signal satisfies the criteria of an IMF. This first IMF is denoted as $IMF_1(t)$. The residue $r_1(t) = x(t) - IMF_1(t)$ is treated as the new data.
4 Repeat steps 1 to 3 on the residual $r_j(t)$ to obtain all the IMFs of the signal:

$$r_j(t) = x(t) - IMF_1(t) - IMF_2(t) - \ldots - IMF_j(t).$$

The procedure ends when $r_j(t)$ is a constant, a monotonic slope, or a function with only one extreme. As a result of the EMD method, the signal $x(t)$ is decomposed into M IMFs:

$$x(t) = \sum_{j=1}^{M} IMF_j(t) + r(t) \tag{1}$$

where $r(t)$ is the final residue.

A major limitation of the classical EMD method is the common presence of mode mixing, which is when one IMF consists of signals of widely disparate scales, or when a signal of a similar scale resides in different IMFs [32]. To address this issue, the ensemble empirical mode decomposition (EEMD) considers that the true IMF components are the mean of an ensemble of trials, each consisting of the signal plus a white noise of finite amplitude [32]. A more recent method, ICEEMDAN (Improved Complete Ensemble Empirical Mode Decomposition with Adaptive Noise) was built on this idea [33]. In this paper, we use the ICEEMDAN method with standard parameter values [33], which reduces the number of ensembles needed and increases the accuracy rate while avoiding spurious modes.

After computing the IMFs, the Hilbert transform can be applied to each IMF. Thus, equation (1) can be rewritten as:

$$x(t) = Real\{\sum_{j=1}^{M} a_j(t) e^{i\varphi_j(t))}\} + r(t), \tag{2}$$

where $\varphi_j(t)$ and $a_j(t)$ are the instantaneous phases and amplitudes of IMF j.

Computation of Cross-Frequency Coupling Measures

PAC is the phenomenon where the instantaneous phase of a low frequency oscillation modulates the instantaneous amplitude of a higher frequency oscillation [12, 34]. To compute PAC, we used the modification to the mean-vector length modulation index [35]:

$$PAC = \left| \frac{1}{N} \sum_{n=1}^{N} a_F(n) \left(e^{i\varphi_S(n)} \ \overline{\varphi} \right) \right|, \ \overline{\varphi} = \frac{1}{N} \sum_{n=1}^{N} e^{i\varphi_S(n)} \quad (3)$$

where N is the total number of time points, a_F is the amplitude of the modulated signal (i.e., the fast frequency component), φ_S is the phase of the modulating signal (i.e., the slow frequency component), and $\overline{\varphi}$ is a factor introduced to remove phase clustering bias.

PPC, which corresponds to the synchronization between two instantaneous phases [14], was calculated by using the *n:m* phase-locking value (PLV) [36]:

$$PPC = \left| \frac{1}{T} \sum_{t=1}^{T} e^{i(n\phi_F(t) - m\varphi_S(t))} \right| \quad (4)$$

where φ_S and φ_F are the instantaneous phases of the slow and fast frequency components, respectively, and m and n are integers. We tested all possible combinations of n and m for $n = 1, 2, \ldots, 30$, $m = 1, 2, \ldots, 30$, with $m > n$, and selected the one producing the highest PPC value.

AAC, the co-modulation of the instantaneous amplitudes a_S and a_F of two signals, was estimated by means of their the correlation [13]:

$$AAC = corr(a_S(n), a_F(n)) \quad (5)$$

A significance value can be attached to any of the above measures through a surrogate data approach where we offset φ_S and a_S by a random time lag. We can thus compute 1,000 surrogate PAC, PPC, and AAC values. From the surrogate dataset, we first computed the mean μ and standard deviation σ, and then computed a Z-score as:

$$Z_{PAC} = \frac{PAC - u_{PAC}}{\sigma_{PAC}}, Z_{PPC} = \frac{PPC - u_{PPC}}{\sigma_{PPC}}, \quad Z_{AAC} = \frac{AAC - u_{AAC}}{\sigma_{AAC}} \quad (6)$$

The normal distribution of the surrogated data was tested with the Jarque-Bera test, and the p-value that corresponded to the standard Gaussian variate was also computed. P-values were corrected by means of a multiple comparison analysis based on the false discovery rate (FDR) [37].

RESULTS

Information Flow in Simulated ER and SF Networks

Figures 1A,C show an example of connectivity (adjacency) matrices for ER and SF networks, respectively. Both networks have the same number of edges m, and nodes, corresponding to a sparsity, e, value of $e = 1 - \frac{m}{N^2} = 0.9$. A number of 10^4 random walkers were placed onto these networks and diffused for 5,000 time steps. One realization of the information flow is shown in **Figures 1B,D** for ER and SF networks, respectively. We then applied a recent version of the EMD method [33] to these two time series (see *Materials and Methods*). **Figure 1E** shows the first 7 IMFs and residue (R) for the ER and SF networks. The first IMF (IMF1) corresponds to the fastest oscillatory mode and the last IMF to the slowest one. Note that IMF7 is the sum of all the slow IMFs up to IMF7. As seen in **Figure 1E**, the EMD method produces amplitude and frequency modulated signals. By applying the Hilbert transform to each IMF, instantaneous amplitudes, phases, and frequencies can be obtained and a time-frequency representation of the original signal (known as the Hilbert spectrum) can be constructed [10]. Since each time instant in **Figure 1E** corresponds to a different node in the network, the time-frequency representation of the Hilbert spectrum can be transformed into a node-frequency matrix. **Figures 1F,G** show the modified Hilbert spectrum for the ER (**Figure 1A**) and SF (**Figure 1C**) networks, respectively. The color scale represents the energy of the spectrum. Our results show that ER networks have more energy in the low frequencies and present a narrow range of node degrees. On the other hand, SF networks present a wide distribution of node degree values where nodes with low degrees are more associated to low frequency oscillations, whereas high degree nodes relate to high frequencies. These results indicate that random walkers strongly link low and high frequency dynamics when they diffuse in SF networks.

To characterize the interaction between frequencies, we computed three types of CFC interactions, PAC_{kl}, AAC_{kl}, and PPC_{kl}, between all possible combinations of the 7 IMFs ($k = 1, 2, \ldots, 7$, $l = 1, 2, \ldots, 7$, $k > l$, thus obtaining a 7×7 upper triangular matrix for each measure) for 3 different values of sparsity ($e = [0.9, 0.8, 0.7]$) of ER and SF networks (**Figure 2**). **Figure 2** shows the average over $K = 10^4$ realizations of PAC_{kl} (**Figure 2A**), AAC_{kl} (**Figure 2B**), and PPC_{kl} (**Figure 2C**) for ER and SF networks. **Supplementary Figure 1** shows the corresponding Z-scores. In the case of *PAC*, Z-score values obtained for SF networks were higher than the corresponding values obtained in ER networks. Strong *PAC* values in SF networks involved the phase of IMF7 (the slowest IMF) and the amplitudes of IMF6 to IMF1. On the other hand, the highest *AAC* and *PPC* values in SF networks involved IMFs with close frequencies such as IMF1 and IMF2. In the case of ER networks, the strongest values were obtained for interactions between slow IMFs for *PAC* (phase of IMF7 and amplitude of IMF5 in **Figure 2A**), *AAC* (amplitudes of IMF7 and IMF6 in **Figure 2B**) and between fast IMFs for *PPC* (phases of IMF2 and IMF1 in **Figure 2C**). When we decreased the level of sparsity (i.e., the network became more connected), the results for SF networks

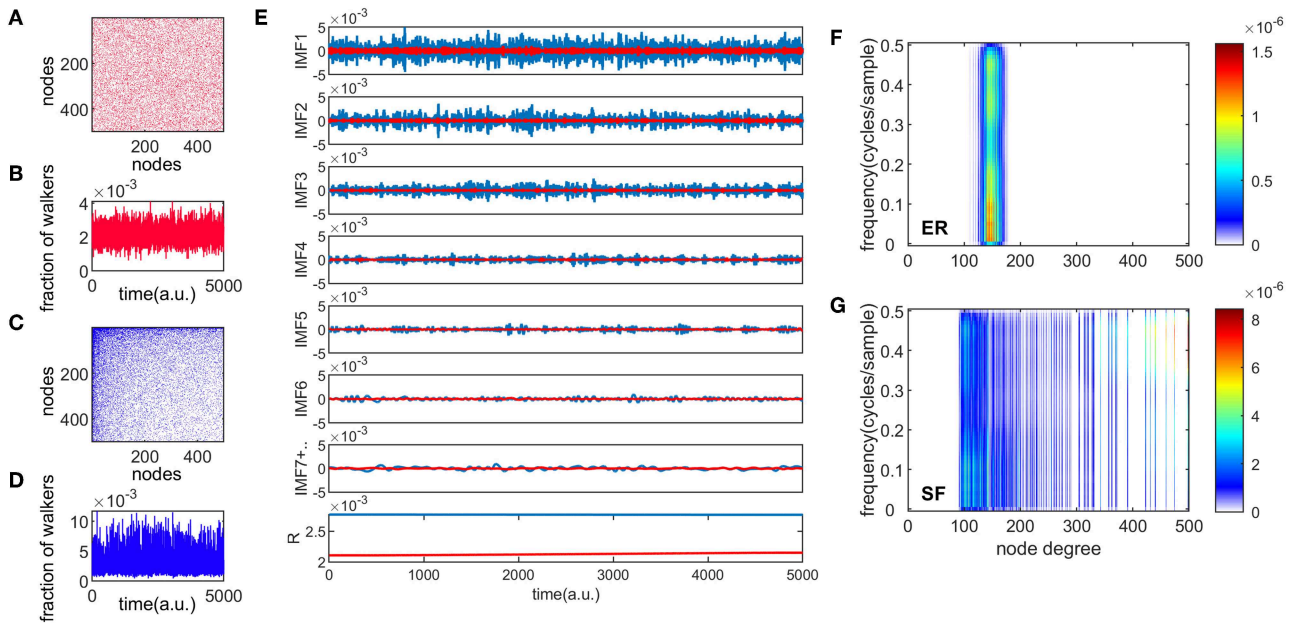

FIGURE 1 | Different temporal modes of information flow in complex networks. Panels **(A,C)** are examples of ER and SF connectivity matrices, respectively, with $N = 500$ and $e = 0.9$. Panels **(B,D)** show one realization of the information flow in the network for 5000 time steps, for ER and SF networks, respectively. The total number of walkers present in each network was 10^4. Panel **(E)** shows the empirical mode decomposition (EMD) of the time series in panels **(B,D)**, producing different intrinsic mode functions (IMF), and a residue (R). This appears in red (blue) for the ER (SF) networks. Panels **(F,G)** show the spectrum of the random walk process organized by the node degree for ER and SF networks, respectively.

turned similar to the ones in ER networks. In conclusion, *PAC* interactions in SF networks were the strongest CFC found (as reflected by the *Z*-scores) and, when compared to results from ER networks, the main difference was the existence of strong *PAC* between slow and fast oscillatory components of the information flow in the network.

To verify our results were not an artifact of the application of the EMD method, we defined seven non-overlapping frequency bands (0.001–0.009, 0.010–0.020, 0.021–0.040, 0.041–0.060, 0.061–0.100, 0.101–0.250, and 0.251–0.490 cycles/sample) based on the seven IMFs and computed the CFC measures. **Supplementary Figure 2** shows similar CFC patterns to the ones obtained for the Z-scores in **Supplementary Figure 1**, suggesting our results are not dependent on the EMD method but a consequence of the network architecture instead. Differences between the two figures are associated to the fact that consecutive IMFs have a small overlap in frequency by design [10].

We also studied the influence of specific nodes in the SF networks in the generation of PAC, AAC, and PPC. The contribution of each node i was computed by removing the node from the network and running the random walker analysis on the new network. The obtained PAC, AAC, and PPC were denoted as PAC_i^r, AAC_i^r, and PPC_i^r, respectively. The contribution of a node to the corresponding CFC measure is the change in the CFC value as a result of removing the node from the network: $\Delta PAC_i = \left|PAC_i^r/PAC - 1\right|$, $\Delta AAC_i = \left|AAC_i^r/AAC - 1\right|$, and $\Delta PPC_i = \left|PPC_i^r/PPC - 1\right|$. Additionally, we computed several local topological properties for all nodes in the network using the Brain Connectivity Toolbox [38], namely: the degree (k); the efficiency (e), which quantifies a network's resistance to failure on a small scale; the clustering coefficient (cc), which measures the degree to which nodes in a graph tend to cluster together; assortativity (a), which indicates if a node tends to link to other nodes with the same or similar degree; betweenness centrality (bc), which is the fraction of shortest paths in the network that contain a given node (a node with higher betweenness centrality has more control over the network because more information will pass through it); eigenvector centrality (ec), which is another measure of centrality where relative scores are assigned to all nodes based on the concept that connections to high-scoring nodes contribute more to the score of the node in question than equal connections to low-scoring nodes; subgraph centrality (sc), which is a weighted sum of closed walks of different lengths in the network starting and ending at the node; and the product of the three centrality measures $(ec \times sc \times bc)$. **Figures 3A–C** show the Pearson correlation between the eight topological measures and ΔPAC, ΔAAC, and ΔPPC, respectively. Different frequency combinations presented different correlation values. The strongest correlations involving ΔPAC were found for the topological measure composed by the product of the three centrality measures $(ec \times sc \times bc)$, between the phase of *IMF*3 and the amplitude of *IMF*1. The amplitude of *IMF*1 was also involved in strong correlations with the phases of *IMF*4, *IMF*5, and *IMF*6. Of the three CFC measures, ΔAAC was most strongly correlated to topology (**Figure 3B**), specifically with centrality

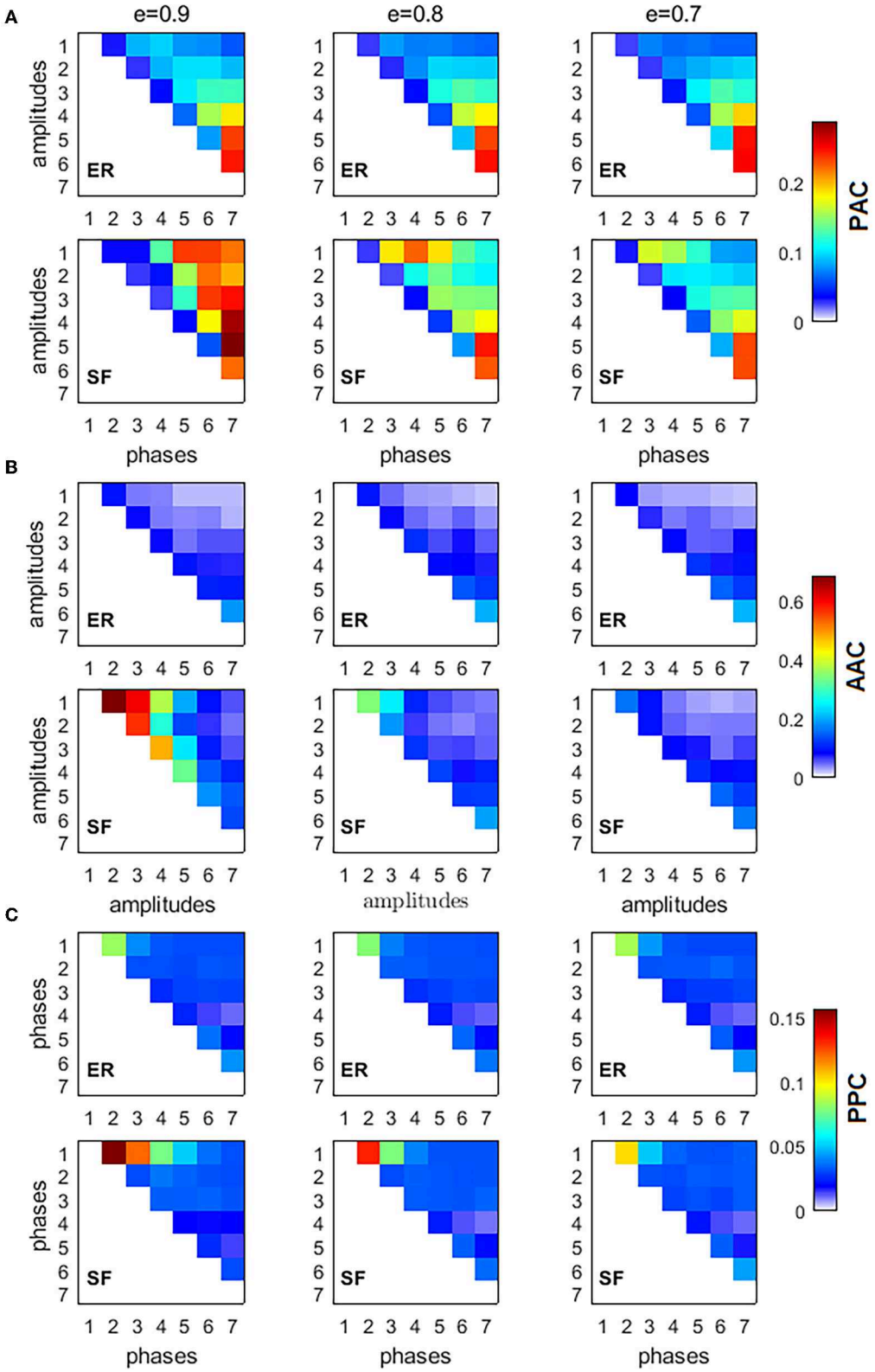

FIGURE 2 | Cross-frequency interactions between the fundamental modes of information flow in ER and SF networks. All simulated networks had $N = 500$ nodes, and 10^4 random walkers were placed over them, each performing 5,000 time steps. Three different values of network sparsity were considered: $e = [0.9,\ 0.8,\ 0.7]$. **(A)** phase-amplitude coupling (PAC), **(B)** amplitude-amplitude coupling (AAC), **(C)** phase-phase coupling (PPC).

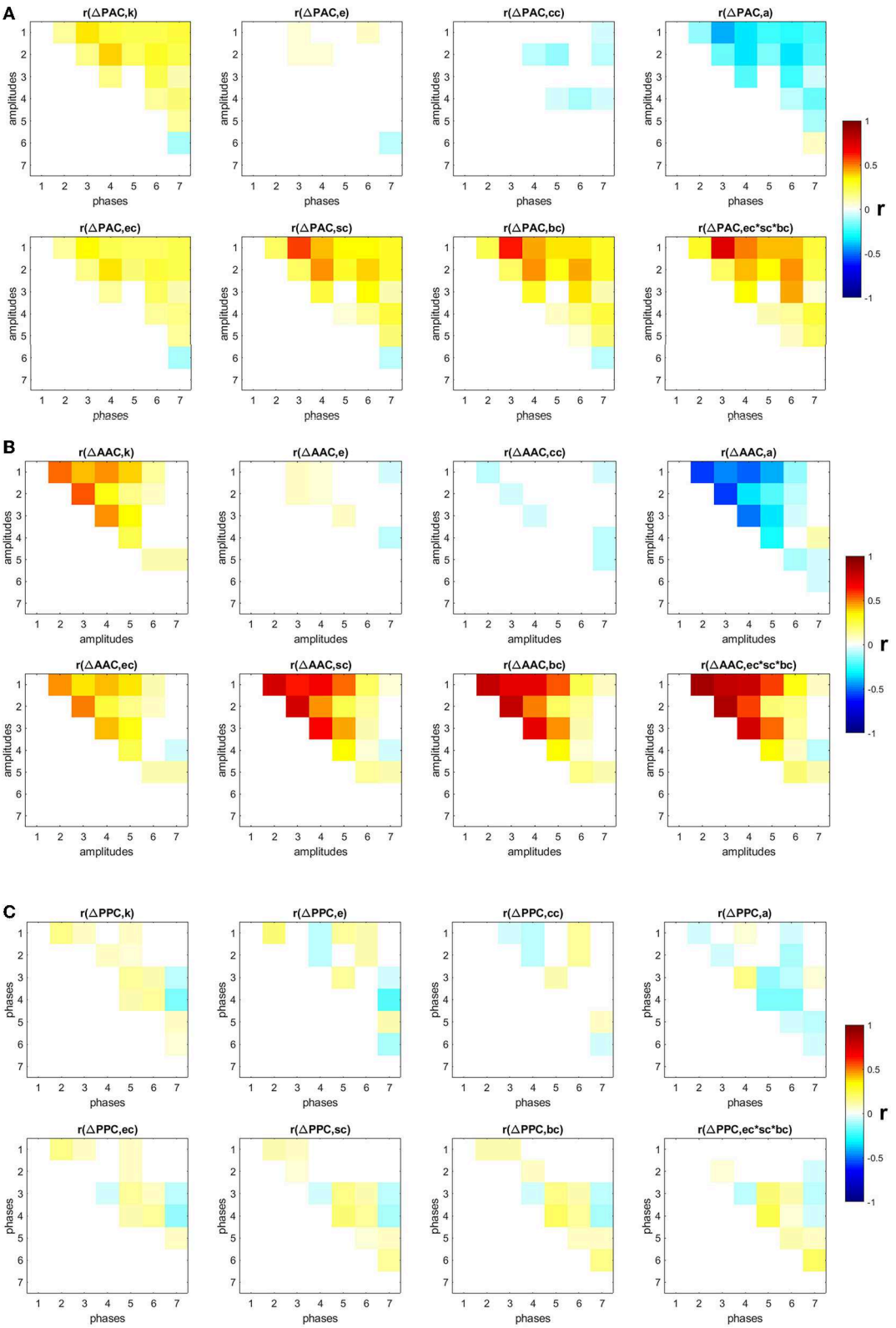

FIGURE 3 | Correlation between changes in CFC and eight topological measures: degree (*k*), efficiency (*e*), clustering coefficient (*cc*), assortativity (*a*), eigenvector centrality (*ec*), subgraph centrality (*sc*), betweenness centrality (*bc*), product of three centrality measures ($ec \times sc \times bc$). Non-significant ($p < 0.05$) correlation values after correction by false-discovery rate are displayed in white **(A)** PAC, **(B)** AAC, **(C)** PPC.

measures, followed by ΔPAC. ΔPPC was weakly correlated to the topology of the network.

Next, by using the degrees k we classified nodes in the network into hubs if their degree was at least one standard deviation above the network mean [39], and into non-hubs otherwise. We then computed the average ΔPAC of all frequency combinations involving the amplitudes of fast frequencies (*IMF*1 and *IMF*2) and the phases of slow frequencies (*IMF*5, *IMF*6, and *IMF*7). Note that the correlations between ΔPAC corresponding to these frequency combinations and the product $ec \times sc \times bc$ are between 0.24 and 0.47 (**Figure 3A**), which suggests that other mechanisms are needed to explain these ΔPAC values.

Figure 4A plots ΔPAC vs. node degree for all nodes in the SF network. Interestingly, hubs, the most connected nodes in the network, are not necessarily involved in the largest ΔPAC values. Non-hubs were classified into three groups by equally dividing the ΔPAC range $(0 - 0.6)$: bottom $(0 - 0.2)$, middle $(0.2 - 0.4)$, and top $(0.4 - 0.6)$. The histogram in **Figure 4B** shows the probability that nodes in the four groups (hubs and three non-hubs groups) have of connecting to nodes of certain degrees. We see that top non-hubs connect to high degree nodes (hubs in **Figure 4A**) with higher probability than middle and bottom non-hubs. On the other hand, hubs connect with high probability to low degree nodes. Since PAC is defined as the coupling from a low to a high frequency, its highest contributor will be the nodes associated more with low frequencies (i.e., nodes with low degrees, see **Figure 1G**) and that also connect to nodes that are more associated to high frequencies (i.e., nodes with high degrees, see **Figure 1G**); that is, the top non-hubs. Accordingly, hubs, which are more connected to low frequency nodes contribute less to PAC, except for only one hub which presented the largest ΔPAC_i of all nodes in the network (**Figures 1A,C,E**). This hub (node with degree 270 in **Figure 4**) is known as a super-hub for having degree significantly higher than other hubs in the network [40]. Since the classification into top, middle, and bottom non-hubs based on ΔPAC values is somewhat arbitrary, we explored the results of changing the ΔPAC range of these three groups. **Figures 4C,D** show the results when the groups were defined by the bands: bottom $(0 - 0.1)$, middle $(0.1 - 0.5)$, and top $(0.5 - 0.6)$. In this case, the number of nodes in the top and bottom groups were reduced and the probability that top non-hubs connected to high degree nodes increased.

In the calculations leading to **Figure 4E** we increased the number of nodes in the top and bottom groups as compared to **Figure 4A** by selecting the ranges: bottom $(0 - 0.35)$, middle $(0.35 - 0.45)$, and top $(0.45 - 0.6)$. In this case, the probability

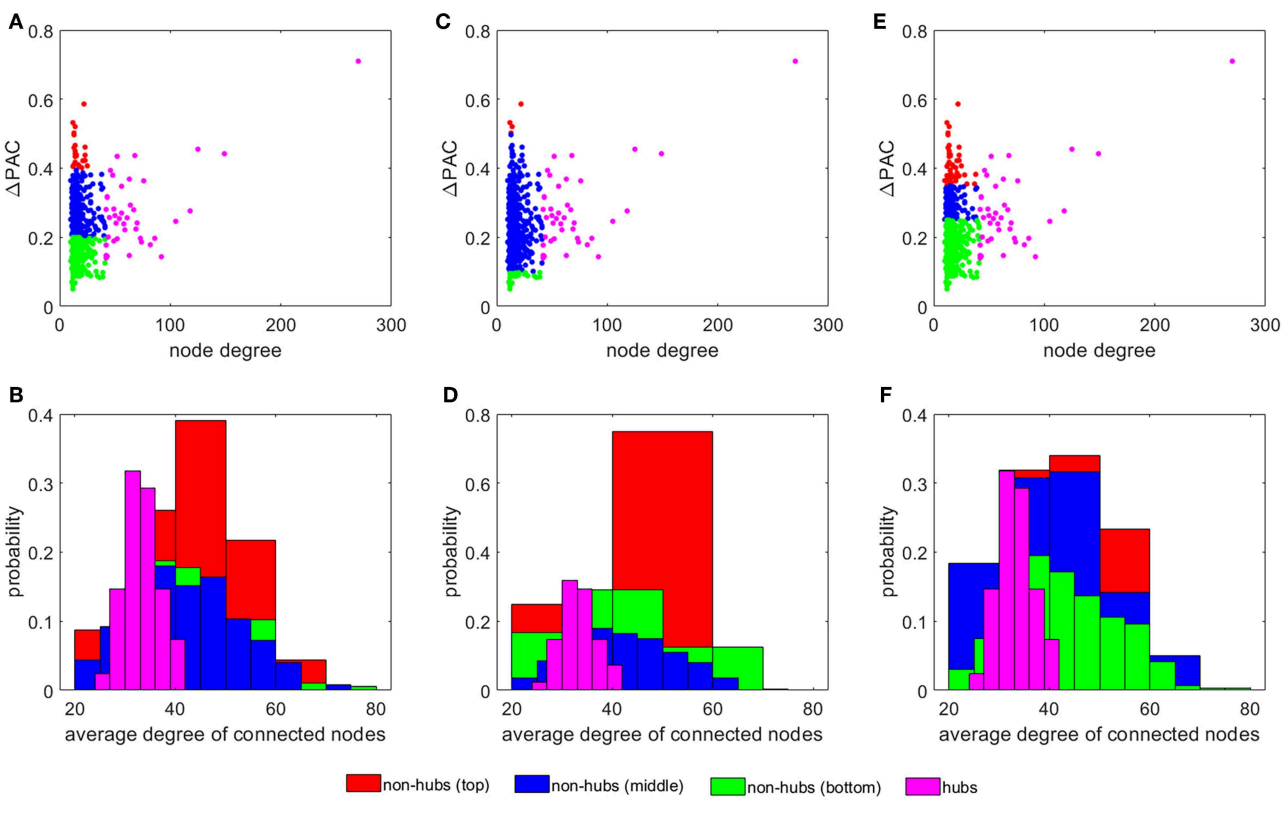

FIGURE 4 | The influence of non-hubs vs. hubs on ΔPAC. Average ΔPAC for each node degree for three different grouping of non-hubs: **(A)** bottom $(0 - 0.2)$, middle $(0.2 - 0.4)$, and top $(0.4 - 0.6)$, **(C)** bottom $(0 - 0.1)$, middle $(0.1 - 0.5)$, and top $(0.5 - 0.6)$, and **(E)** bottom $(0 - 0.25)$, middle $(0.25 - 0.35)$, and top $(0.35 - 0.6)$. Panels **(B,D,F)** present the probability of the four different groups of nodes of connecting to nodes of certain degrees, corresponding to the node distribution presented in panels **(A,C,E)**, respectively.

for the top non-hubs decreased and the results for the top and middle groups were more similar (see **Figure 4F**).

Information Flow in Brain Networks Estimated From Healthy and Alzheimer's Disease Subject's Data

The information flow, as given by the movement of the random walkers, was also investigated in real brain networks. For this, freely available (http://adni.loni.usc.edu) images from ADNI were utilized and brain connectivity matrices for HC and AD subjects were computed. **Figure 5A** shows the connectivity matrix $\boldsymbol{W}$ for a representative HC subject. For each of the 44 HC subjects, we placed 10^4 random walkers on top of its $\boldsymbol{W}$ and recorded a sequence of 5, 000 time steps.

Each time series was decomposed into 8 IMFs. We then focused on PAC since it was the strongest CFC type obtained for both ER and SF networks in our simulations (**Supplementary Figure 1**). **Figure 5B** shows the PAC between all possible combinations of the 8 IMFs, averaged over 10^4 realizations and over the 44 HC subjects, denoted as PAC_{HC}. The strongest PAC values were obtained for interactions between slow IMFs (the phase of IMF8 and the amplitudes of IMF5, IMF6, and IMF7). Additionally, for each subject, we generated 500 ER and 500 SF networks of the same size and number of edges as their $\boldsymbol{W}$ matrices, computed PAC for these matrices and averaged the results, obtaining PAC_{ER} (**Figure 5C**), and PAC_{SF} (**Figure 5D**), respectively. We then computed the following measures: $\frac{PAC_{HC}}{PAC_{ER}} - 1$ (**Figure 5E**), $\frac{PAC_{HC}}{PAC_{SF}} - 1$ (**Figure 5F**). A similar analysis as in **Figure 5**, was performed to data from AD subjects and is shown in **Figure 6**.

Results for HC (**Figure 5**) and AD (**Figure 6**) show that interactions between phases of slow frequencies (IMF 5–8) and amplitudes of high frequencies (IMF1) are stronger in real brain networks than in simulated ER networks but weaker than in SF networks. This result is not surprising since we know that the degree distribution of brain anatomical networks do not follow a pure power law, as in SF networks, and is better described by an exponentially truncated power law [23].

We also compared HC and AD results (**Figure 7**). **Figure 7A** shows the difference between the average connectivity matrix of HC and AD subjects. The comparison between PAC in HC (**Figure 5B**) and AD (**Figure 6B**) shows that PAC between fast frequencies (IMF1) and slower modes (IMFs 3–8) weaken during AD as compared to HCs (see **Figure 7B**).

The contribution of each area to the generation of the PAC phenomenon (ΔPAC) was computed following the procedure described in the previous section. **Figures 8A,B** shows the average ΔPAC across subjects for the areas with the strongest influence on PAC, for the HC and AD groups, respectively. In

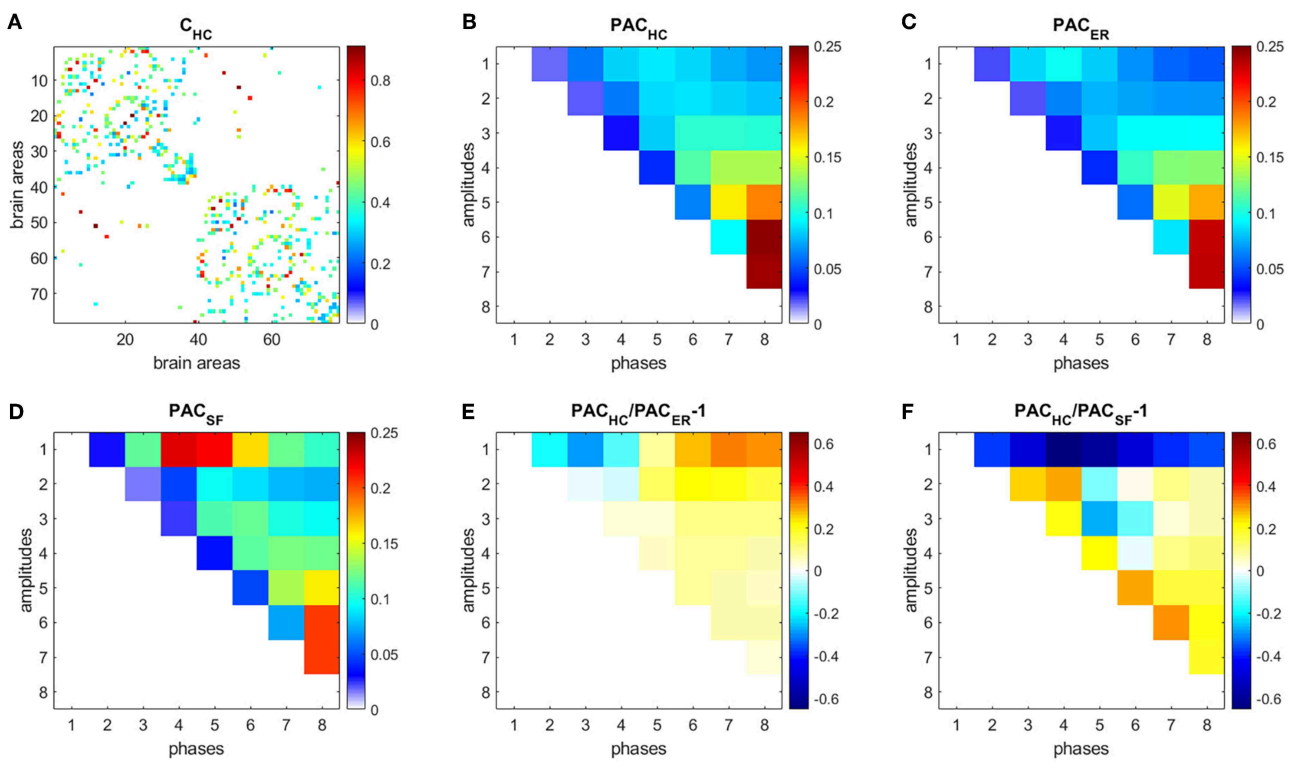

FIGURE 5 | PAC in HC. **(A)** Connectivity matrix. **(B)** PAC averaged over 44 HC subjects. **(C)** Average PAC generated from 500 equivalent ER networks. **(D)** Average PAC generated from 500 equivalent SF networks. **(E)** Comparison of PAC from HC and PAC generated from equivalent ER networks. **(F)** Comparison of PAC from HC and PAC generated from equivalent SF networks.

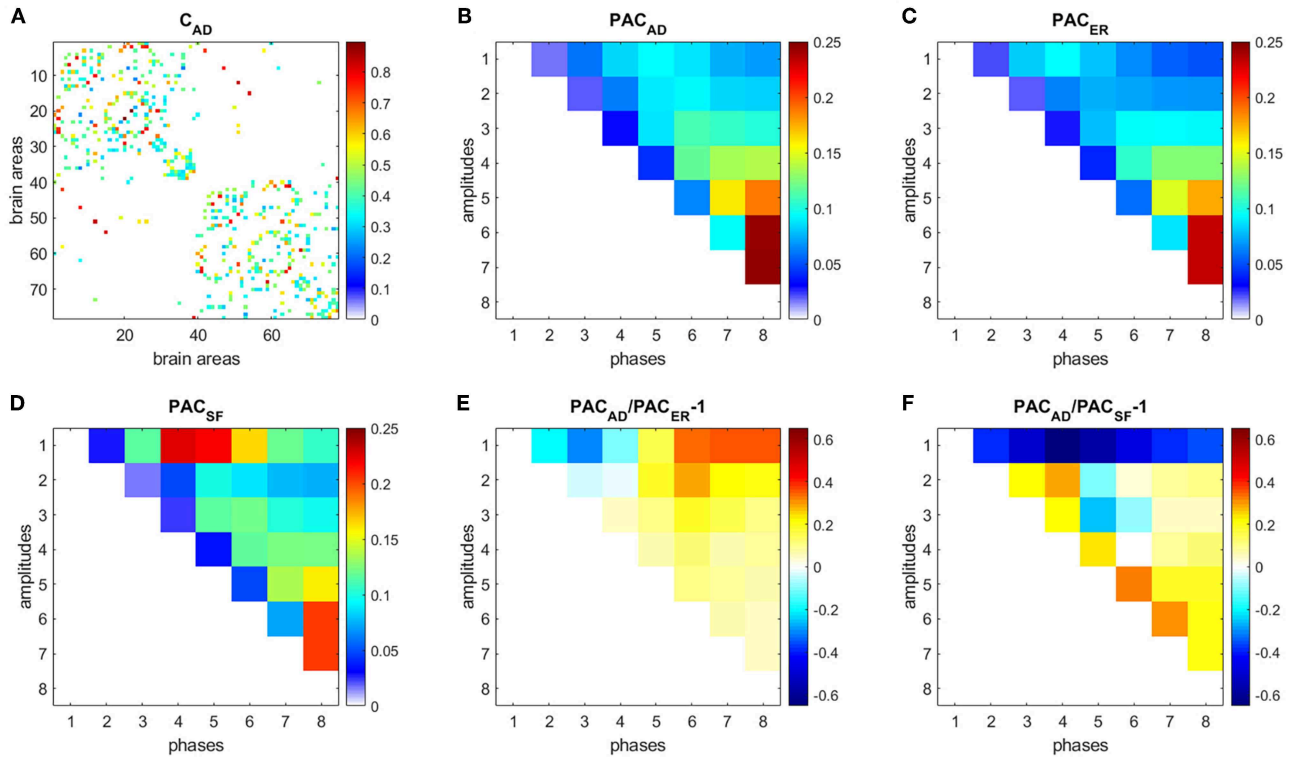

FIGURE 6 | PAC in AD. **(A)** Connectivity matrix. **(B)** PAC averaged over 31 AD subjects. **(C)** Average PAC generated from 500 equivalent ER networks. **(D)** Average PAC generated from 500 equivalent SF networks. **(E)** Comparison of PAC from AD and PAC generated from equivalent ER networks. **(F)** Comparison of PAC from AD and PAC generated from equivalent SF networks.

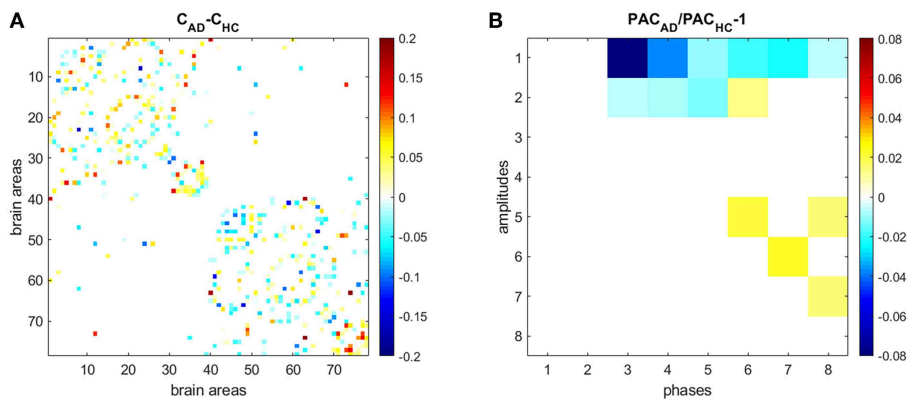

FIGURE 7 | Comparing PAC in HC and AD subjects. **(A)** Difference between the average connectivity matrix of HC and AD subjects. **(B)** Comparison between PAC in HC and AD. Non-significant differences ($p < 0.05$) after correcting by false-discovery rate are displayed in white.

both groups the two areas with the strongest influence were the right superior frontal followed by the right medial orbitofrontal. We also computed the measure $1 - \frac{PAC_{AD}}{PAC_{HC}}$ to determine the areas that changed more between HC and AD. **Figure 8C** shows the areas for which the influence on PAC was stronger in HC than in AD, whereas **Figure 8D** displays the opposite case. We obtained that the influence of the right precentral and right superior parietal areas decreased in AD as compared to HC, whereas the influence of the right amygdala increased.

We also extracted all possible shortest paths [38] in the HC and AD brain networks, and computed the average ΔPAC of the areas involved in those paths. We found that the ΔPAC pathway *right superior frontal-right medial orbitofrontal-left superior frontal* presented the strongest ΔPAC in both HC and

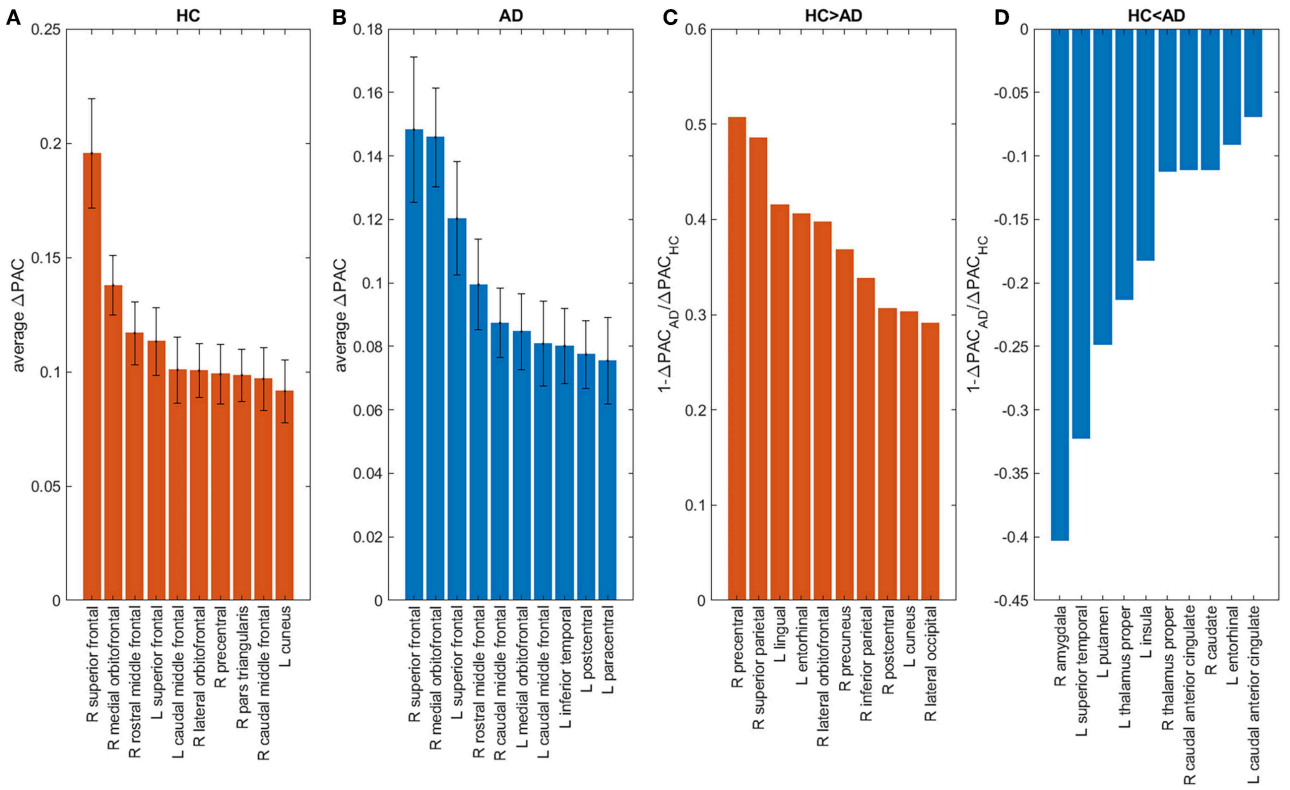

FIGURE 8 | Influence of brain areas on PAC: areas that when removed from the network change PAC the most in HC **(A)**, AD **(B)**. Areas for which the change was larger in HC (AD) than in AD (HC) appear in panels **(C,D)**. "L" and "R" denote left and right hemispheres, respectively.

AD groups (red path in **Figure 9**). On the other hand, the ΔPAC pathway that increased the most during AD was *left insula-left pars opercularis-left superior temporal* (green in **Figure 9**), whereas the PAC route that decreased the most in AD was *right precentral-right paracentral-right precuneus* (cyan in **Figure 9**). This clearly demonstrates an interhemispheric difference in PAC generation during AD.

Here, we also looked at how the scores of two customarily-used cognitive tests are related to the flow of information in AD networks as reflected by PAC. The individual clinical diagnoses assigned by the ADNI experts and used to define the HC and AD groups were based on multiple clinical evaluations [41]. The first test was the Clinical Dementia Rating Sum of Boxes (CDRSB), which provides a global rating of dementia severity through interviews on different aspects [41, 42]. An algorithm conduces to a score in each of the domain boxes, which are later summed. The final score ranges from 0 to 18, with a 0-value meaning "Normal." CDRSB is a gold standard for the assessment of functional impairment [41]. The second test was the Functional Activities Questionnaire (FAQ), where an informant is asked to rate the subject's ability to perform 10 different activities of daily living [43]. The total score ranges from 0 (independent) to 30 (dependent).

For each brain area the linear fit between ΔPAC and CDRSB, and ΔPAC and FAQ was computed. **Figure 10** shows the linear fits in the left y-axis (colored in blue) corresponding to the regions with the strongest correlations. For the case of CDRSB, the brain areas were left middle temporal ($r = 0.61$, $p = 0.0005$), left inferior temporal ($r = 0.53$, $p = 0.004$), and right middle temporal ($r = 0.40$, $p = 0.032$), whereas for the case of FAQ, the left middle temporal ($r = 0.55$, $p = 0.002$), left inferior temporal ($r = 0.47$, $p = 0.011$) were obtained again, with the appearance of the left pars orbitalis ($r = 0.36$, $p = 0.056$) among the top-three now.

We also performed a linear fit for the two cognitive test and the strength of each area (defined as the sum of all the connections associated with area i, $s_i = \sum_{j=1}^{N} w_{ij}$). The results are displayed in the right axis (colored in red) of every panel in **Figure 10**. We obtained the best fits for the same areas that resulted from using ΔPAC. The above-mentioned result is expected since PAC is obtained as a result of the movement of the random walkers on top of the matrices $\boldsymbol{W}$. However, the correlation values obtained were smaller and statistically significant only in two out of the six cases: the CDRSB test with the strength of left middle temporal ($r = 0.42$, $p = 0.0028$) and left inferior temporal ($r = 0.49$, $p = 0.008$) areas. The correlation between CDRSB and the right middle temporal area ($r = 0.23$, $p = 0.237$) was not significant, and neither were the correlations between the three areas and the FAQ test: left middle temporal ($r = 0.31$, $p = 0.109$), left inferior temporal ($r = 0.34$, $p = 0.077$), left

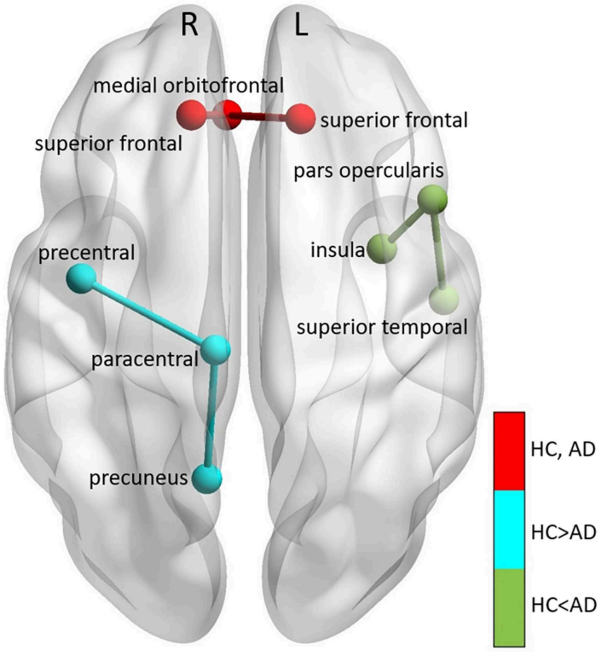

FIGURE 9 | Main PAC paths in HC and AD. Three main paths were found: (1) *right superior frontal-right medial or bitofrontal-left superior frontal* corresponding to the strongest PAC in HC, remaining also the strongest in AD (colored in red), (2) *left insula-left pars opercularis-left superior temporal,* the path that decreased the most in AD compared to HC (colored in cyan), and (3) *right precentral-right paracentral-right precuneus*, which increased the most in AD compared to HC (colored in green). "L" and "R" denote left and right hemispheres, respectively.

pars orbitalis ($r = -0.16$, $p = 0.411$). These results suggest the existence of a relationship between cognitive impairment, functional decline and behavioral symptoms that characterize AD and the perturbations to the information flow in brain networks, as characterized by cross-frequency interactions and not by broadband interactions (functional connectivity).

DISCUSSION

In summary, we employed random walkers to sample the spatial structure of complex networks and converted their movement into time series. To estimate the different temporal scales, these time series were further decomposed into intrinsic mode functions, or IMFs by means of the EMD technique [10]. Expressed in IMFs, the temporal scales have well-behaved Hilbert transforms [10], from which the instantaneous phases and amplitudes can be calculated. Another advantage of using EMD is that it is an adaptive and data-driven method that does not require prior knowledge on the number of temporal modes embedded into the time series. The interaction between IMFs, or CFS, was analyzed, obtaining that cross-frequency interactions were stronger in SF than in ER networks, especially for the case of PAC. SF networks presented strong PAC between slow and high frequency components of the information flow, whereas ER networks presented the strongest PAC between slow-frequency components. Since EMD acts essentially as a dyadic filter bank [44], some overlapping between consecutive IMFs is expected, which can result in strong CFC. This phenomenon can be seen in **Supplementary Figure 1** for the cases of PAC (interaction between the phase of IMF7 and the amplitude of IMF6), AAC (interaction between the amplitudes of IMF2 and IMF1), and PPC (interaction between the phases of IMF2 and IMF1). When filtering the data using non-overlapping bands (**Supplementary Figure 2**) the strength of these couplings decreased, but the CFC patterns, specifically the strong PAC connection between slow phases (IMFs 5–7) and fast frequencies (IMF1), was preserved, supporting the use of EMD in our analysis.

The temporal architectures of complex networks, and specifically of the human brain, have been topics of increasing interest in the past decade [45]. Dynamic functional connectivity studies have demonstrated that brain networks are not stationary but fluctuate over time [46, 47]. To study these dynamic networks, multi-layer network models are commonly employed [48–50]. These models treat the network at each time point as a layer [51]. Alternatively, each layer in the multi-layer network can be linked to a different frequency component [52]. The multi-layer network framework have been used to study the cross-frequency interactions in functional networks estimated from magnetoencephalographic (MEG) data [49]. However, these studies did not establish a link between the multiplex network and the information flow in the brain. This has been done recently for general multilayer networks by means of the so-called directed information measure [53], although cross-frequency interactions were not analyzed [54].

Given a complex network, it is of interest to determine which nodes contribute the most to CFC. We studied in more detail the generation of PAC between low (IMFs 5–7) and high (IMF1) frequencies and found that hubs, the most connected nodes in the network were not involved in the strongest PAC [with the exception of one super-hub [40]]. The most significant influence on PAC was exerted by a group of non-hubs, which connected with high probability to high degree nodes (**Figure 4**). This facilitated the generation of PAC [information flow from low to high frequencies [11]] since low and high degree nodes were generally associated with low and high frequencies, respectively. Our results are in agreement with recent work [55] studying the dynamic patterns of information flow in complex networks by means of a perturbative method. Interestingly, the authors found that the information flow preferred non-hubs and avoided centralized pathways. However, their study only reflected the broadband flow phenomena, i.e., unspecific and ignoring frequency interactions, unlike this work.

We applied our methodology to brain networks from HC subjects and AD patients and found that PAC activity between slow frequencies and IMF1 decreased during AD. The IMFs obtained from simulated ER and SF networks correspond to different oscillatory modes, with normalized frequencies (**Figures 1F,G**). In the case of brain networks, it is tempting to analyze the frequencies in Hz, in order to compare the frequency range of the different IMFs to the known frequency bands

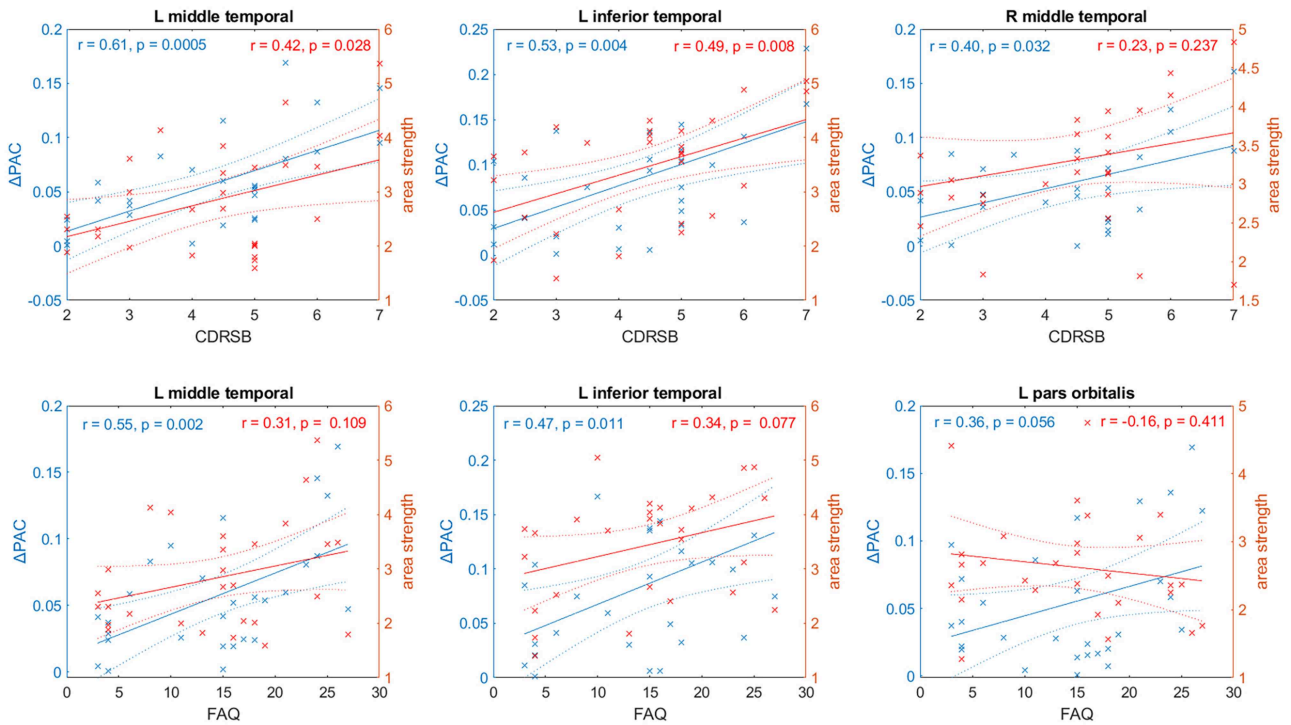

FIGURE 10 | Relationship between two cognitive tests– CDRSB and FAQ– and PAC (in blue) and values of the node strength (in red) for selected areas of the AD networks. Solid and dashed lines represent the linear fit and confidence intervals, respectively.

registered in the human brain. For this, we need to know the conduction delays for signals coming from different brain areas. Delays can range from a few milliseconds to several hundreds of milliseconds depending on the regions involved and the species considered [56–58]. Unfortunately, for the human brain, there is lack of information about conduction delays between all the combinations of areas, which makes the conversion to frequency units unfeasible at this time.

When analyzing the influence of specific brain areas, we found the right superior frontal and the right medial frontal to be the areas that contributed more to PAC in both HC and AD subjects. These areas belong to the default mode network (DMN), a collection of brain structures which intertwined activity increases in the absence of a task and has been associated with memory consolidation. The right superior frontal and the right medial frontal are also involved in the strongest PAC-based information flow pathway found in AD and HC: *right superior frontal-right medial orbitofrontal-left superior frontal*. The DMN is of interest to AD research given the amyloid deposits found in its regions [59, 60]. We also found that the influence of the right amygdala on PAC increased during AD (**Figure 6D**); the amygdala is known to be severely affected in AD [61].

Our results also demonstrated a marked interhemispheric difference in the generation of PAC, with areas within the left hemisphere being more correlated to the cognitive scores (**Figure 8**). Furthermore, the PAC pathway that decreased the most during AD consisted of left hemisphere areas only (*left insula-left pars opercularis-left superior temporal*), whereas the PAC pathway that increased the most in AD was formed by areas from the right hemisphere (*right precentral-right paracentral-right precuneus*). A tentative explanation is that the brain must enhance traffic over this specific pathway we have obtained to maintain at least a minimal information flow on the right hemisphere in AD. The interhemispheric functional disconnection suggested by our results has been previously reported in mild cognitive impairment and AD subjects [62–64], and has been associated with white matter degeneration [64].

One important challenge for the AD research field is the development of efficient biomarkers. Neuroimaging biomarkers in AD are based on brain signals such as MRI, fMRI, and Positron Emission Tomography (PET). For instance, there is a consistently reported decrease in resting-state functional connectivity in AD patients compared to HCs in the DMN [65]. However, when we correlated the strength of functional connections with the reported scores of two different cognitive tests usually employed to diagnose AD, only two areas (both from the DMN), the left middle temporal and left inferior temporal presented significant correlations (0.42 and 0.49, respectively, with $p < 0.05$) with one of the tests, the CDRSB. On the other hand, these two same areas presented significant and stronger correlations between PAC and both tests, the CDRSB ($r = 0.61, r = 0.53$) and FAQ ($r = 0.55, r = 0.47$). Additionally, the right middle temporal PAC presented a significant correlation ($r = 0.40$) with the CDRSB scores. These findings suggest that our PAC-based analysis could

be more sensitive to network changes induced by AD, when compared to the traditional utilization of functional connectivity values. Thus, there exists a potentially elevated clinical value of PAC as a useful biomarker for the disease. These results support the feasibility of translating network properties into functional predictions.

A limitation of our brain networks analysis was the use of the backbone obtained from HC subjects for the AD patients. By using the same backbone matrix, we assumed that the propagation of information at the large-scale via white matter fiber connections is approximately the same for both HC and AD. This assumption is supported by past studies that found that misfolded proteins deposition and structural atrophy patterns in neurodegeneration match with the structural and functional connectome patterns obtained for young healthy subjects [3, 66, 67]. Furthermore, a recent study [68] found that despite changes in the integrity of specific fiber tracts, white matter organization in AD is preserved, suggesting AD does not appear to alter the ability of the anatomical network to mediate pathology spread in AD. However, this is in contrast to prior reports of significant changes in network topology in AD vs. HC [69, 70]. These discrepancies have been attributed to dissimilar methodologies in the network construction such as edge thresholding, binarization, and inclusion of subcortical regions to network graphs [68]. In this paper, we have considered differences between the two groups in terms of the functional matrices only and acknowledge that some bias given by the anatomical backbone may exist.

DATA AVAILABILITY

All MRI and fMRI data used in this study were obtained from the Alzheimer's Disease Neuroimaging Initiative (ADNI) database (http://adni.loni.usc.edu). For researchers who meet the criteria for access to the data; access to the ADNI data is available through an online application, which can be submitted at the following link: http://adni.loni.usc.edu/data-samples/access-data/.

ETHICS STATEMENT

Data used in this article were obtained from the Alzheimer's Disease Neuroimaging Initiative (ADNI) database (adni.loni.usc.edu). The ADNI study was conducted according to Good Clinical Practice guidelines, the Declaration of Helsinki Principles, US 21CFR Part 50-Protection of Human Subjects, and Part 56-Institutional Review Boards, and pursuant to state and federal HIPAA regulations (adni.loni.usc.edu). Study subjects and/or authorized representatives gave written informed consent at the time of enrollment for sample collection and completed questionnaires approved by each participating sites Institutional Review Board.

AUTHOR CONTRIBUTIONS

RS conceived the project. RS, LS-R, MD, YI-M, and JS-B assisted with analysis and interpretation of data, and with writing and editing of the manuscript.

FUNDING

This work was partially supported by grant RGPIN-2015-05966 from the Natural Sciences and Engineering Research Council of Canada. Data collection and sharing for this project was funded by the Alzheimer's Disease Neuroimaging Initiative (ADNI) (National Institutes of Health Grant U01 AG024904) and DOD ADNI (Department of Defense award number W81XWH-12-2-0012). ADNI is funded by the National Institute on Aging, the National Institute of Biomedical Imaging and Bioengineering, and through generous contributions from the following: AbbVie, Alzheimer's Association; Alzheimer's Drug Discovery Foundation; Araclon Biotech; BioClinica, Inc.; Biogen; Bristol-Myers Squibb Company; CereSpir, Inc.; Eisai Inc.; Elan Pharmaceuticals, Inc.; Eli Lilly and Company; EuroImmun; F. Hoffmann-La Roche Ltd. and its affiliated company Genentech, Inc.; Fujirebio; GE Healthcare; IXICO Ltd.; Janssen Alzheimer Immunotherapy Research & Development, LLC.; Johnson & Johnson Pharmaceutical Research & Development LLC.; Lumosity; Lundbeck; Merck and Co., Inc.; Meso Scale Diagnostics, LLC.; NeuroRx Research; Neurotrack Technologies; Novartis Pharmaceuticals Corporation; Pfizer Inc.; Piramal Imaging; Servier; Takeda Pharmaceutical Company; and Transition Therapeutics. The Canadian Institutes of Health Research is providing funds to support ADNI clinical sites in Canada. Private sector contributions are facilitated by the Foundation for the National Institutes of Health (www.fnih.org). The grantee organization is the Northern California Institute for Research and Education, and the study is coordinated by the Alzheimer's Disease Cooperative Study at the University of California, San Diego. ADNI data are disseminated by the Laboratory for Neuro Imaging at the University of Southern California.

SUPPLEMENTARY MATERIAL

The Supplementary Material for this article can be found online at: https://www.frontiersin.org/articles/10.3389/fphy.2019.00107/full#supplementary-material

REFERENCES

1. Gallos LK, Song C, Havlin S, Makse HA. Scaling theory of transport in complex biological networks. *Proc Natl Acad Sci USA*. (2007) **104**:7746–51. doi: 10.1073/pnas.0700250104
2. Gfeller D, De Los Rios P, Caflisch A, Rao F. Complex network analysis of free-energy landscapes. *Proc Natl Acad Sci USA*. (2007) **104**:1817–22. doi: 10.1073/pnas.0608099104
3. Raj A, Kuceyeski A, Weiner M. A network diffusion model of disease progression in dementia. *Neuron*. (2012) **73**:1204–15. doi: 10.1016/j.neuron.2011.12.040
4. Simonsen I, Astrup Eriksen K, Maslov S, Sneppen K. Diffusion on complex networks: a way to probe their large-scale topological structures. *Physica A*. (2004) **336**:163–73. doi: 10.1016/j.physa.2004.01.021
5. Pearson K. The problem of the random walk. *Nature*. (1905) **72**:294. doi: 10.1038/072294b0

6. Bonaventura M, Nicosia V, Latora V. Characteristic times of biased random walks on complex networks. *Phys Rev E.* (2014) **89**:012803. doi: 10.1103/PhysRevE.89.012803
7. Noh JD, Rieger H. Random walks on complex networks. *Phys Rev Lett.* (2004) **92**:118701. doi: 10.1103/PhysRevLett.92.118701
8. Noskowicz SH, Goldhirsch I. First-passage-time distribution in a random walk. *Phys Rev A.* (1990) **42**:2047–64. doi: 10.1103/PhysRevA.42.2047
9. Tejedor V, Bénichou O, Voituriez R. Global mean first-passage times of random walks on complex networks. *Phys Rev E.* (2009) **80**:065104. doi: 10.1103/PhysRevE.80.065104
10. Huang NE, Shen Z, Long SR, Wu MC, Shih HH, Zheng Q, et al. The empirical mode decomposition and the Hilbert spectrum for nonlinear and non-stationary time series analysis. *Proc R Soc A Math Phys Eng Sci.* (1998) **454**:903–95. doi: 10.1098/rspa.1998.0193
11. Sotero RC. Topology, cross-frequency, and same-frequency band interactions shape the generation of phase-amplitude coupling in a neural mass model of a cortical column. *PLoS Comput Biol.* (2016) **12**:e1005180. doi: 10.1371/journal.pcbi.1005180
12. Sotero RC. Modeling the generation of phase-amplitude coupling in cortical circuits: from detailed networks to neural mass models. *Biomed Res Int.* (2015) **2015**:1–12. doi: 10.1155/2015/915606
13. Bruns A, Eckhorn R. Task-related coupling from high- to low-frequency signals among visual cortical areas in human subdural recordings. *Int J Psychophysiol.* (2004) **51**:97–116. doi: 10.1016/j.ijpsycho.2003.07.001
14. Lachaux J-P, Rodriguez E, Martinerie J, Varela FJ. Measuring phase synchrony in brain signals. *Hum Brain Mapp.* (1999) **8**:194–208. doi: 10.1002/(SICI)1097-0193(1999)8:4<194::AID-HBM4>3.0.CO;2-C
15. Erdös P, Rényi A. *On random graphs, I.* Debrecen: Publicationes Mathematicae, **6** (1959).
16. Barabasi A-L, Albert R. Emergence of scaling in random networks. *Science.* (1999) **286**:509–12. doi: 10.1126/science.286.5439.509
17. Barrat A, Barthelemy M, Vespignani A. *Dynamical Processes on Complex Networks. Cambridge: Cambridge University Press.* (2008). doi: 10.1017/CBO9780511791383
18. Taylor A, Higham DJ. CONTEST. *ACM Trans Math Softw.* (2009) **35**:1–17. doi: 10.1145/1462173.1462175
19. Sled JG, Zijdenbos AP, Evans AC. A nonparametric method for automatic correction of intensity nonuniformity in MRI data. *IEEE Trans Med Imaging.* (1998) **17**:87–97. doi: 10.1109/42.668698
20. Evans AC, Kamber M, Collins DL, MacDonald D. An MRI-based probabilistic atlas of neuroanatomy. In: Shorvon SD, Fish DR, Andermann F, Bydder GM, Stefan H, editors. *Magnetic Resonance Scanning and Epilepsy*. Boston, MA: Springer US (1994). p. 263–74. doi: 10.1007/978-1-4615-2546-2_48
21. Ashburner J. A fast diffeomorphic image registration algorithm. *Neuroimage.* (2007) **38**:95–113. doi: 10.1016/j.neuroimage.2007.07.007
22. Klein A, Tourville J. 101 labeled brain images and a consistent human cortical labeling protocol. *Front Neurosci.* (2012) **6**:171. doi: 10.3389/fnins.2012.00171
23. Iturria-Medina Y, Sotero RC, Canales-Rodriguez EJ, Aleman-Gomez Y, Melie-Garcia L. Studying the human brain anatomical network via diffusion-weighted MRI and Graph Theory. *Neuroimage.* (2008) **40**:1064–76. doi: 10.1016/j.neuroimage.2007.10.060
24. Tournier J-D, Yeh C-H, Calamante F, Cho K-H, Connelly A, Lin C-P. Resolving crossing fibres using constrained spherical deconvolution: validation using diffusion-weighted imaging phantom data. *Neuroimage.* (2008) **42**:617–25. doi: 10.1016/j.neuroimage.2008.05.002
25. Sotero RC, Trujillo-Barreto NJ, Iturria-Medina Y, Carbonell F, Jimenez JC. Realistically coupled neural mass models can generate EEG Rhythms. *Neural Comput.* (2007) **19**:478–512. doi: 10.1162/neco.2007.19.2.478
26. Hagmann P, Cammoun L, Gigandet X, Meuli R, Honey CJ, Wedeen VJ, et al. Mapping the structural core of human cerebral cortex. *PLoS Biol.* (2008) **6**:e159. doi: 10.1371/journal.pbio.0060159
27. Young MP. The organization of neural systems in the primate cerebral cortex. *Proc R Soc London Ser B Biol Sci.* (1993) **252**:13–8. doi: 10.1098/rspb.1993.0040
28. Yan C, Zang Y. DPARSF: a MATLAB toolbox for "pipeline" data analysis of resting-state fMRI. *Front Syst Neurosci.* (2010) **4**:13. doi: 10.3389/fnsys.2010.00013
29. Cao J, Wang X, Liu H, Alexandrakis G. Directional changes in information flow between human brain cortical regions after application of anodal transcranial direct current stimulation (tDCS) over Broca's area. *Biomed Opt Express.* (2018) **9**:5296–317. doi: 10.1364/BOE.9.005296
30. Yanagawa T, Chao ZC, Hasegawa N, Fujii N. Large-scale information flow in conscious and unconscious states: an ECoG study in monkeys. *PLoS ONE.* (2013) **8**:e80845. doi: 10.1371/journal.pone.0080845
31. Zhang Z, Shan T, Chen G. Random walks on weighted networks. *Phys Rev E.* (2013) **87**:012112. doi: 10.1103/PhysRevE.87.012112
32. Wu Z, Huang NE. Ensemble empirical mode decomposition: a noise-assisted data analysis method. *Adv Adapt Data Anal.* (2009) **01**:1–41. doi: 10.1142/S1793536909000047
33. Colominas MA, Schlotthauer G, Torres ME. Improved complete ensemble EMD: a suitable tool for biomedical signal processing. *Biomed Signal Process Control.* (2014) **14**:19–29. doi: 10.1016/j.bspc.2014.06.009
34. Sotero RC, Bortel A, Naaman S, Mocanu VM, Kropf P, Villeneuve M, et al. Laminar distribution of phase-amplitude coupling of spontaneous current sources and sinks. *Front Neurosci.* (2015) **9**:454. doi: 10.3389/fnins.2015.00454
35. van Driel J, Cox R, Cohen MX. Phase-clustering bias in phase–amplitude cross-frequency coupling and its removal. *J Neurosci Methods.* (2015) **254**:60–72. doi: 10.1016/j.jneumeth.2015.07.014
36. Tass P, Rosenblum MG, Weule J, Kurths J, Pikovsky A, Volkmann J, et al. Detection of n : m phase locking from noisy data: application to magnetoencephalography. *Phys Rev Lett.* (1998) **81**:3291–4. doi: 10.1103/PhysRevLett.81.3291
37. Benjamini Y, Hochberg Y. Controlling the false discovery rate: a practical and powerful approach to multiple testing. *J R Stat Soc Ser B.* (1995) **57**:289–300. doi: 10.1111/j.2517-6161.1995.tb02031.x
38. Rubinov M, Sporns O. Complex network measures of brain connectivity: uses and interpretations. *Neuroimage.* (2010) **52**:1059–69. doi: 10.1016/j.neuroimage.2009.10.003
39. Sporns O, Honey CJ, Kötter R. Identification and classification of hubs in brain networks. *PLoS ONE.* (2007) **2**:e1049. doi: 10.1371/journal.pone.0001049
40. Hao D, Ren C, Li C. Revisiting the variation of clustering coefficient of biological networks suggests new modular structure. *BMC Syst Biol.* (2012) **6**:34. doi: 10.1186/1752-0509-6-34
41. Defina PA, Moser RS, Glenn M, Lichtenstein JD, Fellus J. Alzheimer's disease clinical and research update for health care practitioners. *J Aging Res.* (2013) **2013**:207178. doi: 10.1155/2013/207178
42. Doody RS, Pavlik V, Massman P, Rountree S, Darby E, Chan W. Predicting progression of Alzheimer's disease. *Alzheimers Res Ther.* (2010) **2**:2. doi: 10.1186/alzrt25
43. Juva K, Mäkelä M, Erkinjuntti T, Sulkava R, Ylikoski R, Valvanne J, et al. Functional assessment scales in detecting dementia. *Age Ageing.* (1997) **26**:393–400. doi: 10.1093/ageing/26.5.393
44. Flandrin P, Rilling G, Goncalves P. Empirical mode decomposition as a filter bank. *IEEE Signal Process Lett.* (2004) **11**:112–4. doi: 10.1109/LSP.2003.821662
45. Betzel RF, Bassett DS. Multi-scale brain networks. *Neuroimage.* (2017) **160**:73–83. doi: 10.1016/j.neuroimage.2016.11.006
46. Kundu S, Ming J, Pierce J, McDowell J, Guo Y. Estimating dynamic brain functional networks using multi-subject fMRI data. *Neuroimage.* (2018) **183**:635–49. doi: 10.1016/j.neuroimage.2018.07.045
47. Li X, Zang Y-F, Zhang H. Exploring dynamic brain functional networks using continuous "state-related" functional MRI. *Biomed Res Int.* (2015) **2015**:1–8. doi: 10.1155/2015/824710
48. Battiston F, Nicosia V, Chavez M, Latora V. Multilayer motif analysis of brain networks. *Chaos.* (2017) **27**:047404. doi: 10.1063/1.4979282
49. Brookes MJ, Tewarie PK, Hunt BAE, Robson SE, Gascoyne LE, Liddle EB, et al. A multi-layer network approach to MEG connectivity analysis. *Neuroimage.* (2016) **132**:425–38. doi: 10.1016/j.neuroimage.2016.02.045
50. Tewarie P, Hillebrand A, van Dijk BW, Stam CJ, O'Neill GC, Van Mieghem P, et al. Integrating cross-frequency and within band functional networks in resting-state MEG: a multi-layer network approach. *Neuroimage.* (2016) **142**:324–36. doi: 10.1016/j.neuroimage.2016.07.057
51. De Domenico M, Solé-Ribalta A, Cozzo E, Kivelä M, Moreno Y, Porter MA, et al. Mathematical formulation of multilayer networks. *Phys Rev X.* (2013) **3**:041022. doi: 10.1103/PhysRevX.3.041022

52. De Domenico M, Sasai S, Arenas A. Mapping multiplex hubs in human functional brain networks. *Front Neurosci.* (2016) **10**:326. doi: 10.3389/fnins.2016.00326
53. Kontoyiannis I, Skoularidou M. Estimating the directed information and testing for causality. *IEEE Trans Inf Theory.* (2016) **62**:6053–67. doi: 10.1109/TIT.2016.2604842
54. Guler B, Yener A, Swami A. Learning causal information flow structures in multi-layer networks. In: *2016 IEEE Global Conference on Signal and Information Processing (GlobalSIP)*. Washington, DC: IEEE (2016). p. 1340–4. doi: 10.1109/GlobalSIP.2016.7906059
55. Harush U, Barzel B. Dynamic patterns of information flow in complex networks. *Nat Commun.* (2017) **8**:2181. doi: 10.1038/s41467-017-01916-3
56. Aboitiz F, López J, Montiel J. Long distance communication in the human brain: timing constraints for inter-hemispheric synchrony and the origin of brain lateralization. *Biol Res.* (2003) **36**:89–99. doi: 10.4067/S0716-97602003000100007
57. Budd JML, Kisvárday ZF. Communication and wiring in the cortical connectome. *Front Neuroanat.* (2012) **6**:42. doi: 10.3389/fnana.2012.00042
58. Stoelzel CR, Bereshpolova Y, Alonso J-M, Swadlow HA. Axonal conduction delays, brain state, and corticogeniculate communication. *J Neurosci.* (2017) **37**:6342–58. doi: 10.1523/JNEUROSCI.0444-17.2017
59. Sheline YI, Raichle ME, Snyder AZ, Morris JC, Head D, Wang S, et al. Amyloid plaques disrupt resting state default mode network connectivity in cognitively normal elderly. *Biol Psychiatry.* (2010) **67**:584–7. doi: 10.1016/j.biopsych.2009.08.024
60. Sperling RA, Laviolette PS, O'Keefe K, O'Brien J, Rentz DM, Pihlajamaki M, et al. Amyloid deposition is associated with impaired default network function in older persons without dementia. *Neuron.* (2009) **63**:178–88. doi: 10.1016/j.neuron.2009.07.003
61. Poulin SP, Dautoff R, Morris JC, Feldman Barrett L, Dickerson BC. Amygdala atrophy is prominent in early Alzheimer's disease and relates to symptom severity on behalf of the Alzheimer's Disease Neuroimaging Initiative. *Psychiatry Res.* (2011) **194**:7–13. doi: 10.1016/j.pscychresns.2011.06.014
62. Korolev I, Bozoki A, Majumdar S, Berger K, Zhu D. Alzheimer's disease reduces inter-hemispheric hippocampal functional connectivity. *Alzheimers Dementia.* (2011) **7**:S739. doi: 10.1016/j.jalz.2011.05.2125
63. Qiu Y, Liu S, Hilal S, Loke YM, Ikram MK, Xu X, et al. Inter-hemispheric functional dysconnectivity mediates the association of corpus callosum degeneration with memory impairment in AD and amnestic MCI. *Sci Rep.* (2016) **6**:32573. doi: 10.1038/srep32573
64. Wang Z, Wang J, Zhang H, Mchugh R, Sun X, Li K, et al. Interhemispheric functional and structural disconnection in Alzheimer's disease: a combined resting-state fMRI and DTI study. *PLoS ONE.* (2015) **10**:e0126310. doi: 10.1371/journal.pone.0126310
65. Dennis EL, Thompson PM. Functional brain connectivity using fMRI in aging and Alzheimer's disease. *Neuropsychol Rev.* (2014) **24**:49–62. doi: 10.1007/s11065-014-9249-6
66. Iturria-Medina Y, Sotero RC, Toussaint PJ, Evans AC, Alzheimer's Disease Neuroimaging I. Epidemic spreading model to characterize misfolded proteins propagation in aging and associated neurodegenerative disorders. *PLoS Comput Biol.* (2014) **10**:e1003956. doi: 10.1371/journal.pcbi.1003956
67. Zeighami Y, Ulla M, Iturria-Medina Y, Dadar M, Zhang Y, Larcher KM-H, et al. Network structure of brain atrophy in *de novo* Parkinson's disease. *ELife.* (2015) **4**:1–20. doi: 10.7554/eLife.08440
68. Powell F, Tosun D, Sadeghi R, Weiner M, Raj A. Preserved structural network organization mediates pathology spread in Alzheimer's disease spectrum despite loss of white matter tract integrity. *J Alzheimers Dis.* (2018) **65**:747–64. doi: 10.3233/JAD-170798
69. Daianu M, Jahanshad N, Nir TM, Toga AW, Jack CR, Weiner MW, et al. Breakdown of brain connectivity between normal aging and Alzheimer's disease: a structural *k* -core network analysis. *Brain Connect.* (2013) **3**:407–22. doi: 10.1089/brain.2012.0137
70. Prescott JW, Guidon A, Doraiswamy PM, Roy Choudhury K, Liu C, Petrella JR, et al. The Alzheimer structural connectome: changes in cortical network topology with increased amyloid plaque burden. *Radiology.* (2014) **273**:175–84. doi: 10.1148/radiol.14132593

Conflict of Interest Statement: The authors declare that the research was conducted in the absence of any commercial or financial relationships that could be construed as a potential conflict of interest.

frontiers in Physics

ORIGINAL RESEARCH
published: 20 August 2019
doi: 10.3389/fphy.2019.00115

Characterization of Visuomotor/Imaginary Movements in EEG: An Information Theory and Complex Network Approach

Roman Baravalle[1], *Natalí Guisande*[1], *Mauro Granado*[1], *Osvaldo A. Rosso*[2,3]* *and Fernando Montani*[1]

[1] *Instituto de Física La Plata (IFLP), CONICET CCT-La Plata & Universidad Nacional de La Plata (UNLP), La Plata, Argentina,* [2] *Departamento de Informática en Salud, CONICET, Hospital Italiano de Buenos Aires, Buenos Aires, Argentina,* [3] *Instituto de Física, Universidade Federal de Alagoas, Maceió, Brazil*

Imagined activities could actually be a cognitive basis for creative thinking. However, it is still unknown how they might be related with the architecture of the brain. A recent study has proved the relevance of the imagined activity when investigating neuronal diseases by comparing variations in the neuronal activity of patients with brain diseases and healthy subjects. One important aspect of the scientific methodologies focused on neuronal diseases is therefore to provide a trustable methodology that could allow us to distinguish between realized and imagined activities in the brain. The electroencephalogram is the result of synchronized action of the cerebrum, and our end is portraying the network dynamics through the neuronal responses when the subjects perform visuomotor and specific imaginary assignments. We use a subtle information theoretical approach accounting for the time causality of the signal and the closeness centrality of the different nodes. More specifically we perform estimations of the probability distribution of the data associated to each node using the Bandt and Pompe approach to account for the causality of the electroencephalographic signals. We calculate the Jensen-Shannon distance across different nodes, and then we quantify how fast the information flow would be through a given node to other nodes computing the closeness centrality. We perform a statistical analysis to compare the closeness centrality considering the different rhythmic oscillation bands for each node taking into account imagined and visuomotor tasks. Our discoveries stress the pertinence of the alpha band while performing and distinguishing the specific imaginary or visuomotor assignments.

Keywords: neuronal dynamics, EEG, alpha oscillations, visuomotor tasks, imagined tasks

OPEN ACCESS

Edited by:
Chris G. Antonopoulos,
University of Essex, United Kingdom

Reviewed by:
Emanuela Formaggio,
University of Padova, Italy
Kelly Cristiane Iarosz,
University of São Paulo, Brazil

***Correspondence:**
Osvaldo A. Rosso
oarosso@gmail.com

Specialty section:
This article was submitted to Biophysics, a section of the journal Frontiers in Physics

Received: *12 March 2019*
Accepted: *31 July 2019*
Published: *20 August 2019*

Citation:
Baravalle R, Guisande N, Granado M, Rosso OA and Montani F (2019) Characterization of Visuomotor/Imaginary Movements in EEG: An Information Theory and Complex Network Approach. Front. Phys. 7:115. doi: 10.3389/fphy.2019.00115

1. INTRODUCTION

One of the principal assumptions in neuroscience is that the brain computes, and this is accepted by most scientists in the area. That is, the cerebrum takes approaching tangible information, encodes it into a few biophysical factors consisting of membrane voltage or neuronal activation costs, after which a wide variety of dynamic operations are played to extract applicable features of the input. The result is that some of these computations can be stored for later access and ultimately, to control

the behavior of the animal in the most convenient way. In addition, the brain processes sensory information in multiple stages in neural circuits. The information is transmitted through trains of action potential or less frequently by local field potentials (LFPs). More specifically for the action potentials, the information can also be transmitted through the counting of spikes, the temporal precision of them, the structure of the time series, the synchronization between groups of neurons, or some combination of these [1–11]. Thus, the brain does not have a single code but multiple which depend on multiple complex dynamic variables.

In particular, the scalp electroencephalogram (EEG), recorded by means of a given electrode, can be taken into consideration as a spatiotemporally smoothed version of the LFP that is incorporated over an area of 10 cm^2 or greater. Electroencephalography can accurately detect brain activity at a time resolution of a single millisecond [12]. This technique provides continuous recording of the brain's electrical processes which allows us to relate changes in signal with a particular cognitive task. It is conceivable to extract from the EEG the functional connectivity network. However, the elucidation of the inter-connectivity from sensor level recordings is not straightforward [13]. In this manner some endeavors to use convenient techniques on the time series dynamics recreated from scalp EEG signals can be found in the literature [14–17]. Network theory is usually based on graph theory, probability theory, statistical mechanics, and dynamical systems [14–28].

The brain is a large-scale complex network and discovering interdependencies between at least two EEG electrodes can be described utilizing a few methodologies [29]. Let us remark that the network analysis of EEG data can help us to gain a deeper understanding of the brain functions as finding the correct functional connectivity of the brain through EEG signal can be used as a biomarker to diagnose mental disorders [17, 30, 31]. Investigating the dynamics of the EEG signals complex network means to estimate the degree of correlation across the different temporal patterns for the different electrodes or nodes. Fluctuations of electrical activity registered by EEG show correlated neuronal activity [32]. The extent of oscillatory coupling between two EEG signals can be used as a measure of strength to reflect network activity of the brain. The human brain can be understood as a large-scale complex network [15, 33, 34], the topological properties of EEG-derived networks describe working memory phases [35], and variations in the path length connectivity across nodes can be linked with mental diseases [17, 31].

Methods of EEG analysis are based on the investigation of dynamic changes of electrical activity in time, frequency, and space. A straight methodology for assessing the associations is finding how comparable the signals' waveforms are of each frequency when a time-lag is used to one of them. This is evaluated through cross-correlation [30, 36, 37]. However, non-linear components of coupling can control the neuronal activity. In this way non-linear affinity measures ought to be considered to determine the brain complex network. Bandt and Pompe (BP) proposed a novel methodology that comprises in changing the signal, by means of a symbolic methodology, into a sequence of patterns and then making inference over them [38–40]. In view of the evaluation of the ordinal structures present in the time series and their neighborhood impact on the related probability density function they include the signals' own temporal causality through a methodology of simple application and direct estimation [38–42]. Thus, the BP approach permits us to find important causative data associated with the hidden non-linear variables that regulate the system. Statistical complexity measures are useful to quantify stochastic systems and to detect whether a system is not deterministic or random. The perfect order and the maximum randomness can be depicted all around effectively on the grounds that they do not have any structure and in the two cases the statistical complexity is zero. In any case, between these two limits there is a wide scope of ordinal structures of important stochastic nature. The complexity measure has been effectively utilized in perception and portrayal of various dynamical regimes [38–43]. The non-linear elements of the cerebrum are of dissipative nature, and subject to non-equilibrium conditions that describe the developing properties of the neurons and portray the conduct of the neuronal capacities. The Jensen-Shannon divergence, which evaluates the contrast between (at least two) probability distribution functions (PDFs), is particularly valuable to compare the symbol-composition of different sequences. Statistical complexity enables us to measure basic features about the dynamic of the PDF related to the EEG recorded activity [38–43]. This measure originally obtained from Information Theory enables us to evaluate the non-linear dynamics of the electro-cortical responses [38–43]. The statistical complexity is the result of two entropies, the Shannon entropy and Jensen–Shannon divergence, however it is a non-trivial mathematical relation of the entropy since it relies upon two probability functions, i.e., the one relating to the condition of the system and the uniform PDF taken as reference state. Essentially, in the present work we estimate the normalized Jensen-Shannon distance between two probabilities, however one comparing to the condition of the electrical activity in one electrode and the state PDF taken from another electrode as reference [44]. The aim of this study is to perform a discrimination of imagined [45] and non-imagined tasks through the application of the Jensen–Shannon divergence of the BP probabilities across different electrodes sites in combination with estimation of the closeness centrality of nodes. We conduct a statistical analysis to examine the closeness centrality for the different rhythmic oscillation bands and nodes, considering imagined and visuomotor tasks. Our current approach allows us to discriminate imagined and non-imagined tasks characterizing the most important nodes within a graph for the different rhythmic oscillation bands using a functional network based on the BP formalism and the Jensen–Shannon divergence.

2. METHODOLOGY

2.1. Time Series Analysis and Ordinal Patterns

Consider $\mathcal{X} \equiv \{x_t\}_{t=1}^{M}$ a time signal of length M, and at first, we expect that there are not equivalent abundance esteems in

the time signal, that is the probability $P(x_{t_1} = x_{t_2}) = 0 \; \forall \; t_1 \neq t_2$. Bandt and Pompe presented in their foundational paper an effective technique for the assessment of PDF related to a time signal utilizing a symbolization system [38]. For a point by point portrayal of the methodology we allude the reader to [46]. The significant symbolic descriptions are (i) made by ranking the magnitudes of the signal and (ii) characterized by reordering the symbols in upward order; this is similar to a state space reconstruction with embedding dimension D and time lag τ. Further subtleties portraying the focal points that make the BP system more helpful than regular techniques dependent on range dividing (i.e., PDF amplitude histograms) can be discovered in Olivares et al. [47, 48], Rosso et al. [49, 50], Rosso and Masoller [39, 40], Saco et al. [51], and Keller and Sinn [52]. The BP approach can be used for any kind of signals, and the main condition for the appropriateness of this procedure is a stationary hypothesis (that is, for $k \leq D$, the likelihood for $x_t < x_{t+k}$ ought not be conditional on t [38]). To utilize the Bandt and Pompe [38] procedure for assessing the PDF, P, related with the signal, one starts considering parcellings of the appropriate D-dimensional space that will "uncover" pertinent subtleties of the ordinal structure of a signal $\mathcal{X}(t) = \{x_t; t = 1, \cdots, M\}$ with $D > 1$ ($D \in \mathbb{N}$) and τ ($\tau \in \mathbb{N}$). Consider the "ordinal pattern" of order (length) D produced by $(s) \mapsto \left(x_{s-(D-1)\tau}, x_{s-(D-2)\tau}, \cdots, x_{s-\tau}, x_s\right)$, that gives to each time s the D-dimensional vector of magnitudes in instants $s, s-\tau, \cdots, s-(D-1)\tau$. Notice that when the $D-$value is greater, more data about the past are incorporated into our vectors. We designate "ordinal pattern" identified with the time (s) to the configuration $\pi = (r_0, r_1, \cdots, r_{D-1})$ of $[0, 1, \cdots, D-1]$ characterized by $x_{s-r_{D-1}\tau} \leq x_{s-r_{D-2}\tau} \leq \cdots \leq x_{s-r_1\tau} \leq x_{s-r_0\tau}$. Vitally, to get a one of a kind outcome we take $r_i < r_{i-1}$ if $x_{s-r_i} = x_{s-r_{i-1}}$. This can be warranted if the x_t comes from a continuous PDF, so similar magnitudes are unlikely. In this manner, for all the $D!$ conceivable configurations π of order D, their related relative frequencies can be determined by the occasions this specific arrangement is found in the signal divided by the full number of configurations:

$$p(\pi_i) = \frac{\sharp\{s | s \leq M - (D-1)\tau; \; (s) \;\; \texttt{is of kind} \, \pi_i\}}{M - (D-1)\tau} \, . \quad (1)$$

We allude the image $\sharp$ to "number." That is, an ordinal PDF $P = \{p(\pi_i), i = 1, \cdots, D!\}$ is obtained from the signal. In this way it is conceivable to measure the variety of the permutations of length D got from a scalar signal by estimating the Shannon Entropy and MPR statistical complexity. The embedding measurement D decides the quantity of possible states $D!$. The signal of length M that one needs so as to work with truthful estimators is $M \gg D!$ [49]. We wish to underline that Bandt and Pompe recommended working with $4 \leq D \leq 6$ and explicitly considered a delay $\tau = 1$ in their foundational paper [38]. Be that as it may, another estimation of τ can likewise generate extra knowledge [47, 48, 53–57].

3. THE JENSEN SHANNON DIVERGENCE

Entropy gives us an amount of incertitude and is the most representative case of the information quantifiers. For a PDF $f(x)$ with $x \in \Delta \subset \mathbb{R}$ and $\int_\Delta f(x) \, dx = 1$, we characterize the *Shannon Entropy* S [58] as

$$S[f] \; = \; - \int_\Delta f \, \log_2(f) \, dx \, . \quad (2)$$

In the discrete case, let be $\mathcal{X}(t) \equiv \{x_t; t = 1, \cdots, M\}$, a time series with M samples and the related PDF, given by $P \equiv \{p_j; j = 1, \cdots, N\}$ with $\sum_{j=1}^{N} p_j = 1$ and N the quantity of conceivable states of the examined physical system. Then, Shannon's logarithmic data measure [58] is characterized by

$$S[P] = - \sum_{j=1}^{N} p_j \log_2(p_j). \quad (3)$$

This quantity is equivalent to zero when we can anticipate with sureness which of the conceivable outcomes j, whose probabilities are given by $P_0 = \{p_{j^*} = 1 \; and \; p_j = 0, \; \forall j^* \neq j\}$, it will truly occur. So, in this condition we have maximum information about the hidden procedure. In contrast, this information is negligible for a uniform PDF $P_e = \{p_j = 1/N, \; \forall j = 1, \cdots, N\}$. Regarding the interpretation, the entropy of $P(X)$ indicates the base number of bits expected to encode the estimations of an arbitrary variable X with probability density function $P(X)$. The Shannon entropy S is a quantity of "global character" that is not extremely susceptible to high changes in the PDF that happens in a short zone. Nonetheless, it is essential to bring up that ordinal structures present in a signal are not evaluated by haphazardness or randomness measures.

Let us now consider a time series measured by a given electrode that can be represented by a symbolization alphabet to which we assign a probability distribution $Q = \{q_j, j = 1, \cdots, N\}$, and another electrode measures a different time series represented also by different symbols that were drawn from a different probability distribution, $P \equiv \{p_j; j = 1, \cdots, N\}$. The "cross-entropy" between Q and P is the Kullback-Leibler (KL) distance that is a very useful way to measure the difference between two probability distributions. The KL distance is

$$KL[P||Q] = - \sum_{j=1}^{N} p_j \log_2 \left(\frac{q_j}{p_j} \right) \, . \quad (4)$$

This can be rewritten as

$$KL[P||Q] = S[P, Q] - S[P]. \quad (5)$$

Thus the KL divergence represents the number of extra bits necessary to code a source whose symbols were drawn from the distribution P, given that the coder was designed for a source whose symbols were drawn from Q. Despite KL usually being referred as a distance measure between probability distributions,

Kullback–Leibler divergence is not a true metric as it does not have the property of symmetry.

On the other hand, Jensen–Shannon divergence enables us to quantify the similitude between two distributions and has been utilized in statistics and probability theory. The Jensen–Shannon divergence is defined as

$$JS(P||Q) = S[(P+Q)/2] - S[P]/2 - S[Q]/2. \quad (6)$$

It is based on the Kullback–Leibler divergence, with some remarkable and important differences: it is symmetric and always provides finite values.

The Jensen–Shannon divergence, which evaluates the distinction between PDFs, is very helpful to analyze the symbolic configuration between various symbolic messages [59]. As non-linear measures ought to be considered to decipher the brain complex network, a straightforward way to investigate this inter-connectivity is using BP formalism in combination with *JS* disparity (or distance). Let us now consider a time series measured by a given electrode in a brain area that can be represented by a BP symbolization alphabet with probability distribution Q and another electrode sited in another brain area and with different time series represented by probability distribution, P. If we estimate $JS(P||Q)$ a smaller *JS* implies greater interconnectivity between electrodes, and greater values of *JS* implies a lower inter-connectivity across them. Thus, the Jensen–Shannon measure in combination with the BP approach can provide us a novel quantification of the network inter-connectivity across EEG electrodes [44].

4. EEG DATASET

Our point in this section is to portray the interconnectivity of the EEG frequency bands when the subjects play out a visuomotor or imagined assignment. We have considered for the present investigation the EEG visuomotor Movement/Imagery Dataset recorded utilizing BCI2000 instrumentation accessible through Physionet [12, 41–43, 45, 60, 61]. **Figure 1** shows the experimental setup that comprises an arrangement of various utilized electrodes.

The experimental setup of the BCI2000 framework [12, 45] incorporates a set of 64 electrodes used to register the electrical

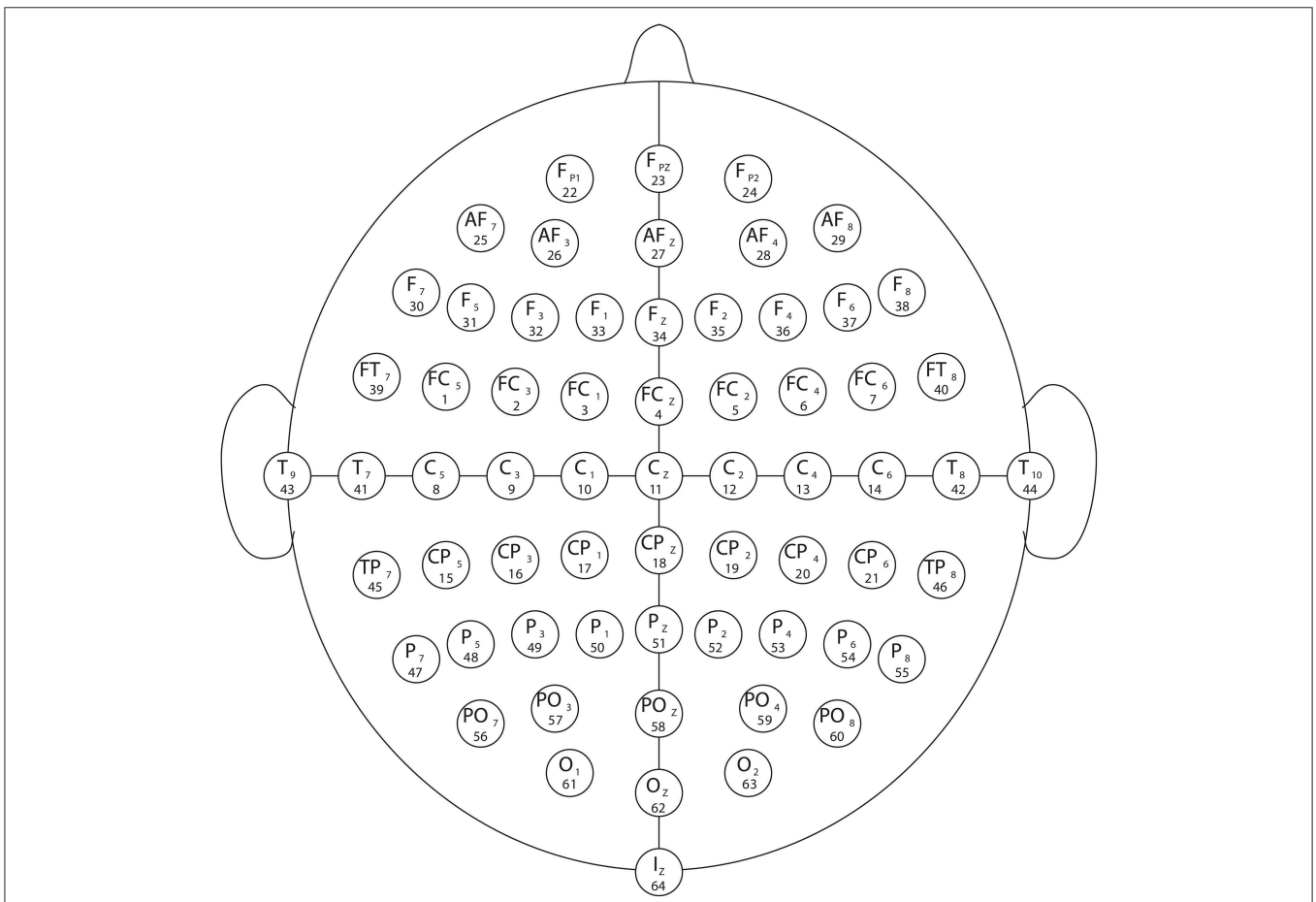

FIGURE 1 | Electrode arrangement as per the international 10–20 system (as in [12, 41–43, 45, 61–63]). The numbers below each electrode name indicate the order in which they appear in the recordings.

responses of the cerebrum through the EEG signals while the subjects perform diverse assignments of visuomotor or imaginary kinds [12, 41–43, 45, 61–63]. Each subject performed one of each of the four after assignments:

TABLE 1 | Frequency bands analyzed.

Band	Frequency interval (*Hz*)
Delta	[1, 4)
Theta	[4, 8)
Alpha 1	[8, 10)
Alpha 2	[10, 13)
Beta 1	[13, 18)
Beta 2	[18, 31)
Gamma 1	[31, 41)
Gamma 2	[41, 50)

1. An objective shows up on either the left or the right half of the screen. The subject opens and shuts the matching hand until the objective vanishes. At that point the subject unwinds.
2. An objective shows up on either the left or the right half of the screen. The subject envisions opening and shutting the matching hand until the objective vanishes. At that point the subject unwinds.
3. An objective shows up on either the upper or the lower half of the screen. The subject opens and closes either the two hands (if the objective is on the upper half) or the two feet (if the objective is on the base) until the objective vanishes. At that point the subject unwinds.
4. An objective shows up on either the upper or the lower half of the screen. The subject envisions opening and closing either the two hands (if the objective is on the upper half) or the two feet (if the objective is on

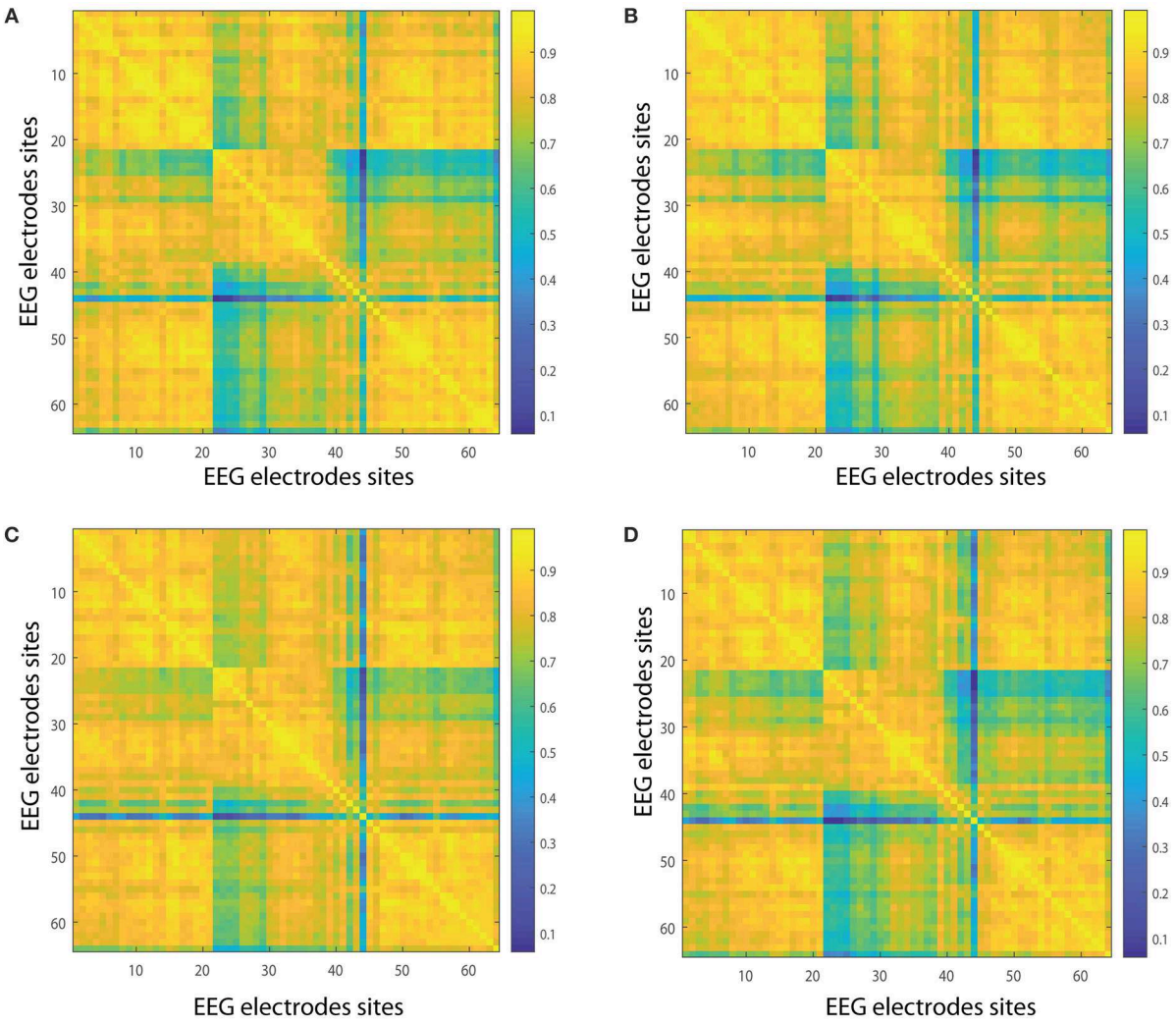

FIGURE 2 | Network interconnectivity. **(A,B)** Show the network averaged values of the interconnectivity considering 109 subjects when performing the visuomotor task for the 64-channel EEG considering the different oscillation bands delta and theta. **(C,D)** Are the same as **(A,B)** but considering the imagined task. We consider $D = 6$ and $\tau = 1$. Delta oscillation band corresponds to $[1, 4)Hz$ and theta oscillation band to $[4, 8)Hz$.

the base) until the objective vanishes. At that point the subject unwinds.

Eye blink artifacts were produced by quick motions of the eyelid along the cornea, for example, amid an eye squint. In any case, muscular artifacts were cautiously checked toward the start of each recording and confirmed all through the experiment [12, 45, 61–63]. Significantly, in our present investigation the muscular and technical artifacts were discarded following the methodology exhibited in Schalk et al. [12] and Schalk and Mellinger [45]. That is, a Common Average Reference (CAR) is carried out before artifact rejection as demonstrated in Schalk et al. [12] and Schalk and Mellinger [45].

Various oscillatory rhythms have been connected to various parts of perception that are very significant to see how actions are prepared in the human brain [12]. The EEG records the electrical activity of the brain that by a sensory incitement, or a visuomotor output, exhibits distinctive rhythms such as delta ($\in [1, 4)$ Hz), theta ($\in [4, 8)$ Hz), alpha ($\in [8, 13)$ Hz), beta ($\in [13, 31)$ Hz), and gamma (≥ 31 Hz).

For a detailed description of the study, the design of the experiment, group of subjects, the condition of the experiment used and the EEG equipment used for the measurements, we refer the reader to [12, 43, 45, 61–63]. The classic scenario where the subjects are performing the motor action using an event-related desynchronization (ERD) analysis is carefully described for the different oscillation bands by Kim et al. [64].

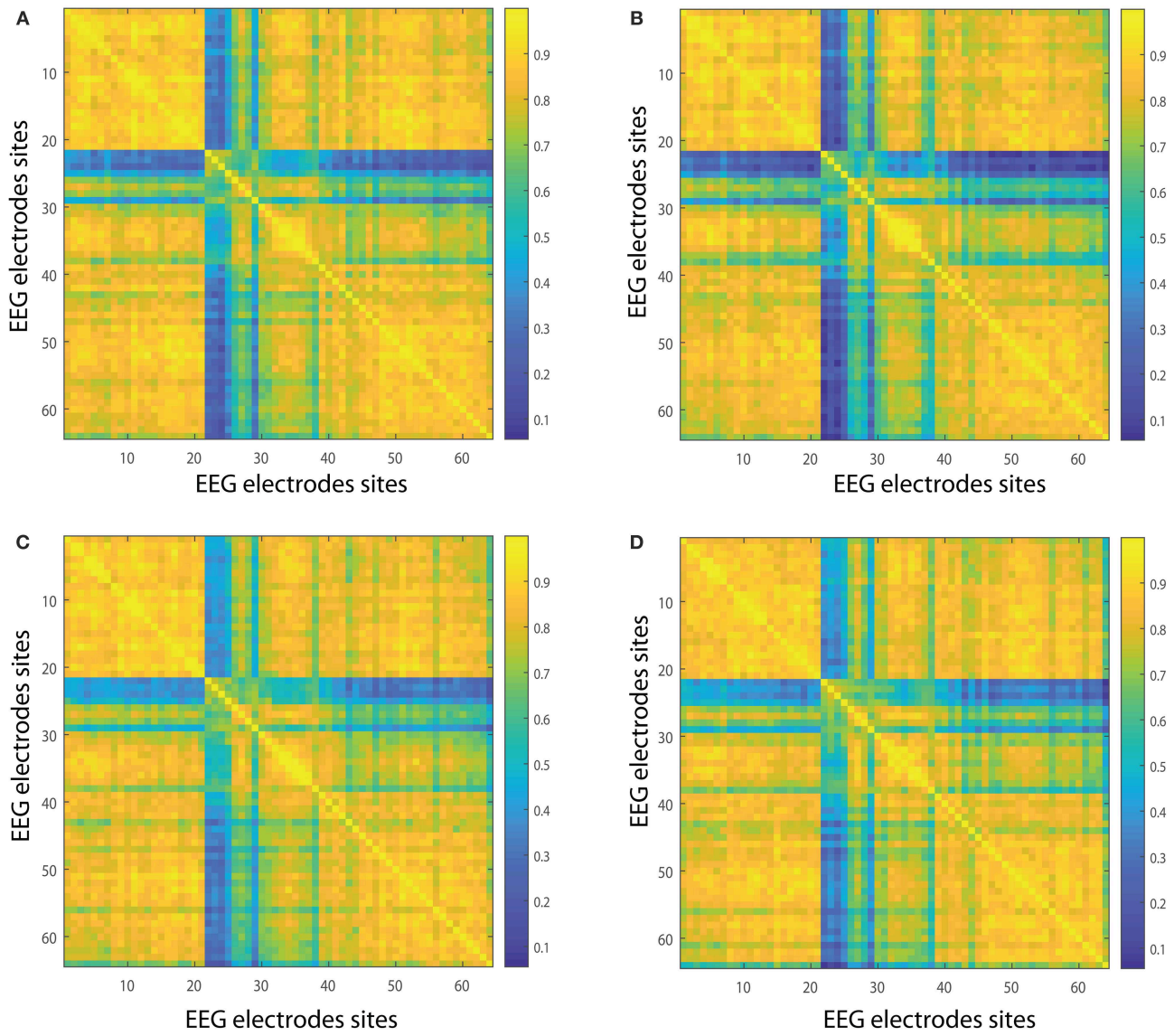

FIGURE 3 | Network interconnectivity. **(A,B)** Show the network averaged values of the interconnectivity considering 109 subjects when performing the visuomotor task for the 64-channel EEG considering the different oscillation bands alpha 1 and alpha 2. **(C,D)** Are the same as **(A,B)** but considering the imagined task. We consider $D = 6$ and $\tau = 1$. Alpha 1 oscillation band corresponds to $[8, 10)Hz$ and alpha 2 oscillation band to $[10, 13)Hz$.

For each subject and for each task we obtain the network, using the *BP* symbolization technique for each electrode and obtaining a weighted graph, with each weight given by the *JS* divergence, normalized by taking the maximum value between realized and imagined tasks. For completeness, we show an ERP signal of the current data in the **Supplemental Material**, and for further details we refer the reader to [43]). Specifically, we utilize the Kaiser filtering window created in Belitski et al. [65] to filter the raw signals for the diverse oscillation bands. The EEG are sampled at 160 *Hz*. But due to the high frequency artifacts that obscured the EEG, and to expel variances at DC level and increment the signal to noise ratio, the records where passed first through a filter between 1 and 50 Hz utilizing a filter created in Belitski et al. [65].

After this filtering, each EEG signal was decomposed, using the Kaiser filtering window created in Belitski et al. [65], in the frequency bands given in **Table 1**. For further insights regarding the filtering we allude the reader to [41].

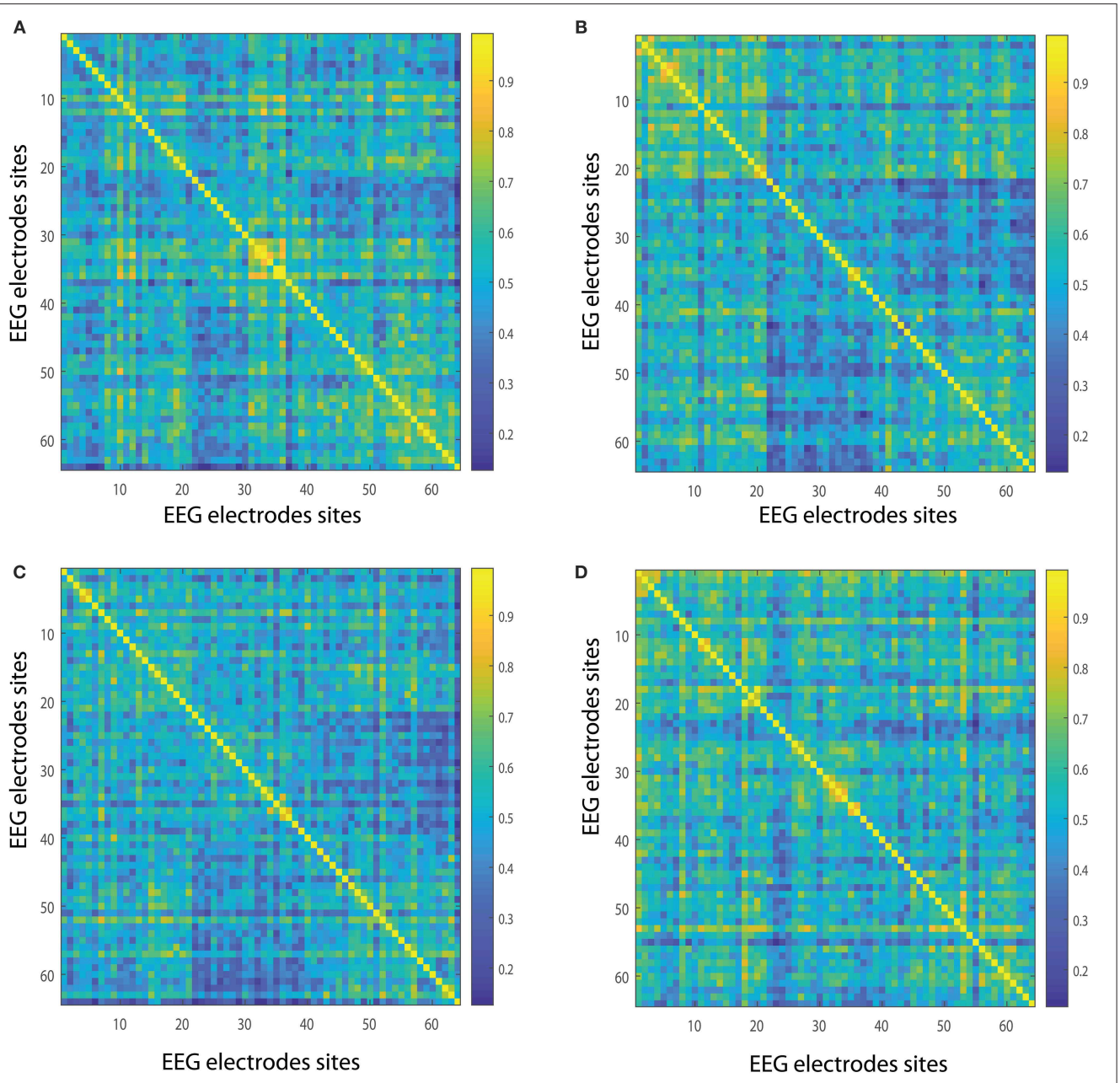

FIGURE 4 | Network interconnectivity. **(A,B)** Show the network averaged values of the interconnectivity considering 109 subjects when performing the visuomotor task for the 64-channel EEG considering the different oscillation bands beta 1 and beta 2. **(C,D)** Are the same as **(A,B)** but considering the imagined task. We consider $D = 6$ and $\tau = 1$. Beta 1 oscillation band corresponds to [13, 18)*Hz* and beta 2 oscillation band to [18, 31)*Hz*.

Networks are usually built considering different thresholds, and then graphs are constructed. This framework allows us to analyze the functional connectome of the brain. We describe the diverse network rhythmic activity of the brain as indicated by unmistakable visuomotor and imagery tasks using an information theory approach. The main idea of the current analysis is to gain a better understanding of situations in which a given oscillation band recruits specific brain networks for a given oscillation supporting a distinction between the forms identified with attention and development of imaginary movements. We estimate the degree of network interconnectivity as the normalized Jensen-Shannon distance JS between two probabilities: one corresponding to the state of the system in one electrode and the state distribution taken of another electrode as reference state, that is to say by estimating the normalized Jensen–Shannon distance between the BP probabilities across different electrodes sites as in Equation (6). We have normalized the Jensen–Shannon distance by taking the maximum value between realized and imagined tasks. Due to the length of time series we consider $D = 6$ and $\tau = 1$ for all BP estimations as in (Bandt and Pompe [38], Rosso and Masoller [39, 40], Baravalle et al. [41, 42]). So as to perform examinations inside the BP formalism, we have to meet the condition ($M \gg D!$); in this case we have 20,000 points for each case.

4.1. Centrality

Graph theory is the investigation of systems of interacting elements, which are structures used to pose pairwise and/or multiple relations between them [66]. A graph in this setting is comprised of nodes which are associated by edges. The centrality of a node in a system $\mathcal{C}$ is a measure of the basic importance of the node. While thinking about a graph, closeness centrality of a given node is a measure of centrality in a system and is evaluated as the quantity of nodes less one, $N - 1$, partitioned by the summation of the length of the shortest path between the node of interest and every single other node in the diagram.

That is

$$\mathcal{C}(i) = \frac{N-1}{\sum_j d(i,j)}, \tag{7}$$

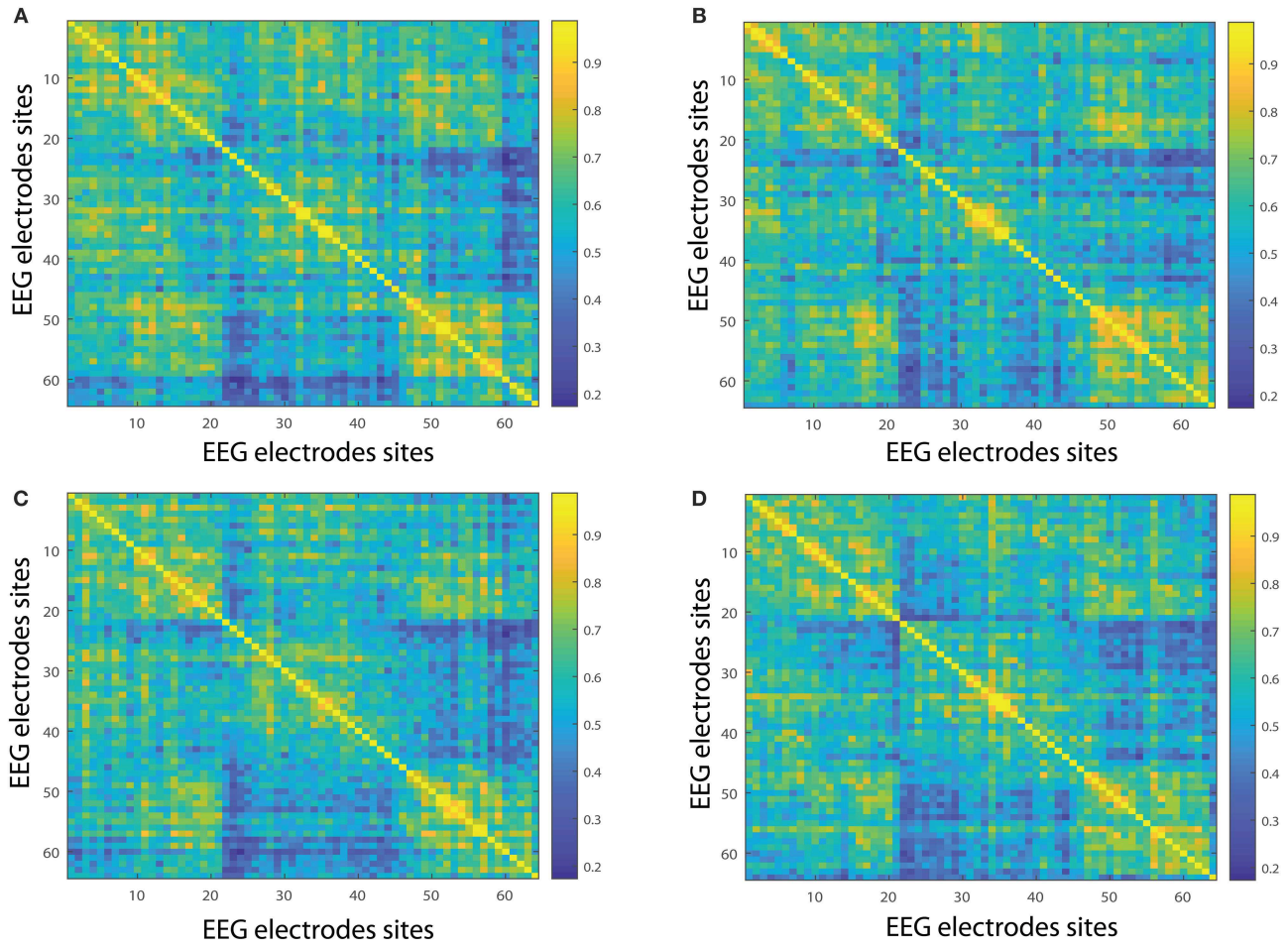

FIGURE 5 | Network interconnectivity. **(A,B)** Show the network averaged values of the interconnectivity considering 109 subjects when performing the visuomotor task for the 64-channel EEG considering the different oscillation bands alpha 1 and alpha 2. **(C,D)** Are the same as **(A,B)** but considering the imagined task. We consider $D = 6$ and $\tau = 1$. Gamma 1 oscillation band corresponds to $[31, 41)Hz$ and gamma 2 oscillation band to $[41, 50)Hz$.

where $d(j, i)$ is the separation between vertices i and j. Closeness centrality measures how short the shortest paths are from node i to all nodes, and we have 62 nodes in total because we exclude the two reference electrodes T_9 and T_{10}. We choose the closeness centrality because it is a helpful measure to estimate level of efficiency and convenience that gauges how quick the transmission of data would be through a given node all the available nodes [17, 67–72].

4.2. Statistical Analysis

As we mentioned previously, our objective is to focus on a better understanding of situations in which a given oscillation band recruits specific brain networks for a given oscillation supporting a distinction between the forms identified with attention and development of imaginary movements. In order to compare the closeness centrality for the different tasks, statistical tests are performed for each node. In consequence, we establish the following statistical analysis protocol for the obtained results of closeness centrality: (a) we first perform a t-test between imagined and realized tasks for each of the considered bands, and (b) in order to obtain a more accurate statistical test we also perform a false discovery rate (FDR) correction. We choose the Benjamini–Hochberg methodology at a specified FDR of 5% as in Benjamini and Hochberg [73] and Nielsen et al. [74].

5. RESULTS

In the following we show the analysis performed for the visuomotor task 1 and its corresponding imagined task 2. Our outcomes are equivalent for the visuomotor/imagery tasks 3 and 4. **Figures 2A,B**, **3A,B** display the mean of the interconnectivity for the 109 subjects when playing out the visuomotor assignment for the 64-channel EEG considering the diverse rhythms

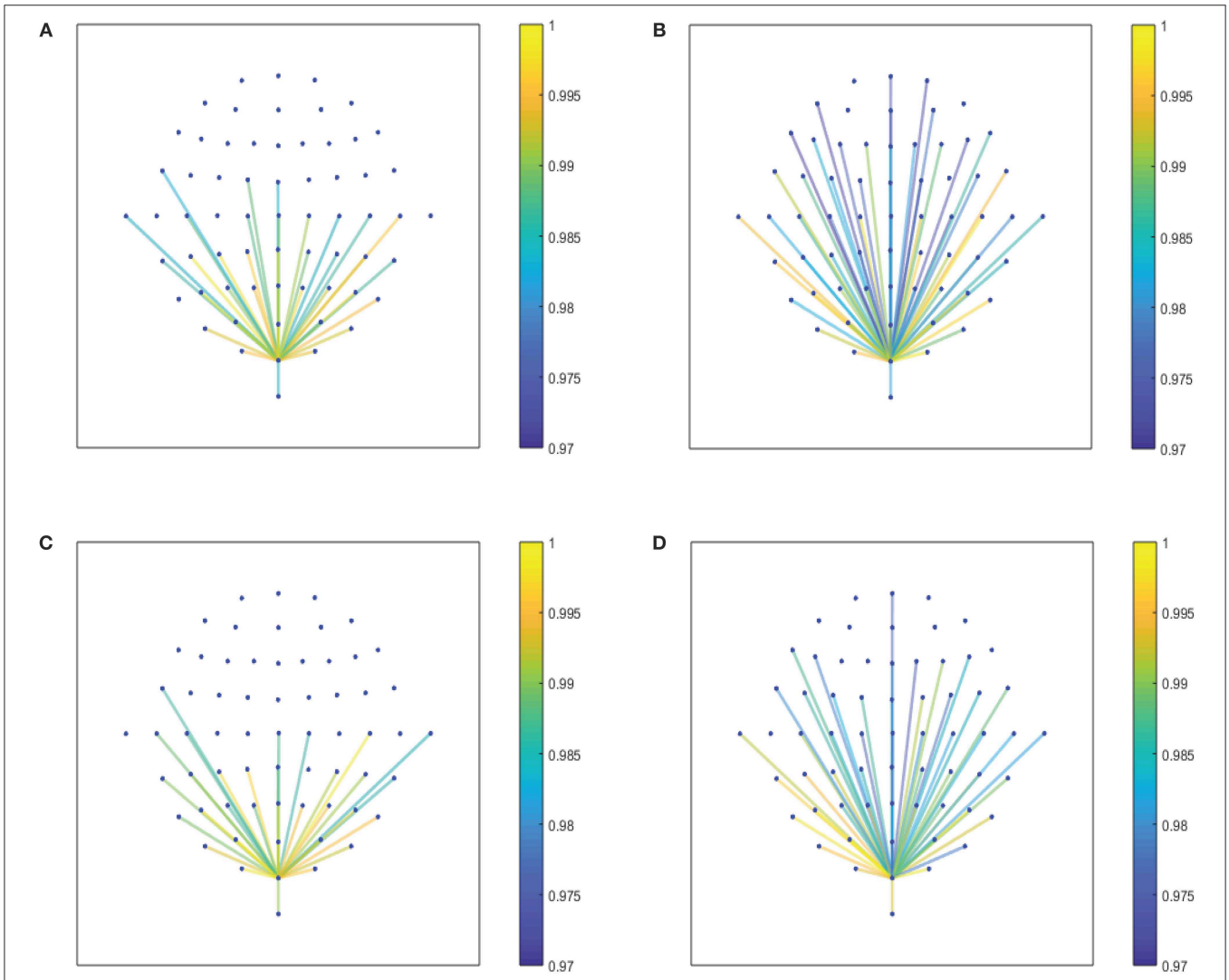

FIGURE 6 | (A,B) Show the node interconnectivity when considering the executed visuomotor task and taking the theta and alpha 1 band for the electrode Oz (or node) in the visual cortex. **(C,D)** Show the node interconnectivity when considering the imagined task. We consider $D = 6$ and $\tau = 1$.

delta, theta, alpha 1 and alpha 2. **Figures 2C,D**, **3C,D** are equivalent to **Figures 2A,B**, **3A,B** but performing the imagined task. **Figures 4A,B**, **5A,B** depict the network averaged values of the interconnectivity for performing the visuomotor task when considering the beta 1, beta 2, gamma 1 and gamma 2 bands, respectively. **Figures 4C,D**, **5C,D** are the same as in **Figures 4A,B**, **5A,B** but performing the imagined task. Small differences can be appreciated between the network of the realized and imagined tasks. Furthermore, **Figures 6A,B** show the node interconnectivity when considering the executed visuomotor task in view of the theta and alpha 1 bands for the electrode O_z (or node) in the visual cortex. **Figures 6C,D** show the node interconnectivity when considering the imagined task taking into account the same node in the visual cortex. **Figures 6A–D** depict also the averaged values considering 109 subjects. We can appreciate from the previous figures that there are differences in the network interconnectivity for the different conditions, however the current results are not quantifying how different the networks are. That is to say we can not infer from the previous figures which are the most relevant network structures. For completeness in the **Supplementary Material** we also include the analysis for all the other bands that are not being depicted in **Figure 6**.

In order to quantify the structural relevance of each node for the realized and imagined tasks, we investigate the closeness centrality of different nodes. **Figures 7A,B** show the closeness centrality $\mathcal{C}$, as in Equation (7), taking into account the average over 109 subjects for the 62-channel EEG considering the realized task when considering delta and theta, respectively. **Figures 7C,D**, are the same as in **Figures 7A,B** but performing the imagined task. Let us emphasize that **Figures 8A**, **9A** depict the closeness centrality $\mathcal{C}$ [as in Equation (7)] considering the alpha 1 and alpha 2 bands, respectively, taking into account the average over 109 subjects for the 62-channels EEG considering the realized task. **Figures 8B**, **9B** are the same as in **Figures 8A**, **9A** but executing the imagined task. **Figures 10A,B**, **11A,B** depict the closeness centrality $\mathcal{C}$ when realizing the visuomotor task considering the beta 1, beta 2, gamma 1 and gamma 2 bands, respectively. **Figures 10C,D**, **11C,D** are the same as in **Figures 10A,B**, **11A,B** but performing the imagined task. The electrodes T_9 and T_{10} have been excluded from the current analysis of the nodes centrality as they are reference electrodes [43].

In the case of the delta band, TP_7 showed the highest closeness centrality for imagined and realized tasks. While in the theta band FP_1, FP_z, and FP_2 depicted the highest centrality, both for both tasks. When considering the beta 1, the highest centrality is given by AF_8, T_8, O_2, and O_z for the realized task. In the case of the imagined task, beta 1 has the highest centrality for AF_7, AF_8, F_6, T_8, and O_z. Beta 2 depicted the highest centrality in AF_8 for the realized task and AF_7, AF_8 for the imagined task. Alpha 1 displays higher centrality for FP_1, FP_z, FP_2, F_7, F_6, FC_2, FC_4, C_4, and P_2 for the realized task. When considering the imagined task alpha 1 showed the highest centrality for the nodes FP_1, FP_2, AF_8, AF_3, F_3, F_2, FT_7, FC_3, FC_4, P_2, P_7, T_8, PO_4, O_z, and O_2. In contrast the highest centrality of the alpha 2 band is given by the nodes FP_z, FP_2, T_8, O_1, and O_z for the realized task. The highest centrality of the imagined task is given by FP_z, O_1, and PO_4 for alpha 2. Gamma 1 and gamma 2 presented the highest centrality in O_z, O_2, and T_z for the realized and imagined tasks. Overall, it is important to point out that delta, theta, beta and gamma bands show lower closeness centrality and therefore

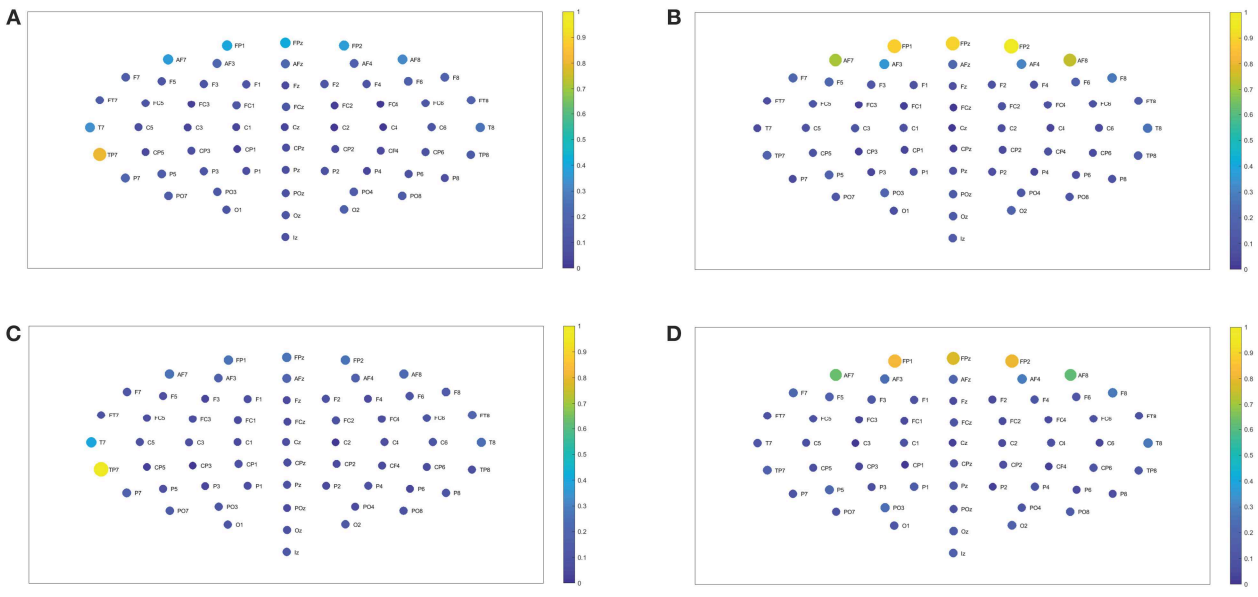

FIGURE 7 | Closeness centrality. **(A,B)** Show the nodes' closeness centrality considering 109 subjects when performing the visuomotor task for the 62-channels EEG considering the different oscillation bands delta and theta. **(C,D)** Are the same as **(A,B)** but considering the imagined task. We consider $D = 6$ and $\tau = 1$. Delta oscillation band corresponds to $[1, 4)Hz$ and theta oscillation band to $[4, 8)Hz$.

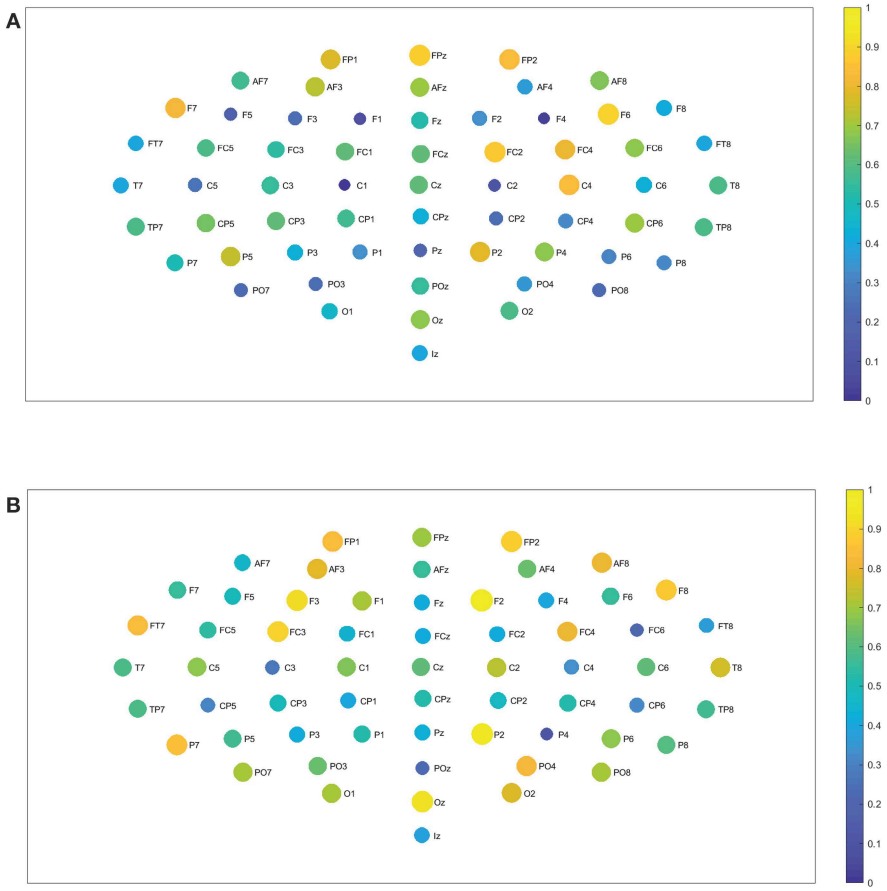

FIGURE 8 | Closeness centrality. **(A)** Shows the node closeness centrality considering 109 subjects when performing the visuomotor task for the 62-channels EEG considering the oscillation band alpha 1. **(B)** Is the same as **(A)** but considering the imagined task. We consider $D = 6$ and $\tau = 1$. Alpha 1 oscillation band corresponds to $[8, 10)Hz$.

depict a lower efficiency of the information of the data that could be transmitted through a given node to all the available nodes.

We find no significant differences between the realized and imagined tasks for most of the different bands, with the exception of the alpha 1 and alpha 2 bands that depict an unequal closeness centrality in several nodes of the network when comparing both tasks (see **Figures 8A,B**, **9A,B**). After performing the FDR correction we find no significant differences between realized and imagined tasks when considering the delta, theta, beta 1, beta 2, gamma 1 and gamma 2 bands. In the case of the alpha 1 band (see **Figures 8A,B**), as mentioned we first performed a t-test between imagined and realized tasks obtaining 26 sites with significant differences. After performing a FDR correction we find 17 nodes/sites that present significant differences between imagined and non-imagined tasks. The electrodes that accomplished both tests were FP_z, AF_8, F_7, F_8, F_3, F_2, F_6, FT_7, AF_z, FC_3, C_5, C_2, T_8, PO_7, PO_8, C_1, and O_z. In the case of alpha 2 (see **Figures 9A,B**) there were eight sites that showed significant differences when performing the t-test, and six electrodes presented significant differences when applying a FDR correction between tasks. The electrodes that accomplished both tests were T_8, TP_7, P_7, O_z, I_z, and PO_4. Finally, for completeness, **Figures 12A–C** depict the results of the closeness centrality derived from statistical comparison between realized and imagined tasks for all the significant nodes within alpha 1. **Figure 12D** shows all the significant nodes within the alpha 2 band. Let us emphasize that the estimation of the network closeness centrality played an ultimate role, as when we implemented other network measures they did not produce any quantifiable difference between realized and imagined tasks for the different analyzed bands. Here, a systematic method in which nodes are weighted by closeness centrality was proposed. We demonstrate how the combination of the estimation of the Jensen–Shannon divergence of the BP probabilities across different nodes encompassed with calculations of the nodes closeness centrality has significance to distinguish imagined from realized motor tasks. We found a higher degree of closeness centrality in the case of the imagined task when compared with the realized ones, looking upon the alpha band. Thus these results shows that imagined processes are linked to changes in the alpha levels of centrality of the different nodes in the brain. Overall we emphasize that the alpha 1 band shows a higher level of closeness centrality than the other bands,

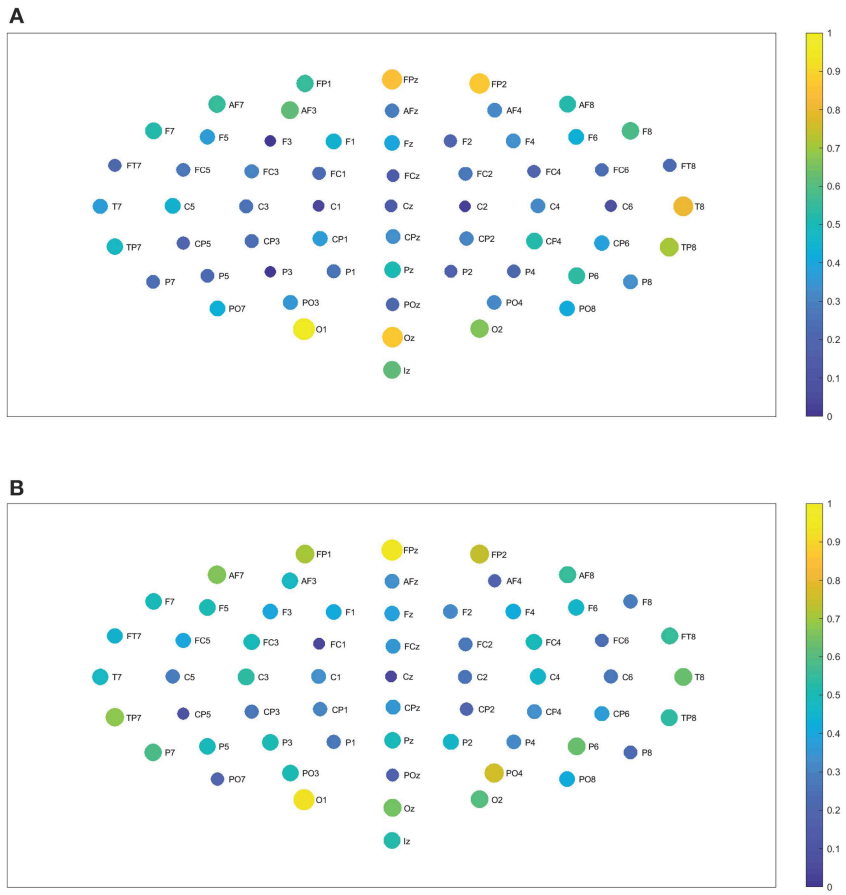

FIGURE 9 | Closeness centrality. **(A)** Shows the node closeness centrality considering 109 subjects when performing the visuomotor task for the 62-channels EEG considering the oscillation band alpha 2. **(B)** Is the same as **(A)** but considering the imagined task. We consider $D = 6$ and $\tau = 1$. Alpha 2 oscillation band corresponds to [10,13)*Hz*.

therefore it depicts a quicker level information flow from a given node to other nodes.

6. CONCLUSION AND DISCUSSIONS

Attention is a mechanism required for focusing on what is critical at each moment of time, while suppressing any unessential information. This mechanism is also required to perform mental imagery, activating the synchronized network of multiple areas of the brain [45]. This synchronized activity of many neurons communicating with one another generates brain waves [45]. Brain waves are rhythmic oscillation patterns that can be registered as macroscopic oscillations utilizing EEG sensors on the scalp. The descriptions are quite broad: delta rhythmic are related to sleep states; theta might be entrance to further understanding learning and memory; alpha is usually related to attention, lucid thinking and integration; beta is present during the state of alert and problem solving; and gamma rhythms modulate perception and consciousness [45]. Moreover, brain oscillation rhythms can provide hints about the network functionality during imagined and realized tasks. In our current study we have considered the causality of the EEG signals using the BP approach, and through a statistical analysis that combined the Jensen–Shannon distance with the estimation of the closeness centrality we estimate the level efficiency on data transmission for a given node to all the available nodes taking into account the different rhythmic oscillation bands. Our current results emphasize the relevance of the alpha 1 band when detecting nodes that spread information with different efficiency through the graph for realized and imagined tasks.

We propose an effective technique that enables us to determine quantitatively the amount of the node closeness centrality inside the diverse rhythms considering the causality of the EEG signals. So as to do it thus, we exactly evaluate the distinctive highlights of oscillatory patterns considering keen estimates representing the causal structure of the signal utilizing the BP procedure. More specifically, we estimate the network interconnectivity by estimating the normalized Jensen–Shannon distance between the BP probabilities across different nodes, quantifying the non-linear dynamics of the EEG signals. We choose thereafter to compute the closeness centrality because it is a helpful measure to estimate the level of efficiency and convenience that gauges how quick the transmission of data

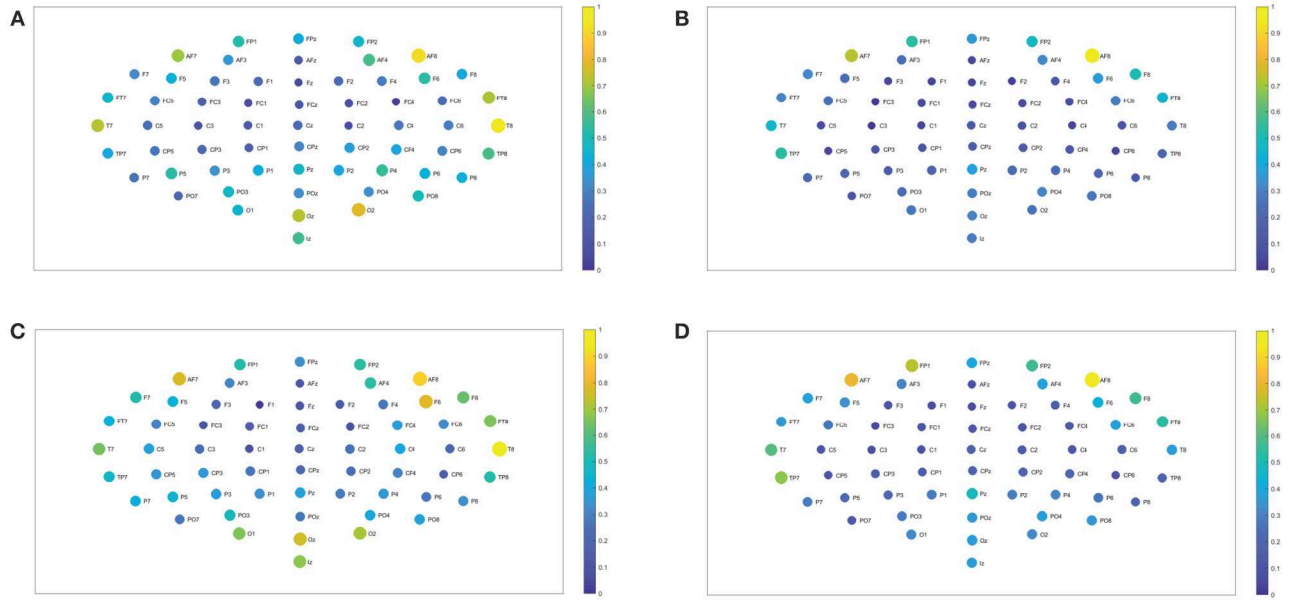

FIGURE 10 | Closeness centrality. **(A,B)** Show the nodes' closeness centrality considering 109 subjects when performing the visuomotor task for the 62-channels EEG considering the different oscillation bands beta 1 and beta 2. **(C,D)** Are the same as **(A,B)** but considering the imagined task. We consider $D = 6$ and $\tau = 1$. Beta 1 oscillation band corresponds to $[13, 18)Hz$ and beta 2 oscillation band to $[18, 31)Hz$.

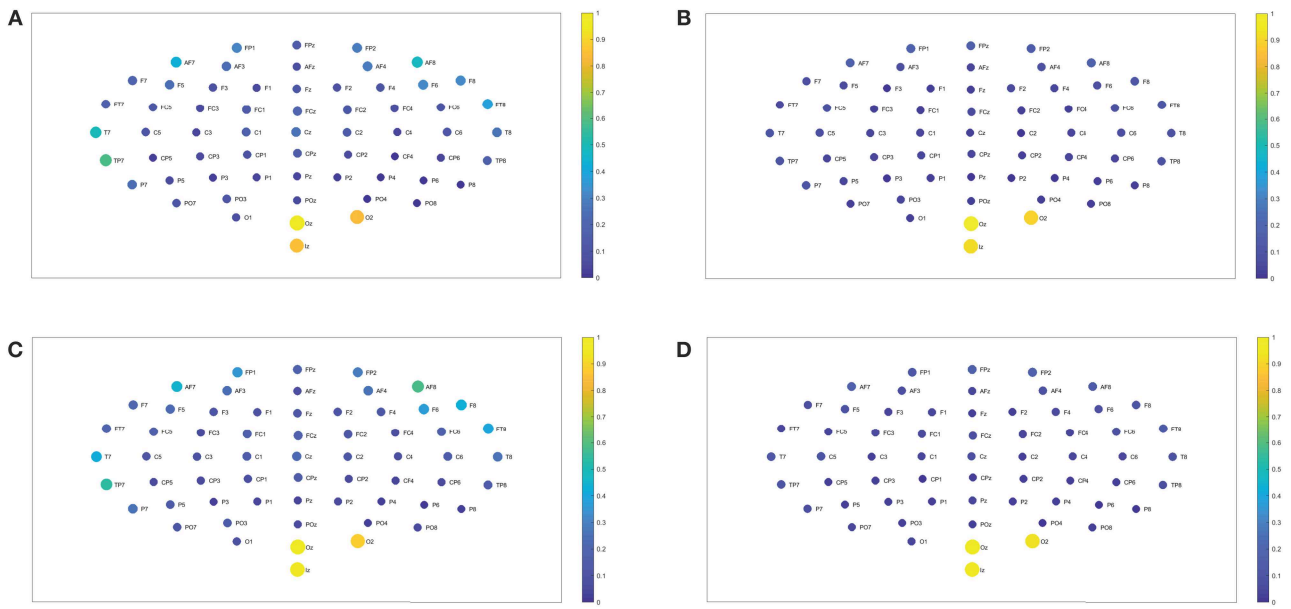

FIGURE 11 | Closeness centrality. **(A,B)** Show the nodes' centrality considering 109 subjects when performing the visuomotor task for the 62-channels EEG considering the different oscillation bands gamma 1 and gamma 2. **(C,D)** Are the same as **(A,B)** but considering the imagined task. We consider $D = 6$ and $\tau = 1$. Gamma 1 oscillation band corresponds to $[31, 41)Hz$ and gamma 2 oscillation band to $[41, 50)Hz$.

would be through a given node all the available nodes [67–72]. Our methodology enables us to characterize the "closeness centrality properties" of various nodes inside the EEG rhythms, considering the causality of the signal and gathering the rising dynamical properties of the diverse oscillation patterns of the brain while performing distinctive visuomotor or imagery tasks. That is to say in the current paper, we analyze EEG network organization through the closeness centrality to study how to discriminate imagined and non-imagined tasks for the different rhythmic oscillations, showing that the alpha 1

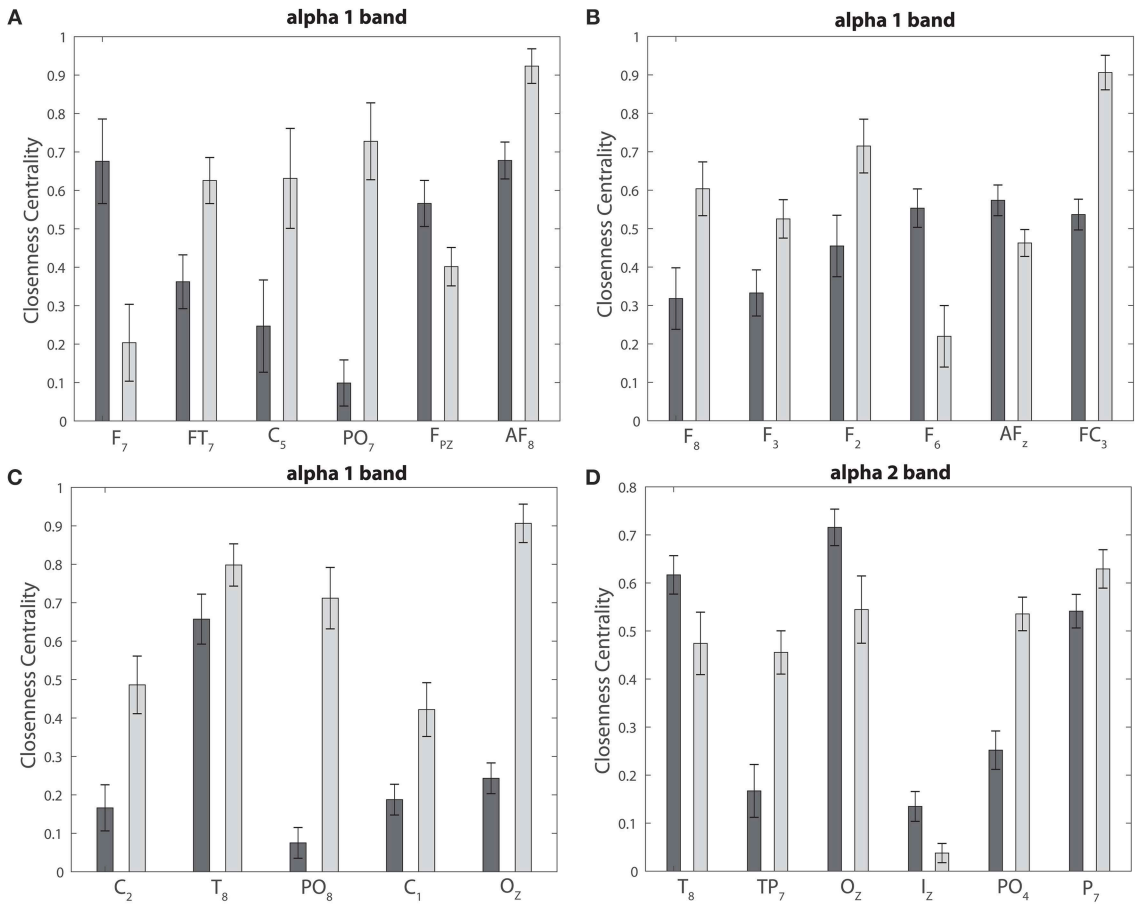

FIGURE 12 | Statistical comparison and closeness centrality. **(A–C)** Depict the closeness centrality for the realized and imagined tasks considering the significant nodes for the alpha 1 band. **(D)** Is the same as **(A–C)** but considering the alpha 2 band. In all cases: dark gray bars, realized task; light gray bars, imagined task.

bands allow us to discriminate between both assignments. Thus, we determine that the current approach combining the BP estimation with the Jensen-Shannon distance and the closeness centrality is a viable option for classification of hand realized and imagined signals.

It has been found that alpha frequency oscillations posses an important role in inhibitory control actions managing access of data of a cognition procedure and working memory [75–77]. Our findings show that several nodes within the gamma 1 band have an overall higher amount of closeness centrality during the imagined task in comparison to realized tasks. These higher amounts of centrality are located within the pre-motor, motor, and visual cortex areas. Thus, we can conclude that the imagined cognitive processes coincide with higher alpha 1 levels of closeness centrality of the different nodes. Our discoveries underscore the significance of the alpha band while taking part in cognitive tasks. That is in concurrence with strong proof that EEG alpha power is especially susceptible to different imagination-related requests, and that is happening due to creativity interventions [78]. We suggest that increased levels of centrality of several nodes for alpha 1 levels during the imaginative tasks might be important neurocognitive processes related to the internal attention required to perform mental imagery tasks.

As far as we can tell, there is still no ideal way to deal with the construction of a brain computer interphase (BCI) based on motor imagined tasks (MI-BCI, [79]). Specifically, features extraction and determination of relevant patterns and biomarkers for developing a successful MI-BCI are still under debate. Thus, it is extremely useful to investigate new methodologies that can offer a better understanding of how motor imagined patterns and connectivity differs from the non-imagined/realized activities. Recently, new research has investigated the possibility of taking measures that were originally developed in graph theory for data classification as they could provide important information about the connectivity [80]. In particular, a recent study has shown that graph metrics can be used for EEG-BCIs based on hand motor imagery graphs, as they are a feasible option for classification of hand motor imagined signals [81]. A recent study showed that the activity of the globulous pallidus is significantly reduced during imagined locomotion in patients with Parkinson disease when compared to healthy subjects [82]. Importantly the authors showed, using fMRI measures, that Parkinson disease patients displayed larger beta weights in the visuomotor zone amid

envisioned turning contrasted with forward or in reverse while controls did not, and that overground marching speed is associated with beta weights amid imagined marching in a few locomotor areas in patients with Parkinson disease and not in controls [82]. The early detection and diagnosis based on extracting features of the neuronal networks EEG topology thought imagined tasks can be of ultimate help for understanding brain functions and neuronal diseases. When one performs a network analysis, markers of closeness centrality allow us to find the most relevant vertices within a graph. Applications means identifying the most important structure of the neuronal network, therefore the main relevance of the nodes' centrality is identifying the different networks that might be related with neural diseases. The detection of those differences between realized and imagined features is a relevant highlight of the EEG topology that can be of assistance for inferring the brain functions. Moreover, we plan future related work to perform estimations of wavelet phase coherence to obtain the connectivity matrices for the different oscillations bands and to estimate the betweenness centrality across them to identify possible nodes that might mediate communication with the other nodes for the different imagined/realized tasks as performed in Makarov et al. [83]. We suggest that the current tool that combines a subtle information theoretical approach, representing the causality of the signal together with a quantification of the levels of centrality for the different nodes, can be very useful for early detection of neuronal diseases.

DATA AVAILABILITY

The datasets EEGMIDB for this study can be found in the physionet database. (https://archive.physionet.org/pn4/eegmmidb/).

AUTHOR CONTRIBUTIONS

Authors contributed equally in the design of this research as well as in the writing of this paper. All authors have read and approved the final manuscript.

FUNDING

We gratefully acknowledge PIP 11220130100327CO (2014/2016) CONICET, Argentina (FM) and Universidad Nacional de La Plata, Argentina (project 11/X812).

SUPPLEMENTARY MATERIAL

The Supplementary Material for this article can be found online at: https://www.frontiersin.org/articles/10.3389/fphy.2019.00115/full#supplementary-material

REFERENCES

1. Averbeck BB, Latham PE, Pouget A. Neural correlations, population coding and computation. *Nat Rev Neurosci*. (2006) **7**:358–66. doi: 10.1038/nrn1888
2. Panzeri S, Schultz SR, Treves A, Rolls ET. Correlations and the encoding of information in the nervous system. *Proc Biol Sci*. (1999) **266**:1001–12. doi: 10.1098/rspb.1999.0736
3. Panzeri S, Schultz SR. A unified approach to the study of temporal, correlational, and rate coding. *Neural Comput*. (2001) **13**:1311–49. doi: 10.1162/08997660152002870
4. Montani F, Kohn A, Smith MA, Schultz SR. The role of correlations in direction and contrast coding in the primary visual cortex. *J Neurosci*. (2007) **27**:2338–48. doi: 10.1523/JNEUROSCI.3417-06.2007
5. Montani F, Ince RA, Senatore R, Arabzadeh E, Diamond ME, Panzeri S. The impact of high-order interactions on the rate of synchronous discharge and information transmission in somatosensory cortex. *Philos Trans R Soc A*. (2009) **367**:3297–310. doi: 10.1098/rsta.2009.0082
6. Montani F, Phoka E, Portesi M, Schultz SR. Statistical modelling of higher-order correlations in pools of neural activity. *Phys A Stat Mech Appl*. (2013) **392**:3066–86. doi: 10.1016/j.physa.2013.03.012
7. Montangie L, Montani F. Quantifying higher-order correlations in a neuronal pool. *Physica A*. (2015) **421**:388–400. doi: 10.1016/j.physa.2014.11.046
8. Montangie L, Montani F. Effect of interacting second- and third-order stimulus-dependent correlations on population-coding asymmetries. *Phys Rev E*. (2016) **94**:1–5. doi: 10.1103/PhysRevE.94.042303
9. Montangie L, Montani F. Higher-order correlations in common input shapes the output spiking activity of a neural population. *Phys A Stat Mech Appl*. (2017) **471**:845–61. doi: 10.1016/j.physa.2016.12.002
10. Montangie L, Montani F. Common inputs in subthreshold membrane potential: the role of quiescent states in neuronal activity. *Phys Rev E*. (2018) **97**:060302. doi: 10.1103/PhysRevE.97.060302
11. Montani F, Oliynyk A, Fadiga L. Superlinear summation of information in premotor neuron pairs. *Int J Neur Syst*. (2017) **27**:1650009. doi: 10.1142/S012906571650009X
12. Schalk G, McFarland DJ, Hinterberger T, Birbaumer N, Wolpaw JR. BCI2000: a general-purpose brain-computer interface (BCI) system. *IEEE Trans Biomed Eng*. (2004) **51**:1034–43. doi: 10.1109/TBME.2004.827072
13. Schoffelen JM, Gross J. Source connectivity analysis with MEG and EEG. *Hum Brain Map*. (2009) **30**:1857–65. doi: 10.1002/hbm.20745
14. Bassett DS, Bullmore ET. Human brain networks in health and disease. *Curr Opin Neurol*. (2009) **22**:340–7. doi: 10.1097/WCO.0b013e32832d93dd
15. Bullmore ET, Sporns O. Complex brain networks: graph theoretical analysis of structural and functional systems. *Nat Rev Neurosci*. (2009) **10**:186–98. doi: 10.1038/nrn2575
16. Bassett DS, Wymbs NF, Porter MA, Mucha PJ, Carlson JM, Grafton ST. Dynamic reconfiguration of human brain networks during learning. *Nat Rev Neurosci*. (2011) **108**:7641–6. doi: 10.1073/pnas.1018985108
17. Stam CJ, Reijneveld JC. Graph theoretical analysis of complex networks in the brain. *Nonlinear Biomed Phys*. (2007) **1**:3. doi: 10.1186/1753-4631-1-3
18. Martínez JH, Buldú JM, Papo D, Fallani F, Chavez M. Role of inter-hemispheric connections in functional brain networks. *Sci Rep*. (2018) **8**:10246. doi: 10.1038/s41598-018-28467-x
19. Martínez JH, López ME, Ariza P, Chavez M, Pineda-Pardo JA, López-Sanz D, et al. Functional brain networks reveal the existence of cognitive reserve and the interplay between network topology and dynamics. *Sci Rep*. (2018) **8**:10525. doi: 10.1038/s41598-018-28747-6
20. Barreiro M, Marti AC, Masoller C. Inferring long memory processes in the climate network via ordinal pattern analysis. *Chaos*. (2011) **21**:013101. doi: 10.1063/1.3545273
21. Schieber TA, Carpi L, Diaz-Guilera A, Pardalos PM, Masoller C, Ravetti MG. Quantification of network structural dissimilarities. *Nat Commun*. (2017) **8**:13928. doi: 10.1038/ncomms13928
22. Rubido N, Masoller C. Impact of lag information on network inference. *C Eur Phys J Spec Top*. (2018) **227**:1243–50. doi: 10.1140/epjst/e2018-800070-1

23. Deza JI, Barreiro M, Masoller C. Assessing the direction of climate interactions by means of complex networks and information theoretic tools. *Chaos*. (2015) **25**:033105. doi: 10.1063/1.4914101
24. Baptista MS, de Carvalho JX, Hussein MS. Finding quasi-optimal network topologies for information transmission in active networks. *PLoS ONE*. (2008) **3**:e3479. doi: 10.1371/journal.pone.0003479
25. Baptista MS, Kurths J. Transmission of information in active networks. *Phys Rev E Stat Nonlin Soft Matter Phys*. (2008) **77**(2 Pt 2):026205. doi: 10.1103/PhysRevE.77.026205
26. Rubido N, Martí AC, Bianco-Martínez E, Grebogi C, Baptista MS, Masoller C. Exact detection of direct links in networks of interacting dynamical units. *N J Phys*. (2014) **16**:093010. doi: 10.1088/1367-2630/16/9/093010
27. Longden KD, Willshaw DJ. An evaluation of recurrent feedforward memory networks and their relevance to the hippocampus. *Neurocomputing*. (2002) **44**:527–31. doi: 10.1016/S0925-2312(02)00413-7
28. Longden KD, Willshaw DJ. Asynchronous inputs and NMDA conductances predict excitatory responses in the cortical-cA1 pathway of the hippocampus. *Network*. (2007) **18**:299–325. doi: 10.1080/09548980701587100
29. Pereda E, Quiroga RQ, Bhattacharya J. Nonlinear multivariate analysis of neurophysiological signals. *Prog Neurobiol*. (2005) **77**:1–37. doi: 10.1016/j.pneurobio.2005.10.003
30. González GF, der Molen MJWV, Saric G, Bonte M, Tijms J, Blomert L, et al. Graph analysis of EEG resting state functional networks in dyslexic readers. *Clin Neurophysiol*. (2016) **127**:3165–75. doi: 10.1016/j.clinph.2016.06.023
31. Stam CJ. Modern network science of neurological disorders. *Nat Rev Neurosci*. (2014) **15**:683–95. doi: 10.1038/nrn3801
32. Nuñez A, Panetsos F, Avendaño C. Rhythmic neuronal interactions and synchronization in the rat dorsal column nuclei. *Neuroscience*. (2000) **100**:599–609. doi: 10.1016/S0306-4522(00)00305-5
33. Bullmore ET, Bassett DS. Brain graphs: graphical models of the human brain connectome. *Annu Rev Clin Psychol*. (2011) **7**:113–40. doi: 10.1146/annurev-clinpsy-040510-143934
34. Stam CJ, van Straaten ECW. The organization of physiological brain networks. *Clin Neurophysiol*. (2012) **123**:1067–87. doi: 10.1016/j.clinph.2012.01.011
35. Toppi J, Astolfi L, Risetti M, Anzolin A, Kober SE, Wood G, et al. Different topological properties of EEG-derived networks describe working memory phases as revealed by graph theoretical analysis. *Front Hum Neurosci*. (2018) **11**:637. doi: 10.3389/fnhum.2017.00637
36. Brazier MA, Casby JU. Crosscorrelation and autocorrelation studies of electroencephalographic potentials. *Electroencephalogr Clin Neurophysiol*. (1952) **4**:201–11. doi: 10.1016/0013-4694(52)90010-2
37. Barlow JS, Brazier MA. A note on a correlator for electroencephalographic work. *Electroencephalogr Clin Neurophysiol*. (1954) **100**:321–5. doi: 10.1016/0013-4694(54)90036-X
38. Bandt C, Pompe B. Permutation entropy: a natural complexity measure for time series. *Phys Rev Lett*. (2002) **88**:174102. doi: 10.1103/PhysRevLett.88.174102
39. Rosso OA, Masoller C. Detecting and quantifying stochastic and coherence resonances via information-theory complexity measurements. *Phys Rev E*. (2009) **79**:040106. doi: 10.1103/PhysRevE.79.040106
40. Rosso OA, Masoller C. Detecting and quantifying temporal correlations in stochastic resonance via information theory measures. *Eur Phys J B*. (2009) **69**:37–43. doi: 10.1140/epjb/e2009-00146-y
41. Baravalle R, Rosso OA, Montani F. Rhythmic activities of the brain: quantifying the high complexity of beta and gamma oscillations during visuomotor tasks. *Chaos*. (2018) **28**:075513. doi: 10.1063/1.5025187
42. Baravalle R, Rosso OA, Montani F. Causal shannon-fisher characterization of motor/imagery movements in EEG. *Entropy*. (2018) **20**:660. doi: 10.3390/e20090660
43. Baravalle R, Rosso OA, Montani F. Discriminating imagined and non-imagined tasks in the motor cortex area: entropy-complexity plane with a wavelet decomposition. *Phys A Stat Mech Appl*. (2018) **511**:27–39. doi: 10.1016/j.physa.2018.07.038
44. Montani F, Rosso OA, Schultz SR. Discrimination measure of correlations in a population of neurons by using the Jensen-Shannon divergence. *AIP Conf Proc*. (2007) **913**:184–9. doi: 10.1063/1.2746745
45. Schalk G, Mellinger J. *A Practical Guide to Brain-Computer Interfacing with BCI2000*. London; Dordrecht; Heidelberg; New York, NY: Springer (2010).
46. Zanin M, Zunino L, Rosso OA, Papo D. Permutation entropy and its main biomedical and econophysics applications: a review. *Entropy*. (2012) **14**:1553–77. doi: 10.3390/e14081553
47. Olivares F, Plastino A, Rosso OA. Ambiguities in the Bandt-Pompe's methodology for local entropic quantifiers. *Physica A*. (2012) **391**:2518–26. doi: 10.1016/j.physa.2011.12.033
48. Olivares F, Plastino A, Rosso OA. Contrasting chaos with noise via local versus global information quantifiers. *Phys Lett A*. (2012) **376**:1577–83. doi: 10.1016/j.physleta.2012.03.039
49. Rosso OA, Larrondo HA, Martín MT, Plastino A, Fuentes MA. Distinguishing noise from chaos. *Phys Rev Lett*. (2007) **99**:154102. doi: 10.1103/PhysRevLett.99.154102
50. Rosso OA, Olivares F, Zunino L, Micco LD, Aquino ALL, Plastino A, et al. Characterization of chaotic maps using the permutation Bandt-Pompe probability distribution. *Eur Phys J B*. (2012) **86**:116. doi: 10.1140/epjb/e2013-30764-5
51. Saco PM, Carpi LC, Figliola A, Serrano E, Rosso OA. Entropy analysis of the dynamics of El Niño/Southern Oscillation during the Holocene. *Physica A*. (2010) **389**:5022–7. doi: 10.1016/j.physa.2010.07.006
52. Keller K, Sinn M. Ordinal analysis of time series. *Physica A*. (2005) **356**:114–20. doi: 10.1016/j.physa.2005.05.022
53. Zunino L, Soriano MC, Fischer I, Rosso OA, Mirasso CR. Permutation-information-theory approach to unveil delay dynamics from time-series analysis. *Phys Rev E*. (2010) **82**:046212. doi: 10.1103/PhysRevE.82.046212
54. Soriano MC, Zunino L, Rosso OA, Fischer I, Mirasso CR. Time scales of a chaotic semiconductor laser with optical feedback under the lens of a permutation information analysis. *IEEE J Quant Electr*. (2011) **47**:252–61. doi: 10.1109/JQE.2010.2078799
55. Zunino L, Soriano MC, Rosso OA. Distinguishing chaotic and stochastic dynamics from time series by using a multiscale symbolic approach. *Phys Rev E*. (2012) **86**:046210. doi: 10.1103/PhysRevE.86.046210
56. Rosso OA, Olivares F, Plastino A. Noise versus chaos in a causal Fisher-Shannon plane. *Pap Phys*. (2015) **7**:070006. doi: 10.4279/pip.070006
57. Montani F, Rosso OA. Entropy–complexity characterization of brain development in chickens. *Entropy*. (2014) **16**:4677–92. doi: 10.3390/e16084677
58. Shannon C, Weaver W. *The Mathematical Theory of Communication*. Champaign, IL: University of Illinois Press (1949).
59. Grosse I, Bernaola-Galván P, Carpena P, Román-Roldán R, Oliver J, Stanley HE. Analysis of symbolic sequences using the Jensen-Shannon divergence. *Phys Rev E*. (2002) **65**:041905. doi: 10.1103/PhysRevE.65.041905
60. Wolpaw JR, McFarland DJ, Vaughan TM, Schalk G. The Wadsworth Center brain-computer interface (BCI) research and development program. *IEEE Trans Neural Syst Rehabil Eng*. (2003) **11**:1–4. doi: 10.1109/TNSRE.2003.814442
61. Goldberger AL, Amaral LAN, Glass L, Hausdorff JM, Ivanov PC, Mark RG, et al. PhysioBank, PhysioToolkit, and PhysioNet: components of a new research resource for complex physiologic signals. *Circulation*. (2000) **101**:e215–20. doi: 10.1161/01.CIR.101.23.e215
62. Huong NTM, Linh HQ, Khai LQ. Classification of left/right hand movement EEG signals using event related potentials and advanced features. In: 6*th IFMBE Proceedings*.Vol. 63, Singapore: Springer (2018). p. 209–2015.
63. Zebende GF, Filho FMO, Cruz JAL. Auto-correlation in the motor/imaginary human EEG signals: a vision about the FDFA fluctuations. *PLoS ONE*. (2017) **12**:e0183121. doi: 10.1371/journal.pone.0183121
64. Kim Y, Ryu J, Kim KK, Took CC, Mandic DP, Park C. Motor imagery classification using Mu and Beta rhythms of EEG with strong uncorrelating transform based complex common spatial patterns. *Comput Intell Neurosci*. (2016) **2016**:1–13. doi: 10.1155/2016/1489692
65. Belitski A, Gretton A, Magri C, Murayama Y, Montemurro MA, Logothetis NK, et al. Low-frequency local field potentials and spikes in primary visual cortex convey independent visual information. *J Neurosci*. (2008) **28**:5696–709. doi: 10.1523/JNEUROSCI.0009-08.2008

66. Castellani G, Intrator N, Remondini D. Systems biology and brain activity in neuronal pathways by smart device and advanced signal processing. *Front Genet*. (2014) **5**:253. doi: 10.3389/fgene.2014.00253
67. Freeman LC. Centrality in social networks conceptual clarification. *Soc Netw*. (1979) **1**:215–39.
68. Freeman LC, Roeder D, Mulholland RR. Centrality in social networks: II. Experimental results. *Soc Netw*. (1979/80) **2**:119–41.
69. Bolland JM. Sorting out centrality: an analysis of the performance of four centrality models in real and simulated networks. *Soc Netw*. (1988) **10**:233–53.
70. Brandes U, Fleischer D. Centrality measures based on current flow. In: Diekert V, Durand B, editors. *STACS 2005*. Berlin; Heidelberg: Springer (2005). p. 533–44.
71. Brandes U, Borgatti SP, Freeman LC. Maintaining the duality of closeness and betweenness centrality. *Soc Netw*. (2016) **44**:153–9. doi: 10.1007/978-3-540-31856-9_44
72. Borgatti SP. Centrality and network flow. *Soc Netw*. (2005) **27**:55–71. doi: 10.1016/j.socnet.2004.11.008
73. Benjamini Y, Hochberg Y. Controlling the false discovery rate: a practical and powerful approach to multiple testing. *J R Stat Soc Ser B Methodol*. (1995) **57**:289–300. doi: 10.1111/j.2517-6161.1995.tb02031.x
74. Nielsen JA, Zielinski BA, Ferguson MA, Lainhart JE, Anderson JS. An evaluation of the left-brain vs. right-brain hypothesis with resting state functional connectivity magnetic resonance imaging. *PLoS ONE*. (2013) **8**:e71275. doi: 10.1371/journal.pone.0071275
75. Klimesch W. Evoked alpha and early access to the knowledge system: the P1 inhibition timing hypothesis. *Brain Res*. (2011) **1408**:52–71. doi: 10.1016/j.brainres.2011.06.003
76. Klimesch W, Sauseng P, Hanslmayr S. The role of inhibition in task switching: a review. *Brain Res*. (2010) **17**:1–14. doi: 10.3758/PBR.17.1.1
77. Wolff N, Zink N, Stock AK, Beste C. On the relevance of the alpha frequency oscillation's small-world network architecture for cognitive flexibility. *Sci Rep*. (2017) **7**:13910. doi: 10.1038/s41598-017-14490-x
78. Fink A, Benedek M. EEG alpha power and creative ideation. *Neurosci Biobehav Rev*. (2014) **44**:111–23. doi: 10.1016/j.neubiorev.2012.12.002
79. Hamedi M, Salleh SH, Noor AM. Electroencephalography motor imagery brain connectivity analysis for BCI: a review. *Neural Comput*. (2016) **28**:999–1041. doi: 10.1162/NECO_a_00838
80. Asensio-Cubero J, Gan JQ, Palaniappan R. Multiresolution analysis over graphs for a motor imagery based online BCI game. *Comput Biol Med*. (2016) **68**:21–6. doi: 10.1016/j.compbiomed.2015.10.016
81. Filhoa CAS, Attux R, Castellano G. Can graph metrics be used for EEG-BCIs based on hand motor imagery? *Biomed Signal Process Control*. (2018) **40**:359–65. doi: 10.1016/j.bspc.2017.09.026
82. Peterson DS, Pickett KA, Duncan RP, Perlmutter JS, Earhart GM. Brain activity during complex imagined gait Tasks in Parkinson disease. *Clin Neurophysiol*. (2014) **5**:995–1005. doi: 10.1016/j.clinph.2013.10.008
83. Makarov VV, Zhuravlev MO, Runnova AE, Protasov P, Maksimenko VA, Frolov NS, et al. Betweenness centrality in multiplex brain network during mental task evaluation. *Phys Rev E*. (2018) **98**:062413. doi: 10.1103/PhysRevE.98.062413

Conflict of Interest Statement: The authors declare that the research was conducted in the absence of any commercial or financial relationships that could be construed as a potential conflict of interest.

frontiers in Computational Neuroscience

ORIGINAL RESEARCH
published: 27 August 2019
doi: 10.3389/fncom.2019.00057

Cellular and Network Mechanisms for Temporal Signal Propagation in a Cortical Network Model

*Zonglu He**

Faculty of Management and Economics, Kaetsu University, Tokyo, Japan

The mechanisms underlying an effective propagation of high intensity information over a background of irregular firing and response latency in cognitive processes remain unclear. Here we propose a SSCCPI circuit to address this issue. We hypothesize that when a high-intensity thalamic input triggers synchronous spike events (SSEs), dense spikes are scattered to many receiving neurons within a cortical column in layer IV, many sparse spike trains are propagated in parallel along minicolumns at a substantially high speed and finally integrated into an output spike train toward or in layer Va. We derive the sufficient conditions for an effective (fast, reliable, and precise) SSCCPI circuit: (i) SSEs are asynchronous (near synchronous); (ii) cortical columns prevent both repeatedly triggering SSEs and incorrectly synaptic connections between adjacent columns; and (iii) the propagator in interneurons is temporally complete fidelity and reliable. We encode the membrane potential responses to stimuli using the non-linear autoregressive integrated process derived by applying Newton's second law to stochastic resilience systems. We introduce a multithreshold decoder to correct encoding errors. Evidence supporting an effective SSCCPI circuit includes that for the condition, (i) time delay enhances SSEs, suggesting that response latency induces SSEs in high-intensity stimuli; irregular firing causes asynchronous SSEs; asynchronous SSEs relate to healthy neurons; and rigorous SSEs relate to brain disorders. For the condition (ii) neurons within a given minicolumn are stereotypically interconnected in the vertical dimension, which prevents repeated triggering SSEs and ensures signal parallel propagation; columnar segregation avoids incorrect synaptic connections between adjacent columns; and signal propagation across layers overwhelmingly prefers columnar direction. For the condition (iii), accumulating experimental evidence supports temporal transfer precision with millisecond fidelity and reliability in interneurons; homeostasis supports a stable fixed-point encoder by regulating changes to synaptic size, synaptic strength, and ion channel function in the membrane; together all-or-none modulation, active backpropagation, additive effects of graded potentials, and response variability functionally support the multithreshold decoder; our simulations demonstrate that the encoder-decoder is temporally complete fidelity and reliable in special intervals contained within the stable fixed-point range. Hence, the SSCCPI circuit provides a possible mechanism of effective signal propagation in cortical networks.

Keywords: nonlinear dynamics, time series modeling, homeostatic encoder, multithreshold decoder, all-or-none modulation, backpropagation, synchronous spiking events, cortical minicolumns

OPEN ACCESS

Edited by:
Chris G. Antonopoulos, University of Essex, United Kingdom

Reviewed by:
Jiang Wang, Tianjin University, China
Rodrigo Felipe De Oliveira Pena, New Jersey Institute of Technology, United States

***Correspondence:**
Zonglu He
zongluhe@kaetsu.ac.jp

Received: *29 April 2019*
Accepted: *07 August 2019*
Published: *27 August 2019*

Citation:
He Z (2019) Cellular and Network Mechanisms for Temporal Signal Propagation in a Cortical Network Model
Front. Comput. Neurosci. 13:57. doi: 10.3389/fncom.2019.00057

1. INTRODUCTION

Cortical mechanisms of information propagation in cognitive processes have not been clarified. Neurons convey this information by sending a sequence of action potentials (a spike train) in the brain, but whether this information is embedded in the spike train by rate or temporal coding is a long-debated topic. Although the input–output function of neurons is classically described as the ratios of mean firing rates (Shadlen and Newsome, 1998), the efficiency of rate coding remains controversial (Gautrais and Thorpe, 1998; van Rossum et al., 2002). Accumulating experimental evidence supports temporal precision with millisecond fidelity and reliability (e.g., Gollisch and Meister, 2008). But temporal coding is challenged by neuronal response latency and irregular firing.

Latencies in axonal conduction and synaptic transmission (Uzuntarla et al., 2012) lower transfer speed due to wait times. Both highly variable reliable neurotransmitter releases and the intrinsic fast activation kinetics of interneuronal K^+ currents can induce highly irregular firing during ongoing, spontaneous activity, and when driven at high firing rates (Stiefel et al., 2013). The irregular firing of cortical neurons may reduce the reliability of spike transmission. That is, temporally effective transfer is seemingly impossible. However, Diesmann et al. (1999) show that precisely synchronized action potentials with millisecond fidelity can propagate within a model of cortical network activity that recapitulates many of the features of biological systems; and Wei and Du (2019) demonstrate that time intervals and periodicity operation can be determined by using an algorithm for simulating a synaptic learning mechanism in a neural circuit model derived from neural-connection structures.

Spiking propagation synchronously through layers is essentially a feed-forward network of neurons (Abeles, 1982a, 1991). Network topology in the feed-forward network determines the propagation of synchronous activity (Guo et al., 2017), suggesting that an optimal network topology relates to synchronous spike events (SSEs) in feed-forward networks. SSEs propagating between groups of neurons in a temporally precise manner through a six-layered, column-arranged neocortex is a hallmark feature of cortical population coding in human and other primate brains. The columnar organization hypothesis is the most widely adopted explanation of cortical information processing. These results suggest that the optimal network topology integrates the functions of SSEs and cortical columns in spiking propagation through the cortex in a feed-forward manner. SSEs occur in various conditions in numerous areas of the cerebral cortex (Abeles, 1982a; Gray et al., 1989). Highly irregular firing is thought only possible from fast, strong dendritic non-linearity or strong SSEs among synaptically connected cells due to inconsistency with the temporal integration of random EPSPs (Softky and Koch, 1993). The temporal sequences of SSEs have been postulated as a working mechanism of activity propagation in the cortex (Abeles and Gerstein, 1988; Diesmann et al., 1999; Ikegaya et al., 2004; Torre et al., 2016a). Neurons within a minicolumn share the same tuning for any given receptive field attribute (Horton and Adams, 2005), while adjacent minicolumns may have different fields (Jones, 2000). Thus, minicolumns may well constitute a fundamental computational unit of the neocortex (Buxhoeveden and Casanova, 2002). Increasing evidence shows that the power of cortical processing is produced by populations of neurons forming dynamic neuronal ensembles (Castejon and Nuñez, 2016). On the other hand, there is an interaction between microscopic and population dynamics (Panzeri et al., 2015). SSEs in temporal encoding depend on single-neuron features (Grewe et al., 2017). Single neuron properties and firing statistics are consistent with physiological data (van Rossum et al., 2002) and the mechanisms of dynamic information storage in cells (Potter et al., 2017).

This study aims to reveal cortical mechanisms that support effective signal propagation over a background of irregular firing and response latencies occurring in cognitive processes. First, we propose the hypothesis of a cortical population circuit from an entry point of rapid transfer of high-intensity signals, incorporating the interneuron encoder-decoder into the cortical population circuit composites a cellular-network model. Then, we derive the conditions for an effective (fast, reliable, and precise) circuit. Finally, we provide evidence from simulations and observations in support of these conditions and hypothesis.

A desirable candidate for action potential encoding should satisfy the following requirements. The neuronal encoder as basic signal processing should be reproducible and reflect the major properties of neurons and circuits in information processing, including inherent non-linearity (Softky and Koch, 1993), ionic homeostasis (Davis and Bezprozvanny, 2001), activity-dependent synaptic dynamics (Fuhrmann et al., 2002), response latency (Uzuntarla et al., 2012), noise (Stiefel et al., 2013), and discreteness (Abbott et al., 2016). Additionally, a spike train is thought to be caused by synaptic stimuli as the bifurcation parameter that triggers a fast transition between quiescent and burst modes by a fixed point and limit cycle (Izhikevich, 2000).

We adopt the non-linear autoregressive integrated (NLARI) process derived by applying Newton's second law to stochastic resilience systems (He, 2007, 2013) in action potential encoding because the model satisfies the above requirements. Moreover, the NALRI's parameter estimation and testing are easy (He, 2014). The dynamics of the cortex have not been thoroughly addressed, although a bifurcation in cortical activity from damped stochastic activity (or a stable fixed point) to high amplitude non-linear oscillations is thought to arise from activity on a limit cycle or chaotic attractor in pathological states such as the onset of a seizure (Deco et al., 2008). The NLARI process can reproduce complete dynamic evolution from a stable to an unstable fixed point and from period cycles to chaos (He, 2018), which prevents missing the possible dynamic mechanisms of neuronal encoding over a wide range of health and disease states.

2. RESULTS

2.1. SSCCPI Circuit

We proposed the Synchronous Spiking Cortical Column Propagation Integration (SSCCPI) circuit for transfer mechanism in cortical networks (**Figure 1**). First, we outlined the organization and flowchart of cortical information processing.

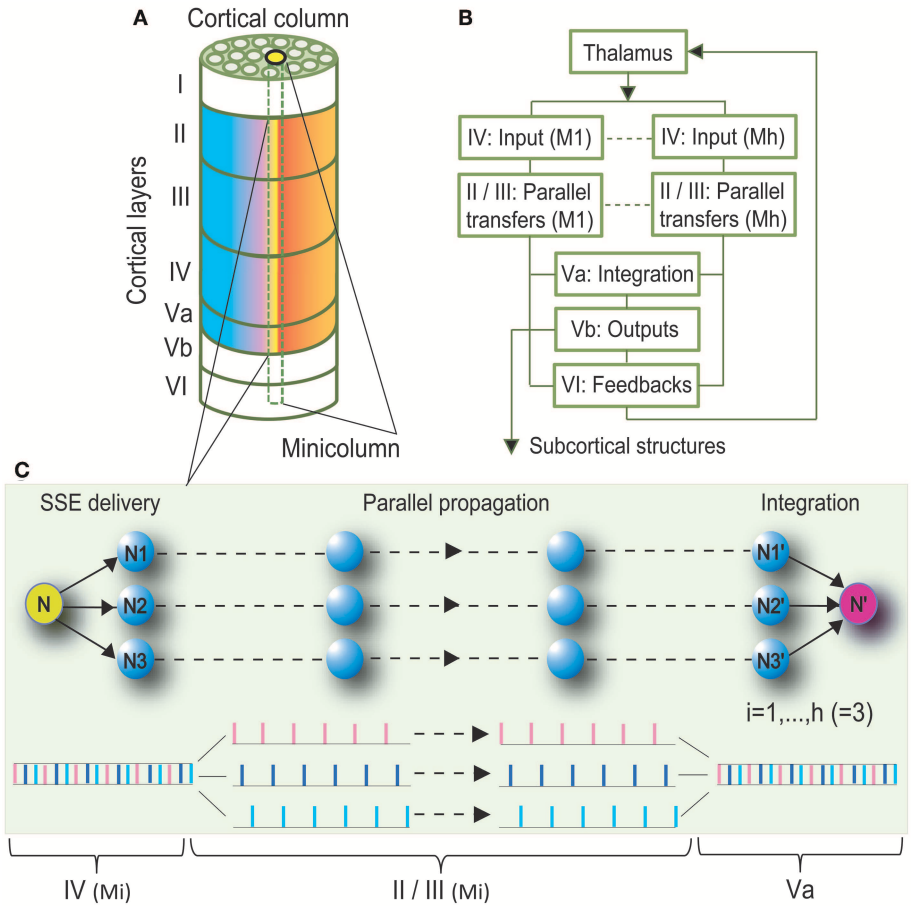

FIGURE 1 | Synchronous Spiking Cortical Column Propagation Integration (SSCCPI) Scheme. **(A)** A cortical organization schematic showing a six-layered, column-arranged neocortex. **(B)** A flowchart showing cortical information processing along the layer IV, →II/III, →Va, and →Vb/VI pathway. **(C)** Schematic illustration of the role of a SSCCPI scheme in response to rapid transfer of high-intensity signals under response latency: a stimulus input from a sensory neuron (N) is delivered by SSEs to neurons (N1–N3) within a cortical column, propagated in parallel to neurons (N1′–N3′), and integrated at a target neuron (N′) for a single-neuron transfer with temporal-complete fidelity.

Figure 1A illustrates an organization schematic of a cortical column through six layers. Neurons in the neocortex are organized vertically into numerous columns with columnar segregation and horizontally in supragranular layers II/III, granular layer IV, and infragranular layers V/VI. **Figure 1B** illustrates a cortical information processing flowchart. When the activation of sensory receptors scattered throughout peripheral body parts generates a nerve impulse, this sensory input is conveyed via the ascending sensory pathways of the spinal cord and brainstem to the thalamus. The thalamic nuclei relay sensory information to a specific region of the neocortex where it can be processed. Sensory information is thought to be propagated through the cortical column along the layer IV, →II/III, and →V/VI pathway (Buonomano and Merzenich, 1998). Layers II/III interpret sensory signals, decide on the appropriate response, and provide the basis of high-level neural activity in the brain. Layer V projects the main outputs to subcortical structures. Layer VI sends feedback connections to its inputs from the thalamus. Notably, layer V is classically subdivided into sublayers Va and Vb based on the following characteristics (Zilles and Wree, 1995): layers Va and Vb differ dramatically in the morphology of pyramidal cells and their correlation with intrinsic and extrinsic physiological parameters; layer Va pyramidal neurons receive most of their excitatory and inhibitory inputs from intracolumnar sources, especially from layer Va itself, but also from layer IV, and the two layers are the main origin for transcolumnar excitatory inputs. Thus, layer Va may predominantly integrate information intralaminarly as well as from layer IV (Schubert et al., 2006). Hence, we postulated that layer Va integrates thalamic and intracortical inputs from the entire cortical column, while layer Vb projects the main outputs to subcortical structures (see Harris and Mrsic-Flogel, 2013).

A key entry point to addressing our issues was based on the idea that the computational properties of groups of neurons should be an emergent property of the group. Rapid task-related performance or attention to complex sounds induces rapid and adaptive reshaping of retrieve field properties of neurons in accordance with specific behavioral demands and salient sensory

cues (Fritz et al., 2003, 2005, 2007; Soto et al., 2006). The rapid and adaptive reshaping of retrieve field properties of neurons could be known as SSEs.

When faced with a behavioral task, sensory neurons need to rapidly elicit high-intensity signals from peripheral nerves to the neocortex, and communication between different areas of the brain substantially increases. A significant increase in the stimulus intensity leads to a high firing rate and high synaptic level. The high firing rate shortens time intervals between consecutive spikes in the spike train, while the high synaptic level lengthens neural response latencies. The shortened spreads of time intervals are far less than the lengthened response latencies, while a spike train is a series of data points indexed in time order. Thus, many spikes in the spike train travel to different neurons from the previous neurons between the last stimulus onset and the beginning of the response. In this manner, many neurons participate in the propagation of the spike train, which is the SSE. SSEs exhibit entire or partial non-overlap-spike delivery (asynchronous SSEs). As the presynaptic discharge rate rises, synaptic depression causes the amplitude of a single postsynaptic current to become inversely proportional to the firing rate. When the presynaptic firing rate exceeds the limiting frequency, the time-averaged postsynaptic current also nearly reaches its saturation value; thus, synaptic connections no longer convey information about the presynaptic discharge rate (Gerstner et al., 1997). That is, once the increased stimulus intensity exceeds the ability of individual neurons to process information, spikes in the spike train have to be delivered synchronously into many neurons. Then, SSEs with entire overlap-spike delivery (rigorous SSEs) occur. The same spike is received in parallel by massive individual neurons. Notably, irregular synaptic inputs makes SSE delivery at least partially non-overlapping. Thus, these individual neurons usually have lower synaptic input levels, which shortens their response latencies. The transfer of a spike train with low density has a shorter latency than that of a spike train with high density; thus, SSEs were effective in enhancing transfer speed by avoiding the lengthened response latency caused by high-intensity signals. Consequently, we assumed that SSEs were a consequence of cortical population responses to rapid transfer of high-intensity signals with neural response latency.

The question then arises as to which mechanism would ensure information fidelity during disassembly signal propagation such that the integration spike train of decomposed spike trains can return to the original spike train. Asynchronous SSEs perform the conversion of a spike train with high density into many spike trains with low density such that intervals between spikes usually become greater than response latency. Accordingly, there is no reason to repeatedly activate SSEs in response to high-intensity signals. After one SSE delivery, those spike trains with low density should be propagated through layers II/III first and then integrated into an output spike train as a convergent input from simultaneously spiking neurons onto a target neuron in layer Va as previously suggested by Diesmann et al. (1999). If the output spike train returns to the thalamic input, the disassembly propagation of high-intensity signals is successful. There are two prerequisites for returning to the initial input. A prerequisite is that SSE delivery is not repeatedly activated; otherwise, these separately propagated spikes disperse and eventually die out. A further prerequisite is that disassembled spikes do not bump into other neurons with different receptive fields during parallel propagation; otherwise, incorrect synaptic connections result in information loss and distortion. Cortical columns (Mountcastle et al., 1955) in the vertical dimension and columnar segregation could meet these two prerequisites. Neurons within a given minicolumn were stereotypically interconnected in the vertical dimension, which prevented repeated activation of SSEs and ensured parallel propagation of spike trains, while columnar segregation could prevent incorrect synaptic connections between adjacent columns. When the stimulus intensity exceeds the ability of individual minicolumns to process information, the stimulus spikes have to be delivered synchronously into multiple minicolumns within a given macrocolumn.

We summarized that rapid transfer of high-intensity signals could be achieved by the following components: SSEs delivering a high-intensity thalamic stimulus input to many neurons within a cortical column as many spike trains with low density in layer IV, parallel propagation of these spike trains with low density along minicolumns through layers II/III, and integrating these spike trains into an output toward or in layer Va. Parallel propagation of many sparse spike trains through SSE delivery enhances the transfer speed of high-intensity signals, while vertical columns with segregation ensure parallel-propagation fidelity. A circuit with these three components is called the SSCCPI Circuit. **Figure 1C** is a simplified SSCCPI circuit. Formally, we have the following definition:

Definition 1. The Synchronous Spiking Cortical Column Propagation Integration (SSCCPI) circuit is a neural circuit by which SSEs deliver dense spikes of a thalamic high-intensity stimulus input into many receiving neurons within a cortical column in layer IV first. Then, many sparse spike trains are propagated in parallel by a propagator along cortical minicolumns through layers II/III and finally integrated into an output spike train toward or in layer Va.

2.2. Effective SSCCPI Conditions

2.2.1. Coding Strategy

Determining whether the rate or temporal coding is more suitable for the SSCCPI circuit in different overlapping degrees of SSE delivery is important. Without loss of generality, we focused on entire overlap deliveries and entire non-overlap deliveries in single-neuron signal transfer with complete fidelity. **Figure 2** showed the performance comparison between these two coding strategies.

In rate coding, when neurons within a cortical column received and propagated the same input spike train (SSEs with entire spike-overlap delivery), the output firing rate after integration could significantly increase up to h-fold greater than the input firing rate if the output spike timing was entirely non-overlapping where h was the number of the receiving neurons, although the firing rate before, and after propagation remained unchanged (**Figure 2A**). When neurons within a cortical column received completely different input spike trains

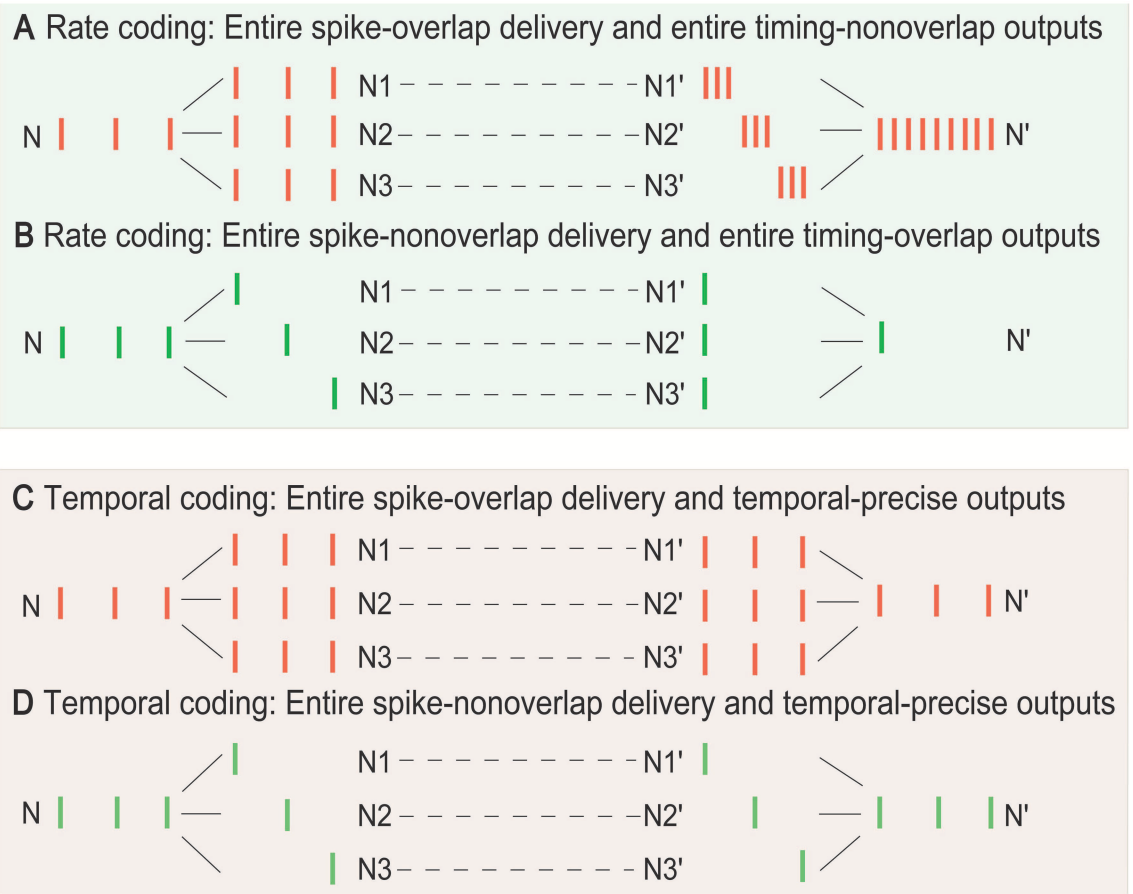

FIGURE 2 | Temporal and rate coding in SSCCPI transfer precision. Consider single-neuron transfer with complete fidelity. **(A)** Entire spike-overlap delivery of SSEs to N1–N3 and entire timing-non-overlap outputs in N1′–N3′ in rate coding. **(B)** Entire spike-non-overlap delivery of SSEs to N1–N3 and entire timing-overlap outputs in N1′–N3′ in rate coding. **(C)** Entire spike-overlap delivery of SSEs to N1–N3 and temporal-precise outputs in N1′–N3′ in temporal coding. **(D)** Entire spike-nonoverlap delivery of SSEs to N1–N3 and temporal-precise outputs in N1′–N3′ in temporal coding.

(SSEs with entire spike-non-overlap delivery), the output firing rate could significantly decrease if the output spike timing was entirely overlapping (**Figure 2B**). Thus, the rate coding could not exactly reflect SSCCPI transfer precision. In contrast, in temporal coding, the output spike train could return to the initial input spike train, regardless of SSEs with entire spike-overlap delivery (**Figure 2C**) or entire spike-non-overlap delivery (**Figure 2D**). Therefore, the SSCCPI circuit should utilize temporal coding because temporal coding makes it possible to maintain SSCCPI transfer precision with complete fidelity (**Figures 2C,D**). In temporal coding, SSEs were effective in enhancing transfer speed for partial or entire spike-non-overlap delivery but ineffective for entire spike-overlap delivery.

2.2.2. Factors Influencing Precision

The symbol error rate is an indicator of signal propagation efficiency in data communications. To distinguish neuronal communications from the data communications, we introduced the propagation success rate to assess the propagation precision of nerve signals. Consider an all-or-none modulation as the conversion rule of a raw input in layer IV and a final output of neurons in layer Va in the firing of neurons. The all-or-none modulation is a principle that the strength of a response of a neuron to a stimulus is not dependent upon the strength of the stimulus whereby the neuron gives a complete response if the stimulus exceeds the threshold potential; otherwise, there is no response. For these reasons, we introduced the propagation success rate as follows:

Definition 2. (i) The propagation success rate of a spike train with n points in single neurons through m relays is defined by:

$$r(m,n) = \left[1 - \frac{(\mathbf{v}_m - \mathbf{v}_0)^{\mathsf{T}} (\mathbf{v}_m - \mathbf{v}_0)}{n}\right] \times 100\% \qquad (1)$$

with

$$v_{0,t} = \begin{cases} 1 & \text{if } \varepsilon_t \geq c_3 \\ 0 & \text{if } \varepsilon_t < c_3 \end{cases}, v_{m,t} = \begin{cases} 1 & \text{if } Y_{m,t} \geq c_3 \\ 0 & \text{if } Y_{m,t} < c_3 \end{cases} \qquad (2)$$

where ε_t is a raw input stimulus, $v_{0,t}$ is the initial received input, $v_{m,t}$ is the final output of a target neuron at time t, and $\mathbf{v}_i = \left(v_{i,1}, \cdots, v_{i,n}\right)^{\mathsf{T}}$ for $i = 0, m$.

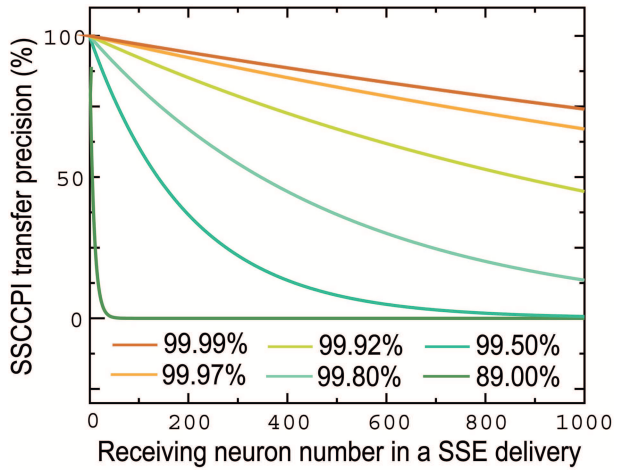

FIGURE 3 | Influences of the number of receiving neurons and single-neuron transfer precision on SSCCPI transfer precision. SSCCPI transfer precision decays exponentially with an increasing number of receiving neurons from 1 to 1,000 in SSE delivery and significantly with a decreasing single-neuron transfer precision from 99.99 to 89.00%.

(ii) The signal transfer has complete fidelity or success if $r(m,n)$ is ∼100% or $v_{m,t} = v_{0,t}$ for almost t and the signal transfer is a complete distortion or failure if $r(m,n)$ is ∼0% or $v_{m,t} \neq v_{0,t}$ for almost t.

The propagation success rate in the SSCCPI circuit can be given by $r^h(m,n)$ where h is the number of receiving neurons in a cortical minicolumn. It is normal for each neuron to have 1, 000 connections. **Figure 3** shows that the SSCCPI propagation success rate decreases distinctly exponentially with an increasing receiving neuron number when the propagation success rate in single neurons is lower than 99.92%. For example, the SSCCPI propagation success rates in 1,000 receiving neurons are 90.48, 74.08, and 44.92% when the single-neuron propagation success rates are 99.99, 99.97, and 99.92%, respectively. Consider minicolumns with 80–120 neurons. The SSCCPI propagation success rate in 80 receiving neurons is almost zero for the single-neuron propagation success rate 89.00%. These results imply that the faster SSCCPI transfer requires the higher interneuron transfer precision; while a rapid SSCCPI transfer certainly results from complete fidelity transfer of temporal information in interneurons. This result shows that parallel communication requires far higher transfer precision per line than serial communication in critical networks.

Furthermore, **Figure 4** demonstrated that the SSCCPI propagation precision could vary with the overlapping degree of SSE delivery plus transfer mistake types in single neurons (or interneurons). When a spike that results in an action potential passes through a neuron, transfer mistakes in single neurons result from a shift in spike timing, the rise of a spike, and the loss of a spike. We considered the SSCCPI circuit with m relays and h receiving neurons and p_s, p_i, and p_d as the probabilities for the occurrence of a shift in spike timing, the rise of a spike, and the loss of a spike, respectively. Without loss of generality, let $p_s = p_i = p_d = p$ ($p = 5\%$, $h = 3$, and $m = 5$ for **Figure 4**).

For the entire spike-overlap delivery of SSEs, the largest output firing rate can be up to h-fold (**Figure 4A**) or $h+1$-fold greater than the input firing rate with probability hmp (**Figure 4C**) because of the transfer mistakes in a shift in spike timing or the rise of a spike, and the output firing rate can become less than the input firing rate with probability $(mp)^h$ (**Figure 4E**) because of the transfer mistake in the loss of a spike. For the entire spike-non-overlap delivery of SSEs, the output firing rate can remain unchanged (**Figure 4B**) or become greater (**Figure 4D**) or less than the input firing rate with probability mp (**Figure 4F**) because of the transfer mistake in a shift in spike timing, the rise of a spike or the loss of a spike. The number of the receiving neurons is usually relatively large. Thus, substantially increased output firing rate could result only from rigorous SSEs plus the interneuron transfer mistake in a shift in spike timing or the rise of a spike, while any change in the output spike train was unlikely to result from asynchronous SSEs plus any interneuron transfer mistakes.

2.2.3. Factors Influencing Speed

To explore what affects the SSCCPI' propagation speed, we gave the following

Definition 3. The speed of signal propagation in neural networks means the speed of travel of a given nerve signal (a spike train as a unit signal) from one place to another in the brain.

The propagation time of signals in neural networks is related to both distances of space and signal intensity. The processing time of an impulse contains time spent on impulse axonal propagation and synaptic transmission. Usually, the processing time of an impulse remains unchanged for an individual neuron. Hence, the propagation time varies primarily with distances of space when signal intensity is not sufficient to trigger a SSE delivery. When high signal intensity triggers a SSE delivery, the propagation time relates not only to distances of space, but also depends crucially on the spike density of those spike trains segregated by SSE delivery. Consider that neurons are able to autochthonously select the shortest pathway in sending the signal to target neurons, that is, the space potential to improving the transfer speed is less. Thus, a great potential for improving the propagation speed relies crucially on shortening the waiting time to process the signal.

Let us consider the case: (i) the processing time for a spike per neuron is 1 ms (usually, the absolute refractory period takes about 1–2 ms), (ii) a thalamic spike train has p spikes and $1/p$ ms equal interval, and (iii) the least interspike interval in these spike trains is q/p ms (equivalent to the least interspike interval is enlarged q times) for $1 \leq q \leq p-1$. The number of spikes in each spike train is not greater than p/q. The waiting time of a spike is not $>1-q/p$ (ms). Thus, the sum of the waiting time of these spike trains is not $>(p/q) \times (1-q/p) = p/q - 1$ (ms). Therefore, the waiting time can be shortened about q times by a SSE delivery. **Figure 5** shows the cases (p,q) is given by $(6,1)$ **(A)**, $(6,2)$ **(B)**, and $(6,5)$ **(C)**. Their waiting times are 5, 4/3, and 1/6 (ms), which are not $>p/q-1$ (ms).

The above results showed that the waiting time of signal processing depends primarily on the degree of overlap of spike

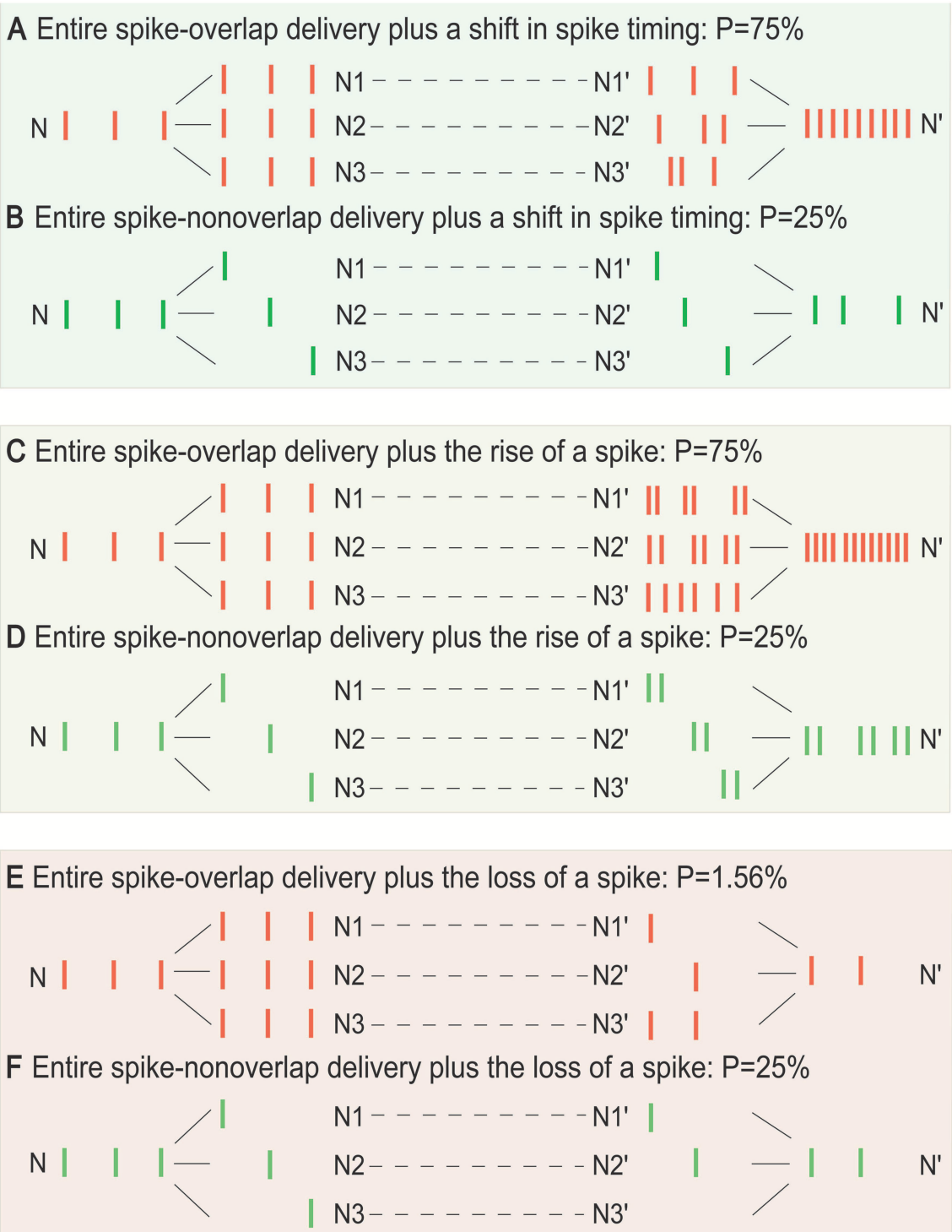

FIGURE 4 | Influence of the overlap degree of SSE delivery and single-neuron transfer mistakes on SSCCPI transfer precision. For the entire spike-overlap delivery of SSEs, the largest output firing rate can be up to h-fold greater than the input firing rate with probability hmp_S **(A)**, $h+1$-fold greater than the input firing rate with probability hmp_i **(C)**, and is less than the input firing rate with probability $(mp_d)^h$ **(E)**. For the entire spike-non-overlap delivery of SSEs, the largest output firing rate can be the same as the input firing rate with probability mp_S **(B)**, be up to 2-fold greater than the input firing rate with probability mp_i **(D)**, and less than the input firing rate with probability mp_d **(F)** for m relays, h receiving neuron number, and p_S, p_i, p_d probabilities of the occurrence of a shift in spike timing, the rise of a spike, and the loss of a spike in single neurons.

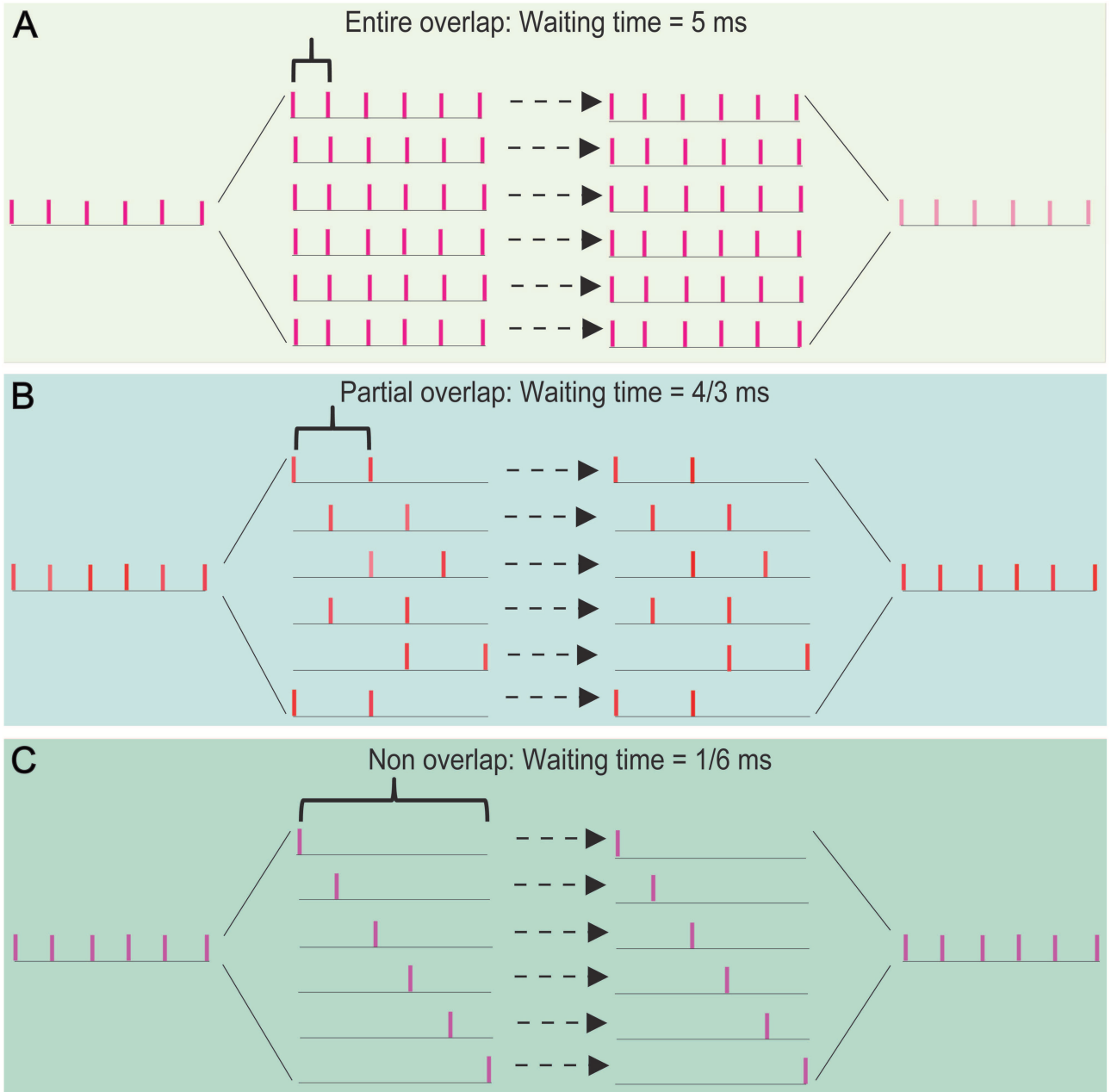

FIGURE 5 | The effects of overlapping degree of spike trains on the propagation speed in a SSE delivery. The waiting time takes 5 ms for an entire spike-overlapping case **(A)**, 4/3 ms for a partial spike-overlapping case **(B)**, and 1/6 ms for a non spike-overlapping case **(C)**. This shows that a lower spike-overlap of a SSE delivery has the shorter waiting time, namely the faster transfer speed.

trains segregated by a thalamic spike train. Thus, the propagation speed could be significantly improved by SSE delivery; a great potential for improving the propagation speed could be realized by increasing the degree of spike-non-overlap of spike trains in interneurons.

2.2.4. Factors Influencing Reliability

Whether the SSCCPI transfer precision remains reliable over a background of irregular synaptic inputs warrants investigation. Hence, it is necessary to define the reliability of signal transfer.

Definition 4. A cortical circuit has a reliable transfer function if the transfer precision of temporal information in the neocortex is not influenced by the input irregularity.

Under the normal states of SSE delivery and cortical columns for a given overlapping degree, the SSCCPI propagation precision depends on whether its single-neuron (or interneuron) transfer has complete fidelity in a temporally precise manner according to the results in the above section. In other words, if the complete

fidelity of a single-neuron (or interneuron) transfer is reliable, then the SSCCPI transfer precision is reliable. Accordingly, SSCCPI transfer reliability is reducible to the reliability of the single-neuron transfer.

2.2.5. Neuronal Encoder

The NLARI process with $\kappa_1 = 1$ can be specified by:

$$X_t = \theta_0 + (1+\theta_1) X_{t-1} - \theta_1 X_{t-2} + \theta_2 \frac{-\left(X_{t-\kappa_2} - \mu_{t-\kappa_2}\right)}{\exp\left((X_{t-\kappa_2} - \mu_{t-\kappa_2})^2\right)} + \varepsilon_t \quad (3)$$

where, $\theta_0 = \omega$, $\theta_1 = 1-\alpha$, $\theta_2 = \beta$, X_{t-j} lags X_t by j steps for $j = 1, \cdots, \kappa_2$; $\mu_t = E(X_t \mid X_0, X_{-1}) = X_0 + (\omega/\alpha)\, t$ if $\varepsilon_t = \epsilon_t - E(\epsilon_t)$ is Gaussian noise. ϵ_t is external disturbance with mean $\omega = E(\epsilon_t)$ and variance $\sigma^2 = var(\epsilon_t)$ at time t. α is the resistance coefficient, β is the restoration coefficient, $\gamma = \beta/(4-2\alpha)$ is the stability coefficient, and κ_1 and κ_2 are time lags in resistance and restoration (He, 2007, 2013). In the absence of a restoring force ($\beta = 0$), Equation (1) is a non-stationary unit root process far from equilibrium (He, 2007). In a lack of background disturbance ($\sigma = 0$), Equation (1) is the deterministic system with a fixed point and a two-period cycle $(-1)^t \sqrt{\ln \gamma}$ for non-null initial values in $\kappa_1 = \kappa_2 = 1$ (He, 2013). The fixed point is exponentially asymptotically stable if $\gamma \in (0, 1)$, while the periodic cycle is exponentially asymptotically stable if $\gamma \in \left(1, \sqrt{e}\right)$. Equation (1) represents unstable period cycles if $\gamma \in (1, 3.07)$ and chaos if $\gamma \in (3.07, +\infty)$ (He, 2018). The fixed point may describe the dynamic mechanism of ionic homeostasis, while together the fixed point and periodic cycle may produce transitions between resting and spiking states.

A dynamic system can be described by the NLARI process if the system sustains an external force, which may cause a deviation from equilibrium (mean), resistance that prevents fast changes, and a restoration force that returns the perturbed system to its mean by a pair of opposite components (He, 2018). For this reason, we focused on exploring whether the membrane potential in response to synaptic stimulus sustains the above-mentioned three forces.

The membrane potential in response to synaptic stimulus is primarily achieved through the difference in membrane permeability to K^+ ions and Na^+ ions. At rest, all Na^+ channels and most K^+ channels are closed, and the Na^+–K^+ transporter pumps K^+ ions into the neuron and Na^+ ions out, creating a net electrochemical force driving Na^+ into the neuron. A synaptic stimulus causes some Na^+ channels of a neuron to open, allowing Na^+ ions to enter the neuron. The net electrochemical force driving Na^+ into the neuron causes the membrane to depolarize. If the threshold of excitation is reached, all the Na^+ channels open. At the peak action potential, Na^+ channels close while K^+ channels open, allowing K^+ ions to leave the neuron. The membrane starts to repolarize through a net electrochemical force driving K^+ out of the neuron and becomes hyperpolarized when more K^+ ions are on the outside than Na^+ ions are on the inside. During a refractory period, the Na^+–K^+ pump moves Na^+ ions to the outside and K^+ ions to the inside using energy from the hydrolysis of ATP against the net electrochemical gradients of both ions. The Na^+ and K^+ distributions are restored to the resting state, and a net electrochemical force driving Na^+ into the neuron brings the membrane back to the resting state.

In summary, excitatory and inhibitory synaptic input (ϵ_t) with mean ω and variance σ^2 drives the membrane potential (X_t) away from the resting potential ($V_{rest} = \mu_t$), which may cause depolarization. A net electrochemical force driving Na^+ ion influx or K^+ ion efflux causes depolarization or repolarization of the neuron, while the Na^+–K^+ pump derives Na^+ out and K^+ into the neuron to return to the ionic distribution across the membrane at rest. Thus, the net electrochemical force and the Na^+–K^+ pump provide a restoration force that maintains homeostasis by returning the perturbed membrane potential to the resting potential. Finally, the plasma membrane provides high resistance that impedes the movement of charges across it, which hinders rapid changes in its potential. Thus, the neuronal response sustains the three required forces. The action potential occurs only at nodes of Ranvier with unmyelinated axons such that the nerve signal appears to jump from node to node and at the trigger zone if an excitatory local potential arrives and remains strong enough to open channels and generate an action potential. Ionic homeostasis is maintained through the regulation of the levels of voltage-gated channels, densities of neurotransmitter receptors, and synapse numbers and strength (Davis and Bezprozvanny, 2001; Dubyak, 2004). Hence, the NLARI process can be used to encode cellular and axonal propagation. Synaptic latency is ∼1 ms. We may wish to consider latencies in the membrane resistance and restoration $\kappa_1 = \kappa_2 = 1$. Let $Y_t = X_t - \mu_t$. Due to $\mu_t = X_0 - (\omega/\alpha)\, t$ for Gaussian noise (He, 2018), $Y_t = X_t - V_{rest} = X_t - X_0 - (\omega/\alpha)\, t$. Then, Equation (3) can be rewritten as:

$$Y_t = (2-\alpha) Y_{t-1} - (1-\alpha) Y_{t-2} + \beta \frac{-Y_{t-1}}{\exp\left(Y_{t-1}^2\right)} + \varepsilon_t \quad (4)$$

which describes the membrane potential variability driven by background synaptic input $\epsilon_t = \varepsilon_t + \omega$ with mean ω and variance σ^2. α is the membrane electrical resistance coefficient that reflects the electrical resistivity of the opposing flows across the membrane for a given electrical potential, depending on the number, and permeability of channels to Na^+, K^+, Ca^{2+}, and Cl^-. β is the membrane potential restoration coefficient that reflects the strength of restoring force to return the resting potential, depending on the magnitude of a net electrochemical force driving Na^+ and K^+ ion influx/efflux across the membrane and synaptic plasticity of strengthening/weakening between neighboring synapses in response to increases and decreases in their activity, and reduced ATP availability lowers the membrane potential restoration coefficient because ATP shortage disrupts K^+/Na^+ homeostasis resulting in a chronic depolarization (Le Masson et al., 2014). γ is the membrane stability coefficient, and κ_1 and κ_2 are response delays in the membrane electrical resistance and membrane potential restoration. If $\gamma \in (0, 1)$, Equation (4) represents a homeostatic encoder with a stable fixed point.

To assess the influence of synaptic stimuli on the membrane potential pattern, we considered the wave indicators developed

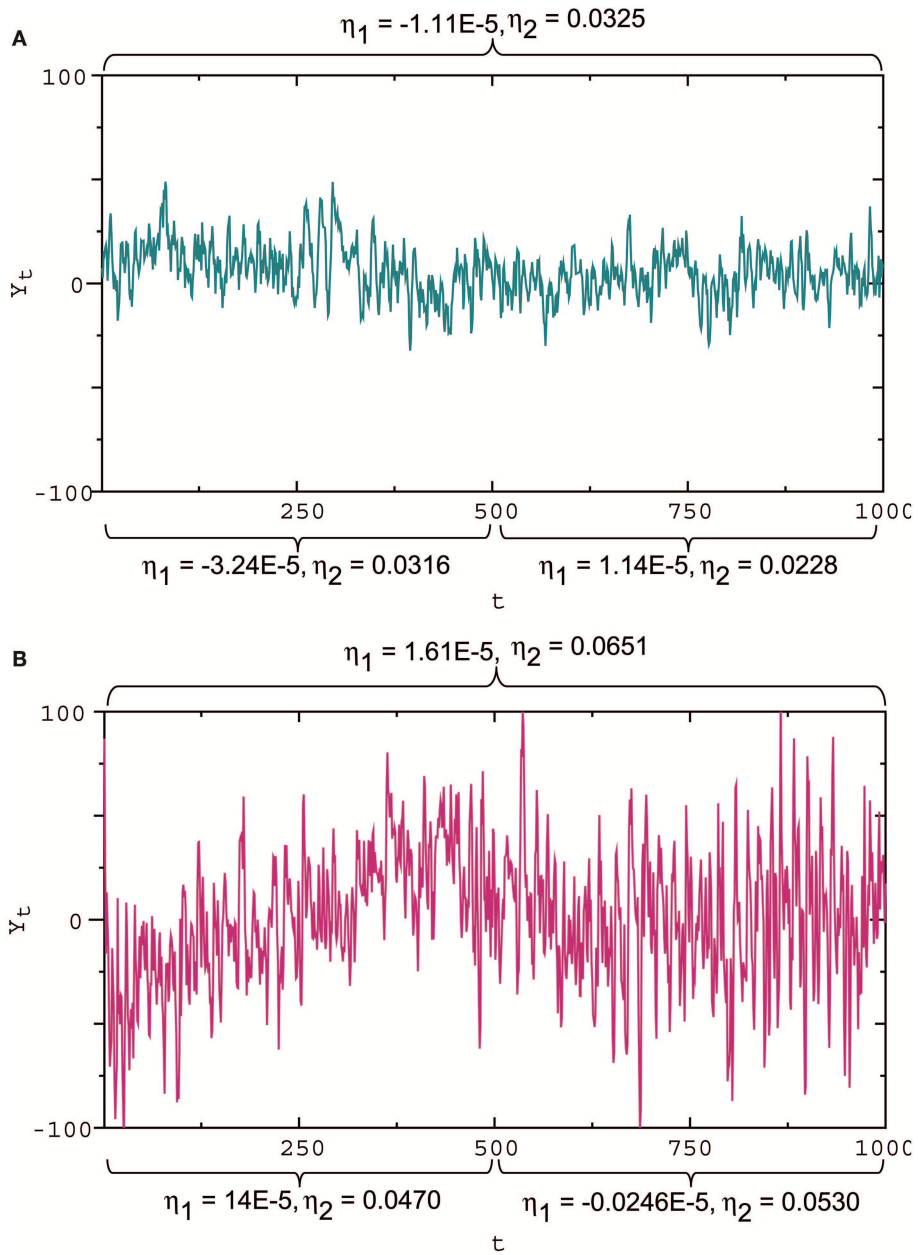

FIGURE 6 | Slope and amplitude of fluctuations and the waveform indicators. **(A)** Small amplitude fluctuations with a gentle downward slope in the first half and almost zero slope in the second half, corresponding to the slope indicator $\eta_1 = -1.11 \times 10^{-5}$ and the amplitude indicator $\eta_2 = 0.0325$ for the whole interval, $\eta_1 = -3.24 \times 10^{-5}$ and $\eta_2 = 0.0316$ for the first half, and $\eta_1 = 1.14 \times 10^{-5}$ and $\eta_2 = 0.0228$ for the second half. **(B)** Large amplitude fluctuations with a steep upward slope in the first half and a gentle downward slope in the second half, corresponding to $\eta_1 = 1.61 \times 10^{-5}$ and $\eta_2 = 0.0651$ for the whole interval, $\eta_1 = 14 \times 10^{-5}$ and $\eta_2 = 0.0470$ for the first half, and $\eta_1 = -0.0246 \times 10^{-5}$ and $\eta_2 = 0.0530$ for the second half. These results show that a positive/negative slope indicator reflects an upward/downward slope, while a large/small absolute slope indicator describes a steep/gentle slope; a large/small amplitude indicator reflects a high/low amplitude. Here these wave indicator values were the estimates based on observational data.

by He (2018). For Gaussian noise, the ratio $\eta_1 = \omega/\alpha$ represents the slope of the mean line provided by $E(X_t \mid X_0, X_{-1}) = X_0 + (\omega/\alpha)\, t$. Thus, the ratio can be viewed as a slope indicator. Moreover, the ratio $\eta_2 = \sigma/\beta$ is strongly positively correlated with the standard deviation of the data generated by Equation (4) (for details see He, 2018), while the standard derivation of disturbances is a measure of how far the signal fluctuates from the mean. For this reason, the σ/β ratio can be viewed as a wave amplitude indicator. From **Figure 6**, we see the capability of the wave indicators to measure the slope and amplitude of fluctuations: the slope and amplitude indicator values in **Figure 6B** are 1.45 times and 2 times the slope and amplitude

indicator values in **Figure 6A**, which is consistent with large and small amplitude fluctuations with steep and gentle slopes (**Figures 6A,B**), respectively. Sometimes the wave indicators have better performance in the subdivided observation intervals. For example, consider the whole interval subdivided into the two intervals. For the first half, the slope and amplitude indicator values in **Figure 6B** are 4.32 times and 1.49 times the slope and amplitude indicator values in **Figure 6A**. The measured results in the subdivided intervals are closer to actual fluctuation patterns than the whole interval. For these reasons, we introduced the membrane potential waveform indicators below:

Definition 5. The membrane potential slope indicator is given by:

$$\eta_1 = \frac{\omega}{\alpha} \tag{5}$$

and the membrane potential amplitude indicator is given by:

$$\eta_2 = \frac{\sigma}{\beta} \tag{6}$$

where, α is the membrane electrical resistance coefficient, β is the membrane potential restoration coefficient, ω is the mean of synaptic stimulus input, and σ is the standard derivation of synaptic stimulus input.

According to the definition of the membrane potential waveform indicators, the relative strength of the membrane electrical resistance and membrane potential restoring force to synaptic input determines the scale of membrane potential fluctuations in slope and amplitude. The standard deviation is a measure of how far the signal fluctuates from the mean, but one cannot extract more information than "a wave amplitude indicator" from it. Furthermore, the waveform indicators are the membrane potential fractal indicators (He, 2018).

2.2.6. Propagator With Encoder

Consider a propagator for a simple reflex circuit. A reflex circuit can be as simple as a single synapse located between sensory and motor neurons. The SSCCPI circuit is a feed-forward network of neurons with multiple layers. Thus, each neuron in the receiving layer is excited by neurons in the previous layer. In this case, the response of the last neuron to a received stimulus could be regarded as the incoming stimulus into the connected neuron. By incorporating the incoming stimulus into (Equation 4), we obtained a propagator with an encoder in nomodulation. Considering all-or-none modulation as the regulation of the incoming stimulus, we could obtain a propagator with an encoder in all-or-none modulation. Formally, we introduced the propagators:

Definition 6. Consider a spike train with n points as the combination of spikes and silences through m relays. The propagator with an encoder is given by:

$$Y_{i,t} = (2-\alpha)\, Y_{i,t-1} - (1-\alpha)\, Y_{i,t-2} + \beta \frac{-Y_{i,t-1}}{\exp\left(Y_{i,t-1}^2\right)} + Y_{i-1,\,t} \tag{7}$$

where, $Y_{i,t}$ represents the response of the ith interneuron to the tth stimulus $Y_{i-1,t}$ at time t for nomodulation and $Y_{i-1,t} = c_1$ if $Y_{i-1,t} \geq c_1$ and $Y_{i-1,t} = v_t^{(1)}$ with $v_t^{(1)} \sim i.i.d.N\left(0, \sigma_1^2\right)$ if $Y_{i-1,t} < c_1$ for $i \geq 2$ for all-or-none modulation; c_1 is a threshold value; and initial values $Y_{0,t} = \varepsilon_t$, $Y_{i,-1} = Y_{i,0} = 0$, and ε_t represents the initial received stimulus at time t for $i = 1, \cdots, m$ and $t = 1, \cdots, n$.

Note that for all-or-none modulation, $Y_{i-1,t} = 0$ if $Y_{i-1,t} < c_1$, but we let $Y_{i-1,t} = v_t^{(1)}$ in order to represent intrinsic noise and extrinsic or synaptic noise with a small variance.

2.2.7. Propagator With Encoder–Decoder

A complex reflex circuit possesses the integration center in the cerebrum, spinal cord, or brainstem where conscious thoughts are initiated. Ascending sensory neurons and descending upper motor neurons (relay interneurons) function as sensory and motor connections and assist in the integration and interpretation of data. The responses of a group of neurons to a stimulus have errors. Whether the accumulated response errors after many relays induce signal loss warrants investigation. Thus, we examined the encoding errors when the propagator with an encoder in Equation (7) for nomodulation and all-or-none modulation (see Definition 6) were operated for m times. As the iteration number increased, the initial stimulus of real spike trains (**Figure 7A**) became significantly enlarged for nomodulation (**Figure 7B**) and was attenuated for all-or-none modulation (**Figure 7C**). The simulation result that nerve impulses are significantly enlarged in the firing of a neuron (**Figure 7B**) reflects the phenomenon that the opening of voltage-gated channels in the course of an action potential produces typically significantly larger currents than the initial stimulating current. Fortunately, all-or-none modulation as a neural regulation of ultra response to stimulus avoids the significant enlargement of impulses (**Figure 7C**). Although all-or-none modulation prevents an over response, it fails to avoid an under response (**Figure 7C**). Interestingly, no evidence that all-or-none modulation fails to avoid an under response suggests the existence of a hidden mechanism by which the under response is modulated by supplementing the attenuated currents. In fact, currents produced by the opening of voltage-gated channels are typically larger than the current of the original stimulus, while a voltage stimulus decays exponentially relative to the distance from the synapse and with neurotransmitter binding time. The two opposite tendencies suggest the existence of a back-propagating action potential under the homeostatic regulation to avoid the under response. Based on these reasons, we developed the following decoder for correcting errors caused by the encoder in Equation (7).

Definition 7. The multithreshold decoder to correct response errors is given by:

$$\varepsilon_{i,t} = \begin{cases} c_1 & \text{if } Y_{i-1,t} \geq c_1 \\ Y_{i-1,t} & \text{if } c_2 \leq Y_{i-1,t} < c_1 \\ c_2 & \text{if } c_3 \leq Y_{i-1,t} < c_2 \\ v_t^{(1)} & \text{if } Y_{i-1,t} < c_3 \end{cases} \tag{8}$$

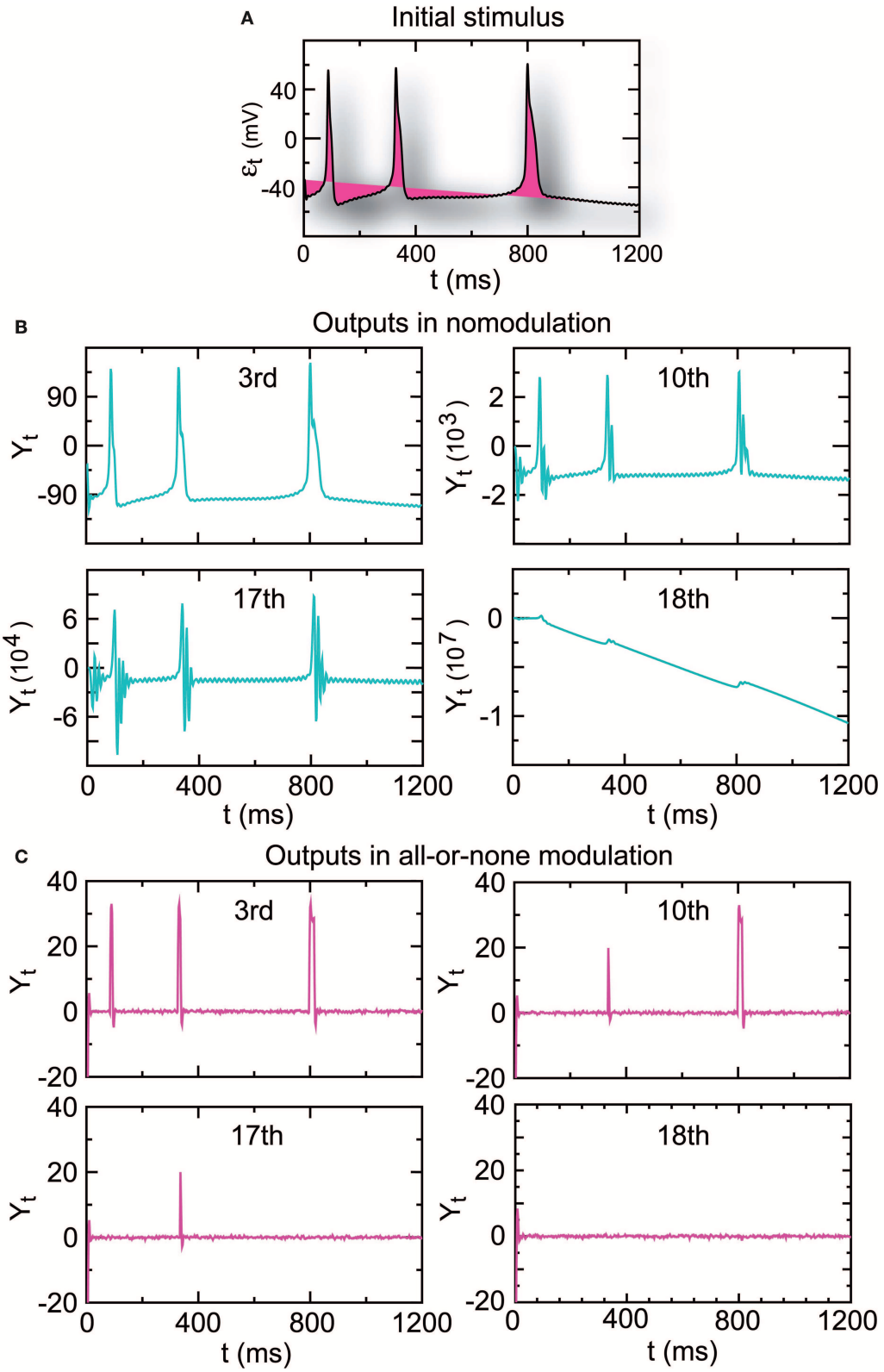

FIGURE 7 | The amplitude of the output spike train driven by real stimuli **(A)** is significantly increased in nomodulation **(B)** and decreased in all-or-none modulation **(C)** by repeatedly running the homeostatic encoder. These results indicate that all-or-none modulation prevents an over response but fails to avoid an under response, which can result in information loss when the encoder is executed repeatedly.

which is the incoming stimulus entering the next neuron in the following encoder:

$$Y_{i,t} = (2-\alpha)\, Y_{i,t-1} - (1-\alpha)\, Y_{i,t-2} + \beta \frac{-Y_{i,t-1}}{\exp\left(Y_{i,t-1}^2\right)} + \varepsilon_{i,t} \quad (9)$$

where c_1, c_2, and c_1 are threshold values; the initial values $Y_{i,-1} = Y_{i,0} = 0$, $\varepsilon_{1,t} = c_1$ if $\varepsilon_t \geq c_1$ and $\varepsilon_{1,t} = \nu_t^{(1)}$ if $\varepsilon_t < c_1$, the initial stimulus variability $\varepsilon_t = \tilde{\varepsilon}_t - \frac{1}{t}\sum_{i=1}^{t} \tilde{\varepsilon}_i$ ($\frac{1}{t}\sum_{i=1}^{t} \tilde{\varepsilon}_i \approx \omega_t$), $\tilde{\varepsilon}_t$ are the synaptic stimulus, and $\nu_t^{(1)}$ represent intrinsic noise and extrinsic or synaptic noise with small variance for $i = 1, \cdots, m$ and $t = 1, 2, \cdots, n$. The encoder–decoder in Equations (8) and (9) describes a propagator of n signals through m relays.

The propagator in Equations (8) and (9) is also suitable for axons because an action potential that initiates in the axon causes back-propagating action potentials—a retrograde signal that travels in the opposite direction (Debanne, 2004) where α and β are the axial resistance and restoration coefficients.

2.2.8. Conditions of Effective SSCCPI Circuit

The above analysis indicated that the precision, speed, and reliability of the SSCCPI circuit depended primarily on rate or temporal coding, rigorous, or near synchronous SSEs, the function of cortical columns, and the signal transfer precision in interneurons. These results led to the following inference:

Inference 1. The SSCCPI circuit is fast, reliable, and precise (or effective) if it satisfies the following conditions:

(i) SSE delivery is at least partial non-overlap of spike trains in interneurons (asynchronous SSEs);
(ii) Cortical columns prevent both repeatedly triggering SSE delivery and incorrectly synaptic connections between adjacent columns; and
(iii) The propagator in interneurons functions as a temporal complete fidelity and reliable information propagator.

The conditions (i) and (ii) are called the effective functions of SSEs and cortical columns, respectively.

2.3. Evidence for Effective SSCCPI Circuit

2.3.1. SSCCPI Scheme

* The SSCCPI circuit follows the leading hypothesis that a synchronous firing chain is connected in a feed-forward manner where nerve impulses travel synchronously back and forth between layers; each neuron in a layer provides an excitatory connection to neurons in the next layer; and each neuron in the receiving layer is excited by neurons in the previous layer proposed by Abeles (1982a, 1991). An effective SSCCPI circuit supports the finding that the network topology of the feed-forward network determines the propagation of synchronous firing chain (Guo et al., 2017; see Han et al., 2015).

2.3.2. Temporal Coding

* Experimental evidence supports temporal coding in the cortex (Abeles et al., 1993; Mainen and Sejnowski, 1995; de Ruyter van Steveninck et al., 1997; Nowak et al., 1997; Riehle et al., 1997; Frisina, 2001; Nemenman et al., 2008; Tiesinga et al., 2008). Most interneurons in subcortical areas utilize temporal coding in processing auditory information (Gao and Wehr, 2015), and temporal information within an acoustic signal is directly represented in the temporal patterns of neural activity throughout most parts of the auditory pathway leading to the auditory cortex (Wang et al., 2008).

2.3.3. Asynchronous SSE Delivery

* High-intensity stimuli from external environment trigger SSEs: Japanese cartoons induce seizures in hundreds of children by intermittent photic stimulation (da Silva and Leal, 2017).
* High-intensity stimuli from task-related actions trigger SSEs: Elective attention and attention switching are fundamental to almost all cognitive tasks, which causes a substantial increase in stimulus intensity. Evidence for task-related SSEs includes that SSEs occur across neurons in the sensorimotor cortex (Murthy and Fetz, 1996) and the primary motor cortex of monkeys in relation to behavior (Riehle et al., 1997; Torre et al., 2016b); transient SSEs correlate not only with behavior but also with a mesoscopic brain signal, corroborating its relevance in cortical processing (Denker et al., 2011); the frequency of synchronous firing is modulated by behavioral performance and is specific for memorized visual stimuli (Pipa and Munk, 2011); neurons can synchronize their spiking in higher cortical areas when monkeys successfully solve visual recognition tasks (Gochin et al., 1994; Anderson et al., 2006) or process facial features (Hirabayashi and Miyashita, 2005); and most neuron pairs in a monkey's secondary somatosensory cortex fire synchronously in switching attention between two different tasks, and the degree of synchrony is affected by the attenuation state (Steinmetz et al., 2000; Roy et al., 2007).
* Response latency induces SSEs: Time delay enhances neural synchrony (Dhamala et al., 2004; Jirsa, 2008).
* Asynchronous SSEs are due primarily to synaptic noise: The uncertainty involved in the exact timing of neurotransmitter release causes synaptic noise even if repeated stimulation with identical stimulus evokes similar but not identical neuronal responses (Softky and Koch, 1992; Mainen and Sejnowski, 1995).
* Asynchronous SSEs relate to healthy neurons in the same areas of the brain fire (Fisher et al., 2005). In contrast, rigorous SSEs relate to brain disorders for Parkinson's disease (Rubchinsky et al., 2012), epilepsy (Jiruska et al., 2013), schizophrenia, autism, and Alzheimer's disease (Uhlhaas and Singer, 2006).
* The response latencies typically become shorter as the stimulus intensity increases (Henry and Lucas, 2008) but are greater at higher synaptic levels regardless of intensity (Klug et al., 2000); the increase in response latency produced by excess GMP is inversely proportional to the stimulus intensity (Nicol and Miller, 1978). The observation suggests the role of SSEs in shortening the wait times. From a commonsense point of view, the higher the signal intensity, the greater the spike density; thus, the waiting time to process the signal, and vice versa. Neuronal latencies can be as small as 0.1 ms and as large

as 44 ms and the first spike latencies range roughly from 5 to 50 ms (Izhikevich, 2006).

Together the above observations support that asynchronous SSEs were usual while synchronous SSEs were unusual; asynchronous SSE delivery improved the transfer speed of high-intensity stimuli by shortening or avoiding the waiting time caused by response latencies.

2.3.4. Parallel Propagation in Minicolumns

* Vertical columns are distributed in numerous cortical areas (Mountcastle, 1957; Buxhoeveden and Casanova, 2002; Opris and Casanova, 2014). Neurons within a minicolumn receive common inputs, have common outputs, and are interconnected (Cruz et al., 2005; Horton and Adams, 2005), which provides the possibility of decomposing the input spike trains and composing the output spike trains. The vibrissae on rodent snouts are topographically represented in the contralateral somatosensory cortex by distinct barrels in layer IV (Woolsey and van der Loos, 1970), which supports information flows in vertical columns starting from layer IV.
* Neurons within a given minicolumn are stereotypically interconnected in the vertical dimension (Rakic, 2008), which prevents repeated SSE delivery and thereby ensures signal parallel propagation within minicolumns.
* Columnar segregation (adjacent columns are segregated) is observed in the cat somatosensory cortex (Mountcastle et al., 1955), macaque somatosensory cortex (Powell and Mountcastle, 1959), and human extrastriate cortex (Horton and Adams, 2005; Tootell and Nasr, 2017). Columnar segregation stays functionally isolated by avoiding indiscriminate connections with local neurons and afferent axons there (Favorov et al., 2015), which prevents information loss and distortion caused by the decomposed propagation.
* The nervous system overwhelmingly prefers parallel computations over serial ones in time-critical applications; upward and downward connections within the thickness of the cortex are much denser than the connections that spread from side to side (Schrader et al., 2009), suggesting a columnar flow of information across layers as well as a laminar flow within some layers (Hawkins et al., 2017).
* The SSCCPI' signal parallel propagation in minicolumns is consistent with Mountcastle's cortical column hypothesis (1957). The latter requires that neurons in middle layers of the cortex, in which thalamic afferents terminate, should be joined by narrow vertical connections to cells in layers lying superficially and deep from them, so that all neurons in the column are excited by incoming stimuli with only small latency differences (Jones, 2000).

2.4. Evidence for Effective Encoder-Decoder

2.4.1. Neural Basis of Multithreshold Decoder

* All-or-none modulation is a rule of a neuron's stimulus-response. Recent research shows that visual perception of simple stimuli is associated with an all-or-none cortical evoked response, the temporal precision of which varies as a function of perceptual strength (Sekar et al., 2012).
* Evidence suggests that active backpropagation facilitates the return of the attenuated stimulus to the original level by augmenting it with its previous excessive current: (i) An action potential that initiates in the cell body evokes a voltage spike to the axonal ending and then back through to the dendritic arbors; the basal, oblique, apical trunk; and tuft dendrites (Stuart and Sakmann, 1994; Waters et al., 2003) from which much of the original current originates. (ii) Backpropagation typically occurs only when the cell is activated to fire an action potential, and the extent of this backpropagation increases with the number and frequency of action potentials and depends on subthreshold excitatory inputs (Larkum et al., 1999), on the preceding rate of depolarization (Azouz and Gray, 2000, 2003) and on the preceding interspike intervals (Henze and Buzsáki, 2001; Badel et al., 2008).
* Graded potentials are on the same scale as the magnitude of stimuli (Purves et al., 2008) and subsequently influence transmembrane ion flow to either increase (excitatory) or decrease (inhibitory) the opportunity to fire. Effects of graded potentials are observed to be additive. Stimulus responses can be summed to increase the amplitude of graded potentials both spatially (multiple simultaneous inputs) and temporally (repeated inputs). Summation is the additive effect of multiple subthreshold graded postsynaptic potentials that determines whether the membrane potential will reach the threshold potential to generate an action potential. Hence, additive effects of graded potentials enable active backpropagation to facilitate the stimulus reconstruction.
* Threshold variation has been observed *in vivo* (Azouz and Gray, 1999; Henze and Buzsáki, 2001; Naundorf et al., 2006; McCormick et al., 2007; Yu et al., 2008), which provides evidence for multithreshold amplitude modulations. The multiple appropriate thresholds can be viewed as the result of evolution.

In summary, together all-or-none modulation, active backpropagation, additive graded potentials, and multithreshold amplitude modulations are neural evidence supporting the decoder in Equations (8) and (9). The all-or-none modulation and active backpropagation play the following key roles: (i) the neural response to stimulus at any strength above the threshold is the same; (ii) no action potential occurs if a neuron does not reach the threshold; and (iii) previous excessive currents compensate for the attenuated synaptic stimulus. Role (ii) prevents an over response that may cause signal distortion or incorrectly identify a noise as a signal. Role (iii) avoids an under response that may cause signal loss by receiving previous excessive current due to Role (i).

2.4.2. Stable Fixed-Point Homeostatic Encoder

According to the current viewpoint, action potential encoding is implemented by transitions between a stable fixed point and a stable periodic cycle. The theoretical parameter intervals of the NLARI process are given by $0 < \alpha < 2, 0 < \beta < 4$, and $0 < \gamma < 1$ for the stable fixed point and $0 < \alpha < 2, 0 < \beta < 4\sqrt{e}$, and

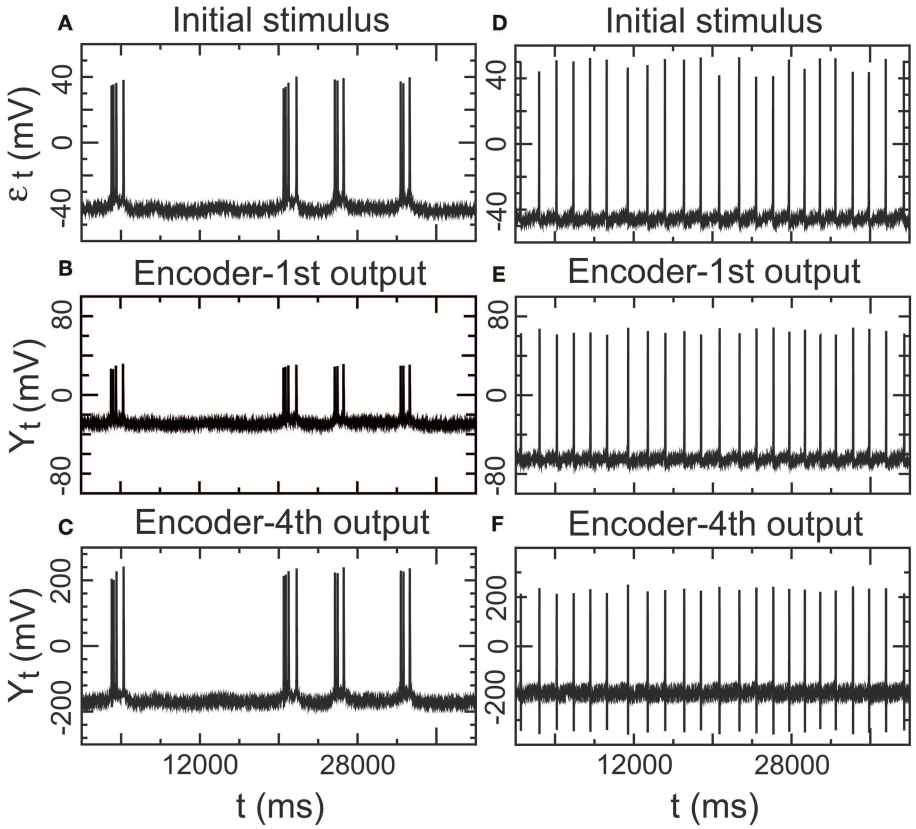

FIGURE 8 | Performance of the encoder in nomodulation using real low-density inputs. **(A)** Initial stimulus: membrane potentials recorded 20 min after the administration of paeonol. **(B)** First encoder output driven by the initial stimulus **(A)**. **(C)** Fourth encoder output based on the initial stimulus **(A)**. **(D)** Initial stimulus: spontaneous action potentials (no paeonol). **(E)** First encoder output driven by the initial stimulus **(D)**. **(F)** Fourth encoder output based on the initial stimulus **(D)**. These results showed that the encoder could exactly encode stimulus input with low density in a simple neural circuit with a few interneurons.

$1 < \gamma < \sqrt{e}$ for the stable periodic cycle where $\gamma = \beta/(4 - 2\alpha)$ (for aperiodic cycles and chaos see He, 2018). Thus, we focused on identifying whether the NLARI's parameter values in Equation (4) lied alternately in the theoretical intervals of the stable fixed point and periodic cycle for real data by carrying out simulations. Independent evidence for precise spike timing in cortical neurons comes from intracellular recordings *in vitro*. Thus, we adopted intracellular recordings from the right parietal 4 (RP4) neuron of a snail elicited by the application of paeonol as the received stimuli entering the encoder. The recordings were made by the method described by Chen et al. (2010).

Surprisingly, our statistical results indicated that the dynamic mechanism of action potential encoding was a single stable fixed point, but not transitions between a stable fixed point and a stable periodic cycle or a single stable periodic cycle. This is because all the confidence intervals of these parameters lied inside the theoretical parameter intervals for a single stable fixed point at the 99% confidence level for all the recordings. This result could be viewed as a consequence of ionic homeostatic regulation for maintaining the resting potential. Whether the stability coefficient lies in $(0, 1)$ or $\left(1, \sqrt{e}\right)$ crucially determines whether the encoding dynamic mechanism is the stable fixed point or the stable periodic cycle. The stability coefficient comprises the membrane resistance coefficient and the membrane restoration coefficient. The permeability of ionic channels causes the membrane resistance, preventing rapid changes in the membrane potential. The electrochemical driving force restores the changed membrane potential into the resting potential by driving Na^+ and K^+ ion influx/efflux across the membrane and synaptic plasticity of strengthening/weakening between neighboring synapses in response to increases and decreases in their activity. Homeostasis is the most basic way the body maintains a stable internal environment. Ionic homeostasis supports a stable fixed-point encoder by regulating changes to synaptic size, synaptic strength, and ion channel function in the membrane (for recent study see Davis and Bezprozvanny, 2001).

Furthermore, we assessed the performance of the encoder as a propagator with an encoder in Equation (7) in nomodulation by the degree of consistency between the input and output spike trains of the encoder. **Figure 8A** presents intracellular recordings from the right parietal 4 (RP4) neuron of a snail elicited by the application of paeonol. **Figure 8D** presents intracellular recordings from the spontaneous action potentials (no paeonol) for the same neuron. All of the first outputs ($Y_{1,t}$) of the encoder

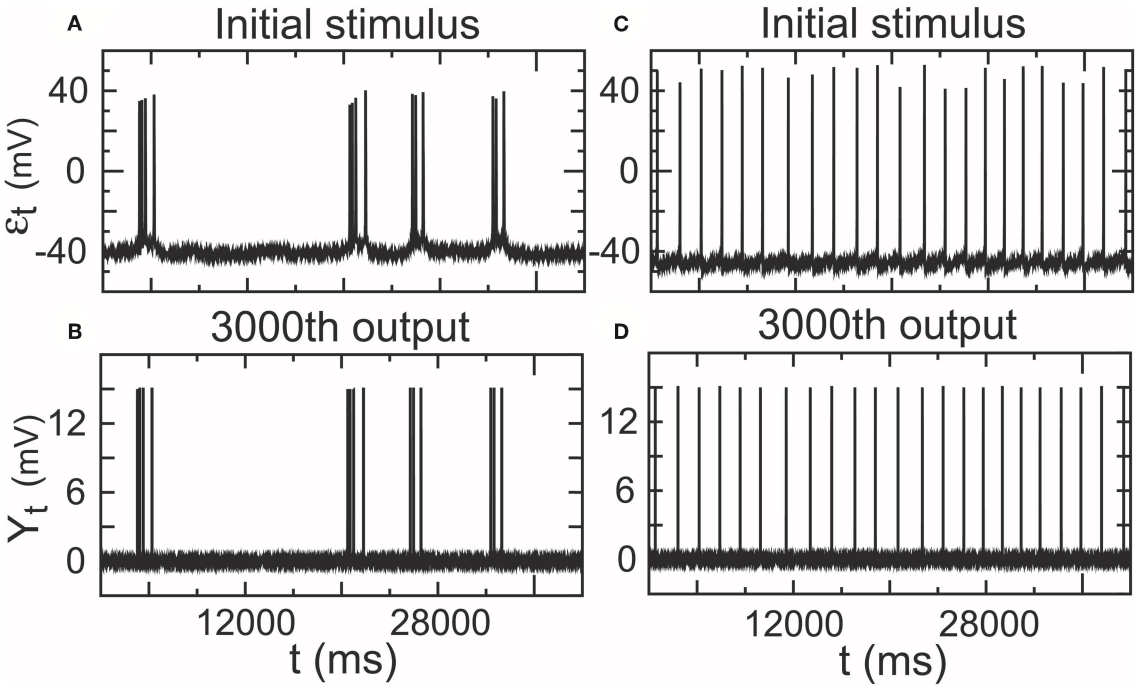

FIGURE 9 | Performance of the encoder–decoder in all-or-none modulation using real low-density inputs. **(A)** Initial stimulus: membrane potentials recorded 20 min after the administration of paeonol. **(B)** 3,000th output of the encoder–decoder based on the initial stimulus **(A)**. **(C)** Initial stimulus: spontaneous action potentials (no paeonol). **(D)** 3,000th output of the encoder–decoder based on the initial stimulus **(C)**. These results showed that the encoder–decoder could exactly encode stimulus input with low density in a complex cortical circuit with many interneurons.

in **Figures 8B,E** and the fourth outputs ($Y_{4,t}$) of the encoder in **Figures 8C,F** were consistent with their received stimuli. This result showed that neuronal responses to background stimuli resembled the stimuli and that the encoder exactly predicted information transfer through a few relays. Additionally, we again observed that nerve impulses were significantly enlarged in the firing as shown in **Figure 7**, which reflected the phenomenon that the opening of voltage-gated channels trends to elicit significantly larger currents than the original stimulus.

2.4.3. Temporal Precision in Real Low Density Inputs

We proved that the encoder-decoder in Equations (8) and (9) was a complete fidelity information propagator as an important condition for an effective SSCCPI circuit. The propagation success rates of the two real input spike trains through 3,000 interneurons could reach 100.00% for the lower density spike train (the application of paeonol) and 99.85% for the higher density spike train (no paeonol). These results satisfied the condition that the encoder-decoder was a complete fidelity information propagator.

Furthermore, we showed that the encoder-decoder in all-or-none modulation gave a good performance that simulated information transfer through 3,000 relays by repeatedly operating the propagator for $m = 3,000$ times initiated by the two real spike trains mentioned above. The outputs ($Y_{3,000,t}$) (**Figures 9C,D**) for the propagator generated by Equations (8) and (9) exhibited consistent trajectories with the initial stimulus (ε_t) (**Figures 9A,B**).

2.4.4. Temporal Precision in Fitting High Density Inputs

In the above simulation studies, we adopted low density stimuli as an input spike train. Recent research indicates that the primary auditory cortex uses a temporal representation to encode slowly varying acoustic signals and a firing rate-based representation to encode rapidly changing acoustic signals (Wang et al., 2008). For this reason, we need to investigate whether the temporal encoder–decoder in Equations (8) and (9) is still a complete fidelity information propagator initialized by high density stimuli. In addition, it is not clear how the decoder in Equation (8) corrects the error of the encoder in Equation (9). Hence, we carried the following simulation. Let a random sound generator produce a spike train with high density spike trains as an original signal input (**Figure 10A**). The fitting initial stimulus input was received by all-or-none modulation ($\varepsilon_{1,t}$) (**Figure 10B**). Although the first output of the encoder ($Y_{1,t}$) somewhat deviated from the initial stimulus (**Figure 10C**), the deviation was removed by the decoder. In the first output of the decoder, the signal had already returned to its initial state ($\varepsilon_{2,t}$) (**Figure 10D**). The 3, 000th output of the encoder ($Y_{3000,t}$) deviated (**Figure 10E**), but the decoder corrected this deviation ($\varepsilon_{3000,t}$) (**Figure 10F**). The simulation result proved that the encoder–decoder retained good performances at high firing rates.

2.4.5. Temporal Reliability of Encoder-Decoder

According to our analysis, the SSCCPI transfer reliability relies on the reliability of single-neuron (or interneuron) transfer

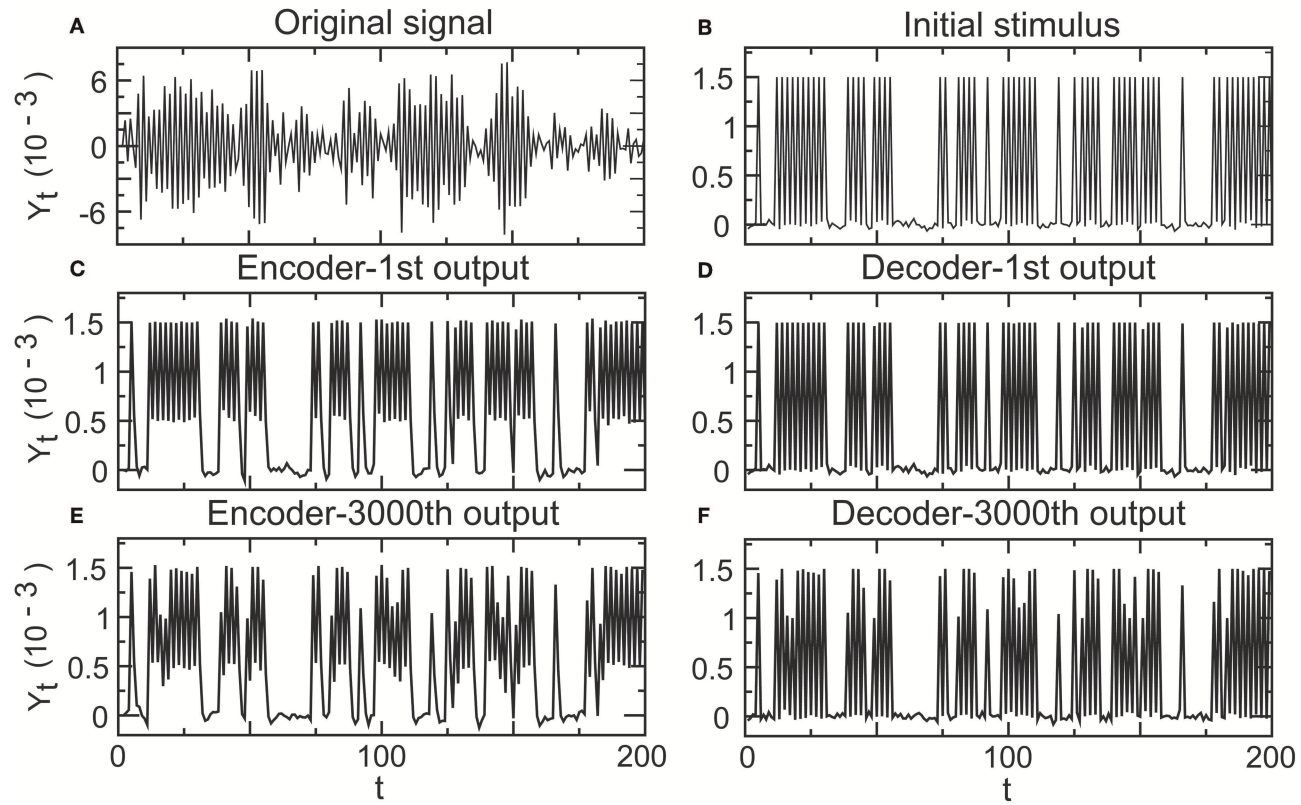

FIGURE 10 | Performance of the encoder–decoder in simulated high-density inputs. **(A)** Original signal: a realization of a sound wave simulator. **(B)** Initial stimulus received by all-or-none modulation. **(C)** First encoder output driven by the initial stimulus. **(D)** First decoder output for correcting the error of the first encoder output. **(E)** 3,000th encoder output based on the initial stimulus. **(F)** 3,000th decoder output for correcting the error of the 3,000th encoder output.

precision if SSE delivery and cortical columns function normally. Thus, we focused on identifying whether the single-neuron transfer precision was influenced by irregular stimuli. To address this issue, we investigated whether there was distinct difference between the precision of one transmission and the average precision of numerous transmissions.

The cerebral cortex typically consists of the six-layered neocortex. If each layer contains at least one interneuron, then the number of interneurons through which signal is transmitted is at least six. For this reason, we considered the number of relays to be 6 and 3000. Each spike train comprised 200 signal points. The original stimuli were generated by the realization of a random sound generator by Equation (4) where the stimuli represented a rapidly changing signal but not a constant stimulus. We simulated the transfer of spike trains driven by one firing and 3,000 firings by repeatedly operating the propagator in Equations (8) and (9) once and 3, 000 times. We calculated the propagation success rates of one transmission and the average propagation success rates of 10,000 transmissions across the stable fixed-point range by increasing the stability coefficient value from 0 to 1 based on Equations (2) and (3).

Figure 11 presented the distribution of these propagation success rates in the stable fixed-point range. The propagation success rate was above 99.982% in $0.118 < \gamma < 0.209$ and 99.974% in $0.500 < \gamma < 0.613$ for six relays (**Figure 11A**), and above 99.986% in $0.118 < \gamma < 0.209$ and 99.982% in $0.500 < \gamma < 0.575$ for 3,000 relays (**Figure 11B**). In contrast, the propagation success rates were under 89% outside the interval $0.099 < \gamma < 0.797$ for six relays (**Figure 11A**) and 82% outside the interval $0.11 < \gamma < 0.77$ for three-thousand relays (**Figure 11B**). According to the results obtained in section 2.2.2, the SSCCPI propagation success rate achieved above 97% for 80 and 74% for 1,000 receiving neurons inside the intervals $0.118 < \gamma < 0.209$ and $0.500 < \gamma < 0.575$ where the single-neuron propagation success rate was above 99.97%, but was almost zero for 80 receiving neurons outside the interval $0.0997 < \gamma < 0.798$ where the single-neuron propagation success rate was under 89%.

From **Figure 11** we surprisingly discovered that there was no distinct difference between the single-neuron transfer precision of one firing and the average transfer precision of many firings in the stable fixed-point range. In particular, there was almost no difference in the complete success propagation interval. This result suggested that the influence of firing irregularity on the transfer precision was not distinct, especially for complete temporal fidelity transfer. We see that an appropriately large stability coefficient played the key role in the achievement of high transfer precision and reliability in single neurons, while the effects of firing irregularity and relay number were not

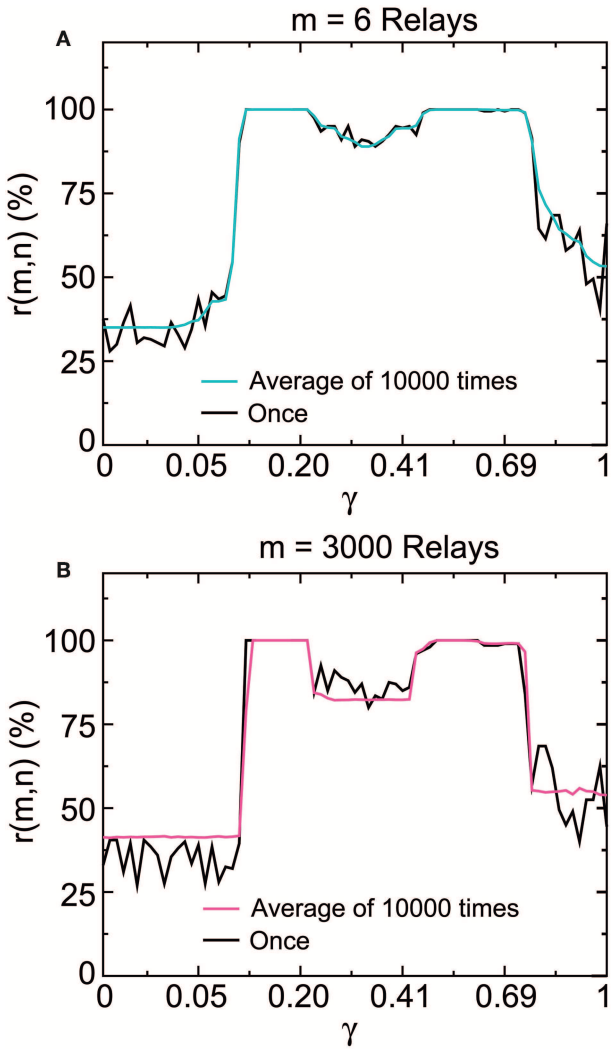

FIGURE 11 | SSCCPI transfer reliability in simulated high-density inputs. Comparison of the propagation success rate of one realization with that of the average over 10,000 realizations by running the encoder–decoder 6 times (6 relays) **(A)** and 3,000 times (3,000 relays) **(B)** where the signal number is 200. These results indicated that SSCCPI transfer precision remained reliable under the irregular firing condition if relay single-neuron transfer was completely successful in a temporally precise manner.

distinct. The ionic homeostasis regulating the stability coefficient into an appropriate stable fixed-point range for the complete propagation success could be regarded as a result of long term evolution.

Our simulation results indicated that the encoder-decoder could be a complete fidelity and reliable information propagator of temporal information in certain specific stable fixed-point interval. Experimental evidence supports temporal precision with millisecond fidelity and reliability (Abeles et al., 1993; Mainen and Sejnowski, 1995; de Ruyter van Steveninck et al., 1997; Ikegaya et al., 2004; Gollisch and Meister, 2008; Nemenman et al., 2008; Tiesinga et al., 2008).

3. DISCUSSION

In this study, we proposed the SSCCPI circuit in a cortical network model for cortical mechanisms of high intensity signal transfer over a background of irregular firing and response latency. We hypothesized that a thalamic high-intensity stimulus input triggered SSEs, and dense spikes were scattered to many receiving neurons within a cortical column in layer IV. Then, many sparse spike trains from the receiving neurons as signals for reversible disassembly were propagated in parallel by the propagator (encoder–decoder) in interneurons along minicolumns through layers II/III with less latency and finally integrated into an output spike train toward or in layer Va. The encoder in interneuron of minicolumns was derived by modeling the membrane potential in response to stimulus as the input and output in a stochastic resilience system using the NLARI process. The multithreshold decoder was introduced to correct encoding errors. We derived the conditions for an effective (fast, reliable, and precise) SSCCPI circuit: SSEs were asynchronous (near synchronous or at least partial non-overlap); critical columns had the capability to prevent both repeated SSE deliveries and incorrect synaptic connections between adjacent columns; and the encoder-decoder in interneurons was a temporal complete fidelity and reliable information propagator. There is evidence supporting the effective transfer functions of SSEs and cortical columns. An increasing body of real evidence suggests that the neuronal coding could be a temporal fidelity and reliable information propagator. Our simulations demonstrated that the encoder-decoder could be temporal complete fidelity and reliable in certain special intervals contained within the stable fixed-point range. Moreover, the encoder-decoder simulated the mechanism by which incoming and outgoing impulses of each neuron remain temporally equational each time by achieving the response error correction at the next fire command. This result explained why the influence of relay number on the signal propagation precision was not distinct.

Our findings also include the following: (i) The transfer speed in the SSCCPI circuit depended crucially on the degree of non-overlap of SSE delivery: the higher the non-overlap, the faster the transfer speed, which reflected the key role of synaptic noise in improving the signal transfer speed. (ii) When SSEs and cortical columns have effective transfer functions, the SSCCPI' reliability depended on the reliability of the single-neuron propagator. (iii) A temporal complete fidelity propagator was reliable and the effect of firing irregularity on the single-neuron transfer precision was not distinct. (iv) Substantially increased output firing rates resulted from rigorous SSEs plus the interneuron-transfer mistake in a shift in spike timing or the rise of a spike, while any change in the output spike train was unlikely to result from asynchronous SSEs plus any single-neuron transfer mistakes. (v) Asynchronous SSEs were a cortical population response to high-intensity thalamic inputs, whereas rigorous SSEs might be viewed as a cortical population response to ultrahigh-intensity thalamic inputs or neural damage that significantly reduced the limiting ability of individual neurons to process information. (v) The dynamic mechanism of action potential encoding was a single stable fixed point, which was

attributed to ionic homeostasis, but not transitions between a fixed point and a limit cycle. (vi) All-or-none modulation prevented an over response but failed to correct an under response. (vii) Backpropagation corrected an under response. (viii) There has been a long-standing debate about the function of SSEs (Abeles, 1982b; Shadlen and Movshon, 1999; Singer, 1999; Pipa and Munk, 2011). Cortical columns are thought to have a structure without a function (Horton and Adams, 2005). Here we hypothesized that a high-intensity thalamic input triggers SSEs. Moreover, we hypothesized that cortical columns prevented repeatedly triggering SSE delivery and fast parallel propagation within minicolumns and information loss caused by the disassembly propagation.

The present results suggest that any neural alterations in the SSCCPI circuit possibly cause brain disorders and thereby may give an insight into the exact etiologies of neurocognitive disorders. For example, according to our analysis, rigorous SSEs plus a single-neuron transfer mistake may induce substantially increased output firing rates as seen in an epileptic seizure; the breakdown of columnar segregation may destroy information during disassembly-parallel propagation through one layer to the next, which may cause cognitive disease. Additionally, this study introduced the membrane potential waveform indicators to assess the influence of synaptic stimulation input on the membrane potential. Together with the wave indicators, the SSCCPI circuit may be applied to the signal processing pathways in cognitive tasks. We expect that these issues will attract more attention and intensive research.

4. METHODS

4.1. Datasets

The real spike trains were intracellular recordings from the right parietal 4 (RP4) neuron of a snail elicited by the application of paeonol (the dataset and programs are presented in **Supplementary Table 1**). Neuronal recordings were obtained with the method described by Chen et al. (2010).

4.2. Statistical Method

4.2.1. Estimations of the Waveform Indicators for (Figure 6)

Let $\Delta Y_t = Y_t - Y_{t-1}$. Equation (4) can be rewritten as:

$$\Delta Y_t = \theta_1 \Delta Y_{t-1} + \theta_2 \frac{-Y_{t-1}}{e^{Y_{t-1}^2}} + \varepsilon_t \tag{10}$$

Note that $Y_t = X_t - X_0 - (\omega/\alpha)\, t$ in Equation (10). Consider the regression line $X_t = a + bt + u_t$ where $a = X_0$ and $b = \omega/\alpha$. We obtained the estimates $\hat{a}$ and $\hat{b} = \hat{\omega}/\hat{\alpha}$ by estimating the regression line using the ordinary least squares (OLS) method with real data $\{X_t\}$. We got the OLS estimates $\hat{\theta}_2 = \hat{\beta}$ and $\hat{\sigma}$ by estimating (Equation 10) using data $\{Y_t\}$ where $Y_t = X_t - \hat{a} - \hat{b}t$. Then, the slope indicator and amplitude indicators were given by $\eta_1 = \hat{b}$ and $\eta_2 = \hat{\sigma}/\hat{\beta}$.

4.2.2. Parameter Estimations for (Figures 7–9)

The NLARI's stable fixed point is exponentially asymptotically stable but not globally stable (He, 2013), which implies that a large stimulus may trigger a poor response. Decreasing the absolute values of the data can usually prevent this problem (He, 2014). Therefore, to make good estimates, we first performed data preprocessing by letting $Y_t =$ real data/1,000 where Y_t were real data or simulated data generated by Equation (4). Thus, we estimated (Equation 10) and obtained the estimates $\hat{\alpha} = 1 - \hat{\theta}_1$, $\hat{\beta} = \hat{\theta}_2$, and $\hat{\gamma} = \hat{\beta}/\left(4 - 2\hat{\alpha}\right)$.

4.2.3. Testing for the Stable Fixed-Point Encoder in Equation (4)

For the NLARI's stable fixed-point range, the theoretical intervals of the parameters α, β, and γ are given by $(-1, 1)$, $(0, 4)$, and $(0, 1)$, respectively (for more detailed information see He, 2014). The confidence intervals of these parameters for large samples are based on the standard normal distribution. When the γ value is significantly greater than zero, the hypothesis tests whether real data are generated by the NLARI process in the stable fixed-point range can be achieved by a confidence interval approach for the standard normal distribution. Therefore, in this case, we only need to perform a test to determine whether the confidence intervals $\hat{\theta}_1 \pm z_0 s\sqrt{s^{11}}$ for α, $\hat{\theta}_2 \pm z_0 s\sqrt{s^{22}}$ for β, and $\hat{\gamma} \pm z_0 \hat{\sigma}_{\hat{\gamma}}$ for γ lie in the intervals $(-1, 1)$, $(0, 4)$, and $(0, 1)$, respectively, where z_0 represents a critical value at a common significance level for the t distribution (e.g., the critical value of 1.645 is significant with ∞ at the 0.05 level in right-hand-tail). Our results based on the OLS estimates of Equation (10) indicated that all the parameter estimations based on the recordings used in this study fell significantly inside the theoretical intervals for the stable fixed-point range.

4.3. Simulation Method

We calculated the outputs of the propagator in Equation (7) initiated by real neuronal data for **Figures 7**, **8**, in Equations (8) and (9) initiated by real neuronal data for **Figure 9**, in Equations (8) and (9) initiated by a random stimulator for **Figure 10**, and the propagation success rate based on Equations (1) and (2) by repeatedly running the propagator in Equations (8) and (9) initiated by a random stimulator for **Figure 11**.

4.3.1. Calculations for (Figures 7–9)

The calculation results were obtained by performing the following steps:

Step 1. Initial values: Raw data set contains 20,000 points from 1 to 40,000 ms in increments of 2 ms. The initial stimuli were given by $\tilde{\varepsilon}_t =$ real data/1,000 in **Figures 7**, **8** and $\varepsilon_t = \tilde{\varepsilon}_t - \frac{1}{t}\sum_{i=1}^{t} \tilde{\varepsilon}_i$ in **Figure 9** where the real data were recordings for paeonol at a concentration of ≥ 1.2 mmol/L in **Figures 7A–9A** and recordings for no paeonol in **Figures 8D**, **9C**. Select the parameters of the encoder $\gamma \in (0.27, 0.41)$, $\alpha \in (0, 2)$, and $\beta = \gamma\,(4 - 2\alpha)$ (e.g., $\alpha = 0.71$, $\beta = 0.7$, $\gamma = 0.2713$) and the parameters of the decoder $c_1 = 0.0015$, $c_2 = 0.0010$, $c_3 = 0.0008$, and $\sigma_1 = 2^{-6}$. Let $n = 600$ and $m = 3, 10, 17, 18$ in **Figure 7**, $n = 20,000$ and $m = 1, 4$ in **Figure 8**, and $n = 20,000$ and $m = 3,000$ in **Figure 9**.

Step 2. Encoder: Produce the outputs of the encoder $Y_{i,t}$ in Equation (7) in nomodulation in **Figures 7B**, **8B,C,E,F**, the encoder $Y_{i,t}$ in Equation (7) in all-or-none modulation by $\varepsilon_{1,t} = c_1$ if $\varepsilon_t \geq c_1$, $\varepsilon_{1,t} = v_t^{(1)}$ if $\varepsilon_t < c_1$, and $Y_{i-1,t} = c_1$ if $Y_{i-1,t} \geq c_1$

and $Y_{i-1,t} = v_t^{(1)}$ if $Y_{i-1,t} < c_1$ for $i \geq 2$ in **Figure 7C**.

Step 3. Encoder-Decoder: Produce the outputs of the encoder $Y_{i,t}$ in Equation (9) and the decoder value $\varepsilon_{i,t}$ were given by Equation (8) in **Figures 9B,D**.

Step 4. Outputs: The final outputs of the encoder and the decoder were given by $\hat{Y}_{i,t} = 10^5 \times Y_{i,t}$ and $\hat{\varepsilon}_{i,t} = 10^5 \times \varepsilon_{i,t}$ where $t = 1, \cdots, n$ and $i = 1, \cdots, m$.

4.3.2. Calculations for (Figures 10, 11)

The simulation results were obtained by performing the following steps:

Step 1. Initial values: Produce the initial stimulus ε_t by $\varepsilon_t = c_1$ if $Y_t \geq c_1$ and $\varepsilon_t = v_t^{(1)}$ if $Y_t < c_1$ where the original signal Y_t was generated by Equation (4) based on $\alpha = 0.71$, $\beta = 0.70$, $\gamma = 0.97$, $\sigma = 0.0011$, and Gaussian white noise $v_t^{(1)} \sim i.i.d.N\left(0, \sigma_1^2\right)$ with $\sigma_1 = 2.7 \times 10^{-5}$ for $n = 200$.

Step 2. Encoder-Decoder: Produce the output of the encoder $Y_{i,t}$ in Equation (9) based on $\alpha = 1 - 0.005j$, $\gamma = 0.0133j$, and $\beta = \gamma\,(4 - 2\alpha)$ for $j = 25$ (i.e., $\alpha = 0.8750$, $\beta = 0.7481$, and $\gamma = 0.3325$) and the decoder $\varepsilon_{i,t}$ in Equation (8) driven by the initial stimulus ε_t based on $c_1 = 0.0015$, $c_2 = 0.0010$, $c_3 = 0.0008$ for $n = 200$ and $m = 1, 100, 3, 000$.

Step 3. Success Rate: Calculate the propagation success rate $r\,(m,n)_j$ by Equation (1) where the initial input $\mathbf{v}_0$ and the final output $\mathbf{v}_m$ are defined by (Equation 2).

Step 4. Average Success Rate: Repeat Steps 1 to 3 for $T = 10,000$ to calculate $r\,(m,n) = \frac{1}{T}\sum_{j=1}^{T} r\,(m,n)_j$.

Step 5. Average Success Rate Distribution: Repeat Steps 1 to 4 for $\gamma = 0.0133k$ within $(0,1)$, $\alpha = 1 - 0.005k$, $\beta = \gamma\,(4 - 2\alpha)$ for $k = k + 1$ from $k = 1$ to $k = 75$.

DATA AVAILABILITY

All datasets generated for this study are included in the manuscript and the **Supplementary Files**.

AUTHOR CONTRIBUTIONS

The author confirms being the sole contributor of this work and has approved it for publication.

ACKNOWLEDGMENTS

This author would like to give special thanks to Yi-Hong Chen of China Medical University (Taiwan) for providing the membrane potential recording data used in the current study. The authors would further like to thank the two reviewers and the editor for their insightful comments and helpful suggestions on an earlier version of this article.

SUPPLEMENTARY MATERIAL

The Supplementary Material for this article can be found online at: https://www.frontiersin.org/articles/10.3389/fncom.2019.00057/full#supplementary-material

Supplementary Table 1 | Real dataset and programs.

REFERENCES

Abbott, L. F., DePasquale, B., and Memmesheimer, R. M. (2016). Building functional networks of spiking model neurons. *Nat. Neurosci.* 19, 350–355. doi: 10.1038/nn.4241

Abeles, M. (1982a). *Local Cortical Circuits: An Electrophysiological Study*. Berlin: Springer.

Abeles, M. (1982b). Role of the cortical neuron: integrator or coincidence detector? *Isr. J. Med. Sci.* 18, 83–92.

Abeles, M. (1991). *Corticonics Neural Circuits of the Cerebral Cortex*. Cambridge: Cambridge University Press.

Abeles, M., Bergman, H., Margalit, E., and Vaadia, E. (1993). Spatiotemporal firing patterns in the frontal cortex of behaving monkeys. *J. Neurophysiol.* 70, 1629–1638.

Abeles, M., and Gerstein, G. L. (1988). Detecting spatiotemporal firing patterns among simultaneously recorded single neurons. *J. Neurophysiol.* 60, 909–924.

Anderson, B., Harrison, M., and Sheinberg, D. L. (2006). A multielectrode study of the inferotemporal cortex in the monkey: effects of grouping on spike rates and synchrony. *Neuroreport* 17, 407–4011. doi: 10.1097/01.wnr.0000203349.22128.e0

Azouz, R., and Gray, C. M. (1999). Cellular mechanisms contributing to response variability of cortical neurons *in vivo*. *J. Neurosci.* 1, 2209–2223.

Azouz, R., and Gray, C. M. (2000). Dynamic spike threshold reveals a mechanism for synaptic coincidence detection in cortical neurons *in vivo*. *Proc. Natl. Acad. Sci. U.S.A.* 97, 8110–8115. doi: 10.1073/pnas.130200797

Azouz, R., and Gray, C. M. (2003). Adaptive coincidence detection and dynamic gain control in visual cortical neurons *in vivo*. *Neuron* 37, 513–523. doi: 10.1016/S0896-6273(02)01186-8

Badel, L., Lefort, S., Brette, R., Petersen, C. C. H., Gerstner, W., and Richardson, M. J. (2008). Dynamic I–V curves are reliable predictors of naturalistic pyramidal-neuron voltage traces. *J. Neurophysiol.* 99, 656–666. doi: 10.1152/jn.01107.2007

Buonomano, D. V., and Merzenich, M. M. (1998). Cortical plasticity: from synapses to maps. *Annu. Rev. Neurosci.* 21, 149–186.

Buxhoeveden, D. P., and Casanova, M. F. (2002). The minicolumn hypothesis in neuroscience. *Brain* 125, 935–951. doi: 10.1093/brain/awf110

Castejon, C., and Nuñez, A. (2016). Cortical neural computation by discrete results hypothesis. *Front. Neural Circuits* 10:81. doi: 10.3389/fncir.2016.00081

Chen, Y. H., Lin, P. L., Hsu, H. Y., Wu, Y. T., Yang, H. Y., Lu, D. Y., et al. (2010). Action potential bursts in central snail neurons elicited by paeonol: roles of ionic currents. *Acta Pharmacol. Sin.* 31, 1553–1563. doi: 10.1038/aps.2010.156

Cruz, L., Buldyrev, S. V., Peng, S., Roe, D. L., Urbanc, B., Stanley, H. E., et al. (2005). A statistically based density map method for identification and quantification of regional differences in microcolumnarity in the monkey brain. *J. Neurosci. Meth.* 141, 321–332. doi: 10.1016/j.jneumeth.2004.09.005

da Silva, A. M., and Leal, B. (2017). Photosensitivity and epilepsy: current concepts and perspectives-A narrative review. *Seizure* 50, 209–218. doi: 10.1016/j.seizure.2017.04.001

Davis, G. W., and Bezprozvanny, I. (2001). Maintaining the stability of neural function: a homeostatic hypothesis. *Annu. Rev. Physiol.* 63, 847–869. doi: 10.1146/annurev.physiol.63.1.847

de Ruyter van Steveninck, R. R., Lewen, G. D., Strong, S. P., Koberle, R., and Bialek, W. (1997). Reproducibility and variability in neural spike trains. *Science* 275, 1805–1808.

Debanne, D. (2004). Information processing in the axon. *Nat. Rev. Neurosci.* 5, 304–316. doi: 10.1038/nrn1397

Deco, G., Jirsa, V. K., Robinson, P. A., Breakspear, M., and Friston, K. (2008). The dynamic brain: from spiking neurons to neural masses and cortical fields. *PLoS Comput. Biol.* 4:e1000092. doi: 10.1371/journal.pcbi.1000092

Denker, M., Roux, S., Lind, H., Diesmann, M., Riehle, A., and Grün, S. (2011). The local field potential reflects surplus spike synchrony. *Cereb. Cortex* 21, 2681–2695. doi: 10.1093/cercor/bhr040

Dhamala, M., Jirsa, V. K., and Ding, M. (2004). Enhancement of neural synchrony by time delay. *Phys. Rev. Lett.* 92:074104. doi: 10.1103/PhysRevLett.92.074104

Diesmann, M., Gewaltig, M. O., and Aertsen, A. (1999). Stable propagation of synchronous spiking in cortical neural networks. *Nature* 402, 529–533.

Dubyak, G. R. (2004). Ion homeostasis, channels, and transporters: an update on cellular mechanisms. *Adv. Physiol. Educ.* 28, 143–154. doi: 10.1152/advan.00046.2004

Favorov, O. V., Whitsel, B. L., and Tommerdahl, M. (2015). "Discrete, place-defined macrocolumns in somatosensory cortex: lessons for modular organization of the cerebral cortex," in *Recent Advances on the Modular Organization of the Cortex*, eds M. F. Casanova and I. Opris (Dordrecht: Springer Science+Business Media), 143–155. doi: 10.1007/978-94-017-9900-3-9

Fisher, R. S., Van Emde Boas, W., Blume, W., Elger, C., Genton, P., Lee, P., et al. (2005). Epileptic seizures and epilepsy: definitions proposed by the International League Against Epilepsy (ILAE) and the International Bureau for Epilepsy (IBE). *Epilepsia* 46, 470–472. doi: 10.1111/j.0013-9580.2005.66104.x

Frisina, R. D. (2001). Subcortical neural coding mechanisms for auditory temporal processing. *Hear. Res.* 158, 1–27. doi: 10.1016/S0378-5955(01)00296-9

Fritz, J. B., Elhilali, M., and Shamma, S. A. (2005). Differentialdynamic plasticity of A1 receptive fields during multiple spectraltasks. *J. Neurophysiol.* 25, 7623–7635. doi: 10.1523/JNEUROSCI.1318-05.2005

Fritz, J. B., Elhilali, M., and Shamma, S. A. (2007). Adaptive changesin cortical receptive fields induced by attention to complex sounds. *J. Neurophysiol.* 98, 2337–2346. doi: 10.1152/jn.00552.2007

Fritz, J. B., Shamma, S. A., Elhilali, M., and Klein, D. (2003). Rapid task-related plasticity of spectrotemporal receptive fields in primaryauditory cortex. *Nat. Neurosci.* 6, 1216–1223. doi: 10.1038/nn1141

Fuhrmann, G., Segev, I., Markram, H., and Tsodyks, M. (2002). Coding of temporal information by activity-dependent synapses. *J. Neurophysiol.* 87, 140–148. doi: 10.1152/jn.00258.2001

Gao, X., and Wehr, M. (2015). A coding transformation for temporally structured sounds within auditory cortical neurons. *Neuron* 86, 292–303. doi: 10.1016/j.neuron.2015.03.004

Gautrais, J., and Thorpe, S. (1998). Rate coding versus temporal order coding: a theoretical approach. *BioSystems* 48, 57–65. doi: 10.1016/S0303-2647(98)00050-1

Gerstner, W., Kreiter, A. K., Markram, H., and Herz, A. V. M. (1997). Neural codes: firing rates and beyond. *Proc. Natl. Acad. Sci. U.S.A.* 94, 12740–12741. doi: 10.1073/pnas.94.24.12740

Gochin, P. M., Colombo, M., Dorfman, G. A., Gerstein, G. L., and Gross, C. G. (1994). Neural ensemble coding in inferior temporal cortex. *J. Neurophysiol.* 71, 2325–2337. doi: 10.1152/jn.1994.71.6.2325

Gollisch, T., and Meister, M. (2008). Rapid neural coding in the retina with relative spike latencies. *Science* 319, 1108–1111. doi: 10.1126/science.1149639

Gray, C. M., König, P., Engel, A. K., and Singer, W. (1989). Oscillatory responses in cat visual cortex exhibit inter-columnar synchronization which reflects global stimulus properties. *Nature* 338, 334–337. doi: 10.1038/338334a0

Grewe, J., Kruscha, A., Lindner, B., and Benda, J. (2017). Synchronous spikes are necessary but not sufficient for a synchrony code in populations of spiking neurons. *Proc. Natl. Acad. Sci. U.S.A.* 114, e1977–e1985. doi: 10.1073/pnas.1615561114

Guo, X., Yu, H., Wang, J., Liu, J., Cao, Y., and Deng, B. (2017). Local excitation–inhibition ratio for synfire chain propagation in feed-forward neuronal networks. *Physica A Stat. Mech. Appl.* 482, 308–316. doi: 10.1016/j.physa.2017.04.040

Han, R., Wang, J., Yu, H., Deng, B., Wei, X., Qin, Y., et al. (2015). Intrinsic excitability state of local neuronal population modulates signal propagation in feed-forward neural networks. *Chaos* 25:043108. doi: 10.1063/1.4917014

Harris, K. D., and Mrsic-Flogel, T. D. (2013). Cortical connectivity and sensory coding. *Nature* 503, 51–58. doi: 10.1038/nature12654

Hawkins, J., Ahmad, S., and Cui, Y. (2017). A theory of how columns in the neocortex enable learning the structure of the wworld. *Front. Neural Circuits* 11:81. doi: 10.3389/fncir.2017.00081

He, Z. L. (2007). A new class of nonlinear integrated models. *Far East J. Theor. Stat.* 23, 31–50. Available online at: https://www.statindex.org/journals/531/23

He, Z. L. (2013). Dynamics and stability of a new class of nonlinear integrated models with resilience mechanisms. *Far East J. Dyn. Syst.* 21, 1–32. Available online at: http://www.pphmj.com/journals/articles/1084.htm

He, Z. L. (2014). Estimation and tests of nonlinear autoregressive integrated models. *Far East J. Theor. Stat.* 49, 129–164. Available online at: https://www.statindex.org/journals/531/49

He, Z. L. (2018). Integer-dimensional fractals of nonlinear dynamics, control mechanisms, and physical implications. *Sci. Rep.* 8:10324. doi: 10.1038/s41598-018-28669-3

Henry, K. S., and Lucas, J. R. (2008). Coevolution of auditory sensitivity and temporal resolution with acoustic signal space in three ongbirds. *Anim. Behav.* 76, 1659–1671. doi: 10.1016/j.anbehav.2008.08.003

Henze, D. A., and Buzsáki, G. (2001). Action potential threshold of hippocampal pyramidal cells *in vivo* is increased by recent spiking activity. *Neuroscience* 105, 121–130. doi: 10.1016/S0306-4522(01)00167-1

Hirabayashi, T., and Miyashita, Y. (2005). Dynamically modulated spike correlation in monkey inferior temporal cortex depending on the feature configuration within a whole object. *J. Neurosci.* 25, 10299–10307. doi: 10.1523/JNEUROSCI.3036-05.2005

Horton, J. C., and Adams, D. L. (2005). The cortical column: a structure without a function. *Philos. Trans. R. Soc. Lond. B. Biol. Sci.* 360, 837–862. doi: 10.1098/rstb.2005.1623

Ikegaya, Y., Aaron, G., Cossart, R., Aronov, D., Lampl, I., Fester, D., et al. (2004). Synfire chains and cortical songs: temporal modules of cortical activity. *Science* 304, 559–564. doi: 10.1126/science.1093173

Izhikevich, E. M. (2000). Neural excitability, spiking, and bursting. *Int. J. Bifur. Chaos* 10, 1171–1266. doi: 10.1142/S0218127400000840

Izhikevich, E. M. (2006). Polychronization: computation with spikes. *Neural Comput.* 18, 245–282. doi: 10.1162/089976606775093882

Jirsa, V. K. (2008). Dispersion and time delay effects in synchronized spike–burst networks. *Cogn. Neurodyn.* 2, 29–38. doi: 10.1007/s11571-007-9030-0

Jiruska, P., de Curtis, M., Jefferys, J. G. R., Schevon, C. A., Schiff, S. J., and Schindler, K. (2013). Synchronization and desynchronization in epilepsy: controversies and hypotheses. *J. Physiol.* 591, 787–797. doi: 10.1113/jphysiol.2012.239590

Jones, E. G. (2000). Microcolumns in the cerebral cortex. *Proc. Natl. Acad. Sci. U.S.A.* 97, 5019–5021. doi: 10.1073/pnas.97.10.5019

Klug, A., Khan, A., Burger, R. M., Bauer, E. E., Hurley, L. M., Yang, L., et al. (2000). Latency as a function of intensity in auditory neurons: influences of central processing. *Hear. Res.* 148, 107–123. doi: 10.1016/S0378-5955(00)00146-5

Larkum, M. E., Kaiser, K. M., and Sakmann, B. (1999). Calcium electrogenesis in distal apical dendrites of layer 5 pyramidal cells at a critical frequency of back-propagating action potentials. *Proc. Natl. Acad. Sci. U.S.A.* 96, 14600–14604.

Le Masson, G., Przedborski, S., and Abbott, L. F. (2014). A computational model of motor neuron degeneration. *Neuron* 83, 975–988. doi: 10.1016/j.neuron.2014.07.001

Mainen, Z. F., and Sejnowski, T. J. (1995). Reliability of spike timing in neocortical neurons. *Science* 268, 1503–1506.

McCormick, D. A., Shu, Y., and Yu, Y. (2007). Neurophysiology: Hodgkin and Huxley model–still standing? *Nature* 445, E1–E2. discussion: E2–E3. doi: 10.1038/nature05523

Mountcastle, V. B. (1957). Modality and topographic properties of single neurons of cat's somatic sensory cortex. *J. Neurophysiol.* 20, 408–434.

Mountcastle, V. B., Berman, A. L., and Davies, P. W. (1955). Topographic organization and modality representation in first somatic area of cat's cerebral cortex by method of single unit analysis. *Am. J. Physiol.* 183:464.

Murthy, V. N., and Fetz, E. E. (1996). Oscillatory activity in sensorimotor cortex of awake monkeys: synchronization of local field potentials and relation to behavior. *J. Neurophysiol.* 76, 3949–3967.

Naundorf, B., Wolf, F., and Volgushev, M. (2006). Unique features of action potential initiation in cortical neurons. *Nature* 440, 1060–1063. doi: 10.1038/nature04610

Nemenman, I., Lewen, G. D., Bialek, W., and de Ruyter van Steveninck, R. R. (2008). Neural coding of natural stimuli: information at sub-millisecond resolution. *PLoS Comput. Biol.* 4:e1000025. doi: 10.1371/journal.pcbi.1000025

Nicol, G. D., and Miller, W. H. (1978). Cyclic GMP injected into retinal rod outer segments increases latency and amplitude of response to illumination. *Proc. Natl. Acad. Sci. U.S.A.* 75, 5217–5220. doi: 10.1073/pnas.75.10.5217

Nowak, L. G., Sanchez-Vives, M. V., and McCormick, D. A. (1997). Influence of low and high frequency inputs on spike timing in visual cortical neurons. *Cereb. Cortex* 7, 487–501.

Opris, I., and Casanova, M. F. (2014). Prefrontal cortical minicolumn: from executive control to disrupted cognitive processing. *Brain* 137, 1863–1875. doi: 10.1093/brain/awt359

Panzeri, S., Macke, J. H., Gross, J., and Kayser, C. (2015). Neural population coding: combining insights from microscopic and mass signals. *Trends Cogn. Sci.* 19, 162–172. doi: 10.1016/j.tics.2015.01.002

Pipa, G., and Munk, M. H. (2011). Higher order spike synchrony in prefrontal cortex during visual memory. *Front. Comput. Neurosci.* 5:23. doi: 10.3389/fncom.2011.00023

Potter, G. D., Byrd, T. A., Mugler, A., and Sun, B. (2017). Dynamic sampling and information encoding in biochemical networks. *Biophys. J.* 112, 795–804. doi: 10.1016/j.bpj.2016.12.045

Powell, T. P., and Mountcastle, V. B. (1959). Some aspects of the functional organization of the cortex of the postcentral gyrus of the monkey: a correlation of findings obtained in a single unit analysis with cytoarchitecture. *Bull. Johns. Hopkins Hosp.* 105, 133–162.

Purves, D., Augustine, G. J., Fitzpatrick, D., Katz, L. C., LaMantia, A. S., McNamara, J. O., et al. (2008). *Neuroscience, 4th Edn.* Sunderland MA: Sinauer Associates.

Rakic, P. (2008). Confusing cortical columns. *Proc. Natl. Acad. Sci. U.S.A.* 105, 12099–12100. doi: 10.1073/pnas.0807271105

Riehle, A., Grün, S., Diesmann, M., and Aertsen, A. (1997). Spike synchronization and rate modulation differentially involved in motor cortical function. *Science* 278, 1950–1953.

Roy, A., Steinmetz, P. N., Hsiao, S. S., Johnson, K. O., and Niebur, E. (2007). Synchrony: a neural correlate of somatosensory attention. *J. Neurophysiol.* 98, 1645–1661. doi: 10.1152/jn.00522.2006

Rubchinsky, L. L., Park, C., and Worth, R. M. (2012). Reeves AG, Swenson RS. Intermittent neural synchronization in Parkinson's disease. *Nonlinear Dyn.* 68, 329–346. doi: 10.1007/s11071-011-0223-z

Schrader, S., Gewaltig, M. O., Körner, U., and Körner, E. (2009). Cortext: a columnar model of bottom-up and top-down processing in the neocortex. *Neural Netw.* 22, 1055–1070. doi: 10.1016/j.neunet.2009.07.021

Schubert, D., Köter, R., Luhmann, H. J., and Staiger, J. F. (2006). Morphology, electrophysiology and functional input connectivity of pyramidal neurons characterizes a genuine layer Va in the primary somatosensory cortex. *Cereb. Cortex* 16, 223–236. doi: 10.1093/cercor/bhi100

Sekar, K., Findley, W. M., and Llinás, R. R. (2012). Evidence for an all-or-none perceptual response: single-trial analyses of magnetoencephalography signals indicate an abrupt transition between visual perception and its absence. *Neuroscience.* 206, 167–182. doi: 10.1016/j.neuroscience.2011.09.060

Shadlen, M. N., and Movshon, J. A. (1999). Synchrony unbound: a critical evaluation of the temporal binding hypothesis. *Neuron* 24, 67–77, 111–125. doi: 10.1016/S0896-6273(00)80822-3

Shadlen, M. N., and Newsome, W. T. (1998). The variable discharge of cortical neurons: implications for connectivity, computation, and information coding. *J. Neurosci.* 18, 3870–3896. doi: 10.1523/JNEUROSCI.18-10-03870.1998

Singer, W. (1999). Neuronal synchrony: a versatile code for the definition of relations? *Neuron* 24, 49–65, 111–125. doi: 10.1016/S0896-6273(00)80821-1

Softky, W. R., and Koch, C. (1992). Cortical cells should fire regularly, but do not. *Neural. Comput.* 4, 643–646.

Softky, W. R., and Koch, C. (1993). The highly irregular firing of cortical cells is inconsistent with temporal integration of random EPSPs. *J. Neurosci.* 13, 334–350.

Soto, G., Kopell, N., and Sen, K. (2006). Network architecture,receptive fields, and neuromodulation: computational and func-tional implications of cholinergic modulation in primary auditorycortex. *J. Neurophysiol.* 96, 2972–2983. doi: 10.1152/jn.00459.2006

Steinmetz, P. N., Roy, A., Fitzgerald, P. J., Hsiao, S. S., Johnson, K. O., and Niebur, E. (2000). Attention modulates synchronized neuronal firing in primate somatosensory cortex. *Nature* 404, 187–190. doi: 10.1038/35004588

Stiefel, K. M., Englitz, B., and Sejnowski, T. J. (2013). Origin of intrinsic irregular firing in cortical interneurons. *Proc. Natl. Acad. Sci. U.S.A.* 110, 7886–7891. doi: 10.1073/pnas.1305219110

Stuart, G. J., and Sakmann, B. (1994). Active propagation of somatic action potentials into neocortical pyramidal cell dendrites. *Nature* 367, 69–72.

Tiesinga, P., Fellous, J. M., and Sejnowski, T. J. (2008). Regulation of spike timing in visual cortical circuits. *Nat. Rev. Neurosci.* 9, 97–107. doi: 10.1038/nrn2315

Tootell, R. B. H., and Nasr, S. (2017). Columnar segregation of magnocellular and parvocellular streams in human extrastriate cortex. *J. Neurosci.* 37, 8014–8032. doi: 10.1523/JNEUROSCI.0690-17.2017

Torre, E., Canova, C., Denker, M., Gerstein, G., Helias, M., and Grün, S. (2016a). ASSET: analysis of sequences of synchronous events in massively parallel spike trains. *PLoS Comput. Biol.* 12:e1004939. doi: 10.1371/journal.pcbi.1004939

Torre, E., Quaglio, P., Denker, M., Brochier, T., Riehle, A., and Grün, S. (2016b). Synchronous spike patterns in macaque motor cortex during an instructed-delay reach-to-grasp task. *J. Neurosci.* 36, 8329–8340. doi: 10.1523/JNEUROSCI.4375-15.2016

Uhlhaas, P. J., and Singer, W. (2006). Neural synchrony in brain disorders: relevance for cognitive dysfunctions and pathophysiology. *Neuron* 52, 155–168. doi: 10.1016/j.neuron.2006.09.020

Uzuntarla, M., Ozer, M., and Guo, D. Q. (2012). Controlling the first-spike latency response of a single neuron via unreliable synaptic transmission. *Eur. Phys. J. B.* 85:282. doi: 10.1140/epjb/e2012-30282-0

van Rossum, M. C., Turrigiano, G. G., and Nelson, S. B. (2002). Fast propagation of firing rates through layered networks of noisy neurons. *J. Neurosci.* 22, 1956–1966. doi: 10.1523/JNEUROSCI.22-05-01956.2002

Wang, X., Lu, T., Bendor, D., and Bartlett, E. (2008). Neural coding of temporal information in auditory thalamus and cortex. *Neuroscience* 154, 294–303. doi: 10.1016/j.neuroscience.2008.03.065

Waters, J., Larkum, M. E., Sakmann, B., and Helmchen, F. (2003). Supralinear Ca^{2+} influx into dendritic tufts of layer 2/3 neocortical pyramidal neurons *in vitro* and *in vivo*. *J. Neurosci.* 23, 8558–8567. doi: 10.1523/JNEUROSCI.23-24-08558.2003

Wei, H., and Du, Y. F. (2019). A temporal signal-processing circuit based on spiking neuron and synaptic learning. *Front. Comput. Neurosci.* 13:41. doi: 10.3389/fncom.2019.00041

Woolsey, T. A., and van der Loos, H. (1970). The structural organization of layer IV in the somatosensory region (SI) of mouse cerebral cortex. The description of a cortical field composed of discrete cytoarchitectonic units. *Brain Res.* 17, 205–242. doi: 10.1016/0006-8993(70)90079-X

Yu, Y., Shu, Y., and McCormick, D. A. (2008). Cortical action potential backpropagation explains spike threshold variability and rapid-onset kinetics. *J. Neurosci.* 28, 7260–7272. doi: 10.1523/JNEUROSCI.1613-08.2008

Zilles, K., and Wree, A. (1995). "Cortex: areal and laminar structure," in *The Rat Nervous System*, ed G. Paxinos (New York, NY: Academic Press), 649–685.

Conflict of Interest Statement: The author declares that the research was conducted in the absence of any commercial or financial relationships that could be construed as a potential conflict of interest.

frontiers in Neuroscience

ORIGINAL RESEARCH
published: 29 August 2019
doi: 10.3389/fnins.2019.00912

Pinpointing Morphology and Projection of Excitatory Neurons in Mouse Visual Cortex

*Yalun Zhang[1,2], Siqi Jiang[1,2], Zhengchao Xu[1,2], Hui Gong[1,2], Anan Li[1,2], Qingming Luo[1,2], Miao Ren[1,2], Xiangning Li[1,2], Hao Wu[1,2], Jing Yuan[1,2] and Shangbin Chen[1,2]**

[1] Britton Chance Center for Biomedical Photonics, Wuhan National Laboratory for Optoelectronics-Huazhong University of Science and Technology, Wuhan, China, [2] MoE Key Laboratory for Biomedical Photonics, School of Engineering Sciences, Huazhong University of Science and Technology, Wuhan, China

The excitatory neurons in the visual cortex are of great significance for us in understanding brain functions. However, the diverse neuron types and their morphological properties have not been fully deciphered. In this paper, we applied the brain-wide positioning system (BPS) to image the entire brain of two Thy1-eYFP H-line male mice at 0.2 μm × 0.2 μm × 1 μm voxel resolution. A total of 103 neurons were reconstructed in layers 5 and 6 of the visual cortex with single-axon-level resolution. Based on the complete topology of neurons and the inherent positioning function of the imaging method, we classified the observed neurons into six types according to their apical dendrites and somata location: star pyramidal cells in layer 5 (L5-sp), slender-tufted pyramidal cells in layer 5 (L5-st), tufted pyramidal cells in layer 5 (L5-tt), spiny stellate-like cells in layer 6 (L6-ss), star pyramidal cells in layer 6 (L6-sp), and slender-tufted pyramidal cells in layer 6 (L6-st). By examining the axonal projection patterns of individual neurons, they can be categorized into three modes: ipsilateral circuit connection neurons, callosal projection neurons and corticofugal projection neurons. Correlating the two types of classifications, we have found that there are at least two projection modes comprised in the former defined neuron types except for L5-tt. On the other hand, each projection mode may consist of four dendritic types defined in this study. The axon projection mode only partially correlates with the apical dendrite feature. This work has demonstrated a paradigm for resolving the visual cortex through single-neuron-level quantification and has shown potential to be extended to reveal the connectome of other defined sensory and motor systems.

Keywords: visual cortex, excitatory neuron, morphology, projection pattern, neuron type

OPEN ACCESS

Edited by:
Chris G. Antonopoulos, University of Essex, United Kingdom

Reviewed by:
Joshua C. Brumberg, Queens College (CUNY), United States
Caroline Rouaux, Institut National de la Santé et de la Recherche Médicale (INSERM), France

***Correspondence:**
Shangbin Chen
sbchen@mail.hust.edu.cn

Specialty section:
This article was submitted to Systems Biology, a section of the journal Frontiers in Neuroscience

Received: *06 March 2019*
Accepted: *16 August 2019*
Published: *29 August 2019*

Citation:
Zhang Y, Jiang S, Xu Z, Gong H, Li A, Luo Q, Ren M, Li X, Wu H, Yuan J and Chen S (2019) Pinpointing Morphology and Projection of Excitatory Neurons in Mouse Visual Cortex. Front. Neurosci. 13:912. doi: 10.3389/fnins.2019.00912

INTRODUCTION

The visual system of mammals receives most of the sensory information. The understanding of visual circuits requires the morphologic characterization and classification of individual neurons (Liang et al., 2015). Recently, tremendous progress has been achieved in studying the projection mode of the mouse visual cortex (Kim et al., 2015; Kondo and Ohki, 2016; Roth et al., 2016; Sun et al., 2016; Atlan et al., 2017). A mouse mesoscale connectome among different brain regions

has been constructed by combining adeno-associated virus (AAV) tracer labeling and serial two-photon (STP) imaging (Oh et al., 2014). With both rabies virus and AAV co-injection, it is possible to study the input and output connection of the visual neural network (Zhang et al., 2016). However, most studies perform only bulk tracing of gross projection patterns for a large number of neuronal populations (Jeong et al., 2016). The revealed region-level connectivity fails to reflect the collateral arborization patterns of each projection neuron (Mitra, 2014). Our previous work has demonstrated the feasibility of performing single-axon-level morphological analysis of projection neurons in the mouse barrel cortex and secondary motor cortex (Guo C. et al., 2017; Lin et al., 2018; Sun et al., 2019). Thus, it is possible to explore the excitatory neurons of the visual cortex at single-neuron resolution.

Advances in techniques have boosted the morphological analysis of individual neurons (Molnar and Cheung, 2006; Ascoli et al., 2008; Costa et al., 2010; Meyer et al., 2010; Oberlaender et al., 2012; Huang, 2014). Molyneaux et al. (2007) reviewed the major subtypes of projection neurons classified by axonal hodology. Fame et al. (2011) summarized the specification and diversity of callosal projection neurons. Oberlaender et al. (2012) defined excitatory neuron types in the rat barrel cortex based on morphological features. Markram et al. (2015) reconstructed masses of neurons with the cortical part morphology and classified them according to their location of somata and morphology. Nevertheless, the long-range projection neurons are not sufficiently available for linking dendritic classification and axonal hodology (Gouwens et al., 2018; Kanari et al., 2019). To pinpoint the excitatory neurons in the visual cortex, it is timely to study their complete morphology, neuron types and corresponding projection patterns.

Here, we applied the brain-wide positioning system (BPS) (Gong et al., 2016) to obtain volumetric imaging of the whole mouse brain dataset with a resolution of 0.2 μm $\times$ 0.2 μm $\times$ 1 μm. A total of 103 excitatory neurons in layers 5 and 6 were reconstructed. Due to the inherent positioning feature of the BPS system, it is possible to localize each neuron's soma and its neurites at the nucleus level. This will allow us to quantify the morphology, neuron types and projection patterns with unprecedented precision.

MATERIALS AND METHODS

Tissue Preparation

All the animal experiments followed procedures that had been approved by the Institutional Animal Ethics Committee of Huazhong University of Science and Technology. Animal care and use were performed in accordance with the guidelines of the Administration Committee of Affairs Concerning Experimental Animals in Hubei Province of China. Two 8-week-old Thy1-eYFP H-line transgenic male mice (Jackson Laboratory, Bar Harbor, ME, United States) were used (Feng et al., 2000; Porrero et al., 2010). All histological procedures had been previously described (Gang et al., 2017; Guo W. et al., 2017). Briefly, the mouse was anesthetized with a 1% solution of sodium pentobarbital and subsequently intracardially perfused with 0.01 M PBS (Sigma-Aldrich Inc., St. Louis, MO, United States), followed by 4% paraformaldehyde (Sigma-Aldrich Inc., St. Louis, MO, United States). The whole brain was excised and post-fixed in 4% paraformaldehyde at 4°C for 24 h. Then, the brain was rinsed overnight at 4°C in 0.01 M PBS and subsequently dehydrated in a graded ethanol series (50, 70, and 95% ethanol at 4°C for 1 h each). After dehydration, the brain was immersed in a series of graded glycol methacrylate (GMA) (Ted Pella Inc., Redding, CA, United States) including 0.2% Sudan Black B (SBB): 70, 85, and 100% GMA for 2 h each and 100% GMA overnight at 4°C. The brain sample was impregnated in a prepolymerized solution of GMA for 3 days at 4°C and finally embedded in a vacuum oven at 48°C for 24 h. The 100% GMA solution contained 67 g A solution, 29.4 g B solution, 2.8 g deionized water, 0.2 g SBB, and 0.6 g AIBN as initiator. The 70 and 85% GMA (wt/wt) were prepared from 95% ethanol and 100% GMA.

Whole-Brain Imaging

The resin-embedded whole-brain sample that could provide a certain hardness was sectioned and imaged automatically using BPS. Before imaging, we immobilized the mouse whole-brain sample in the anterior-posterior direction in a water bath on a 3D translation stage. The water bath was filled with 0.01 M Na_2CO_3 and propidium iodide (PI) solution, in which the sample was immersed to provide a matched refractive index for the objective lens during imaging. In addition, the PI molecules could quickly stain nucleic acids inside the cell body to provide the position of the cell, and the Na_2CO_3 solution could enhance the fluorescence of eYFP. Sectioning was achieved using a fixed diamond knife and a 3D translation stage for wide-field large-volume tomography. The single sectioning thickness was set to 2 μm, and the sectioning width was 2 mm. The imaging was performed using a 20$\times$ water immersion objective on a fast structured illumination microscope (1.0 NA, XLUMPLFLN 20XW, Olympus, Shinjuku, Tokyo, Japan). The imaging plane was set below the surface of the sample block. The eYFP and PI molecules were excited simultaneously, and the emitted fluorescence signals were separated by a dichroic mirror and detected by two cameras. During the imaging process, we performed axial scanning using the piezoelectric translational stage, which acquired two sectioning images at depths of 1 and 2 μm. Following axial scanning, the sample was moved to the next mosaic field of view (FOV), with a 10 μm overlap between adjacent FOVs. The mosaic imaging process was repeated until the entire coronal section was acquired. Finally, we acquired the dataset sections with a 1 μm thickness and performed imaging with a voxel size of 0.2 μm $\times$ 0.2 μm $\times$ 1 μm.

Image Processing

Image preprocessing was applied to standardize the datasets. First, the tiles at the same position of the eYFP and PI channels were resized and shifted to obtain the perfectly matched tiles by the parameters of the model experiment. Second, we stitched the tiles of the same section to obtain a mosaic section based on the accurate spatial orientation and neighboring overlap (approximately 10 pixels). The anchor points of the tiles were

spaced equally in two orthogonal directions. Third, transverse illumination correction was performed separately in each section. Fourth, axial illumination correction was performed based on the average intensity of each section. The two illumination correction steps were based on our previously developed algorithm (Ding et al., 2013). Finally, we obtained the standard dataset for both the eYFP and PI channels. Image preprocessing was implemented with C++, parallel optimized using the Intel MPI Library and then executed on a computing server (72 cores, 2 GHz/core) for 6 h for each mouse brain dataset at a voxel resolution of 0.2 μm × 0.2 μm × 1 μm.

Reconstruction and Statistics

We localized the mouse's visual cortex in the PI channel image series from the Thy1-eYFP H-line datasets by referring to the Allen Mouse Brain Reference Atlas[1] (**Figure 1**). We manually reconstructed 103 neurons through man-machine interactive annotation in layers 5 and 6 of the visual cortex from the whole brain fluorescence imaging dataset using the Amira software (FEI, Mérignac Cedex, France) with a homemade TDat plugin (Li et al., 2017). Every neuron was reconstructed and checked back-to-back. The morphological information was saved as a *.swc file. Meanwhile, we parceled the layers of the cortex on the PI channel image series based on the cytoarchitectural features. We corrected the neurons based on the normal vector of the cortex's layers and located the position of the neuron's soma and dendrites by the location of the cortex's layers. Based on the PI channel image series according to the Allen Reference Atlas, we mapped the brain regions (**Figure 2A**) and determined the route and terminal location of the axon fibers. All morphology parameters were measured using Neurolucida Explorer (MBF Bioscience, Williston, VT, United States). For the morphological statistics (**Tables 1**, **2**), we performed multiple group comparisons assessed with one-way ANOVA followed by *post hoc* Tukey's test. These analyses were performed using the SPSS software (v22, IBM, New York, NY, United States).

[1]http://atlas.brain-map.org/

RESULTS

Dendritic Classification of Neuron Types

Using the BPS system (Gong et al., 2016), we obtained two whole brain datasets of Thy1-eYFP H-line male mice with a voxel resolution of 0.2 μm × 0.2 μm × 1 μm (**Figure 1** and **Supplementary Figure 1**). With the aid of PI staining, it is feasible to parcel the brain regions and cortex layers

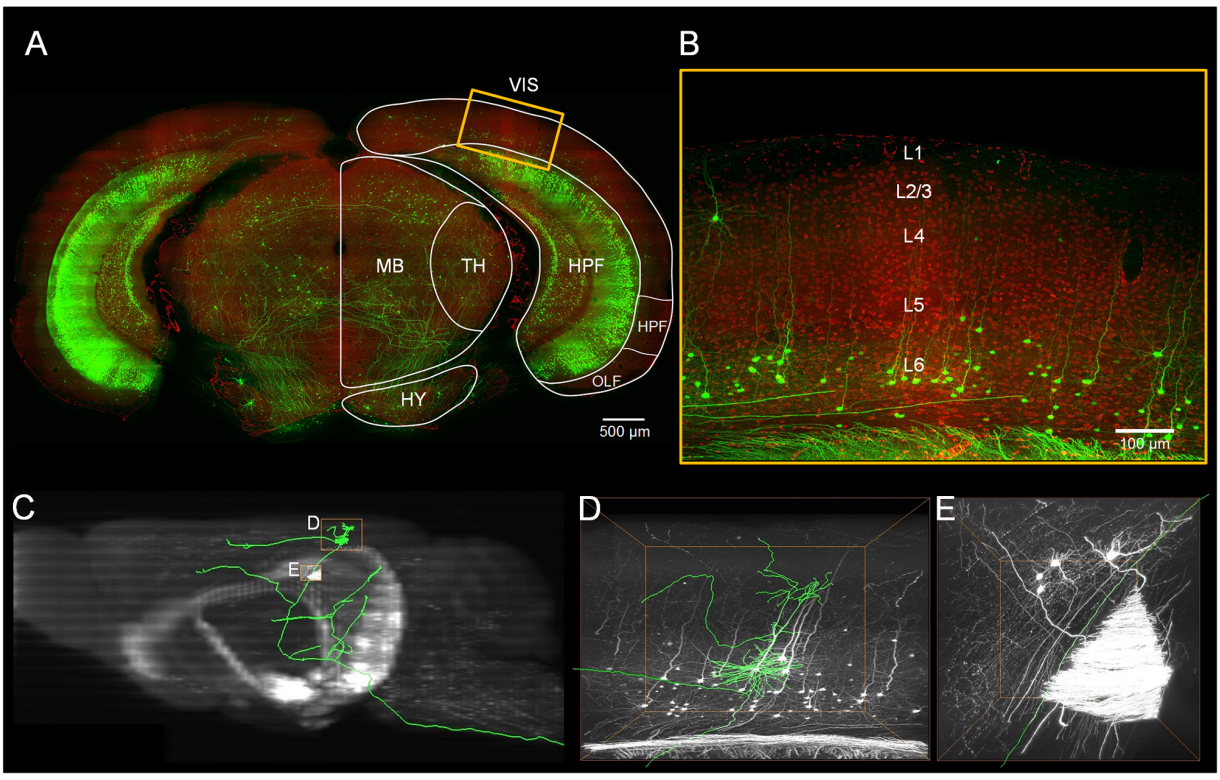

FIGURE 1 | Localization of the visual cortex and annotating the individual neurons inside. **(A)** Merged image with green channel (thickness of projection: 500 μm) and red channel (thickness of projection: 5 μm). The white outline indicates brain regions: the visual areas (VIS), the hippocampal formation (HPF), the thalamus (TH), the midbrain (MB) and the hypothalamus (HY). Scale bar: 500 μm. **(B)** Enlarged view of the region marked with the yellow rectangle in **(A)**. The YFP-labeled individual neurons and the propidium iodide (PI)-stained cytoarchitecture are shown. Scale bar: 100 μm. **(C)** The maximal projection of the sagittal plane of the green channel dataset. **(D,E)** Three-dimensional enlarged view of the region marked with the yellow rectangle in **(C)**.

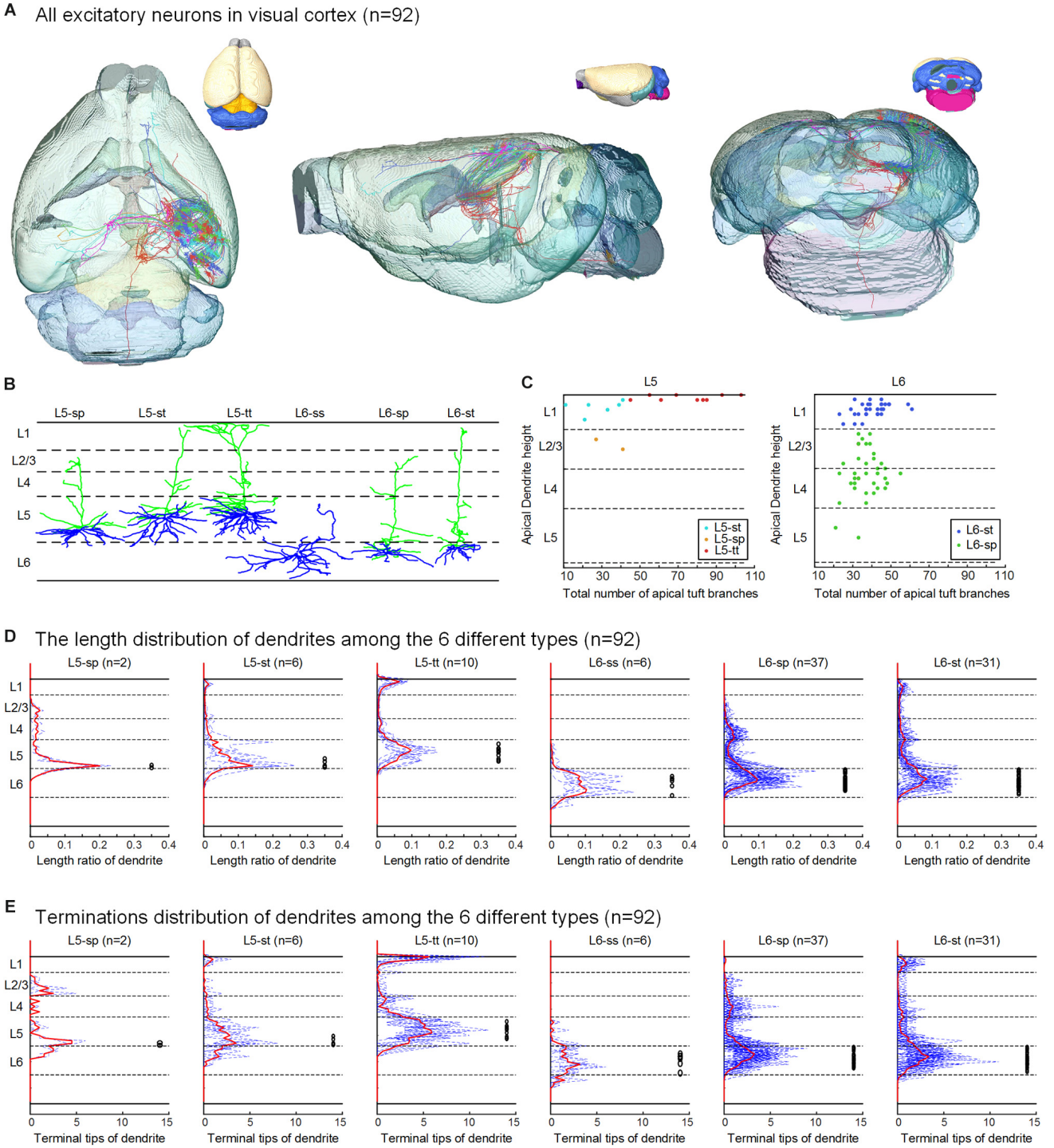

FIGURE 2 | Excitatory neurons in the visual cortex and their classification based on dendritic features. **(A)** The 92 neurons with their complete morphologies are shown in the mouse brain, the six colors of neurons represent the six types defined in **(B)**, and the different colors of the mouse brain represent the mapped brain regions according to the Allen Reference Atlas. **(B)** According to the layer of the cell body and the dendrite morphology, the reconstructed neurons are separated into six categories: star pyramidal cell in layer 5 (L5-sp), slender-tufted pyramidal cell in layer 5 (L5-st), tufted pyramidal cell in layer 5 (L5-tt), spiny stellate-like cell in layer 6 (L6-ss), star pyramidal cell in layer 6 (L6-sp), and slender-tufted pyramidal cell in layer 6 (L6-st). **(C)** Scatter plots with the two parameters: the relative height of the apical dendrites and the number of apical dendrites. The L5-sp, L5-st, L5-tt, L6-sp, and L6-st neurons show relatively clustered groups. **(D)** Laminar percentage distribution of dendritic L5-sp, L5-st, L5-tt, L6-ss, L6-sp, and L6-st neurons. For each type of neuron, the solid red line is the mean result, and the black circles to the right indicate the location of somata. **(E)** Laminar distribution of dendrite terminals of the 6 types of neurons.

TABLE 1 | Morphological statistics of excitatory neurons in layer 5 of visual cortex.

	L5-sp(n = 2)	L5-st(n = 6)	L5-tt(n = 10)
Length of apical dendrite (μm)	1453.2 ± 7.3	1711.8 ± 288.7	3780.3 ± 259.5
Branches of apical dendrite	34.0 ± 7.0	28.0 ± 4.2	73.5 ± 5.3
Max branch order of apical dendrite	12.5 ± 1.5	9.2 ± 1.2	20.1 ± 1.2
Terminal tips of apical dendrite	17.5 ± 3.5	14.5 ± 2.1	37.3 ± 2.8
Length of basal dendrite (μm)	1428.4 ± 683.0	2468.8 ± 225.2	3271.7 ± 224.7
Branches of basal dendrite	28.5 ± 9.5	38.7 ± 3.5	66.6 ± 4.3
Max branch order of basal dendrite	4.0 ± 1.0	5.0 ± 0.4	5.8 ± 0.2
Terminal tips of basal dendrite	17.0 ± 4.0	22.5 ± 1.9	37.7 ± 2.2
Axonal length (μm)	6798.6 ± 682.4	12585.7 ± 2904.0	16694.0 ± 3498.6
Axonal branches	14.0 ± 1.0	104.3 ± 19.9	68.6 ± 17.9
Max branch order of axon	6.0 ± 1.0	20.7 ± 3.0	10.3 ± 1.8
Terminal tips of axon	7.5 ± 0.5	52.7 ± 10.0	34.8 ± 9.0

TABLE 2 | Morphological statistics of excitatory neurons in layer 6 of visual cortex.

	L6-ss(n = 6)	L6-sp(n = 37)	L6-st(n = 31)
Length of apical dendrite (μm)	–	1595.4 ± 48.1	1898.9 ± 66.5
Branches of apical dendrite	–	36.6 ± 1.3	40.0 ± 1.5
Max branch order of apical dendrite	–	14.6 ± 0.5	16.1 ± 0.5
Terminal tips of apical dendrite	–	18.8 ± 0.6	20.6 ± 0.8
Length of basal dendrite (μm)	2922.1 ± 203.2	1080.4 ± 41.2	1213.7 ± 62.4
Branches of basal dendrite	45.0 ± 3.5	25.7 ± 1.1	26.3 ± 1.4
Max branch order of basal dendrite	7.7 ± 1.0	4.2 ± 0.1	4.0 ± 0.2
Terminal tips of basal dendrite	25.8 ± 2.0	15.9 ± 0.6	16.4 ± 0.7
Axonal length (μm)	5964.2 ± 688.2	6720.7 ± 358.3	8021.1 ± 481.9
Axonal branches	49.7 ± 11.8	40.3 ± 6.9	47.2 ± 5.7
Max branch order of axon	14.5 ± 3.2	10.4 ± 1.2	11.5 ± 1.0
Terminal tips of axon	25.3 ± 5.9	20.6 ± 3.5	24.2 ± 2.9

(**Figures 1B**, **2A**). A total of 103 excitatory neurons were randomly selected and reconstructed in layers 5 and 6 (L5 and L6) of the visual cortex (**Figure 2A** and **Supplementary Figure 1**). The 92 neurons confirmed in the visual cortex (**Supplementary Table 1**) of the same mouse brain were analyzed and classified with details. The 11 neurons from another mouse brain were used to validate the classification. The inherent positioning function of BPS allows us to precisely locate the soma and neurite extension in the whole brain space and quantify the reconstructed morphology.

According to the laminar position of the soma and apical dendritic morphology (Molnar and Cheung, 2006; Oberlaender et al., 2012; Guo C. et al., 2017), we divided the 92 neurons into six categories: 2 star pyramidal cells in layer 5 (L5-sp), 6 slender-tufted pyramidal cells in layer 5 (L5-st), 10 tufted pyramidal cells in layer 5 (L5-tt), 6 spiny stellate-like cells in layer 6 (L6-ss), 37 star pyramidal cells in layer 6 (L6-sp), and 31 slender-tufted pyramidal cells in layer 6 (L6-st) (**Figure 2B**). The dendrites of the st- and tt-type reach the first layer of the cortex, while the tt-type has tufted apical dendrites. The dendrites of sp-type do not reach the first layer. The ss-type has no typical apical dendritic morphology of the pyramidal neurons (**Figure 2B**). Considering the significant differences in thickness among the wide span of the visual cortex, laminar normalization of layer thickness was performed before quantifying the apical dendrite morphology. The total number of branches and the height of the apical dendrites clearly showed five groups corresponding to the five types of neurons: L5-sp, L5-st, L5-tt, L6-sp, and L6-st (**Figure 2C**). Including the basal dendrites, the length distribution of the dendrites among the 6 different types was analyzed (**Figure 2D**). The results showed that (1) L5-sp neurons have a peak dendritic length ratio in L5 and a zero value in L1; (2) L5-st neurons have a peak distribution in L5 and a small ratio in L1; (3) L5-tt neurons show a bimodal distribution of dendritic length in L5 and L1; (4) L6-ss neurons present a wide peak in the L6 layer but without distribution in L4, L23, or L1; (5) L6-sp neurons have an obvious distribution from L4 to L6 but not L1; and (6) L6-st-type neurons show a peak distribution in L6 and a small ridge in L1. The laminar distribution of the dendrite terminals of the six types of neurons (**Figure 2E**) has a similar tendency to the corresponding length distribution. In addition, the L5-tt neuron presented the most complex arborization and the longest total length of neurites among all the abovementioned types (**Tables 1**, **2**).

Even for the 11 neurons from the visual cortex of the second mouse brain, we found all 6 dendrite-defined types with consistent morphological features: 1 L5-sp, 2 L5-st, 1 L5-tt, 2 L6-ss, 3 L6-sp, and 2 L6-st (**Supplementary Figure 1**).

Axonal Classification and Projection Patterns

Because the 92 neurons are long-range excitatory neurons, the projection paths and terminals of their axons were analyzed. In addition to neuronal dendrite-defined types, 92 neurons could be classified as 7 ipsilateral circuit connection neurons, 11 callosal projection neurons and 74 corticofugal projection neurons (CFuPNs) based on axonal extension (Molyneaux et al., 2007; Fame et al., 2011; Greig et al., 2013). The axonal classification and projection patterns were separated into the L5 and L6 groups and are shown in **Figures 3**, **4**. To make the results more rational, we excluded neurons with the ratio of pretended termination in a fiber tract to all the terminations

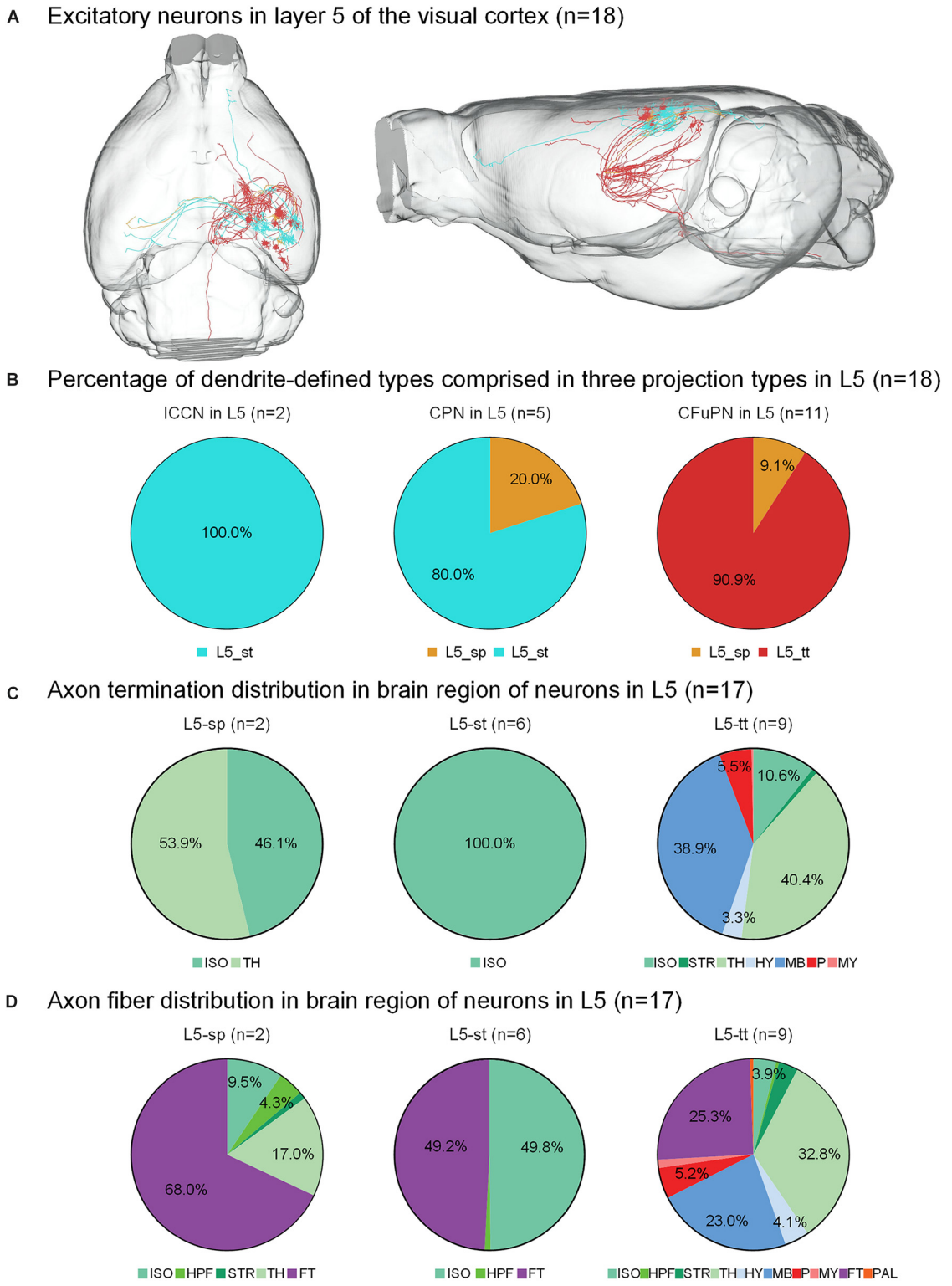

FIGURE 3 | Axonal classification and projection patterns of 18 excitatory neurons in layer 5. **(A)** The 18 neurons in L5 with their complete morphologies are shown in the mouse brain. **(B)** The percentage of dendrite-defined types comprises the ipsilateral circuit connection neurons (ICCNs), the callosal projection neurons (CPNs) and the corticofugal projection neurons (CFuPNs) in L5. **(C)** The pie charts show the regional distribution of axonal terminals for different neuronal types in L5. **(D)** The pie charts show the percentage distribution of axonal length in different brain regions for the L5 neurons. For brain regions: isocortex (ISO), hippocampal formation (HPF), striatum (STR), thalamus (TH), hypothalamus (HY), midbrain (MB), pons (P), medulla (MY), fiber tracts (FT), and pallidum (PAL).

over 0.1 from the terminal distribution analyses (**Figures 3C,D**, **4C,D**). Thus, 17 L5 neurons and 68 L6 neurons were pooled for the quantification.

For the 18 neurons in layer 5 of the visual cortex, the L5-tt type only has corticofugal projections, while the L5-sp and L5-st types of neurons have two possible projection modes (**Figure 3B**). For example, L5-st neurons match both the typical subtypes of ipsilateral circuit connection neuron and callosal projection neuron (Fame et al., 2011), and the L5-sp is distributed into the callosal projection neuron and CFuPN subtypes. Along with the difference in axon types, their projection patterns are also significantly different (**Figure 3C**). The projection terminals of L5-st are mainly concentrated in the isocortex, presenting possible intracortical regulation. The L5-sp and L5-tt types of neurons all have subcortical projection targets. L5-sp mainly extends axon terminals in thalamus, while the L5-tt type shows frequent terminals in both thalamus and midbrain for over 30% of the distribution. On the other hand, the percentage of axon length in different brain regions was also calculated for all neurons (**Figure 3D**). The main distributions of L5-st are in the fiber tracts and isocortex. L5-sp has a large number of axon distributions in the fiber tracts and thalamus, and L5-tt axons are distributed in thalamus, midbrain, and the fiber tracts all at greater than 20%. Specifically, an L5-st neuron spreads its axon to the anterior part of the cortex and projects to the orbital area, lateral part (**Figure 3A**).

The 74 neurons in layer 6 can be divided into three categories: 6 L6-ss, 37 L6-sp and 31 L6-st. The L6-ss, L6-sp, and L6-st types of neurons all have at least two possible projection modes (**Figure 4B**). For example, L6-ss neurons match both the typical subtypes of ipsilateral circuit connection neuron and callosal projection neuron. The L6-st match both the ipsilateral circuit connection neuron and CFuPN subtypes. The L6-sp can be distributed into all the ipsilateral circuit connection neuron, callosal projection neuron and CFuPN subtypes. Although the axon types of excitatory neurons in L6 are similar to those of excitatory neurons in L5, they have differences in projection patterns (**Figure 4C**). The L6-sp and L6-st types of neurons all have subcortical projection targets and mainly extend axon terminals in thalamus for over 80% of the distribution, and the projection terminal of L6-ss is mainly concentrated in the isocortex, presenting possible intracortical regulation the same as L5-st. For the axon fiber distribution in the brain region of 74 neurons in L6, the fiber tracts and thalamus both present a length distribution of more than 40% in the L6-sp and L6-st types (**Figure 4D**). In particular, the main distributions of L6-ss are in the fiber tracts and the isocortex. An L6-st neuron spreads its axon to the anterior part of the cortex and projects to both the secondary motor area and anterior cingulate area, dorsal part (**Figure 4A**).

Similarly, the 11 neurons from the second mouse brain can be classified into 3 axonal types: 8 CFuPNs, 2 callosal projection neurons and 1 ipsilateral circuit connection neuron. They also present typical axon projections to different brain regions (**Supplementary Figure 1**).

Axon Targets of the Corticofugal Projection Neurons (CFuPNs)

The 74 CFuPNs consist of 1 L5-sp, 10 L5-tt, 33 L6-sp and 30 L6-st neurons. Both the CFuPNs in L5 and L6 exhibit multi-region projections. For the 11 CFuPNs in L5, 9 neurons of the 10 L5-tt neurons was analyzed using the collaboration and coexistence matrices defined in our previous work (Guo C. et al., 2017) (**Figure 5**). We found that thalamus, midbrain and hypothalamus are the most popular targets of the CFuPNs in L5. The axon terminals of individual L5-tt neuron are found in at least two or more brain regions. All the axon terminals of the L5-tt type in this work are distributed in seven brain regions. Here, the axon-defined type of L5-tt should be subcerebral projection neurons introduced in the references (Molyneaux et al., 2007).

For the 63 CFuPNs in L6, the L6-sp type consisting of 33 neurons and the L6-st type consisting 30 neurons are quantified using the matrices (**Figure 6**). We found that thalamus are the most popular targets of the two types of neurons. Almost all the neurons that project to other brain regions have terminal points in thalamus at the same time. According to the features of long-range neurons (Molyneaux et al., 2007; Harris and Shepherd, 2015), the L6-sp and L6-st of the CFuPNs belong to corticothalamic neurons.

Correlates Between Dendritic Types and Axon Projection Patterns

Taking the aforementioned results together, we could form a wiring map with cell-type specificity. For the CFuPN subtype, we found that they had two typical projection patterns. The L5-tt neurons have the subcerebral projection mode only, and they spread their axons to several brain regions, for example, striatum, thalamus, hypothalamus, midbrain, pons and medulla. The corticofugal projection neurons of the L6-st and L6-sp have the corticothalamic projection mode. The corticofugal projection neurons of the L6-st and L6-sp types could distribute their axons to striatum, thalamus, and midbrain, and most of them project to thalamus (**Figure 7A**).

The ipsilateral circuit connection neuron and callosal projection neuron located in L5 and L6 have undistinguishable dendrite features but have different axon projection patterns. The axons of the ipsilateral circuit connection neurons are distributed in the ipsilateral hemisphere and do not cross the corpus callosum. These neurons with somata located in the 5th or 6th layer of the cortex can be classified as L5-st, L6-st, L6-sp, and L6-ss dendritic types. The axons of the callosal projection neurons are distributed across the corpus callosum to the contralateral hemisphere, and their fibers and terminals are distributed in both the ipsilateral and contralateral hemisphere. The callosal projection neurons with cell bodies located in layer 5 or 6 can be distinguished as L5-sp, L5-st, L6-sp, and L6-ss types (**Figure 7B**).

Considering the classified neuron types and the corresponding distribution of axon projections, it is easy to notice a partial correlation between the neuron dendrite complexity and the axon projection mode.

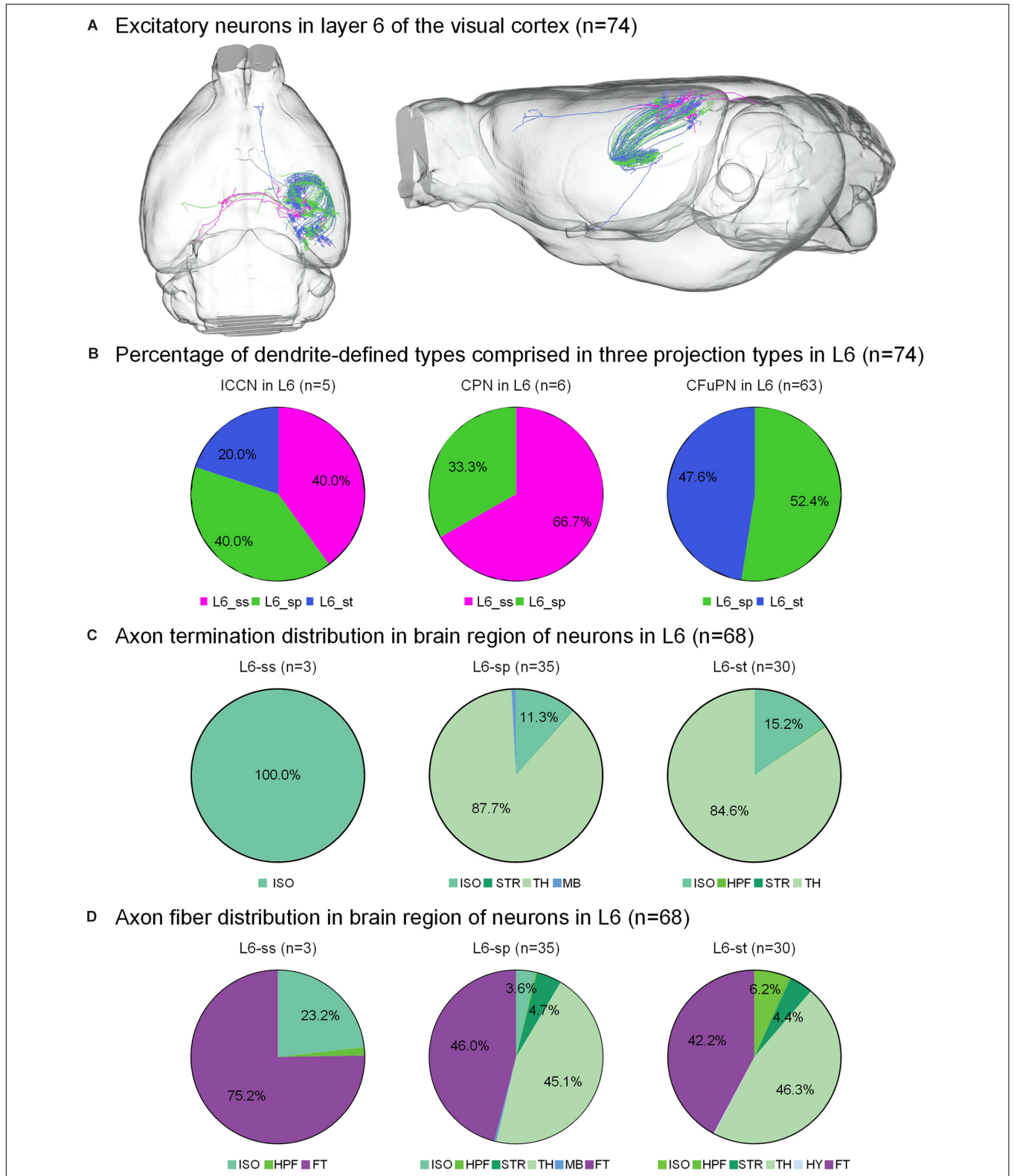

FIGURE 4 | Axonal classification and projection patterns of 74 excitatory neurons in layer 6. **(A)** The 74 neurons in L6 with their complete morphologies are shown in the mouse brain. **(B)** The percentage of dendrite-defined types comprises the ICCNs, CPNs and CFuPNs in L6. **(C)** The pie charts show the regional distribution of axonal terminals for different neuronal types in L6. **(D)** The pie charts show the percentage distribution of axonal length in different brain regions for the three types of L6 neurons.

A Corticofugal projection neurons in layer 5 of the visual cortex (n=11)

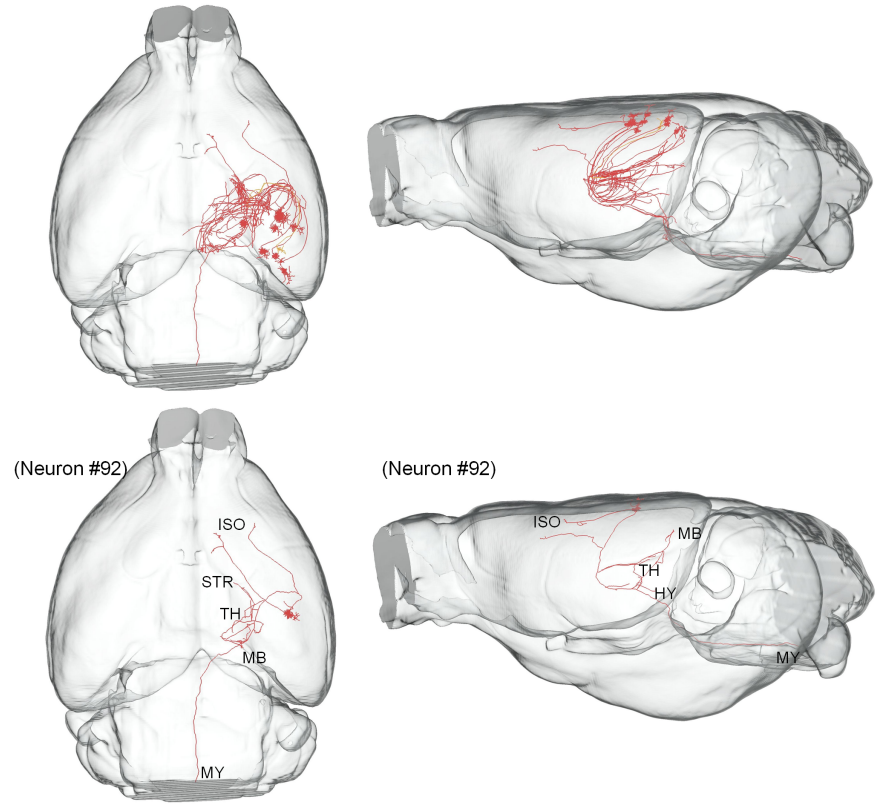

B The collaboration matrix (L5-tt of the CFuPN: n=9)

	ISO	STR	TH	MB	HY	P	MY
ISO	-	0.33	1	1	0.33	0	0.33
STR	1	-	1	1	1	0	1
TH	0.38	0.13	-	0.75	0.50	0.25	0.13
MB	0.43	0.14	0.86	-	0.43	0.29	0.14
HY	0.25	0.25	1	0.75	-	0.50	0.25
P	0	0	1	1	1	-	0
MY	1	1	1	1	1	0	-

The coexistence matrix (L5-tt of the CFuPN: n=9)

	ISO	STR	TH	MB	HY	P	MY
ISO	-	0.14	0.43	0.43	0.14	0	0.14
STR	0.14	-	0.14	0.14	0.14	0	0.14
TH	0.43	0.14	-	0.86	0.57	0.29	0.14
MB	0.43	0.14	0.86	-	0.43	0.29	0.14
HY	0.14	0.14	0.57	0.43	-	0.29	0.14
P	0	0	0.29	0.29	0.29	-	0
MY	0.14	0.14	0.14	0.14	0.14	0	-

FIGURE 5 | Distribution of axon terminals for the CFuPN in L5. **(A)** In the panel of top row, the 11 CFuPN in L5 with their complete morphologies are shown in the mouse brain. In the panel of bottom row, a typical neuron (#92) presents multiple axonal terminals in different brain regions. **(B)** The L5-tt of CFuPN: $n = 9$. The collaboration matrix of L5-tt of the CFuPN quantifies the "posterior probability" of another projection region given the neuron projection to the current region. Taking the values in the first row and second column as examples, "0.33" means 33% of the neurons projected to isocortex project to striatum. The values in the first row and third column: "1" means the neurons projected to isocortex must project to thalamus. The coexistence matrix of L5-tt of the CFuPN measures the occurrence frequency of two directional projection modes. Every element of the matrix represents the ratio of some neurons projecting to the two regions to all the neurons having at least two projection regions.

DISCUSSION

Digital reconstruction of neuron morphology is non-trivial in neuroscience (Parekh and Ascoli, 2013). Considering the bottleneck presented by the low speed of construction, the total number of 103 neurons from the visual cortex is relatively large. This is a systematic work on neuroanatomy with single-neuron resolution. Based on the BPS (Gong et al., 2016), we could achieve not only high resolution (voxel resolution of 0.2 μm × 0.2 μm × 1 μm) but also coherent positioning

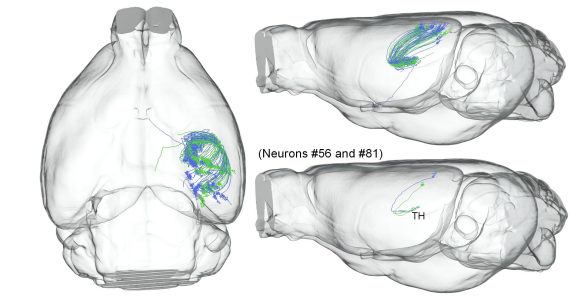

B

The collaboration matrix (L6-sp of the CFuPN: n=33)

	ISO	STR	TH	MB
ISO	-	0	1	0
STR	0	-	1	1
TH	0.30	0.03	-	0.03
MB	0	0.50	1	-

The coexistence matrix (L6-sp of the CFuPN: n=33)

	ISO	STR	TH	MB
ISO	-	0	0.56	0
STR	0	-	0	0
TH	0.56	0	-	0.06
MB	0	0	0.06	-

C

The collaboration matrix (L6-st of the CFuPN: n=30)

	ISO	STR	TH
ISO	-	0	1
STR	0	-	1
TH	0.59	0.03	-

The coexistence matrix (L6-st of the CFuPN: n=30)

	ISO	STR	TH
ISO	-	0	0.71
STR	0	-	0.04
TH	0.71	0.04	-

FIGURE 6 | Distribution of axon terminals for the CFuPN in L6. **(A)** The 63 CFuPN in L6 with their complete morphologies are shown in the mouse brain. In the bottom right of panel **(A)**, two representative L6-sp (#56) and L6-st (#81) neurons show their axonal terminals in thalamus. **(B)** The collaboration and coexistence matrices of L6-sp. L6-sp in corticofugal projection neurons: $n = 33$. **(C)** The collaboration and coexistence matrices of L6-st. L6-st in corticofugal projection neurons: $n = 30$.

functions. This work demonstrates an alternative platform for single-neuron mapping, reconstruction and quantification (Albanese and Chung, 2016; Economon et al., 2016; Gong et al., 2016). In this way, we could pinpoint the dendrite features and axon projection patterns without ambiguity, and correlate the dendritic classification and axonal hodology. This is one of a series of works by the authors on single-neuron mapping (Gong et al., 2016; Guo C. et al., 2017; Li et al., 2018), which focuses on the visual cortex.

We applied simple and agreed-upon criteria to classify excitatory neurons in the visual cortex (Molnar and Cheung, 2006; Oberlaender et al., 2012). All the identified types based on dendritic morphologies are consistent with previous reports. This could allow our work to be linked to previous studies. With quantitative analysis, we noticed that the apical dendrite height and branches show the natural clustering group (**Figure 2C**). These are the basis for a clear distinction for different types. Moreover, we have performed both dendritic and axonic-based neuron classification. Correlating the apical dendrite-based neuron types and the projection types, we found partial correlations between dendrites and axon projections. It suggested the significance of incorporating multiple and quantitative features for cell-type classification (Zeng and Sanes, 2017).

Our results were consistent with previous work (Molyneaux et al., 2007; Harris and Shepherd, 2015). We have found that neurons in the visual cortex could project to several areas. The results supported the concept of "one neuron-multiple targets" (Han et al., 2018). The most anterior projection of axons to the orbital area in lateral part, the secondary motor area and anterior cingulate area in dorsal part may account for their secondary activation following visual stimulation or visual cortex stimulation (Lim et al., 2012). These characteristics are related to the possible function of brains. Additionally, the corticothalamic neurons in L6 of visual cortex may have surficial dendrites within L1–L3. The subcerebral projection neurons in L5 of visual cortex (**Supplementary Table 1**) project to the isocortex, striatum, thalamus, midbrain, medulla, pons, and hypothalamus (**Figure 5**). The connection between visual area and motor area, anterior cingulate area have been demonstrated by both anterograde and retrograde labeling (Zingg et al., 2014). In our case, an individual L5 neuron in the visual area projects to motor area, anterior cingulate area and multiple subcortical brain regions at the same time (**Figure 5A**, neuron #92). The single axon-level have presented some unique and striking findings when compared with the previous report (Oh et al., 2014; Zingg et al., 2014). However, there may be some artifact of projection (e.g., axon terminals located in the fiber tracts) resulted from the technical limitation of imaging in current work. No doubt, better labeling and imaging technique will help to decipher the wiring map of brain.

Due to the labeling of the Thy1 H-line of mice, neuron somata are frequently located in layers 5 and 6. The cell type is not as specific but this is an opportunity to study neuronal classification in less mice. An explanation on the small number of animals ($n = 2$) is due to both the nature of conserved anatomy and the consistency of the reported neuron types. Genetic labeling of H-line is not as sparse but can be used for complete reconstruction according to our previous practices. The selection of Thy1-eYFP H-line may benefit us to do comparison with the reported studies in the mouse brain of the same line (Kim et al., 2016; Richter et al., 2018). To compensate the fact that the number of neurons in L5 is smaller than the number in L6 in visual cortex of the Thy1-eYFP H-line transgenic mice, it would be helpful to design experiments from different lines of mice, such as Thy1-eYFP G-line, Thy1-CFP 4-line (Feng et al., 2000) and Sim1_KJ18, Efr3a_NO108, et al. (Gerfen et al., 2013). In the future, more specific genetically labeled neurons may be studied with the same paradigm of this work. How to integrate the morphological, electrical and genetic characterization of neurons will be a critical issue in neuroscience (Gouwens et al., 2018). There is no electrophysiological recording for the neurons in this study. It may be possible to perform cell-type-specific recordings after morphological classification (Economo et al., 2018). We hope that a morphological study could guide further functional studies (Zeng and Sanes, 2017). Additionally, the realistic reconstruction of neurons will be helpful for the modeling and simulation of neural circuits (Markram et al., 2015).

In summary, our high-precision imaging system with single-axon-level reconstruction provides unique and detailed

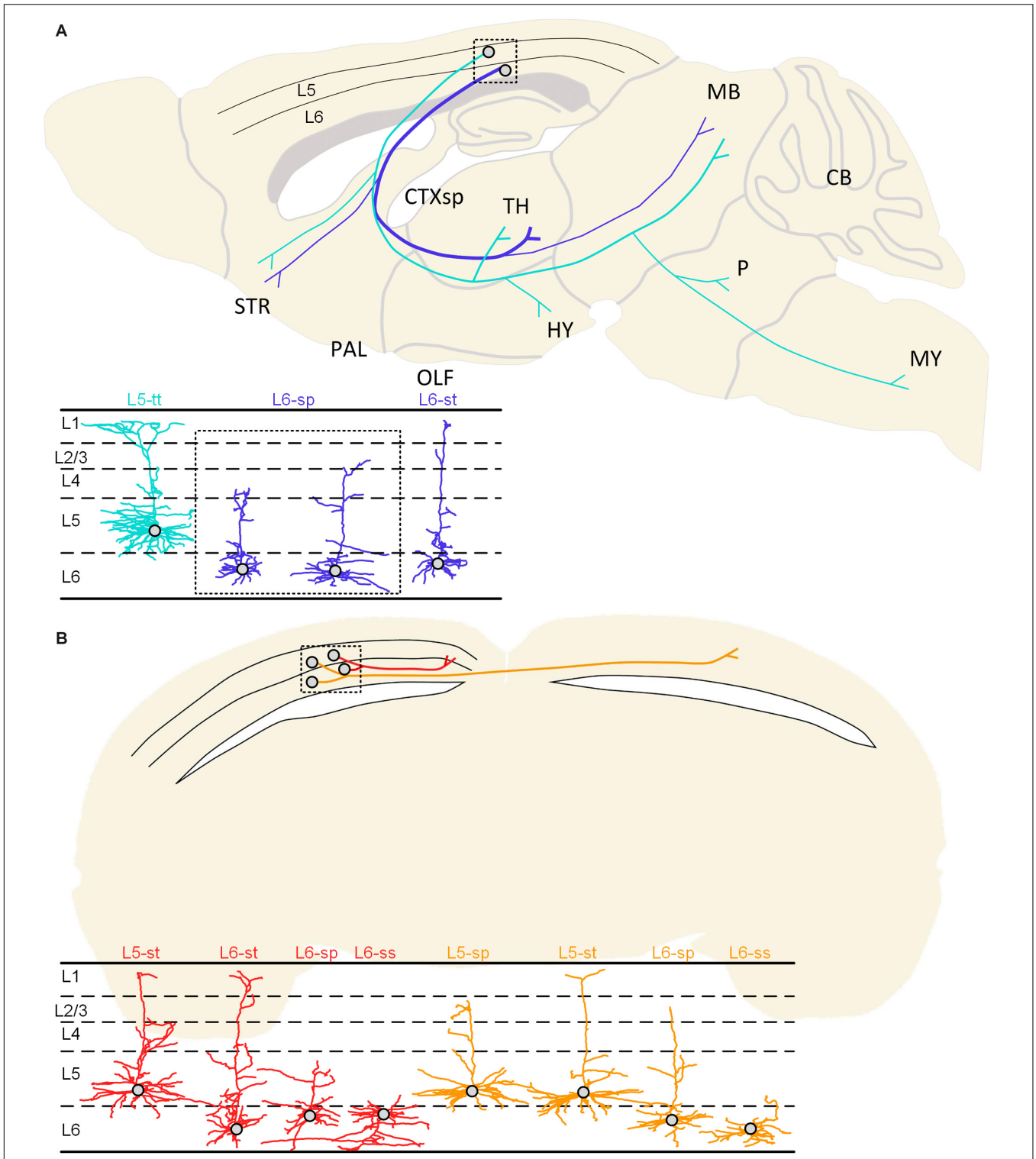

FIGURE 7 | Summarized projection patterns of the studied neurons in the visual cortex. **(A)** Two typical projection patterns of corticofugal projection neurons. The cyan-colored neuron shows a cell body located in L5 of the cortex and the subcerebral projection mode. The same cyan-colored dendrites in the lower left corner indicate the L5-tt type. The blue colored neuron presents soma in the L6 and the corticothalamic projection mode. The blue-colored dendrites may be classified as L6-sp and L6-st types according to the dendritic morphology. **(B)** The projection patterns of the ipsilateral circuit connection neurons and the callosal projection neurons. The ipsilateral circuit connection neurons (red) with somata located in the 5th or 6th layer of the cortex can be classified as L5-st, L6-st, L6-sp, and L6-ss dendritic types. The callosal projection neurons (orange) with cell bodies located in layer 5 or 6 can be distinguished as L5-sp, L5-st, L6-sp, and L6-ss types.

information for long-range projection patterns, which may provide interesting implications for the function of individual neurons.

DATA AVAILABILITY

The raw morphological data (*.swc files) supporting the conclusions of this manuscript will be made available by the authors, without undue reservation, to any qualified researcher. The data will be shared with community via NeuroMorpho.org once the manuscript is published.

ETHICS STATEMENT

All the procedures followed in the animal experiments were approved by the Institutional Animal Ethics Committee of Huazhong University of Science and Technology. The animal care and use were done in accordance with the guidelines of the Administration Committee of Affairs Concerning Experimental Animals in Hubei Province of China.

AUTHOR CONTRIBUTIONS

YZ, SC, and HG designed the study. YZ and SC wrote the manuscript. MR, XL, HW, and JY performed the tissue preparation and whole-brain data acquisition. YZ, ZX, SJ, and AL performed the image processing and visualization. YZ and SJ finished the neuron reconstruction. QL served as project advisor and participated in the planning and organizing of the project.

FUNDING

This work was supported by the Science Fund for Creative Research Groups (Grant No. 61721092), the National Natural Science Foundation of China (Grant Nos. 81671374 and 61371014), and the Director Fund of WNLO.

ACKNOWLEDGMENTS

We thank the Optical Bioimaging Core Facility of WNLO-HUST, and the Analytical and Testing Center of HUST for the support in data acquisition.

SUPPLEMENTARY MATERIAL

The Supplementary Material for this article can be found online at: https://www.frontiersin.org/articles/10.3389/fnins.2019.00912/full#supplementary-material

REFERENCES

Albanese, A., and Chung, K. (2016). Whole-brain imaging reaches new heights (and lengths). *eLife* 5:e13367. doi: 10.7554/eLife.13367

Ascoli, G. A., Alonso-Nanclares, L., Anderson, S. A., Barrionuevo, G., Benavides-Piccione, R., Burkhalter, A., et al. (2008). Petilla terminology: nomenclature of features of GABAergic interneurons of the cerebral cortex. *Nat. Rev. Neurosci.* 9, 557–568. doi: 10.1038/nrn2402

Atlan, G., Terem, A., Peretz-Rivlin, N., Groysman, M., and Citri, A. (2017). Mapping synaptic cortico-claustral connectivity in the mouse. *J. Comp. Neurol.* 525, 1381–1402. doi: 10.1002/cne.23997

Costa, L. D. F., Zawadzki, K., Miazaki, M., Viana, M. P., and Taraskin, S. N. (2010). Unveiling the neuromorphological space. *Front. Comput. Neurosci.* 4:150. doi: 10.3389/fncom.2010.00150

Ding, W., Li, A., Wu, J., Yang, Z., Meng, Y., Wang, S., et al. (2013). Automatic macroscopic density artefact removal in a nissl-stained microscopic atlas of whole mouse brain. *J. Microsc.* 251, 168–177. doi: 10.1111/jmi.12058

Economo, M. N., Viswanathan, S., Tasic, B., Bas, E., Winnubst, J., Menon, V., et al. (2018). Distinct descending motor cortex pathways and their roles in movement. *Nature* 563, 79–84. doi: 10.1038/s41586-018-0642-9

Economon, M. N., Clack, N. G., Levis, L. D., Gerfen, C. R., Svoboda, K., Myers, E. W., et al. (2016). A platform for brain-wide imaging and reconstruction of individual neurons. *eLife* 5:e10566. doi: 10.7554/eLife.10566

Fame, R. M., MacDonald, J. L., and Macklis, J. D. (2011). Development specification, and diversity of callosal projection neurons. *Trends Neurosci.* 34, 41–50. doi: 10.1016/j.tins.2010.10.002

Feng, G., Mellor, R., Bernstein, M., Kellerpeck, C. R., Nguyen, Q. T., Wallace, M., et al. (2000). Imaging neuronal subsets in transgenic mice expressing multiple spectral variants of GFP. *Neuron* 28, 41–51. doi: 10.1016/S0896-6273(00)00084-82

Gang, Y., Zhou, H., Jia, Y., Liu, L., Liu, X., Rao, G., et al. (2017). Embedding and chemical reactivation of green fluorescent protein in the whole mouse brain for optical micro-imaging. *Front. Neurosci.* 11:121. doi: 10.3389/fnins.2017.00121

Gerfen, C. R., Paletzki, R., and Heintz, N. (2013). GENSAT BAC cre-recombinase driver lines to study the functional organization of cerebral cortical and basal ganglia circuits. *Neuron* 80, 1368–1383. doi: 10.1016/j.neuron.2013.10.016

Gong, H., Xu, D., Yuan, J., Li, X., Guo, C., Peng, J., et al. (2016). High-throughput dual-colour precision imaging for brain-wide connectome with cytoarchitectonic landmarks at the cellular level. *Nat. Commun.* 7:12142. doi: 10.1038/ncomms12142

Gouwens, N. W., Sorensen, S. A., Berg, J., Lee, C., Jarsky, T., Ting, J., et al. (2018). Classification of electrophysiological and morphological types in mouse visual cortex. *bioRxiv*

Greig, L. C., Woodworth, M. B., Galazo, M. J., Padmanabhan, H., and Macklis, J. D. (2013). Molecular logic of neocortical projection neuron specification, development and diversity. *Nat. Rev. Neurosci.* 14, 755–769. doi: 10.1038/nrn3586

Guo, C., Peng, J., Zhang, Y., Li, A., Li, Y., Yuan, J., et al. (2017). Single-axon level morphological analysis of corticofugal projection neurons in mouse barrel field. *Sci. Rep.* 7:2846. doi: 10.1038/s41598-017-03000-8

Guo, W., Liu, X., Liu, Y., Gang, Y., He, X., Jia, Y., et al. (2017). Chemical reactivation of resin-embedded pHuji adds red for simultaneous two-color imaging with EGFP. *Biomed. Opt. Express* 8, 3281–3288. doi: 10.1364/BOE.8.003281

Han, Y., Kebschull, J. M., Campbell, R. A. A., Cowan, D., Imhof, F., Zador, A. M., et al. (2018). The logic of single-cell projections from visual cortex. *Nature* 556, 51–56. doi: 10.1038/nature26159

Harris, K. D., and Shepherd, G. M. (2015). The neocortical circuit: themes and variations. *Nat. Neurosci.* 18, 170–181. doi: 10.1038/nn.3917

Huang, Z. J. (2014). Toward a genetic dissection of cortical circuits in the mouse. *Neuron* 83, 1284–1302. doi: 10.1016/j.neuron.2014.08.041

Jeong, M., Kim, Y., Kim, J., Ferrante, D. D., Mitra, P. P., Osten, P., et al. (2016). Comparative three-dimensional connectome map of motor cortical projections in the mouse brain. *Sci. Rep.* 6:20072. doi: 10.1038/srep20072

Kanari, L., Ramaswamy, S., Shi, Y., Morand, S., Meystre, J., Perin, R., et al. (2019). Objective classification of neocortical pyramidal cells. *Cereb. Cortex* 29, 1719–1735. doi: 10.1093/cercor/bhy339

Kim, E. J., Juavinett, A. L., Kyubwa, E. M., Jacobs, M. W., and Callaway, E. M. (2015). Three types of cortical layer 5 neurons that differ in brain-wide connectivity and function. *Neuron* 88, 1253–1267. doi: 10.1016/j.neuron.2015.11.002

Kim, T. H., Zhang, Y., Lecoq, J., Jung, J. C., Li, J., Zeng, H., et al. (2016). Long-term optical access to an estimated one million neurons in the live mouse cortex. *Cell Rep.* 17, 3385–3394. doi: 10.1016/j.celrep.2016.12.004

Kondo, S., and Ohki, K. (2016). Laminar differences in the orientation selectivity of geniculate afferents in mouse primary visual cortex. *Nat. Neurosci.* 19, 316–319. doi: 10.1038/nn.4215

Li, X., Yu, B., Sun, Q., Zhang, Y., Ren, M., Zhang, X., et al. (2018). Generation of a whole-brain atlas for the cholinergic system and mesoscopic projectome analysis of basal forebrain cholinergic neurons. *Proc. Natl. Acad. Sci. U.S.A.* 115, 415–420. doi: 10.1073/pnas.1703601115

Li, Y., Gong, H., Yang, X., Yuan, J., Jiang, T., Li, X., et al. (2017). TDat: an efficient platform for processing petabyte-scale whole-brain volumetric images. *Front. Neural Circuits* 11:51. doi: 10.3389/fncir.2017.00051

Liang, F., Xiong, X. R., Zingg, B., Ji, X., Zhang, L. I., and Tao, H. W. (2015). Sensory cortical control of a visually induced arrest behavior via corticotectal projections. *Neuron* 86, 755–767. doi: 10.1016/j.neuron.2015.03.048

Lim, D. H., Mohajerani, M. H., Ledue, J., Boyd, J., Chen, S., and Murphy, T. H. (2012). In vivo large-scale cortical mapping using channelrhodopsin-2 stimulation in transgenic mice reveals asymmetric and reciprocal relationships between cortical areas. *Front. Neural Circuit* 6:11. doi: 10.3389/fncir.2012.00011

Lin, H., Kuang, J., Sun, P., Li, N., Lv, X., and Zhang, Y. (2018). Reconstruction of intratelencephalic neurons in the mouse secondary motor cortex reveals the diverse projection patterns of single neurons. *Front. Neuroanat.* 12:86. doi: 10.3389/fnana.2018.00086

Markram, H., Muller, E., Ramaswamy, S., Reimann, M. W., Abdellah, M., Sanchez, C. A., et al. (2015). Reconstruction and simulation of neocortical microcircuitry. *Cell* 163, 456–492. doi: 10.1016/j.cell.2015.09.029

Meyer, H. S., Wimmer, V. C., Hemberger, M., Bruno, R. M., de Kock, C. P. J., Frick, A., et al. (2010). Cell type-specific thalamic innervation in a column of rat vibrissal cortex. *Cereb. Cortex* 20, 2287–2303. doi: 10.1093/cercor/bhq069

Mitra, P. P. (2014). The circuit architecture of whole brains at the mesoscopic scale. *Neuron* 83, 1273–1283. doi: 10.1016/j.neuron.2014.08.055

Molnar, Z., and Cheung, A. F. P. (2006). Towards the classification of subpopulations of layer V pyramidal projection neurons. *Neurosci. Res.* 55, 105–115. doi: 10.1016/j.neures.2006.02.008

Molyneaux, B. J., Arlotta, P., Menezes, J. R. L., and Macklis, J. D. (2007). Neuronal subtype specification in the cerebral cortex. *Nat. Rev. Neurosci.* 8, 427–437. doi: 10.1038/nrn2151

Oberlaender, M., de Kock, C. P. J., Bruno, R. M., Ramirez, A., Meyer, H. S., Dercksen, V. J., et al. (2012). Cell type-specific three-dimensional structure of thalamocortical circuits in a column of rat vibrissal cortex. *Cereb. Cortex* 22, 2375–2391. doi: 10.1093/cercor/bhr317

Oh, S. W., Harris, J. A., Ng, L., Winslow, B., Cain, N., Mihalas, S., et al. (2014). A mesoscale connectome of the mouse brain. *Nature* 508, 207–214. doi: 10.1038/nature13186

Parekh, R., and Ascoli, G. A. (2013). Neuronal morphology goes digital: a research hub for cellular and system neuroscience. *Neuron* 77, 1017–1038. doi: 10.1016/j.neuron.2013.03.008

Porrero, C., Rubiogarrido, P., Avendano, C., and Clasca, F. (2010). Mapping of fluorescent protein-expressing neurons and axon pathways in adult and developing Thy1-eYFP-H transgenic mice. *Brain Res.* 1345, 59–72. doi: 10.1016/j.brainres.2010.05.061

Richter, M., Negrodemontel, M. L., Blancoocampo, D., Taranto, E., Lago, N., and Peluffo, H. (2018). Thy1-YFP-H mice and the parallel rod floor test to evaluate short- and long-term progression of traumatic brain injury. *Curr. Protoc. Immunol.* 120, 24.1.1–24.1.25. doi: 10.1002/cpim.42

Roth, M. M., Dahmen, J. C., Muir, D. R., Imhof, F., Martini, F. J., and Hofer, S. B. (2016). Thalamic nuclei convey diverse contextual information to layer 1 of visual cortex. *Nat. Neurosci.* 19, 299–307. doi: 10.1038/nn.4197

Sun, Q., Li, X., Ren, M., Zhao, M., Zhong, Q., Ren, Y., et al. (2019). A whole-brain map of long-range inputs to GABAergic interneurons in the mouse medial prefrontal cortex. *Nat. Neurosci.* 22, 1357–1370. doi: 10.1038/s41593-019-0429-9

Sun, W., Tan, Z., Mensh, B. D., and Ji, N. (2016). Thalamus provides layer 4 of primary visual cortex with orientation- and direction-tuned inputs. *Nat. Neurosci.* 19, 308–315. doi: 10.1038/nn.4196

Zeng, H., and Sanes, J. R. (2017). Neuronal cell-type classification: challenges, opportunities and the path forward. *Nat. Rev. Neurosci.* 18, 530–546. doi: 10.1038/nrn.2017.85

Zhang, S., Xu, M., Chang, W., Ma, C., Do, J. P. H., Jeong, D., et al. (2016). Organization of long-range inputs and outputs of frontal cortex for top-down control. *Nat. Neurosci.* 19, 1733–1742. doi: 10.1038/nn.4417

Zingg, B., Hintiryan, H., Gou, L., Song, M. Y., Bay, M., Bienkowski, M. S., et al. (2014). Neural networks of the mouse neocortex. *Cell* 156, 1096–1111. doi: 10.1016/j.cell.2014.02.023

Conflict of Interest Statement: The authors declare that the research was conducted in the absence of any commercial or financial relationships that could be construed as a potential conflict of interest.

frontiers in Physics

BRIEF RESEARCH REPORT
published: 01 October 2019
doi: 10.3389/fphy.2019.00142

Significant Instances in Motor Gestures of Different Songbird Species

Javier N. Lassa Ortiz[1,2], *Cecilia T. Herbert*[1,2], *Gabriel B. Mindlin*[1,2] *and Ana Amador*[1,2]*

[1] *Physics Department, Faculty of Natural and Exact Sciences, University of Buenos Aires, Buenos Aires, Argentina,* [2] *Instituto de Física de Buenos Aires (IFIBA), CONICET, Buenos Aires, Argentina*

The nervous system representation of a motor program is an open problem for most behaviors. In birdsong production, it has been proposed that some special temporal instances, linked to significant aspects of the motor gestures used to generate the song, are preferentially represented in the cortex. In this work, we compute these temporal instances for two species, and report which of them is better suited to test the proposed coding (as well as alternative models) against data.

Keywords: songbirds, motor gestures, cortical representation, sparse coding, birdsong production

OPEN ACCESS

Edited by:
Chris G. Antonopoulos, University of Essex, United Kingdom

Reviewed by:
Sarah E. London, University of Chicago, United States
Devin Merullo, UT Southwestern Medical Center, United States

***Correspondence:**
Ana Amador
anita@df.uba.ar

Specialty section:
This article was submitted to Biophysics, a section of the journal Frontiers in Physics

Received: *09 May 2019*
Accepted: *13 September 2019*
Published: *01 October 2019*

Citation:
Lassa Ortiz JN, Herbert CT, Mindlin GB and Amador A (2019) Significant Instances in Motor Gestures of Different Songbird Species. Front. Phys. 7:142. doi: 10.3389/fphy.2019.00142

INTRODUCTION

Behavior emerges from the interaction between a nervous system and a biomechanical body whose dynamics are complex and ruled by non-linear phenomena. For this reason, it is not trivial to unveil how the nervous system represents the motor program behind a given behavior. A particularly complex behavior is vocal communication, which in several species requires the coordination of many muscles in order to generate the rich variety of acoustic signals necessary to convey a message. Even in phylogenetically distant species such as humans and birds, it has been recognized that a wide variety of sounds can be achieved through the temporal coordination of simple motor instructions, or motor gestures. In the case of human speech, those are the object of study of articulatory phonology [1]. The coordination of very simple motor gestures controlling the tongue, lips, and jaw [2] is capable of accounting for the acoustic features that allow a message to be shared between humans. Recent work reports that reasonably simple somatotopic representations of these gestures can be found in cortical regions of the human brain [3]. In the case of the sounds generated by songbirds, it has also been reported that a variety of different acoustic signals can be generated by changing only the phase difference between simple gestures controlling the respiration and the configuration of the avian vocal organ [4]. Moreover, some subtle features of a sound's timbre have been directly associated with the dynamics exhibited by the biomechanics involved in its generation [5], relieving the nervous system from controlling a myriad of subtle instructions in order to produce a complex sound. This suggests that a complex and rich behavior can be decomposed into simpler motor instructions, whose simplicity might help to understand its representation coding at the level of the nervous system.

Songbirds are an optimal neuroethological model to study motor control. Singing behavior is easy to record, stereotyped, and stable throughout a bird's adult life. It emerges from a subtle interaction between a dedicated brain circuit and a biomechanical device. The outcome of the nervous system is a set of electrical signals that activate the muscles responsible for the time dependent configurations of the avian vocal organ and the respiratory system. A complex song typically consists of a sequence of sounds whose acoustic features evolve continuously in time.

The time dependent physiological instructions necessary for the generation of those continuous segments are the motor gestures. The question then naturally arises: how are these motor gestures represented in the nervous system?

Unveiling how different parts of the nervous system code this rich behavior has proven to be a difficult task. Fee and collaborators proposed a model in a seminal work published in 2004 [6]. The analysis of the neural activity in a cortical nucleus of zebra finches (*Taenopygia guttata*) [7] led the authors to claim that a sequence of projecting neurons was activated continuously during the execution of the song. Each projecting neuron was active during approximately 10 ms, and the set of consecutively activated projecting neurons continuously spanned the duration of the song.

Amador and collaborators proposed an alternative view [8]. In that work, they recorded the neural activity of singing birds of the same species analyzed by Fee et al. The work was originally designed to study the neural response of sleeping birds to synthetic songs generated by a dynamical model. Therefore, the authors had a motor template in terms of which to interpret the temporal instances of the recorded neural activity for each syllable (defined as a segment of continuous sound flanked by silence). Moreover, they preferentially used birds with long syllables of constant pitch to enable a more accurate song synthesis. The neural recordings, in light of the motor gestures obtained by the biomechanical model, led to the claim that there was preferential neural activity at significant motor instances of the song, which they called gesture trajectory extrema (GTEs). A sound requiring complex motor instructions would be characterized by a large number of GTEs.

That work originated a series of replies [9–12]. A suggestive argument for the continuous representation hypothesis was that many neurons were measured in a large set of birds, which led the authors to claim that the neural activity was distributed continuously during the songs. None of those studies reported a bias toward birds with simple songs, although the somewhat simpler songs of juveniles were investigated in one of them [9].

In this work, we show that the GTE distribution in zebra finch song seems to continuously cover the duration of the song, and therefore, these two models cannot be easily disambiguated using this species. Another songbird species might be more suitable for this task. For this reason, we studied the song structure of a different songbird species, the domestic canary (*Serinus canaria*), which has longer and simpler syllables than the zebra finch. Here, we quantify these features and relate them to the GTEs. In this way, we suggest a way to distinguish between the two alternative models of neural coding by studying birds that produce syllables with specific acoustic features. One of the two models predicts a continuous neural representation of the motor patterns, regardless of the acoustic features of the songs. The second model predicts a sparser neural representation for simpler syllables (i.e., syllables with sparser GTEs).

MATERIALS AND METHODS

Zebra Finch and Canary Song Structure

We randomly selected 20 zebra finch songs and 20 canary songs from our historical records. The birds were obtained from commercial breeders as adults within the last 10 years, with no familial relationship between them. They were recorded with a directional microphone from adult male birds (zebra finches and canaries) individually housed in a sound-isolation chamber. Food and water were provided *ad libitum*, in accordance with a protocol approved by the University of Buenos Aires (FCEN-UBA) Institutional Animal Care and Use Committee (CICUAL). The recordings were obtained using the software Avisoft—RECORDER (https://www.avisoft.com/recorder.htm). All sound files were filtered using Praat 6.0.04 software (http://www.fon.hum.uva.nl/praat/) to eliminate environment noise (pass Hann band from 200 Hz to half the sampling rate). This is the standard recording protocol in our laboratory.

Zebra finch song has a different structure than canary song (see examples in **Figures 1A,B**, respectively). A zebra finch song is composed of a repetition of motifs: M1, M2, M3 in **Figure 1A**. A motif is a sequence of syllables sung once in a stereotyped order, as shown in **Figure 1C** where each different letter indicates a syllable [13, 14]. Canary songs show a different organization. A phrase is formed by the repetition of a given syllable, and the song is composed of a sequence of different phrases. A representative example is shown in **Figure 1B**, indicating different phrases with different numbers: Ph1, Ph2, …, Ph6 [15, 16].

We compared the motifs in the songs of zebra finches to a construction of what we called *pseudo-motifs* of the songs of canaries. The pseudo-motifs have the same syllables in the same order as in the original canary song, but each syllable is repeated only once (**Figure 1D**). In other words, in the pseudo-motifs, the original phrases in the song are shortened to one repetition of each syllable. In this way, syllable "k" in **Figure 1D** ($k = 1, \ldots, 6$) is a representative example of the syllables that compose the phrase Phk in **Figure 1B**. The silent gap between two syllables in a pseudo-motif corresponds to the gap between the original phrases.

Automatic Calculation of Gesture Trajectory Extrema (GTEs)

An automatic procedure for detecting GTEs was proposed by Boari et al. [17]. The key observation behind this procedure is that the transitions between the song segments with qualitatively different acoustic features are reflected as minima in the envelope of the songs. In this work, we used a similar approach to the one used in [17] to obtain the GTEs of the songs in two species and study them comparatively.

The envelope of the song was obtained as follows. First, we computed the Hilbert transform of the sound, obtaining a time trace $s(t)$. Then, we smoothed $s(t)$ by integration of the linear system:

$$\frac{dz}{dt} = -\frac{1}{\tau} z + s(t),$$

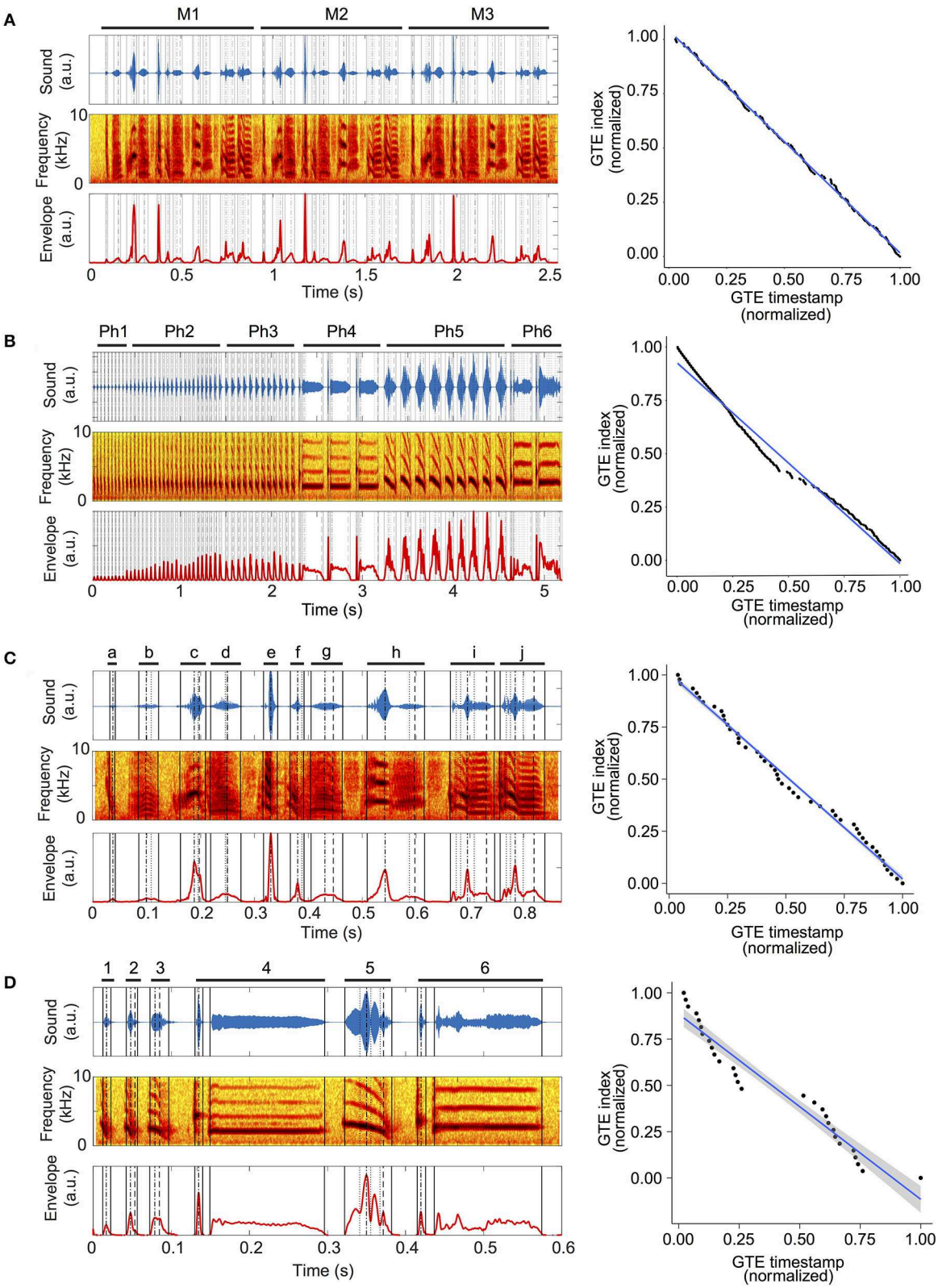

FIGURE 1 | GTEs in zebra finch and canary songs. **(A)** Left top: sound of a zebra finch song. Labels M1–M3 and bars indicate a motif that is repeated three times during the song. Left middle: spectrogram of the song. Left bottom: envelope trace calculated from the sound in the left top panel. Vertical lines indicate the

(Continued)

FIGURE 1 | timestamps of the Gesture Trajectory Extrema (GTEs) calculated from the envelope trace: solid lines indicate onset and offset GTEs; dotted lines, minima; dashed-and-dotted lines, absolute maximum and dashed lines indicate last maximum. Right: normalized GTE position plots of the zebra finch song. The GTE timestamps in the song and the GTE indices are normalized. The blue line shows the best fit using ordinary least squares. The gray area corresponds to the 95% confidence interval (see Methods). **(B)** Left top: sound of a canary song. Labels Ph1–Ph6 and bars indicate repetitions of one syllable, also called phrases. Left middle, left bottom, and right panel as in **(A)**. **(C)** Left top: sound of zebra finch motif M1 from **(A)**. Letters a–j and bars indicate individual syllables. Left middle, left bottom, and right panel as in **(A)**. **(D)** Left top: sound of a canary pseudo-motif. Letters a–f and bars indicate unique instances of the syllables in each phrase showed in **(C)**. Left middle, left bottom, and right panel as in **(A)**.

with $\tau = 1\ ms$. After this, we applied a Savitzky-Golay filter [18] (window size = 513 samples, 4th order of the smoothing polynomial). Finally, the obtained time trace was normalized with respect to the absolute maximum of the envelope, obtaining $n(t)$. A five-point stencil derivation of the signal was computed and further filtered with a Savitzky-Golay filter (same parameters as before) to obtain $d(t)$, representing a smoothed derivative function of the original sound.

Additionally, we obtained a time trace without artifacts in syllable beginnings and ends, by filtering $s(t)$ using a moving window average (window size = 250 samples, that at 40 kHz correspond to 6.25 ms), both in the forward and reverse directions to avoid introducing spurious phase delays. We normalized the resulting time trace with respect to the absolute maximum of the envelope, obtaining $a(t)$.

We used $a(t)$ to compute syllable beginnings and ends. We set a threshold of 3% of the maximum value of $a(t)$. A syllable onset was defined when the signal $a(t)$ went over the threshold, and its offset when the signal went back under the threshold.

The intra-syllabic maxima and minima were computed analyzing sign changes in the smoothed derivative $d(t)$. After calculating all the timestamps of the minima in $d(t)$, we considered minima to be significant if their values in $n(t)$ were at least 5% smaller than the maxima before and after. The absolute maximum and the last maximum in signal $n(t)$ were considered significant regardless of their relative value.

For canaries, even though syllables of the same phrase are expected to have the same GTEs, occasionally, due to variations in song production, syllables of the same phrase have different GTEs. In those cases, we only considered the GTEs that were systematic for all the uttered syllables.

Using these definitions, we extracted GTEs from the sound which corresponded to beginnings and ends of syllables, significant minima (indicating the instances when gesture transitions within a syllable take place), and significant maxima (taken as proxies of maxima of the air sac pressure). The codes for implementing this procedure can be downloaded from http://www.lsd.df.uba.ar.

Normalized GTE Position Plots for a Song

To visualize the distribution of GTEs in a song, we plotted the GTE index normalized to the total number of GTEs in the song against the GTE timestamp normalized to the song duration. Then, the data was fitted using lm function from R (Version 3.5.3—https://www.r-project.org). **Figure 1** shows examples of sound waves of different songs, their spectrogram and sound envelope, together with the associated GTEs (vertical lines). The corresponding normalized GTE position plot for each song is shown in the right panels of **Figure 1**.

Chi^2 Parameter

The Chi^2 parameter defined in this work was calculated from the *normalized GTE position plots* (right panels of **Figures 1**, **2A,B**) using the following formula

$$Chi = \sum_{i=1}^{n} \frac{(Obs_i - Exp_i)}{|Exp_i|} \cdot \frac{1}{n}$$

where n is the number of data points; Obs_i is the observed value of the normalized timestamp (x-axis value) of the GTE whose index value is i; Exp_i is the value of the normalized GTE timestamp (x-axis value in the normalized GTE position plots) that the line of best fit takes when the GTE index value is i. The Chi^2 parameter increases as the data points fall further away from the line of best fit.

Spectrogram Metrics of Syllables

Each song was segmented using Avisoft Bioacoustics SAS Lab Pro (Version 5.2.13—www.avisoft.com/) using automatic detection of waveform events with a threshold and hold time such that we obtained the same syllables as the automatic procedure for detecting GTEs. We sought to identify one salient syllable type that was long and simple in each species. The clearest to categorize were tonal whistles in the case of canaries (constant frequency, low energy in the harmonics) and harmonic stacks (constant frequency with high energy in distinct harmonics) for zebra finches. Two trained independent observers inspected all syllables and labeled harmonic stacks and whistles.

SAS Lab Pro was used to automatically calculate syllable duration, duration of a constant frequency segment within the syllable, and mean entropy of the syllable from the song spectrograms (shown in **Figure 3**). The spectrograms were computed with FFT length 512, frame size 100%, gauss window and a temporal overlap of 87.5% for all songs. To calculate the constant frequency segment duration, the tolerance was set to 300 Hz. For zebra finches, we found that the software sporadically detected peak frequencies in the high energy harmonics instead of at the fundamental frequency, and thus underestimated the constant frequency segment durations. In order to limit the detection of segments to low frequencies that included the fundamental frequency of harmonics stacks, we filtered the syllables in which the peak frequency during the whole syllable was <3.5 kHz in SAS Lab using the lowpass Frequency

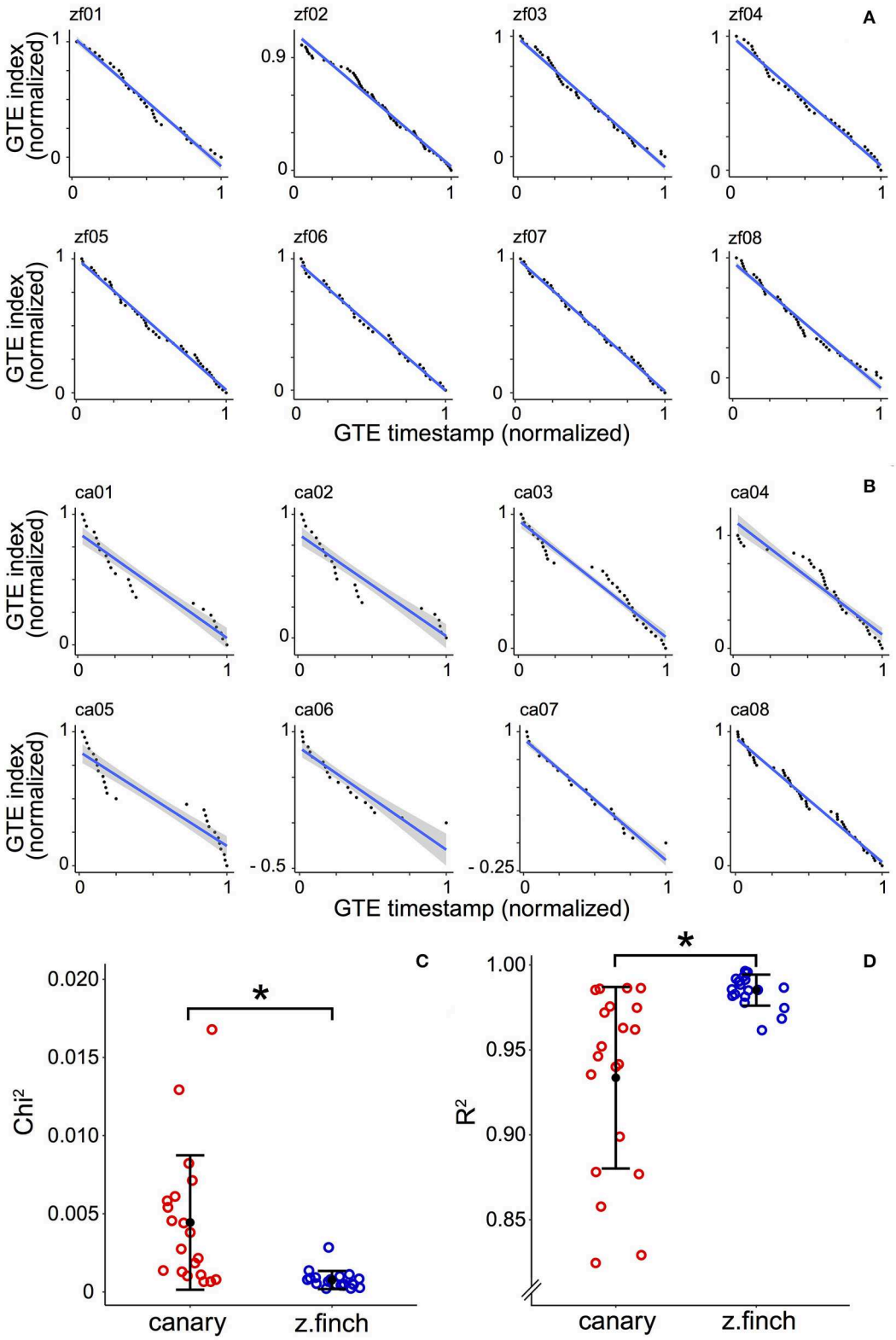

FIGURE 2 | Normalized Gesture Trajectory Extrema (GTE) position plots for zebra finches and canaries. **(A)** Normalized GTE position plots for eight zebra finch motifs selected at random. The GTE timestamps in the motif and the GTE indices are normalized. The blue line shows the best fit using ordinary least squares. The gray area

(Continued)

FIGURE 2 | corresponds to the 95% confidence interval (see Methods). **(B)** Normalized GTE position plots for eight canary pseudo-motifs selected at random. Same analysis as in **(A)** of the 20 analyzed (the remaining 12 plots are shown in **Supplementary Figure 2**). **(C)** Each circle shows the Chi^2 value of the linear fit for one individual. Black dots represent the mean Chi^2 while error bars represent ± SD of the data. The average Chi^2 is 0.0044 ± 0.0043 (mean ± SD) for canaries ($n = 20$) and 0.0008 ± 0.0006 (mean ± SD) for zebra finches ($n = 20$). **(D)** Each circle shows the R^2 value of the linear fit for one individual. Black dots represent the mean R^2 while error bars represent ± SD of the data. The average R^2 is 0.93 ± 0.05 (mean ± SD, $n = 20$) for canaries and 0.99 ± 0.01 (mean ± SD, $n = 20$) for zebra finches. In **(C,D)** asterisks indicate that both distributions are statistically different (Kolmogorov-Smirnov test, $p < 0.01$).

Domain Transformation with a cutoff at 3.5 kHz and re-ran the calculation of this metric.

The mean entropy ranges from close to zero for tonal signals and one for random noisy signals. We calculated the sample density probability estimates using the default probability density estimation in the ksdensity function from MathWorks Matlab (Version 2018a—www.mathworks.com) with appropriate bin size. For each metric, the bin size was determined as 10% of the metric's value range, and the minimum bin size of the two species was used for both species. This strategy allowed us to use the same bin size for each metric for both species.

Example and non-example bird syllable subgroups shown in **Supplementary Figure 3** were tested for differences in the probability densities of each metric using the Kolmogorov-Smirnov test (kstest2 function in Matlab). Bin sizes for each metric were the same as those used for the complete sample in **Figure 3**.

RESULTS

Motor Gesture Extrema in Birdsong

Motor gestures have previously been identified as *the time dependent parameters of a dynamical system capable of synthesizing a realistic replica of the birdsong* [4, 8, 19]. GTEs were defined in [8] as a measure of a song's complexity and consist of a set of temporal instances that include syllable beginnings, syllable endings, maxima of the parameter representing the air sac pressure used in the vocalization, and the discontinuities of the fundamental frequency during continuous vocalization (see Methods). The rationale behind defining GTEs is that many continuous acoustic features of a song occur between discrete (impulse-like) instructions, constituting significant temporal instances in the song. For example, the characteristic down-sweep syllables of a zebra finch (i.e., syllables with fundamental frequencies that decay as time evolves) are generated with a pulse like contraction of the *syringealis ventralis* muscle at the beginning of the vocalization. This pulse is passively transduced into a smooth stretching of the oscillating labia responsible for the sound [20]. In complex syllables that require using both sound sources, a discontinuity of the fundamental frequency can arise when the sound ceases to be generated by one of the two sound sources and starts to be generated by the other sound source. This requires the rapid alternating activation of gating muscles (e.g., [21, 22]).

In this work, we analyzed 40 songs from adult male birds: 20 from zebra finches and 20 from canaries (see Methods). We show an example of a zebra finch song in **Figure 1A** and one of a canary song in **Figure 1B**. The average duration of the canary songs was 14.65 ± 4.60 s (mean ± SD) while for zebra finches the song duration was 2.2 ± 1.4 s (mean ± SD), and their motifs lasted on average 0.67 ± 0.21 s (mean ± SD). An example of a zebra finch motif is shown in **Figure 1C**.

The songs of canaries and zebra finches both consist of sequences of continuous sounds called syllables, separated by brief silences. Yet they differ in two important ways. First, acoustic features within a syllable vary smoothly in canary song, while there can be abrupt changes in acoustic features within a zebra finch syllable. Second, the syntax is different. A canary will repeat a syllable several times, before switching to sing several copies of a different one. A canary song is built as a sequence of repeated syllables. A zebra finch song, however, consists of a succession of different syllables (a motif), which is sung repeatedly. We are interested in the first difference, at syllabic level, between zebra finch and canary song, since it suggests that syllable generation by each species might require a different degree of motor sophistication. For this reason, we constructed what we called pseudo-motifs for the canary songs. This allowed us to generate a song with structure similar to the zebra finch motif and compare syllable complexity. Briefly, the syllable repetitions present in canary songs were removed in the pseudo-motifs (example shown in **Figure 1D**). See Methods for a detailed description of the procedure. The average duration of canary pseudo-motifs was 0.99 ± 0.40 s (mean ± SD), which is comparable to zebra finch motif duration.

Using an adaptation of previously developed software [17], we extracted GTEs automatically from the song recordings. The left panels of **Figure 1** show the resulting GTEs as vertical lines overlaid on the sound, spectrogram, and sound envelope of the zebra finch and canary songs. Note that in the syllables of the canary pseudo-motif in **Figure 1D**, only the GTEs that are systematic throughout the phrase remain. For example, the reported GTEs in syllable 6 are only those present in all syllables of Phrase 6 in **Figure 1B**. Our next step was to investigate the differences in the distribution of the GTEs of both species. In the rest of this article, we will refer to analyses performed on canary pseudo-motifs and true zebra finch motifs, unless stated otherwise.

GTE Distribution in Canaries Is More Heterogeneous Than in Zebra Finches

To visualize the distribution of GTEs in a song, we created the normalized GTE position plots (right panels in **Figure 1**). These show the normalized index of each GTE against its normalized timestamp, fitted to a linear model (see Methods). The right panel of **Figure 1A** shows that the zebra finch complete song closely follows the linear fit. However, the patterning of points around the line are repeated, because the stereotyped motif is repeated three times in the song. In the case of the complete canary song

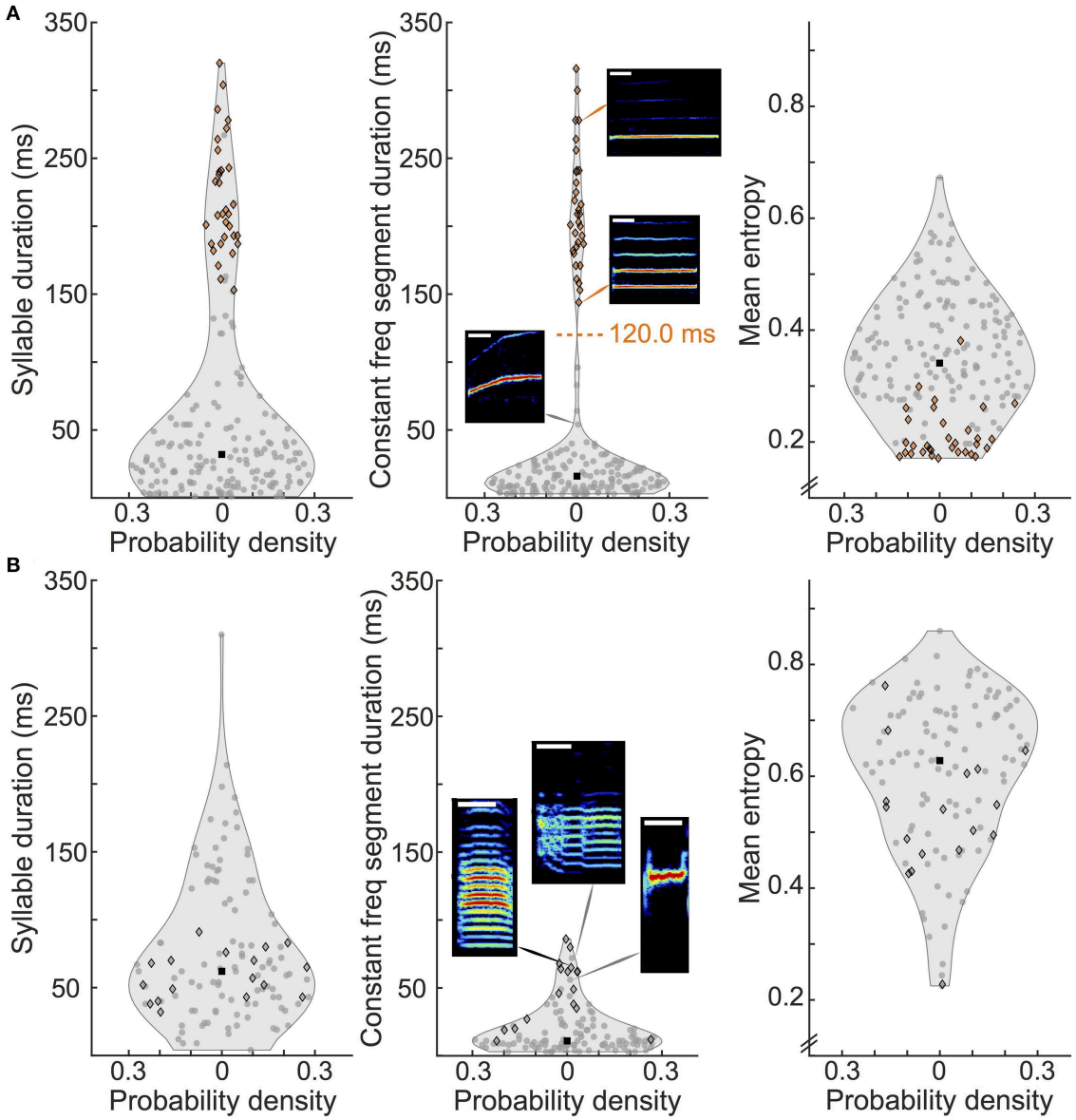

FIGURE 3 | Distribution of spectrogram metrics of canary and zebra finch syllables. **(A)** Violin plots showing the distributions of syllable duration (left panel), duration of constant frequency segment (middle panel) and mean entropy (right panel) for canary syllables. The gray area represents the distribution density (symmetrically plotted on the x-axis) and its median is shown with a black square. One hundred and eighty seven canary syllables total, bin sizes are 30, 10, and 50 ms for each metric respectively. A scatter graph with the y-value of each individual syllable is overlaid on each distribution plot. Scatter points are orange if the syllable contains a constant frequency segment duration larger than the threshold value (120 ms) indicated with a dashed line in the middle panel, and gray otherwise. Syllables of a categorized type are outlined with a black diamond (whistles in canaries and harmonic stacks in zebra finches). Note that all syllables that surpass the threshold are whistles. Constant segment duration ranges from 3 to 96 ms and 144 to 316 ms. Spectrogram insets show example syllables (see text). Height of spectrograms is 10 kHz. White bar indicates 50 ms. **(B)** Same as in **(A)**, for zebra finches, 119 syllables total and same bin sizes per metric. Constant segment duration range: 3–86 ms. Harmonic stacks are not isolated in any of the metrics analyzed.

(**Figure 1B**), there is a large deviation from the linear fit, which makes the song seem more heterogeneous, but is exaggerated because it considers all the repeated syllables in each phrase. The corresponding analysis for one motif of the zebra finch song and one syllable per phrase of the canary song (pseudo-motif) are shown in the right panels of **Figures 1C,D**. To study differences between species at the syllabic level, we compared the distribution of GTEs in zebra finch motifs with the distribution of GTEs in canary pseudo-motifs.

In **Figures 2A,B**, we show eight examples of the GTE index distribution from each species (selected randomly, see Methods). The plots for the remaining 12 songs are shown in

Supplementary Figures 1, **2**. We calculated the Chi² parameter (see Methods) and the R^2 (coefficient of determination) from the normalized GTE position plots. The Chi² parameter takes larger values as data points fall further away from the line of best fit. We calculated the mean Chi² for every bird (**Figure 2C**) and obtained 0.0044 ± 0.0043 (mean ± SD) for canaries ($n = 20$) and 0.0008 ± 0.0006 (mean ± SD) for zebra finches ($n = 20$). A Kolmogorov-Smirnov test (KS test) showed that the distributions are statistically different ($p < 0.01$). A similar result was obtained for R^2 (KS test, $p < 0.01$). The average R^2 value for canaries was 0.93 ± 0.05 (mean ± SD) and for zebra finches it was 0.99 ± 0.01 (mean ± SD, see **Figure 2D**). All these results suggest that the GTE distribution in canary songs is more heterogeneous than in zebra finch songs. To further investigate the origin of this heterogeneity, we studied the acoustical properties of syllables and further analyzed the distribution of GTEs.

Spectrogram Metrics of Canary and Zebra Finch Syllables

To further quantify song characteristics and compare both species, we analyzed the distribution of three syllable metrics, including a temporal and a spectrum-based parameter. These metrics were syllable duration, duration of a constant frequency segment within the syllable, and mean entropy (**Figure 3**). We looked with particular attention at one salient type of syllables in each species: whistles in canaries and harmonic stacks in zebra finches (see Methods, black diamond outlined points in **Figure 3**). Song segmentation produced 187 syllables for canaries (from 20 pseudo-motifs) and 119 for zebra finches (from 20 motifs).

Canary syllable duration (**Figure 3A**, left panel) fell into two defined groups: syllables that ranged up to 100 ms (max 96 ms), including very short syllables (note the amount of points indicating syllables with duration below 10 ms), and long syllables that lasted from 121 to 320 ms. Within the group of longer syllables, whistles had durations from 153 to 320 ms and made up 74% of this group.

To investigate in further detail syllables that contained long and simple sounds, we calculated the duration of a constant frequency segment within the syllable (see Methods). The distribution of this metric in canaries (**Figure 3A**, middle panel) has a defined minimum at 120 ms, separating two groups. We treated this value as a threshold. All the syllables that contain a constant frequency segment above threshold (orange points) were whistles (black diamond outline) and correspond to percentile 82.9. This shows that this metric is suitable for separating long simple syllables such as whistles. The constant frequency segment duration of the syllables above threshold ranged from 144 to 316 ms, whereas the rest of the syllables were in the range of 3–96 ms.

Examples of simple syllable spectrograms are shown as insets in the middle panel of **Figure 3A**. The supra-threshold, more tonal syllables are characterized in the top two insets: long whistle of a single fundamental frequency (other examples in **Figure 1D**, syllables 4 and 6). Other syllables that contained a mid-range constant frequency segment duration were made up of an upward or downward sweep as well as a tone and are usually shorter in length (bottom inset example of subthreshold syllable).

In the right panel of **Figure 3A,** we show the distribution of the entropy of canary syllables. The black dot indicates the median value of 0.34. Note that the canary whistle syllables take the lowest of the entropy values. Even though they ranged from 0.17 to 0.38, we found that the median of only the whistles was 0.19 (not shown in plot).

In the case of zebra finches, syllable duration was less widespread (see **Figure 3B**, left panel). Syllables lasted from 4 to 310 ms (note that the largest value is an outlier and that the second largest is 214 ms), with a median of 62 ms. Harmonic stacks are outlined with a black diamond. Their durations ranged from 32 to 91 ms, which is around the median value.

The middle panel of **Figure 3B** shows that constant frequency segments do occur in zebra finches (in the tail of the distribution), but they are shorter than those in canaries: their maximum value was 86 ms. This distribution did not present a well-defined feature that would allow us to naturally set a threshold. Harmonic stacks tend to have longer constant frequency segments but do not dominate the tail. However, almost all harmonic stacks surpassed the median value of the syllables which is 11 ms. They range from 11 to 86 ms and the median of only the harmonic stacks is 49 ms (not shown in plot). Examples of syllables from the tail of the distribution are shown in the insets of **Figure 3B**, middle panel. These include canonical harmonic stacks such as the one shown in the left inset, and syllables not classified as harmonic stacks: in the middle inset we show a syllable with two abrupt transitions containing two segments with harmonic stacks and in the right inset, one which is a short high frequency tone.

In terms of entropy, zebra finches tend to produce syllables of higher entropy than canaries (median 0.63 and ranging from 0.23 to 0.86, see right panel of **Figure 3B**). This agrees with the fact that their song is characteristically "noisier" than canary song. Harmonic stacks do not cluster in this metric as canary whistles do, since they have a wider entropy range and more variation in values (from 0.23 to 0.76). All but three of the harmonic stacks had an entropy value less than the median, which points out that they are not typically noisy syllables nor completely flat.

In summary, there is no equivalent long and simple syllable for the canary whistle in the zebra finch songs we analyzed. The syllable type we considered as a candidate were harmonic stacks, but not only do they fall short of the length of the canary whistles, they also do not emerge as an isolated group within this set of metrics.

Time Differences Between Consecutive GTEs

To further analyze the GTEs distribution, we analyzed the time difference between consecutive GTEs (20 canary pseudo-motifs, 505 GTE time intervals and 20 zebra finch motifs, 637 GTE time intervals). The silent gaps between syllables were not considered.

The time difference between consecutive GTEs for each bird is shown in **Figure 4A**, using red markers for canaries and blue markers for zebra finches. In the canary distribution, all birds have at least one large time difference. We identified the largest time differences (belonging to the 95th percentile, larger than 173 ms) in canaries (red filled markers) and found all these are from whistle syllables (diamond markers). Note that the largest GTE time difference in zebra finches was 76 ms, while in canaries it was 330 ms.

The distribution of time differences between consecutive GTEs is shown in **Figure 4B** for canaries and in **Figure 4C** for zebra finches. For both species, the mean time difference between consecutive GTEs is marked by solid vertical lines. For canaries, the mean was 28.0 ± 2.2 ms (mean $\pm$ SEM) and for zebra finches, it was 15.1 ± 0.4 ms (mean $\pm$ SEM). The values of the means are significantly different (t-test, $p < 0.01$). The larger value for canaries is due to the long tail in the distribution of time differences between GTEs. The 95th percentile is indicated in both distributions with black arrowheads (173 ms for canaries and 35 ms for zebra finches). It is worth mentioning that the median values were similar for both species: 12.2 ms for zebra finches and 12.6 ms for canaries. The standard deviation was 50.2 ms ($n = 505$) for canaries and for zebra finches it was 10.5 ms ($n = 637$). The standard deviations of the time difference distribution of the two species were significantly different (Levene test centering with the median, $p < 0.05$). These significant differences between the means and the standard deviations of the two species indicate that the distributions of GTE time intervals are more heterogeneous in canaries than in zebra finches.

We hypothesized that the difference between distributions was driven by the time differences from whistle notes in canaries. To test this hypothesis, we discarded all intervals that belonged to whistle syllables in canaries, i.e., we removed the values shown as diamonds in **Figure 4A** from the distribution of canary time differences. The mean of this new distribution was 14.7 ± 0.6 ms (mean $\pm$ SEM, $n = 472$), and the standard deviation was 12.4 ms ($n = 472$). The histogram of the new distribution is shown in the inset of **Figure 4B**. We did not modify the distribution of zebra finch time differences, but it is plotted with the same range in the inset of **Figure 4C** for comparison. In contrast with the previous comparison, the mean and the standard deviation of the modified canary distribution were not significantly different to the zebra finch unmodified distribution (t-test, $p > 0.5$ and Levene test centering with median, $p > 0.5$). This result shows that the difference between distributions were mainly driven by the canary whistle syllables.

DISCUSSION

The study of animal behavior requires contributions from many disciplines. An animal's nervous system acts upon its environment through a biomechanical device. Therefore, neural coding is best understood in the context of the specific motor instructions needed to control this device. In the case of birdsong, the control of the avian vocal organ and the respiratory system can be described in terms of continuous time dependent parameters called motor gestures. Complex songs imply a succession of different motor gestures, and the distribution of the instances known as GTEs is an indication of the complexity of the song. In this work, we studied the distribution of these significant temporal instances in the song of two species.

In this work, we show that the distribution of time differences between GTEs was significantly different between the compared species: canaries have long intervals between GTEs that occur mostly during their characteristic whistle syllables. We analyzed the acoustical properties of all syllables and found that canary whistles can be easily discriminated from other syllables by their long segments of constant frequency. In contrast, the distribution constant frequency segments in zebra finch syllables reaches a smaller value and does not contain two separate groups.

Birdsong requires the control of the respiration and of the syringeal configuration, which both affect acoustic features such as the song's fundamental frequency. The acoustic features of some simple syllables emerge from the interaction of a biomechanical process with brief interventions of the nervous system. As previously noted for zebra finches, it has been recently shown that some syllables only require impulsive activity in a syringeal muscle right before the onset of the sound and that the passive posterior relaxation of the labia is wholly responsible for the slow decay of the syllable's fundamental frequency [20]. Therefore, it is sensible to ask whether this simplicity in the muscle control of the biomechanical device requires simple instructions from the nervous system.

In the field of birdsong, it is debated whether telencephalic regions display a continuous code for the song, or a sparser code that reflects the song's structure. The original claim by Amador and collaborators that projecting neurons in the cortical nucleus HVC spike mostly at specific temporal instances (GTEs) falls into the latter alternative [8]. In 2015, this claim was refuted by Okubo and collaborators, since they found that neuronal bursts in HVC spanned almost the complete duration of the song [9]. However, their description of the ontogenesis of the song reveals that the heterogeneity of gestures does leave a fingerprint in the mature cortical activity. Studying the songs of juvenile zebra finches, the authors found that close to 50% of the recorded neurons were active only at the beginning of the simple syllables that the juveniles uttered. As the birds developed, they started to sing complex syllables that were different simple proto-syllables joined together. For those syllables, the projecting neurons in HVC kept their relative timing with respect to the song and, therefore, the temporal instances at which there were changes in the acoustics remained coded in the timing of the HVC-projecting neurons. As the birds continued to develop more complex songs, neuronal activity covered the duration of the song almost continuously. Given that developmental processes leave their fingerprint as a temporal heterogeneity in the cortical coding, our comparative study of the complexity of the motor gestures between two species allows us to identify a more suitable species

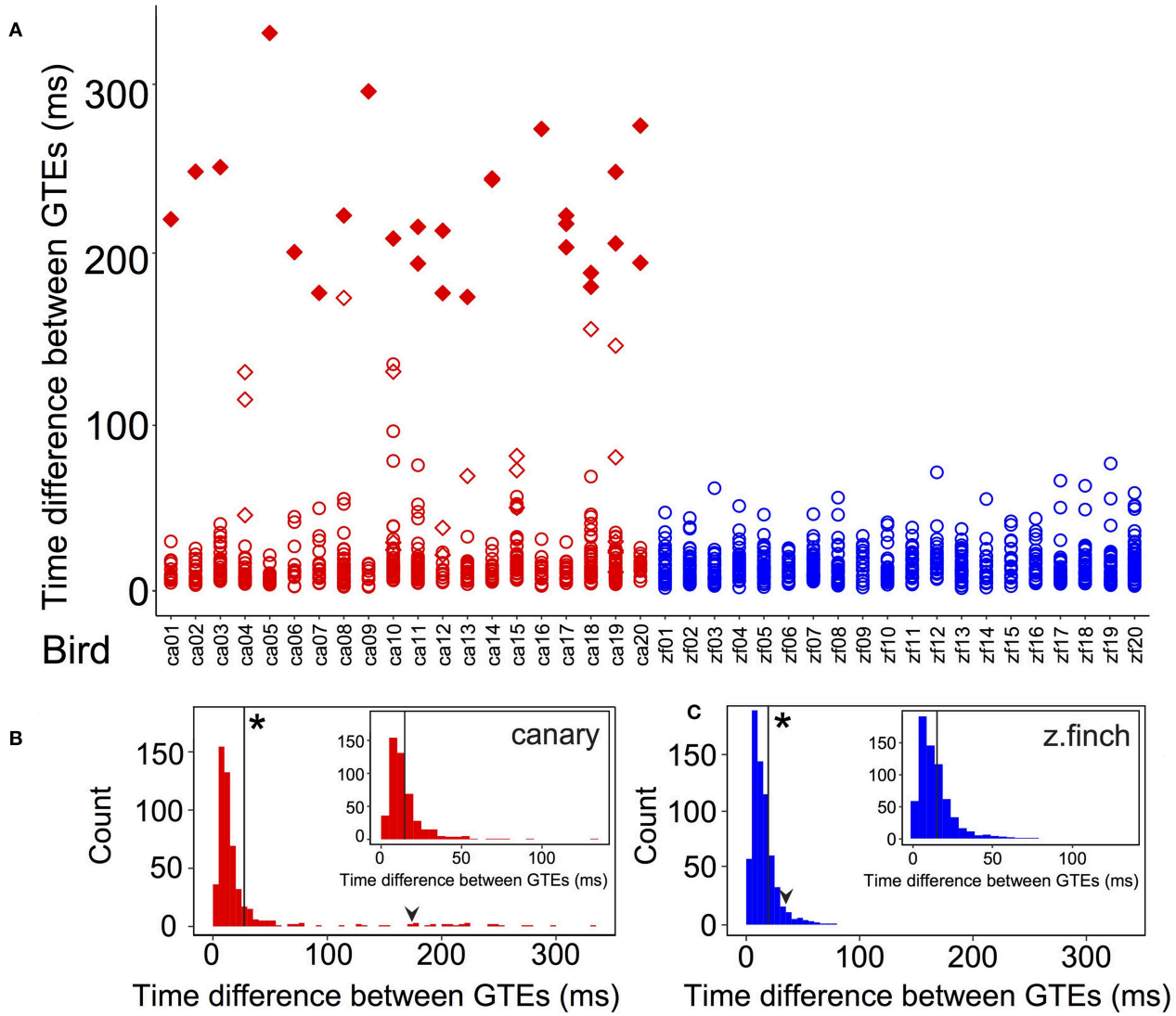

FIGURE 4 | Time differences between GTEs of each bird and grouped by species. **(A)** Time differences between GTEs for canaries (red markers) and zebra finches (blue markers). In canaries, diamonds indicate that the time difference belongs to a whistle syllable. Note that every canary has at least one diamond. The largest time differences of the canary distribution (in the 95th percentile, larger than 173 ms) are indicated with filled markers. Every time difference included in this group was from a whistle. **(B)** Histogram (5 ms bins) of time differences between consecutive GTEs in canaries and **(C)** in zebra finches. The black arrowheads show the value of the 95th percentile of each distribution (173 ms for canaries and 35 ms for zebra finches). The vertical black lines show the value of the mean of each distribution: 28.0 ± 2.2 ms (mean ± SEM) for canaries ($n = 505$) and 15.1 ± 0.4 ms (mean ± SEM) for zebra finches ($n = 637$). Asterisks in **(B,C)** indicate that these means were significantly different (*t*-test, $p < 0.01$). In canaries, the longest GTE time interval was 330 ms while in finches it was 76 ms. The standard deviation was 50.2 ms ($n = 505$) in canaries and 10.5 ms ($n = 637$) in zebra finches. These were significantly different (Levene test centering with the median, $p < 0.05$). (Inset B) Histogram (5 ms bins) of time differences between consecutive GTEs in canaries discarding those from whistle syllables. (Inset C) Zebra finch distribution of time differences as in **(C)**, at the same scale as (Inset B) for comparison. The vertical black lines in the insets show the mean of each distribution. For the new canary distribution, the value was 14.7 ± 0.6 ms (mean ± SEM, $n = 472$). The value for zebra finches is unchanged from **(C)**. In the new canary distribution, the standard deviation was 12.4 ms and the longest GTE time interval was 134 ms. The new canary mean and standard deviation were not significantly different from those of zebra finches (*t*-test, $p > 0.5$ and Levene test, $p > 0.5$).

to disambiguate between a heterogeneous, motor related, coding and a continuous one.

Recently, a neural model of the song system capable of reproducing the pressure and syringeal gestures of canaries during song production, incorporated a sparse activity pattern in HVC mounted on a continuous component [23]. Having a model is useful because it not only integrates anatomical and functional data, but also helps to understand plausible dynamical mechanisms behind the observed behavior. A puzzling aspect of observing cortical activity simultaneous with a temporally significant instance of the song (like a GTE) is that, intuitively, a delay between causally connected parts of the nervous system is expected. Yet, in the mentioned study of juvenile songs [9], neurons in HVC were found bursting simultaneously with

the beginning of syllables. In recent work [24], a model with continuous and sparse HVC coding describes the way in which causally connected regions of the song system can display activity simultaneous with the output of the nervous system, after a brief introductory transient. This makes it possible to predict, for example, an important increase of neural activity in the population of projection neurons at the beginning of the whistle syllables in canary song [23, 25]. Given the existence of large time differences between GTEs in the whistle syllables quantified in this work, we provide a specific and testable prediction.

We generated a visual representation of GTEs as a function of time similar to the way in which the neural activity in the HVC nucleus of zebra finches has been presented in the literature. We showed that, for the case of zebra finches, it is very difficult to distinguish between the representation that would be obtained if the coding were continuous from one produced by sparse coding. On the contrary, the whistle syllables of domestic canaries make it a suitable animal model to discriminate between a continuous and mostly uniform coding, and one where the fingerprints of the motor gestures are present. In the spirit of neuroethology, which studies behavior in the species that better displays it, we compared the distribution of GTEs in zebra finches and canaries and identified canaries as the species in which is it possible to discriminate between alternative models of cortical coding.

DATA AVAILABILITY STATEMENT

Datasets are available on request. The raw data supporting the conclusions of this manuscript will be made available by the authors, without undue reservation, to any qualified researcher.

ETHICS STATEMENT

Experimentation was conducted following protocols approved by the Institutional Animal Care and Use Committee (IACUC) of the University of Buenos Aires (FCEN, UBA).

AUTHOR CONTRIBUTIONS

GM and AA conceived and designed the experiments. JL and AA performed the experiments. JL, CH, AA, and GM analyzed the data and wrote the manuscript.

FUNDING

This work describes research partially funded by Consejo Nacional de Investigaciones Científicas y Técnicas (CONICET, Argentina), Agencia Nacional de Promoción Científica y Tecnológica (ANCyT, Argentina), Universidad de Buenos Aires (UBA, Argentina).

ACKNOWLEDGMENTS

We also wish to thank all the members of the Laboratorio de Sistemas Dinámicos (DF, FCEN, UBA, Argentina) for comments and discussions.

SUPPLEMENTARY MATERIAL

The Supplementary Material for this article can be found online at: https://www.frontiersin.org/articles/10.3389/fphy.2019.00142/full#supplementary-material

REFERENCES

1. Goldstein L. Temporal patterning in speech and birdsong. In: Bowern C, Horn L, Zanuttini R, editors. *On Looking Into Words (and Beyond): Structures, Relations, Analyses.* Berlin: Language Science Press (2017). p. 457–70.
2. Assaneo MF, Ramirez Butavand D, Trevisan MA, Mindlin GB. Discrete anatomical coordinates for speech production and synthesis. *Front Commun.* (2019) **4**:13. doi: 10.3389/fcomm.2019.00013
3. Bouchard KE, Mesgarani N, Johnson K, Chang EF. Functional organization of human sensorimotor cortex for speech articulation. *Nature.* (2013) **495**:327–32. doi: 10.1038/nature11911
4. Gardner T, Cecchi G, Magnasco M, Laje R, Mindlin GB. Simple motor gestures for birdsongs. *Phys Rev Lett.* (2001) **87**:208101. doi: 10.1103/PhysRevLett.87.208101
5. Amador A, Mindlin GB. Beyond harmonic sounds in a simple model for birdsong production. *Chaos.* (2008) **18**:043123. doi: 10.1063/1.3041023
6. Fee MS, Kozhevnikov AA, Hahnloser RHR. Neural mechanisms of vocal sequence generation in the songbird. *Ann N Y Acad Sci.* (2004) **1016**:153–170. doi: 10.1196/annals.1298.022
7. Hahnloser RHR, Kozhevnikov AA, Fee MS. An ultra-sparse code underlies the generation of neural sequences in a songbird. *Nature.* (2002) **419**:65–70. doi: 10.1038/nature00974
8. Amador A, Perl YS, Mindlin GB, Margoliash D. Elemental gesture dynamics are encoded by song premotor cortical neurons. *Nature.* (2013) **495**:59–64. doi: 10.1038/nature11967
9. Okubo TS, Mackevicius EL, Payne HL, Lynch GF, Fee MS. Growth and splitting of neural sequences in songbird vocal development. *Nature.* (2015) **528**:352–7. doi: 10.1038/nature15741
10. Picardo MA, Merel J, Katlowitz KA, Vallentin D, Okobi DE, Benezra SE, et al. Population-level representation of a temporal sequence underlying song production in the zebra finch. *Neuron.* (2016) **90**:866–76. doi: 10.1016/j.neuron.2016.02.016
11. Lynch GF, Okubo TS, Hanuschkin A, Hahnloser RHR, Fee MS. Rhythmic continuous-time coding in the songbird analog of vocal motor cortex. *Neuron.* (2016) **90**:877–92. doi: 10.1016/j.neuron.2016.04.021
12. Katlowitz KA, Picardo MA, Long MA. Stable sequential activity underlying the maintenance of a precisely executed skilled behavior. *Neuron.* (2018) **98**:1133–40.e3. doi: 10.1016/j.neuron.2018.05.017
13. Sossinka R, Böhner J. Song types in the zebra finch *Poephila guttata* castanotis. *Z Tierpsychol.* (1980) **53**:123–32. doi: 10.1111/j.1439-0310.1980.tb01044.x
14. Konishi M. Birdsong: from behavior to neuron. *Annu Rev Neurosci.* (1985) **8**:125–70. doi: 10.1146/annurev.ne.08.030185.001013
15. Nottebohm F, Stokes TM, Leonard CM. Central control of song in the canary, Serinus canarius. *J Comp Neurol.* (1976) **165**:457–86. doi: 10.1002/cne.901650405
16. Hartley RS, Suthers RA. Airflow and pressure during canary song: direct evidence for mini-breaths. *J Comp Physiol.* (1989) 165:15–26. doi: 10.1007/BF00613795
17. Boari S, Sanz Perl Y, Amador A, Margoliash D, Mindlin GB. Automatic reconstruction of physiological gestures used in a model of birdsong production. *J Neurophysiol.* (2015) **114**:2912–22. doi: 10.1152/jn.00385.2015

18. Ziegel E, Press W, Flannery B, Teukolsky S, Vetterling W. *Numerical Recipes: The Art of Scientific Computing*. 3rd ed. Cambridge: Cambridge University Press (2007).
19. Perl YS, Arneodo EM, Amador A, Goller F, Mindlin GB. Reconstruction of physiological instructions from zebra finch song. *Phys Rev E Stat Nonlin Soft Matter Phys.* (2011) **84**:051909. doi: 10.1103/PhysRevE.84.051909
20. Döppler JF, Bush A, Amador A, Goller F, Mindlin GB. Gating related activity in a syringeal muscle allows the reconstruction of zebra finches songs. *Chaos.* (2018) **28**:75517. doi: 10.1063/1.5024377
21. Goller F, Suthers RA. Role of syringeal muscles in gating airflow and sound production in singing brown thrashers. *J Neurophysiol.* (1996) **75**:867–76. doi: 10.1152/jn.1996.75.2.867
22. Suthers RA, Vallet E, Tanvez A, Kreutzer M. Bilateral song production in domestic canaries. *J Neurobiol.* (2004) **60**:381–93. doi: 10.1002/neu.20040
23. Alonso RG, Amador A, Mindlin GB. An integrated model for motor control of song in Serinus canaria. *J Physiol.* (2016) **110**:127–39. doi: 10.1016/j.jphysparis.2016.12.003
24. Dima GC, Copelli M, Mindlin GB. Anticipated synchronization and zero-lag phases in population neural models. *Int J Bifurc Chaos.* (2018) **28**:1830025. doi: 10.1142/S0218127418300252
25. Alonso RG, Trevisan MA, Amador A, Goller F, Mindlin GB. A circular model for song motor control in Serinus canaria. *Front Comput Neurosci.* (2015) **9**:41. doi: 10.3389/fncom.2015.00041

Conflict of Interest: The authors declare that the research was conducted in the absence of any commercial or financial relationships that could be construed as a potential conflict of interest.

Advantages of publishing in Frontiers

OPEN ACCESS
Articles are free to read for greatest visibility and readership

FAST PUBLICATION
Around 90 days from submission to decision

HIGH QUALITY PEER-REVIEW
Rigorous, collaborative, and constructive peer-review

TRANSPARENT PEER-REVIEW
Editors and reviewers acknowledged by name on published articles

Frontiers
Avenue du Tribunal-Fédéral 34
1005 Lausanne | Switzerland

Visit us: www.frontiersin.org
Contact us: info@frontiersin.org | +41 21 510 17 00

REPRODUCIBILITY OF RESEARCH
Support open data and methods to enhance research reproducibility

DIGITAL PUBLISHING
Articles designed for optimal readership across devices

FOLLOW US
@frontiersin

IMPACT METRICS
Advanced article metrics track visibility across digital media

EXTENSIVE PROMOTION
Marketing and promotion of impactful research

LOOP RESEARCH NETWORK
Our network increases your article's readership